Modelling Detailed-Chemistry Effects on Turbulent Diffusion Flames using a Parallel Solution-Adaptive Scheme

by

Pradeep Kumar Jha

A thesis submitted in conformity with the requirements
for the degree of Doctor of Philosophy
Graduate Department of Aerospace Science and Engineering
University of Toronto

Abstract

Modelling Detailed-Chemistry Effects on Turbulent
Diffusion Flames using a Parallel Solution-Adaptive Scheme

Pradeep Kumar Jha

`<jhapk@utias.utoronto.ca>`

Doctor of Philosophy
Graduate Department of Aerospace Science and Engineering
University of Toronto
2011

Capturing the effects of detailed-chemistry on turbulent combustion processes is a central challenge faced by the numerical combustion community. However, the inherent complexity and non-linear nature of both turbulence and chemistry require that combustion models rely heavily on engineering approximations to remain computationally tractable. This thesis proposes a computationally efficient algorithm for modelling detailed-chemistry effects in turbulent diffusion flames and numerically predicting the associated flame properties. The cornerstone of this combustion modelling tool is the use of parallel Adaptive Mesh Refinement (AMR) scheme with the recently proposed Flame Prolongation of Intrinsic low-dimensional manifold (FPI) tabulated-chemistry approach for modelling complex chemistry. The effect of turbulence on the mean chemistry is incorporated using a Presumed Conditional Moment (PCM) approach based on a β-probability density function (PDF). The two-equation k-ω turbulence model is used for modelling the effects of the unresolved turbulence on the mean flow field. The finite-rate of methane-air combustion is represented here by using the GRI-Mech 3.0 scheme. This detailed mechanism is used to build the FPI tables. A state of the art numerical scheme based on a parallel block-based solution-adaptive algorithm has been developed to solve the Favre-averaged Navier-Stokes (FANS) and other governing partial-differential equations using a second-order accurate, fully-coupled finite-volume formulation on body-fitted, multi-block, quadrilateral/hexahedral mesh for two-dimensional and three-dimensional flow

geometries, respectively. A standard fourth-order Runge-Kutta time-marching scheme is used for time-accurate temporal discretizations. Numerical predictions of three different diffusion flames configurations are considered in the present work: a laminar counter-flow flame; a laminar co-flow diffusion flame; and a Sydney bluff-body turbulent reacting flow. Comparisons are made between the predicted results of the present FPI scheme and Steady Laminar Flamelet Model (SLFM) approach for diffusion flames. The effects of grid resolution on the predicted overall flame solutions are also assessed. Other non-reacting flows have also been considered to further validate other aspects of the numerical scheme. The present schemes predict results which are in good agreement with published experimental results and reduces the computational cost involved in modelling turbulent diffusion flames significantly, both in terms of storage and processing time.

Contents

List of Tables

List of Figures

Nomenclature

α scalar value

χ scalar dissipation rate of mixture fraction

δ_{ij} Kroneckar delta function

ΔA_{m} unit surface area of the mth cell face

$\dot{\omega}_k$ mass reaction rate of species k produced by the chemical reactions

ϵ dissipation rate of turbulent kinetic energy

κ mixture thermal conductivity

$\mathbf{F}_{\mathrm{I}}$ inviscid flux vector in the x direction

$\mathbf{F}_{\mathrm{V}}$ viscous flux vector in the x direction

$\mathbf{G}_{\mathrm{I}}$ inviscid flux vector in the y direction

$\mathbf{G}_{\mathrm{V}}$ viscous flux vector in the y direction

$\mathbf{H}_{\mathrm{I}}$ inviscid flux vector in the z direction

$\mathbf{H}_{\mathrm{V}}$ viscous flux vector in the z direction

$\mathbf{R}_{\mathrm{i,j}}$ residual operator for the control volume (i, j)

$\mathbf{S}_{\mathrm{aI}}$ source terms associated with the axisymmetric coordinate for inviscid and viscous fluxes

$\mathbf{S}_{\mathrm{aV}}$ source terms associated with the axisymmetric coordinate for inviscid and viscous fluxes

$\mathbf{S}$ source term vector

$\mathbf{S}_c$ source terms associated with the finite-rate chemical kinetics

$\mathbf{S}_p$ source terms associated with the transport equations for PCM-FPI scalars

$\mathbf{S}_t$ source terms associated with the turbulence modelling

$\mathbf{U}$ vector of conserved variables

$\mathcal{A}_k$ atomic weight of species k

$\mathcal{D}^k$ molecular diffusivity of the species k relative to the mixture

$\mathcal{D}_f$ molecular diffusion coefficient of mixture fraction $= \zeta/\rho/c_p$

$\mathcal{D}_k$ diffusion coefficient for turbulent kinetic energy $= (\mu + \sigma^* \mu_t)$

$\mathcal{D}_t$ turbulent diffusion coefficient $= \mu_t/\mathrm{Sc}_t$

$\mathcal{D}_{Y_c}$ molecular diffusivity of the progress of reaction variable $= \mu/\rho/\mathrm{Sc}_{Y_c}$

$\mathcal{M}_k$ molecular mass of species k

$\mathcal{T}$ time-scale

$\mathcal{T}_c$ chemical time-scale

$\mathcal{T}_t$ turbulence time-scale

μ molecular viscosity

μ_t eddy-viscosity

ν kinematic viscosity

Ω closed surface of the control volume

ω specific dissipation rate of turbulent kinetic energy

$\overline{\phi}$ Reynolds-averaged mean component of quantity ϕ

ϕ^* sample space variable for variable ϕ

ϕ'' fluctuating component of quantity ϕ in Favre averaging

ϕ' fluctuating component of quantity ϕ in Reynolds averaging

ϕ_v variance of quantity ϕ

ρ mixture density

Sc^k Schmidt number of species k

Sc_t turbulent Schmidt number, set to 1.0

Sc_{Y_c} progress of reaction Schmidt number, set to 1.0

$\varkappa$ Kármán constant $= 0.41$

$\mathbf{F}$ flux dyad

$\vec{\mathcal{J}}^k$ molecular diffusive flux of the species k

$\overset{\rightrightarrows}{\lambda}$ Reynolds stress tensor

$\overset{\rightrightarrows}{\tau}$ viscous force tensor

$\vec{g}$ body force vector

$\vec{n}$ unit outward vector normal to the closed surface

$\vec{q}$ molecular heat flux vector

$\vec{u}$ velocity vector

$\vec{x}$ position vector

$\vec{\mathcal{J}}_t$ turbulent diffusive flux

$\vec{q_t}$ turbulent heat flux vector

$\widetilde{\phi}$ Favre-averaged mean component of quantity ϕ

ζ mixture thermal conductivity

A pre-exponential constant

C integration constant in law of the wall $= 0.5$

c progress variable $= Y_c(\phi, x)/Y_c^{\mathrm{Eq}}(\phi, x)$

C_f closure coefficient for mixture fraction variance, f_v, transport equation $= 1.0$

c_p gas specific heat at constant pressure

C_{Y_c} closure coefficient for progress of reaction variable variance, Y_{cv}, transport equation $= 1.0$

e specific total energy $(u_i u_i/2 + h - p/\rho + k)$

f mixture fraction

G_k Gibbs free energy for species k

h specific total enthalpy, $\displaystyle\sum_{k=1}^{N} Y_k h_k$

h_k absolute (chemical plus sensible) internal enthalpy for species k

h_k^f heat of formation of species k

k turbulent kinetic energy

l_t turbulent integral length scale

M number of species in the reduced set of FPI tabulation

m total mass of gas in the volume

m_k mass of species k present in the given volume

N total number of species

n_{C_k} number of carbon atom in species k

p mixture pressure

R_k gas constant of species k

Re Reynolds number

s stoichiometric oxygen-to-fuel mass ratio

s_k entropy of species k

T mixture temperature

t time coordinate

T_A activation temperature

u_τ friction velocity $= \sqrt{\tau_w/\rho}$

V control volume

V_{corr} correction velocity

x spatial coordinate in the direction normal to the flame front

y^+ dimensionless distance from the wall $= u_\tau y_{\text{wall}}/\nu$

Y_F fuel mass fraction

Y_O oxidizer mass fraction

Y_k mass fraction of species $k = m_k/m$

y_{wall} normal distance from the wall

τ_w wall shear stress

Pr_t turbulent Prandtl number, set to 0.9

Y_c^{Eq} Y_c value in the burnt state (or equilibrium)

ϕ equivalence ratio

Y_c progress of reaction

Da   Damköhler number

Re_t turbulent Reynolds number

"Don't take it all too seriously."

Kurt Vonnegut - *Palm Sunday*

1

Introduction

This thesis aims at developing a computationally efficient algorithm for the numerical prediction of turbulent reactive flows - specifically for non-premixed turbulent combustion. Combustion is the most important physico-chemical process used presently for meeting most of mankinds' energy needs and is expected to continue to be so for the foreseeable future. The Oxford dictionary defines combustion as *"rapid chemical combination of a substance with oxygen, involving the production of heat and light"*. This definition is useful in providing an insight into the general combustion process. However, both the production of heat and light are a result of fairly complex chemical and physical processes and the details involved in these processes comprises the focus of the majority of the combustion research community.

Studying combustion is of immense practical importance to society today. From the smallest day to day domestic needs of heat for cooking food to the huge burners in aircraft engines - combustion plays an important role in many modern day devices, either directly or indirectly. Most of these combustion devices rely heavily on fossil fuels as their fuel source. Despite the large variety of alternate energy sources available, such as nuclear, solar, wind, hydroelectric, geothermal etc., the chemical energy derived from burning fossil fuels continues to be the major source for meeting the total world energy needs - around 85% at present [1, 2]. Figure 1.1 gives a fair indication of the dependence of the present day economy on fossil fuels. The figure shows that in 2009, the amount of energy consumed by the United States of America by burning fossil fuels (petroleum, natural gas and coal) was collectively more than 10 times the sum of energy consumed by all other sources. At the same time, the world energy production is growing at a rate of 2.3 percent per annum [3]. This places a lot of pressure on the existing finite resources of fossil fuels and obviously calls for the design of more efficient burners and engines which
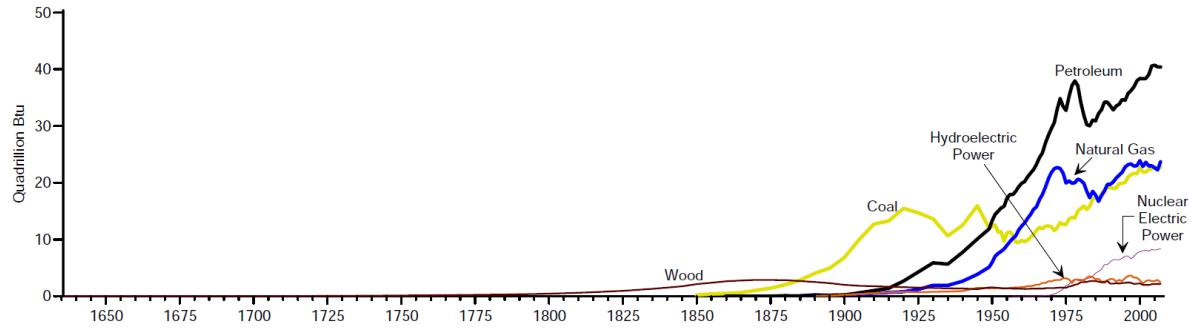
Figure 1.1: Trend of energy consumption in the United States of America over the last few centuries. The USA tends to be one of the largest consumers of energy in the world, and its primary dependence is still on fossil fuels. *Source: U. S. Energy Information Administration* [1].

can use fuels more effectively.

Apart from the increasing need for more and more energy, the dependence on fossil fuels is also an alarming environmental issue. Combustion of fossil fuels contribute to the increase in greenhouse gases in the atmosphere more than any other form of energy production. Carbon dioxide (CO_2) is a major byproduct produced in significant amounts when burning any fossil fuel. The annual CO_2 emissions from fuel combustion has increased seven fold in the last 50 years [4]. Apart from CO_2, other byproducts can also be formed as a result of improper combustion. Poor or non-optimized combustor designs can result in the formation of excessive amounts of carbon monoxide (CO), oxides of sulfur (SO_x), and nitrogen oxides (NO_x). These oxides are detrimental to human respiratory health if inhaled in large quantities. Also, these oxides tend to react with ozone and water present in the atmosphere and can cause unwanted and harmful effects like reduction in ozone layer thickness and acid rain which are detrimental to the environment.

The concerns summarized above and many other similar issues have resulted in the formulation and enforcement of strict environmental regulations by many governments [5, 6]. Newer and more efficient engines are being demanded which can give similar or better performance, but will lower levels of pollutant formation and lower costs. This makes it important to study combustion from a fundamental point of view - to understand the physical and chemical structure of flames, their properties and how they can be better controlled.

1.1 Combustion and Computational Fluid Dynamics

Combustion is a complex phenomenon, that is controlled by many physical processes including thermodynamics, buoyancy, chemical kinetics, radiation, mass and heat transfers and fluid mechanics. This makes conducting experiments for multi-species reacting flames extremely challenging and financially expensive. For these reasons, computer modelling of these processes is also playing a progressively important role in producing multi-scale information that is not available by using other research techniques. In many cases, numerical predictions are typically less expensive and can take less time than similar experimental programs and therefore can effectively complement experimental programs. Computational models can help in predicting flame composition, regions of high and low temperature inside the burner, and detailed composition of byproducts being produced. Detailed computational results can also help us better predict the chemical structure of flames and understand flame stabilization processes.

These capabilities make Computational Fluid Dynamics (CFD) an excellent tool to complement experimental methods for understanding combustion and thus help in designing and choosing better fuel composition according to the specific needs of a burner. With the advent of more and more powerful computing resources, better algorithms, and the numerous other computational tools in the last couple of decades, CFD has evolved as a powerful tool to study and analyze combustion. However, numerous challenges are involved in making CFD a reliable and robust tool for design and engineering purposes.

1.1.0.1 Turbulence and Combustion

Both turbulence and chemistry are highly non-linear and complex phenomena. Turbulence, even just by itself, is complex and is probably the most significant unresolved problem of classical physics. Since the flow is turbulent in nearly all engineering applications, the urgent need to resolve engineering problems has provided a strong need for engineering models of turbulence. Although a number of mathematical models have been developed which tend to give a fair prediction of turbulent flow properties, a universally accepted numerical formulation of turbulence has really not yet been achieved.

Modelling the effects of turbulence on chemistry is one of the most important challenges in numerical combustion modelling. Combustion requires fuel and oxidizer to be mixed at the molecular level. In turbulent flows, the turbulent mixing process is an important factor in determining how the mixing takes place. Not only does turbulence
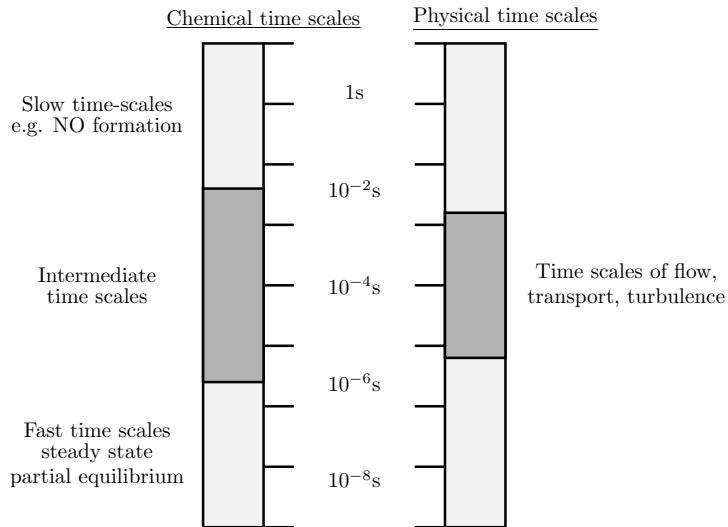
Figure 1.2: Time-scales in a turbulent combusting flow[7].

enhance the mixing of reactants, once the flame has developed, the conduction of heat and the diffusion of radicals are also strongly affected by turbulence. Furthermore, combustion involves a large number of elementary chemical reactions that can occur on very different time-scales from each other and from that of the flow. Figure 1.2 provides a rough approximation of the general range of variation in the time-scales of the turbulent and chemical time-scales in a flow. An accurate modelling of turbulence chemistry will require resolving or including the effects of all of these scales in the simulation. To complicate things further, still not much is known about the detailed chemistry of most common fuels, other than for a few simple hydrocarbons. The few detailed reaction mechanisms which have been developed tend to involve a large number of intermediate species and reaction steps. Solving by numerical means such large systems of partial differential equations, which accounts for all the above mentioned criteria, places heavy demands on computational resources in terms of processor time, memory and storage requirements and so limits the application of Direct numerical simulation (DNS) to combustion problems of more academic interest. DNS, in which all of the spatial and temporal scales for the reactive flow are fully resolved, for practical combusting flows is currently not possible nor will it be in the foreseeable future.

The many challenges faced by the current CFD community in dealing with turbulent combustion makes numerical modelling of turbulent combustion processes an area of active research and interest. The present thesis tries to address a few of these numerical challenges for a specific class of flames called diffusion flames.

(a) Premixed Combustion   (b) Nonpremixed Combustion
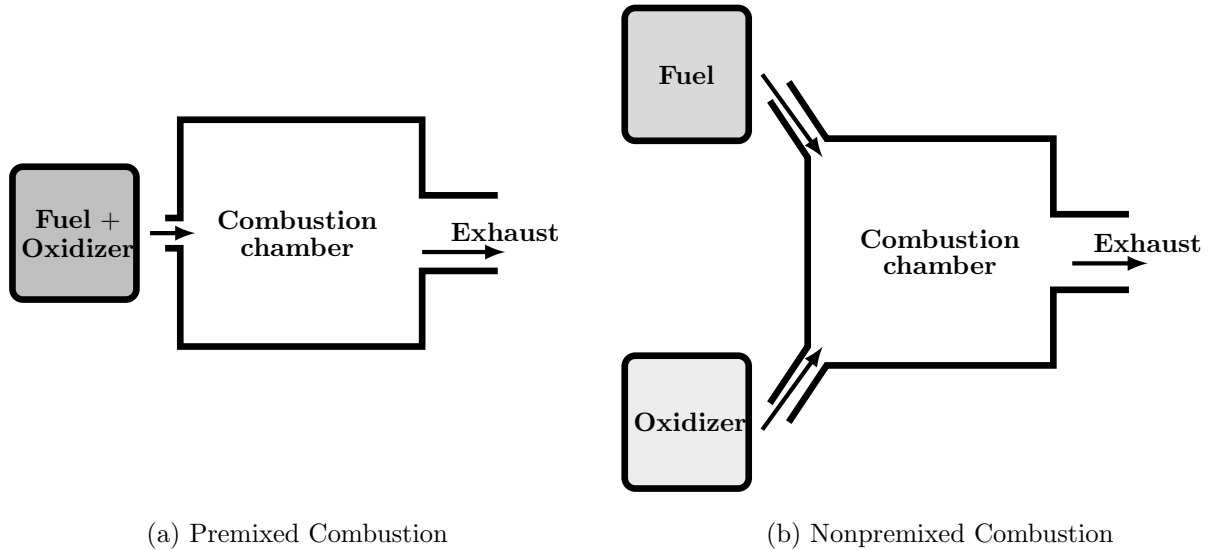
Figure 1.3: Schematic diagrams showing the two broad categorization of combustion processes for premixed and non-premixed flames.

1.2   Diffusion Flames

All flames can be broadly classified into one of two categories:

1. premixed flames; and

2. non-premixed or diffusion flames.

Figure 1.3 clearly illustrates the key differences between a premixed and a non-premixed combustion process. Combustion processes where the fuel and oxidizer are mixed with each other at a molecular level before they enter the combustion chamber are called premixed processes while combustion processes where fuel and oxidizer mix with each other only in the combustion chamber are called non-premixed processes. Turbulent non-premixed flames occur in a wide array of practical applications such as gas turbine and diesel engines, oil, gas, pulverized coal-fired boilers and furnaces, chemical lasers, rocket exhaust plumes, and fires and are of primary interest here. Moreover, because fuels and oxidizers are stored separately before the combustion takes place, non-premixed flames tend to operate with greater safety.

Figure 1.4 shows a schematic representation for the structure of a non-premixed flame. As shown in the figure, the fuel and the oxidizer are on opposite sides of the reaction zone where heat is released. In diffusion flames the rate of reaction is often controlled by the rate of mixing and the molecular diffusion of the reactants toward the reaction
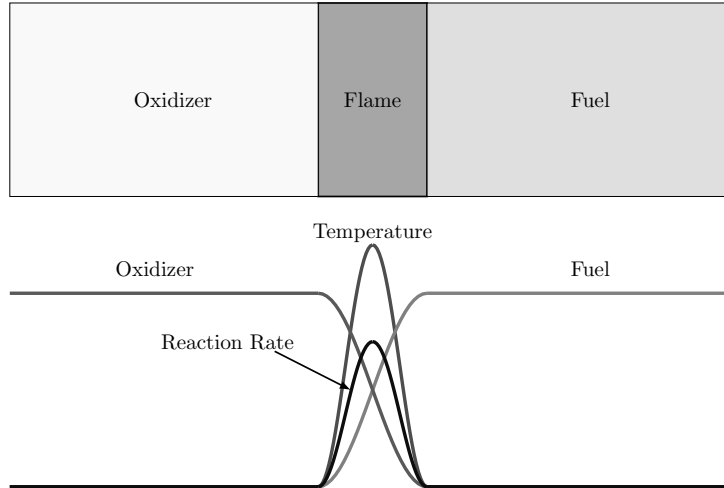
Figure 1.4: Schematic diagram showing general structure of a laminar diffusion flame [8].

zone. Because diffusive transport is essential in the effecting mixing of reactants at the molecular level, non-premixed combustion is also known as "diffusion combustion". Diffusion flames differ from premixed flames in a number of ways. Unlike premixed flames, these flames tend not to be self-propagating and the combustion is not characterized by the propagation of a well-defined flame surface. Also, they do not have a reference "thickness" like premixed flames and the thickness depends on local flow properties and, because diffusion flames are dependent on the molecular mixing of reactants, they also tend to be more sensitive to turbulence than premixed flames.

Turbulent reacting flows are complex and obtaining robust analytical solutions is almost impossible. As noted previously, a range of length and time scales are involved in turbulent flow fields with chemical reactions. Physical analysis based on the comparison of these scales can provide good insight into the structure of turbulent flames and help derive models for turbulent combustion. The turbulent flow is characterized by a turbulent Reynolds number, Re_t, comparing turbulent transport to viscous forces:

$$Re_t = \frac{u' l_t}{\nu} \tag{1.1}$$

where u' velocity rms, l_t is the turbulent integral length scale and ν is the kinematic viscosity of the flow. The Damköhler number compares the ratio of turbulent and chemical time-scales:

$$Da = \frac{\mathcal{T}_t}{\mathcal{T}_c} \tag{1.2}$$

where $\mathcal{T}_t$ is the turbulence time-scale and $\mathcal{T}_c$ is the chemical time-scale.
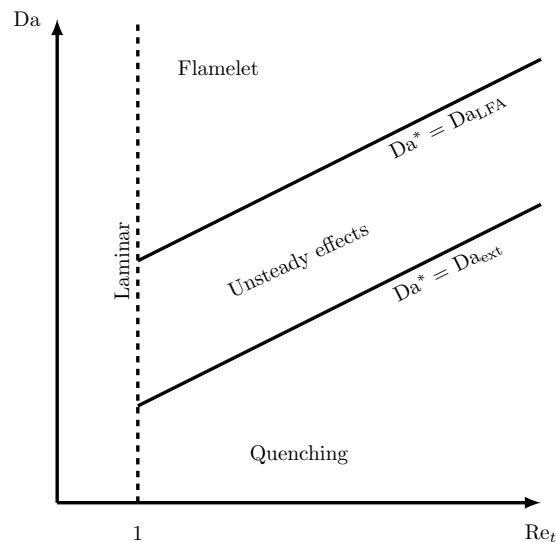
Figure 1.5: Schematic diagram of non-premixed turbulent combustion regimes as function of the Damköhler number Da= $\mathcal{T}_t/\mathcal{T}_c$ (constructed from the turbulent integral time-scale $\mathcal{T}_t$ and chemical time-scale $\mathcal{T}_c$) and Re$_t$, the turbulent Reynolds number [8] (log scales are used for both Da and Re$_t$ in the graph).

In the limit of high Damköhler number (Da$\gg$ 1), the chemical time-scale is short compared to the turbulent time-scale and this corresponds to a non-premixed flame with a thin reaction zone distorted and convected by the flow field. The internal structure of the flame is not strongly affected by turbulence and is described as a laminar flame element called a 'flamelet'. The turbulent structures merely wrinkle and strain the flame surface. In these regions, the laminar flamelet assumptions (LFA) is valid. On the other hand, a low Damköhler number corresponds to a slow chemical reaction. Reactants and products are mixed by turbulent structures before reaction. This is called the *perfectly stirred reactor* limit.

Most practical combustion processes correspond to high or medium Damköhler numbers and these regimes will be of primary concern in the present thesis. Veynante and Vervisch [8] have shown that Da and Re$_t$ can be related by the expression

$$Da = \alpha\sqrt{Re_t Da^*} \tag{1.3}$$

where α is a proportionality constant and Da* is a constant or reference Damköhler number. The preceding expression shows that constant Damköhler numbers correspond to lines of slope 1/2 on a log-log plot of Da versus Re$_t$ - a so called (Da, Re$_t$) diagram. When the chemistry is sufficiently fast, the flame is expected to have a local laminar

flame structure locally. This condition may be simply expressed as $\mathrm{Da}^* \geq \mathrm{Da}_{\mathrm{LFA}}$. On the other hand, for large chemical time scales (when $\mathrm{Da}^* \geq \mathrm{Da}_{\mathrm{ext}}$) extinction occurs. Laminar flames are encountered for low Reynolds numbers ($\mathrm{Re}_t < 1$). These findings are summarized in Figure 1.5. This thesis will focus on addressing flames that lie in the so-called 'flamelet' region of the figure.

1.3   Computational Research in Combustion

Computational research in combustion is a vast topic, and it is impossible to summarize the field fully in the brief review given in this section. Bilger et al. [9], Veynante and Vervisch [8] and Eaton et al. [10] are some useful readings which give a wide perspective of the various numerical approaches being used presently in the numerical modelling of reactive flows. In this section, previous and currently ongoing computational combustion research relevant to this thesis is discussed, i.e., current advances in turbulence modelling, parallel adaptive mesh refinement (AMR), and modelling turbulence-chemistry interactions.

   Three primary tools for performing simulations of turbulent combusting flows have emerged: (i) direct numerical simulation (DNS); (ii) large-eddy simulation (LES); (iii) and Reynolds- or Favre-averaged Navier-Stokes (RANS/FANS) simulation techniques. As discussed earlier in Section 1.1, due to the heavy computational costs involved, DNS is generally restricted to generic simplified and/or more academic combustor configurations. LES is an alternative to DNS in which the large eddies are computed directly and the small, generally more universal, dissipative, turbulent-scales are modelled, thereby offering potential computational savings [11–14]. Over the last decade, the approach has evolved to become a truly predictive tool for non-reacting flows [11–13, 15, 16] and has been shown to provide more accurate predictions of the flow fields than the more conventional RANS-based methods for reacting flows [17]. Nevertheless, universal and accurate sub-filter scale models for non-premixed and premixed reacting flows are not currently available and the accurate and reliable numerical solution of the filtered Navier-Stokes equations remains a significant computational challenge for many practical problems.

   As LES is still at an early stage of development for combusting flows [14, 18, 19] and due to the still relatively high cost of performing such simulations, especially in three-dimensional geometries, RANS/FANS-based methods are the predominant approach in engineering CFD applications for combusting flows involving complex flow geome-

tries [20]. Nevertheless, in spite of simplifications offered by time-averaging approaches, the system of time-averaged equations governing turbulent combusting flows can be both large and stiff and its solution can still place severe demands on available computational resources. Therefore solution techniques are required to reduce the computational costs of simulating combusting flows using RANS-based methods, thereby permitting their application on a more routine basis to a wider range of problems.

Two approaches which can significantly help in reducing the computational costs are using more "intelligent" solution-adaptive grids and to parallelize the computational process. The AMR algorithm, as originally proposed by Berger [21], is a smart way of generating efficient grids depending on the flow geometry. Given an initially coarse mesh, that hopefully can be generated in a relatively short period of time, AMR algorithms can then automatically produce more refined meshes according to the solution profile and can thus help in significantly reduce the manpower and computational cost associated with the mesh generation. AMR techniques have been applied to a wide range of engineering problems [22–40]. A discussion of popular AMR techniques in use today can be found in the thesis of Gao [41].

Large massively-parallel distributed-memory computers provide another approach by enabling a many fold increase in processing power and memory resources beyond those of conventional single-processor computers [42, 43]. These parallel computers provide an obvious avenue for greatly reducing the time required to obtain numerical solutions of combusting flows. Parallel computing has been used by a number of researchers for different combustion problems like flame-sheet problem [44, 45], finite-rate chemistry [45, 46], two-step sequential reaction mechanism [47] and computation of a dispersed spray in a turbulent flow [48].

Combined parallel AMR algorithms have also been considered in previous studies. Recent progress in the development and application of parallel AMR algorithms for low-Mach-number reacting flows and premixed turbulent combustion is described by Day and Bell [49–54]. More recently, Northrup and Groth [55], Gao and Groth [56, 57] and Charest et al. [58] have proposed parallel block-based AMR methods using body-fitted multiblock meshes for application to both laminar and turbulent non-premixed combusting flows. The present work will be an extension of these parallel block-based AMR methods.

Another important goal of the present work is to model the effect of detailed-chemistry in turbulent combustion. Broadly speaking, the various turbulent combustion models for

diffusion flames generally rely heavily on two approaches: a geometrical or structural analysis of the flames as well as statistical representations of the flames [8]. In the structural analysis, the flame is usually linked to a flamelet assumption (the flame is thin compared to flow scales). Following this view, scalar fields (like mixture fraction) are studied in terms of dynamics and physical properties of iso-value surfaces. The flame is envisioned as an interface between fuel and oxidizer. This concept will be discussed in greater detail later in Chapter 3 to follow.

Statistical approaches make use of probability density distributions (PDFs), which permit the relaxation of the assumptions made by geometrical approaches regarding flame surfaces and interfaces. Statistical approaches based on transported PDFs [59–61] involve the solution of an additional transport equation for the full filtered joint PDF of the various flow quantities. This is in addition to the usual transport equations for the filtered mass fractions, momentum, and energy. By directly solving for the full joint PDF, such approaches are not dependent on any hypotheses regarding the PDF shape. However, as the chemical kinetic scheme becomes generally larger and more complicated, the number of additional dimensions in which PDF transport equation is defined and must be solved can increase quite significantly, making its solution increasingly expensive [62].

In another approach, called the conditional moment closure (CMC) method as first proposed by Bilger [63] and Klimenko [64], the Navier-Stokes transport equations for a reactive flow are conditionally averaged and solved in physical space, time, as well as the space defined by an appropriate conditioning variable. The conditioning variable is selected depending on the chemical reaction rates on the combustion regime of interest. For turbulent diffusion flames, the mixture fraction is used as the conditioning variable and the CMC approach has been shown to provide accurate predictions for a range of flames [65–68]. The development of the CMC method for turbulent premixed flames requires the definition of an alternate conditioning variable and has been considered by Swaminathan and Bilger [69] with modest success to date. Recently, Steiner and Bushe [70] have also recently proposed a new and related combustion modelling approach based on the CMC chemical closure hypothesis, referred to as the Conditional Source-term Estimation (CSE) method. The CSE method has been shown to work very well for diffusion flames [70, 71] and its performance for premixed flames is currently under investigation [72, 73].

The particular method of interest for modelling detailed chemistry in the present work is the Flame Prolongation of Intrinsic low dimensional manifold (FPI). The presumed

conditional moments (PCM) approach [74] is used in conjunction with the FPI approach to model the effect of turbulence on the detailed-chemistry reaction mechanism. The PCM-FPI method is of current interest as it is a potentially unifying approach capable of modelling both premixed and non-premixed flames. The promising features and predictive capabilities of the PCM-FPI method, and similar variants thereof [75–78], for the full range of combustion regimes has resulted in the active development of the approach by a number of different research groups [19, 79–83]. A detailed discussion of the PCM-FPI approach and various other tabulated-chemistry algorithms developed to model turbulent-chemistry interaction is reserved for later in Chapter 3 and will not be discussed further here.

1.4 Thesis Objectives

Before stating the primary objectives of this thesis, a brief summary of the key points discussed above is first given. As the available resources of fossil fuels are finite, there is a continuous rise in the demand for more efficient and powerful combustion devices. At the same time, there is a need for designing engines which are environmentally friendly and not detrimental to human health. CFD is evolving as a powerful tool to study and analyze combustion numerically and hence help in designing better combustion devices. However, there are numerous challenges involved in modelling combustion numerically: two important challenges being modelling the effect of detailed-chemistry and modelling turbulence-chemistry interaction.

This thesis then aims at devising a robust and efficient computational algorithm that harnesses the potential of high-end parallel computers and thereby enables more routine prediction of practical combustion processes. The focus of this work is fourfold: (1) to incorporate the effects of detailed chemistry on diffusion flames; (2) to provide an accurate modelling of turbulence-chemistry interactions for numerical simulation of turbulent diffusion flames; (3) to integrate the turbulence-detailed-chemistry interaction model with the existing solution-adaptive mesh-refinement capability of Gao et al. [41, 57, 84, 85] as described above to achieve a computationally more efficient scheme for diffusion flames having disparate spatial scales; and (4) the parallelization of the resulting numerical scheme so as to improve the computational performance for practical simulations. The thesis will be novel in its attempt to integrate the PCM-FPI approach, a fully-compressible FANS-based approach for non-premixed flames, and the

parallel solution-adaptive mesh-refinement numerical framework for the first time. Finally, it should be noted that in the present work, somewhat simplified flow geometries and flame configurations will be studied. However, the validity and efficiency of the final algorithm for practical combustion processes depends on the validity and efficiency of its components, so the importance of these fundamental validation studies should not be underestimated.

The starting point for the proposed method development considered here is the highly-scalable parallel AMR numerical framework developed previously by the UTIAS CFD and Propulsion group for both two-dimensional planar and axisymmetric laminar and turbulent reactive flows [55–58, 84] and fully three-dimensional laminar and turbulent reactive flows [41, 85]. The existing numerical framework was limited to prediction of laminar diffusion flames with detailed chemistry and turbulent diffusion flames using a simplified eddy dissipation model with one-step finite-rate chemistry models. It was incapable of accurately incorporating the effects of detailed-chemistry on the mean flow quantities of turbulent reactive flows. The solution of FANS equations for reactive flows in two- and three-dimensional geometries is considered here and tabulated chemistry based on the FPI approach discussed above is adopted for dealing with detailed chemistry in the turbulent diffusion flame regime. While primarily developed for premixed combustion, the extension extension of the FPI algorithm to diffusion flames using a parallel block-based AMR solution scheme is one of the major focuses of the present research.

The influence of the unresolved turbulence on the FANS-based numerical solutions of the turbulent reactive flows is handled by using the two-equation k-ω turbulence model of Wilcox [86]. A PCM approach is used in conjunction with the FPI approach to account for the turbulence-chemistry interactions in nonpremixed turbulent combusting flows. Actually, turbulent premixed flames can also be described with this approach but will not considered herein. Such studies are left for future research. The two-equation k-ω turbulence and PCM-FPI combustion models have all been implemented within the parallel AMR framework for treating both two- and three-dimensional flame geometries.

To summarize, the tasks involved in order to achieve the thesis goals are as follows:

- Develop a table-generation and table-data-extraction algorithm for implementing the FPI algorithm. The table-generation algorithm must be flexible in terms of the size and structure of the table, which can become a huge concern for turbulent non-premixed tables.

- Develop an algorithm to extend the FPI method to non-premixed flames. The FPI method is primarily based on laminar premixed flame solution and an extrapolation technique needs to be developed for using it in non-premixed regimes.

- Implement the two-equation k-ω turbulence model with appropriate low-Reynolds number formulations to deal with wall bounded turbulent flows.

- Implement the presumed conditional moment (PCM) approach with the FPI approach to account for the turbulence-chemistry interaction.

- Extend the PCM-FPI FANS approach to be used in the parallel AMR framework so that it can be used both for two- and three-dimensional flow geometries.

- Validate the new framework for detailed-chemistry for different flow configurations. In particular, investigate

  - the FANS implementation for several non-reacting wall-bounded turbulent flows;

  - the performance of FPI approach for two-dimensional axisymmetric laminar flames and compare the performance of FPI tabulation method to more standard non-premixed flamelet models (the latter are presently among the more popular ways of dealing with diffusion flames and the comparisons will be a good demonstration of the FPI model validity);

  - the results of PCM-FPI for two- and three-dimensional turbulent diffusion flames, comparing predicted results to available experimental data and other numerical results obtained using simplified turbulent combustion models so as to assess the performance of the proposed methodology.

1.5   Thesis Organization

The thesis is organized in the following order. Chapter 2 discusses the mathematical description, i.e., the equations used to describe a turbulent combusting flow. Chapter 3 describes the PCM-FPI algorithm in detail. Chapter 4 elaborates on the fundamentals of the finite-volume formulation and the parallel AMR algorithm. Application of these

algorithms to different flame configurations for validation studies, by comparing the results to experimental and other numerical models, is done in Chapter 5. Finally, the conclusions, contributions and recommendations are given in Chapter 6.

2

Mathematical Description of Turbulent Combustion

2.1   Chapter Overview

This chapter reviews the mathematical formulation used here for describing non-premixed turbulent combustion processes. The compressible form of the Navier-Stokes equations, which govern the reactive flow in this case are summarized first. The fluid transport and mass diffusion processes used to predict the flame behaviour are also described. This discussion is followed by a discussion of the modelling used to incorporate the effect of turbulence on the mean flow. The chapter ends with the discussion of chemical kinetic models and discusses simplified one-step mechanisms for laminar flames and their use in conjunction with the Eddy Dissipation Model (EDM) for turbulent flames. Such simplified chemical kinetic models account for the effects of finite-rate chemistry and mixture variations in mixture composition without significant computational overheads but cannot in general provide a full description of the complex chemical kinetics and pollutant formation associated with many combustion processes. As stated in the previous chapter, the focus of this thesis is to incorporate detailed-chemistry effects on turbulent flames. Modelling detailed-chemistry and turbulence-chemistry interaction will be discussed in full detail in Chapter 3. It should be noted that the simplified reduced mechanisms considered herein are used merely to provide a baseline for comparison of computational costs and not for any assessment of the accuracy of the tabulated chemistry approaches of interest in this thesis.

2.2   Basic Equations

Neglecting soot formation and radiation transport, reactive flows can be fully described by the Navier-Stokes equations for a compressible, thermally-perfect, reactive mixture governing the conservation of mass, momentum, and energy for the mixture and the transport of mass for each of the individual species. These balance equations, in tensor notation for a N-species reactive mixture, are given by [87, 88]

- Mass conservation:

$$\frac{\partial \rho}{\partial t} + \frac{\partial}{\partial x_i}\left(\rho u_i\right) = 0 \tag{2.1}$$

  where x_i is the position vector, t is the time coordinate, ρ is the mixture density and u_i is the velocity vector.

- Momentum ($i = 1, 2, 3$) conservation:

$$\frac{\partial}{\partial t}\left(\rho u_i\right) + \frac{\partial}{\partial x_j}\left(\rho u_j u_i\right) = -\frac{\partial p}{\partial x_i} + \frac{\partial \tau_{ji}}{\partial x_j} + g_i \tag{2.2}$$

  where p is the pressure, τ_{ji} denotes the viscous stress tensor and g_i is a body force vector.

- Energy conservation:

$$\frac{\partial}{\partial t}\left(\rho e\right) + \frac{\partial}{\partial x_j}\left[\rho u_j \left(h + \frac{u_i u_i}{2}\right)\right] = \frac{\partial}{\partial x_j}\left(u_i \tau_{ij}\right) - \frac{\partial q_j}{\partial x_j} + u_i g_i \tag{2.3}$$

  where e is the specific total energy ($u_i u_i/2 + h - p/\rho$), h is the specific total enthalpy $\sum_{k=1}^{N} Y_k h_k$, Y_k is the mass fraction of species k, h_k is the absolute (chemical plus sensible) internal enthalpy for species k and q_j is the molecular heat flux vector.

- Species (N species with $k = 1, 2, \cdots, N$) conservation:

$$\frac{\partial}{\partial t}\left(\rho Y_k\right) + \frac{\partial}{\partial x_j}\left(\rho u_j Y_k\right) = -\frac{\partial \mathcal{J}_j^k}{\partial x_j} + \dot{\omega}_k \tag{2.4}$$

  where $\mathcal{J}_j^k$ is the molecular diffusive flux vector of the species k, and $\dot{\omega}_k$ is the mass reaction rate of species k produced by the chemical reactions.

The molecular heat flux and the species diffusivity are modelled using Fourier's law and Fick's laws, respectively, and are given by

$$q_j = -\left(\kappa \frac{\partial T}{\partial x_j} - \sum_{k=1}^{N} h_k \mathcal{J}_j^k \right) \tag{2.5}$$

$$\mathcal{J}_j^k = -\frac{\mu}{\mathrm{Sc}^k} \frac{\partial Y_k}{\partial x_j} \tag{2.6}$$

where κ is the mixture thermal conductivity, T is the mixture temperature, and μ is the molecular viscosity depending on fluid properties. The dimensionless parameter Sc^k is the Schmidt number of species k, defined as

$$\mathrm{Sc}^k = \frac{\mu}{\rho \mathcal{D}^k} \tag{2.7}$$

where $\mathcal{D}^k$ is the molecular diffusivity of the species k relative to the mixture. In order to maintain the physical consistency that all of the species diffusive fluxes should add up to zero, a correction factor called the correction velocity, V_{corr}, is introduced. The correction velocity is defined as

$$V_{\mathrm{corr}j} = \sum_{k=1}^{N} \frac{\mu}{\mathrm{Sc}^k} \frac{\partial Y_k}{\partial x_j} \tag{2.8}$$

The final form of Equation (2.6) used in the computations looks like

$$\mathcal{J}_j^k = -\frac{\mu}{\mathrm{Sc}^k} \frac{\partial Y_k}{\partial x_j} + \rho Y_k V_{\mathrm{corr}j} \tag{2.9}$$

The mixture pressure is given by the ideal gas law

$$p = \sum_{k=1}^{N} \rho Y_k R_k T \tag{2.10}$$

where R_k is the species gas constant. All components of the gaseous reactive mixture are assumed to be Newtonian. As such, the viscous stress tensor is given by the constitutive relation

$$\tau_{ij} = \mu \left(\frac{\partial u_i}{\partial x_j} + \frac{\partial u_j}{\partial x_i} \right) - \frac{2}{3} \delta_{ij} \frac{\partial u_k}{\partial x_k} \tag{2.11}$$

where δ_{ij} is the Kroneckar delta function.

2.2.1   Thermodynamic and Transport Properties

Thermodynamic relationships and transport coefficients are required to close the system of equations given above. In this study, the compressible reactive gaseous mixture is assumed to be thermally perfect, i.e., a gaseous mixture in which the specific heats are only functions of temperature [89].

Thermodynamic and molecular transport properties of each gaseous species are prescribed using the empirical database compiled by Gordon and McBride [90, 91], which provides curve fits for the species enthalpy, h_k, specific heat, c_{p_k}, entropy, viscosity, μ_k, and thermal conductivity, κ_k, as functions of temperature, T. For example, the enthalpy and viscosity for a particular species are given by

$$h_k = R_k T - a_{1,k} T^{-2} + a_{2,k} T^{-1} \ln T + a_{3,k} + \frac{a_{4,k}}{2} T + \frac{a_{5,k}}{3} T^2 +$$
$$\frac{a_{6,k}}{4} T^3 + \frac{a_{7,k}}{5} T^4 + b_1 T^{-1} + \Delta h_{f_k}^o \,, \tag{2.12}$$

and

$$\ln \mu_k = A_k \ln T + \frac{B_k}{T} + \frac{C_k}{T^2} + D_k \,, \tag{2.13}$$

where $a_{k,k}$, A_k, B_k, C_k, and D_k are the coefficients for the curve fits and $\Delta h_{f_k}^o$ is heat of formation. The Gordon-McBride data set contains curve fits for over 2000 substances, including 50 reference elements.

The molecular viscosity, μ, and thermal conductivity, κ, of the reactive mixture are determined using the mixture rules of Wilke [92] and Gardiner [93], respectively. All these expressions are given in detail in the previous theses by both Gao [41] and Northrup [94].

2.3   Modelling Turbulent Flows

Turbulent flows are characterized by the presence of intense local swirling and formation of eddies. These eddies are present in a wide range of sizes, ranging from the length-scales of the flow to the thickness of wall boundary layers, and transport most of the turbulent kinetic energy. One of the main physical process that spreads the motion over this wide range of wavelengths is vortex stretching. The large scale eddies are significant as they carry most of the energy and are responsible for enhanced diffusivity and stresses. A turbulent energy cascade exists, where the energy is passed on from large eddies to

smaller and smaller eddies until reaching the smallest eddies, where the viscous effects are strong and energy is dissipated into heat through viscous dissipation.

It is generally acknowledged that the Navier-Stokes equations fully describe all of this turbulent flow phenomena, as despite the wide range of length-scales, the smallest scales of turbulence are ordinarily far larger than the mean free path of the flow [95]. The smallest length scales of turbulence are referred to as the Kolmogorov scale and can be estimated using the universal equilibrium theory of Kolmogorov [96, 97], which states that the rate of receiving energy from the larger eddies is very nearly equal to the rate at which the smallest eddies dissipate the energy to heat. For a typical turbulent flow, the large-scales in a turbulent flow, generally set by the flow geometry, can be larger than smaller scales by as much as six orders of magnitude (i.e., 10^6). The ratio between the largest and smallest scales increases rapidly as a function of Reynolds number. To make an accurate numerical simulation of a turbulent flow, all relevant physical scales must be resolved. However, resolving all the length-scales is not practical due to the computational resources required to resolve the smallest turbulent eddies.

As an alternative, instead of directly solving the Navier-Stokes equations for turbulent flows, statistically time-averaged forms of the Navier-Stokes equations, called the RANS or the FANS equations are often solved in many engineering applications. These equations describe the behaviour of the mean or time-averaged flow quantities instead of the exact instantaneous values, and incorporate the effect of unresolved turbulence on the mean flow through the use of turbulence models.

2.3.1   Time Averaging Methods

The present section describes the Reynolds and Favre time-averaging methods. A more detailed and complete description of the other averaging methods present can be found in Wilcox [98].

In the averaging procedure for the Navier-Stokes equations, every instantaneous flow quantity, $\phi(\vec{x}, t)$, is expressed as the sum of a mean component, $\overline{\phi}(\vec{x}, t)$, and a fluctuating component, $\phi'(\vec{x}, t)$, such that

$$\phi(\vec{x}, t) = \overline{\phi}(\vec{x}, t) + \phi'(\vec{x}, t) \qquad (2.14)$$

Averaging $\phi(\vec{x}, t)$ over a time-scale, $\mathcal{T}$, the Reynolds average or time average of the

quantity is given by

$$\overline{\phi}(\vec{x}, t) = \frac{1}{\mathcal{T}} \int_{t-\mathcal{T}/2}^{t+\mathcal{T}/2} \phi(\vec{x}, t) dt \tag{2.15}$$

Using Equation (2.15), it can be shown that the time average of the fluctuating component is zero. This averaging procedure simplifies Equation (2.1) for a incompressible flow (constant density) and even after averaging it retains the exact same form as before:

$$\rho \frac{\partial \overline{u}_i}{\partial x_i} = 0 \tag{2.16}$$

However, this averaging process does not work as elegantly when dealing with compressible flows with non-constant density. A Reynolds averaging on the quantity, ρu_i, results in the following:

$$\overline{\rho u_i} = \overline{(\overline{\rho} + \rho')(\overline{u}_i + u')} = \overline{\overline{\rho}\,\overline{u}_i + \rho'\overline{u}_i + \overline{\rho}u' + \rho'u'} = \overline{\rho}\,\overline{u}_i + \overline{\rho'u'} \tag{2.17}$$

The last quantity in the above equation is not closed and requires additional modelling to be used, which is not desirable.

To address this issue, the concept of Favre or mass-weighted time averaging is introduced [99]. The notation used for Favre averaging is

$$\phi(\vec{x}, t) = \widetilde{\phi}(\vec{x}, t) + \phi''(\vec{x}, t) \tag{2.18}$$

where $\widetilde{\phi}$ is the mean component of Favre averaged quantities and ϕ'' is the fluctuating component. Favre averaging also uses the time-averaged density, $\overline{\rho}$, but a new mass-weighted time-averaged velocity, $\widetilde{u}_i$ is introduced which is defined by

$$\widetilde{u}_i(\vec{x}, t) = \frac{1}{\overline{\rho}\mathcal{T}} \int_{t-\mathcal{T}/2}^{t+\mathcal{T}/2} \rho u(\vec{x}, t) dt \tag{2.19}$$

In terms of Reynolds averaging, the above terms are related as

$$\overline{\rho}\widetilde{u}_i = \overline{\rho u_i} = \overline{\rho}\,\overline{u}_i + \overline{\rho'u'} \tag{2.20}$$

Performing Reynolds averaging on the compressible form of continuity equation, Equation (2.1), and substituting Equation (2.20) in Equation (2.17), the averaged continuity equation simplifies and takes the following form

$$\frac{\partial \overline{\rho}}{\partial t} + \frac{\partial}{\partial x_i}\left(\overline{\rho}\widetilde{u}_i\right) = 0 \tag{2.21}$$

This is a significant simplification as it expresses the averaged continuity equation in exactly the same form as the continuity equation in the original Navier-Stokes equations without any averaging applied.

2.3.2 Favre-Averaged Navier-Stokes Equations

Applying the Favre-time-averaging procedure outlined above to the transport equations given in Equations (2.1) to (2.4), one arrives at the following set of time-averaged equations:

$$\frac{\partial \bar{\rho}}{\partial t} + \frac{\partial}{\partial x_i}\left(\bar{\rho}\widetilde{u}_i\right) = 0 \tag{2.22}$$

$$\frac{\partial}{\partial t}\left(\bar{\rho}\widetilde{u}_i\right) + \frac{\partial}{\partial x_i}\left(\bar{\rho}\widetilde{u}_j\widetilde{u}_i\right) = -\frac{\partial \bar{p}}{\partial x_i} + \frac{\partial}{\partial x_i}\left(\bar{\tau}_{ji} - \underbrace{\overline{\rho u_j'' u_i''}}_{\text{unclosed}}\right) \tag{2.23}$$

$$\frac{\partial}{\partial t}\left(\bar{\rho}\widetilde{Y}_k\right) + \frac{\partial}{\partial x_j}\left(\bar{\rho}\widetilde{u}_j\widetilde{Y}_k\right) = -\frac{\partial}{\partial x_i}\left(\bar{\rho}\underbrace{\overline{u_j'' Y_k''}}_{\text{unclosed}}\right) - \frac{\partial}{\partial x_j}\left(\mathcal{D}^k\frac{\partial \widetilde{Y}_k}{\partial x_j}\right) + \bar{\dot{\omega}}_k \tag{2.24}$$

$$\frac{\partial}{\partial t}\left[\bar{\rho}\left(\widetilde{e} + \frac{\widetilde{u}_i\widetilde{u}_i}{2}\right) + \underbrace{\frac{\overline{\rho u_i'' u_i''}}{2}}_{\text{unclosed}}\right] + \frac{\partial}{\partial x_j}\left[\bar{\rho}\widetilde{u}_j\left(\widetilde{h} + \frac{\widetilde{u}_i\widetilde{u}_i}{2}\right) + \widetilde{u}_j\underbrace{\frac{\overline{\rho u_i'' u_i''}}{2}}_{\text{unclosed}}\right]$$

$$= \frac{\partial}{\partial x_j}\left[-q_j - \underbrace{\overline{\rho u_i'' h''}}_{\text{unclosed}} + \underbrace{\overline{t_{ji} u_i''}}_{\text{unclosed}} - \underbrace{\overline{\rho u_j'' \frac{u_i'' u_i''}{2}}}_{\text{unclosed}}\right] + \frac{\partial}{\partial x_j}\left[\widetilde{u}_i\left(\bar{\tau}_{it}\right) - \underbrace{\overline{\rho u_i'' s_j''}}_{\text{unclosed}}\right] \tag{2.25}$$

The above equations show that several unclosed "fluctuating/turbulent" terms are introduced as a result of the averaging procedure. A number of different theories and approximations are used to close these terms.

The Boussinesq eddy-viscosity approximation is one of the most important approximations used to close the time-averaged Navier-Stokes equations. In this modelling approach it is argued that the effect of the mean of the product of the fluctuating parts of the turbulent velocities is to add additional stress in the momentum flux. Thus, this additional "turbulent stress", or Reynolds-stress, λ, can be expressed as

$$\lambda_{ij} = -\overline{\rho u'' v''} \tag{2.26}$$

The Reynolds-stress tensor, λ_{ij}, is dependent on the local mean flow strain-rate tensor and is given by

$$\bar{\rho}\lambda_{ij} = \mu_t\left[\frac{\partial \widetilde{u}_i}{\partial x_j} + \frac{\partial \widetilde{u}_j}{\partial x_i} - \frac{2}{3}\delta_{ij}\frac{\partial \widetilde{u}_k}{\partial x_k}\right] - \frac{2}{3}\delta_{ij}\bar{\rho}k \tag{2.27}$$

where μ_t is the eddy-viscosity.

A number of turbulent models have been proposed over the past few decades based on the Reynolds-stress/eddy-viscosity concept. Some initial models like the Cebeci-Smith [100] and Baldwin-Lomax [101] models provide algebraic formulations to account for the effect of turbulence based on estimates of turbulent length and time scales. These estimates are very empirical in nature and give good results only for specific kinds of flows. The next generation of turbulence models were based on solving additional transport equations to get an estimate of turbulence scales based on the local flow properties. Most of these models are based on solving for a new quantity, the turbulent kinetic energy, k, which accounts for the energy carried by the turbulence fluctuations and can be defined as

$$\bar{\rho} k = \frac{1}{2} \overline{\rho u_i'' u_i''} \qquad (2.28)$$

This quantity was first defined by Prandtl [102]. The transport equation for k, given later in this section in Equation (2.38), can be determined by taking the trace the Reynolds-stress tensor. Some one-equation models based on k were proposed by Prandtl [102], and Bradshaw et al. [103]. Baldwin and Barth [104], and Spalart and Allmaras [105] subsequently devised one-equation models which provide values for the eddy viscosity more directly. The model by Spalart and Allmaras is tuned for external flows over airfoils and to this date continues to be a very popular turbulence model for aerodynamiscists. However, this model does not generally reproduce as good results for internal and free-shear layer flows [98].

Over the last few decades, two-equation turbulence models have become popular and have proven to give good results for different turbulent flow regimes. These models are based on solving two additional transport equations so as to determine the turbulent length and time scales in terms of local flow properties and these scalar fields are used to calculate the eddy-viscosity. A number of two-equation models have been proposed [106–110], but the two most popular models presently are the k-ϵ model [111] and the k-ω model [112], where ϵ is the dissipation rate of turbulent kinetic energy and ω is the specific dissipation rate of turbulent kinetic energy, such that

$$\omega = \frac{\epsilon}{k} \qquad (2.29)$$

In the k-ω model, the quantity, ω, has the dimension of $[1/T]$ and gives an indication of the characteristic time-scales associated with turbulence.

In the present work, the k-ω turbulence model proposed by Wilcox [86] has been used, as it has been shown that it works better for free-shear layer flows [98] and also because

it can be integrated directly to the wall, which obviates the need of any empirical wall-functions needed by k-ϵ model in near-wall regions. Note that the k-ϵ and k-ω models both have their strengths and weaknesses, which are discussed in greater detail by Menter [113]. In the k-ω models, the eddy-viscosity is defined as

$$\mu_t = \frac{\bar{\rho}k}{\omega} \tag{2.30}$$

Some other assumptions are made to close the other unclosed terms in the averaged-equations, Equation (2.22) - Equation (2.25). A turbulent heat flux vector, $\vec{q_t}$, is introduced to account for the effect of turbulence on heat flux based on the classic analogy between momentum and heat transfer so that

$$q_{t_j} = \overline{\rho u_j'' h''} = \frac{\mu_t c_p}{\mathrm{Pr}_t} \frac{\partial \widetilde{T}}{\partial x_j} = \frac{\mu_t}{\mathrm{Pr}_t} \frac{\partial \widetilde{h}}{\partial x_j} \tag{2.31}$$

where Pr_t is the turbulent Prandtl number. In the present work, the Pr_t is set to a constant value of 0.9. This constant Pr_t assumption may however fail in flows with extremely high speed or high temperature regions, like hypersonic flows [114–116]. In such cases, additional transport equations are solved for calculating a Pr_t at each point in the flow.

The turbulent transport term in Equation (2.25) is modelled as

$$\overline{t_{ji}u_i''} - \overline{\rho u_j'' \frac{u_i'' u_i''}{2}} = (\mu + \sigma^* \mu_t) \frac{\partial k}{\partial x_j} \tag{2.32}$$

and the unclosed terms in the species transport equation, Equation (2.24), are modelled using the gradient transport hypothesis

$$\bar{\rho} \overline{u_j'' Y_k''} = \mathcal{D}_t \frac{\partial \widetilde{Y_k}}{\partial x_i} \tag{2.33}$$

where $\mathcal{D}_t = \mu_t / \mathrm{Sc}_t$ is the turbulent diffusivity and Sc_t is turbulent Schmidt number which is set to a constant value of 1.0.

The final set of FANS equations which are considered herein are then as follows:

- Mass conservation:
$$\frac{\partial \bar{\rho}}{\partial t} + \frac{\partial}{\partial x_i} (\bar{\rho} \widetilde{u_i}) = 0 \tag{2.34}$$

- Momentum ($i = 1, 2, 3$) conservation:
$$\frac{\partial}{\partial t} (\bar{\rho} \widetilde{u_i}) + \frac{\partial}{\partial x_i} (\bar{\rho} \widetilde{u_j} \widetilde{u_i}) = -\frac{\partial \bar{p}}{\partial x_i} + \frac{\partial}{\partial x_i} (\bar{\tau}_{ji} + \bar{\rho} \lambda_{ji}) \tag{2.35}$$

- Species (N species with $k = 1, 2, \cdots, N$) conservation:

$$\frac{\partial}{\partial t} \left(\bar{\rho} \widetilde{Y}_k \right) + \frac{\partial}{\partial x_j} \left(\bar{\rho} \widetilde{u}_j \widetilde{Y}_k \right) = -\frac{\partial}{\partial x_j} \left[\left(\mathcal{D}^k + \mathcal{D}_t \right) \frac{\partial \widetilde{Y}_k}{\partial x_j} \right] + \bar{\dot{\omega}}_k \qquad (2.36)$$

- Energy conservation:

$$\frac{\partial}{\partial t} \left[\bar{\rho} \left(\widetilde{e} + \frac{\widetilde{u}_i \widetilde{u}_i}{2} + k \right) \right] + \frac{\partial}{\partial x_j} \left[\bar{\rho} \widetilde{u}_j \left(\widetilde{h} + \frac{\widetilde{u}_i \widetilde{u}_i}{2} + k \right) \right]$$
$$= \frac{\partial}{\partial x_j} \left[\left(\frac{\mu}{\mathrm{Pr_L}} + \frac{\mu_t}{\mathrm{Pr}_t} \right) \frac{\partial \widetilde{h}}{\partial x_j} + \left(\mu + \sigma^* \mu_t \right) \frac{\partial k}{\partial x_j} \right] + \frac{\partial}{\partial x_j} \left[\widetilde{u}_i \left(\bar{\tau}_{ij} + \bar{\rho} \lambda_{ij} \right) \right] \qquad (2.37)$$

- Turbulent kinetic energy:

$$\frac{\partial}{\partial t} \left(\bar{\rho} k \right) + \frac{\partial}{\partial x_j} \left(\bar{\rho} \widetilde{u}_j k \right) = \bar{\rho} \lambda_{ij} \frac{\partial \widetilde{u}_i}{\partial x_j} - \beta^* \bar{\rho} k \omega + \frac{\partial}{\partial x_j} \left[\left(\mu + \sigma^* \mu_t \right) \frac{\partial k}{\partial x_j} \right] \qquad (2.38)$$

- Specific dissipation rate of turbulent kinetic energy:

$$\frac{\partial}{\partial t} \left(\bar{\rho} \omega \right) + \frac{\partial}{\partial x_j} \left(\bar{\rho} \widetilde{u}_j \omega \right) = \alpha \frac{\omega}{k} \bar{\rho} \lambda_{ij} \frac{\partial \widetilde{u}_i}{\partial x_j} - \beta \bar{\rho} \omega^2 + \frac{\partial}{\partial x_j} \left[\left(\mu + \sigma \mu_t \right) \frac{\partial \omega}{\partial x_j} \right] \qquad (2.39)$$

where $\mathrm{Pr_L}$ is the laminar Prandtl number, and σ^*, β^*, α, σ, and β are closure coefficients for the k-ω turbulence model and are defined as follows

$$\alpha = \frac{13}{25}, \qquad\qquad \sigma = \sigma^* = \frac{1}{2},$$

$$\beta = \beta_\circ f_\beta - \beta_\circ^* f_{\beta^*} \xi^* F, \qquad \beta^* = \beta_\circ^* f_{\beta^*} \left(1 + \xi^* F \right), \qquad \beta_\circ = \frac{9}{125}, \qquad \beta_\circ^* = \frac{9}{100}$$

$$f_\beta = \frac{1 + 70 \chi_\omega}{1 + 80 \chi_\omega}, \quad f_{\beta^*} = \frac{1 + 680 \chi_k^2}{1 + 400 \chi_k^2},$$

$$\chi_\omega = \left| \frac{\Omega_{ij} \Omega_{jk} S_{ki}}{\beta_\circ^* \omega^3} \right|, \quad \chi_k = \max \left(0, \frac{1}{\omega^3} \frac{\partial k}{\partial x_i} \frac{\partial \omega}{\partial x_i} \right)$$

$$\xi^* = \frac{3}{2} \quad \mathrm{M}_\circ = \frac{1}{4} \quad F = \mathcal{H} \left(\mathrm{M}_t - \mathrm{M}_\circ \right) \left(\mathrm{M}_t^2 - \mathrm{M}_\circ^2 \right)$$

where Ω_{ij} and S_{ij} are the mean-rotation and mean-strain-rate tensors defined as

$$\Omega_{ij} = \frac{1}{2} \left(\frac{\partial U_i}{\partial x_j} - \frac{\partial U_j}{\partial x_i} \right), \qquad S_{ij} = \frac{1}{2} \left(\frac{\partial U_i}{\partial x_j} + \frac{\partial U_j}{\partial x_i} \right) \qquad (2.40)$$

and $\mathcal{H}(x)$ is the Heaviside step function.

In the set of FANS equations given above, the only unresolved part is the $\bar{\dot{\omega}}_k$ term. Modelling of this term will be discussed in detail in Section 2.4.3 to follow.

2.3.2.1 Near Wall Treatment of Turbulence

The k and ω transport equations can be integrated through the laminar sublayer right to the solid boundary, eliminating the need for two-layer models [117, 118] or wall functions [119]. The no-slip boundary condition dictates that the turbulent kinetic energy must go to zero at the wall. Perturbation analysis of the ω transport equation for laminar sublayer shows that [98]

$$\lim_{y_{\text{wall}} \to 0} \omega = \frac{6\nu}{\beta y_{\text{wall}}^2} \tag{2.41}$$

where ν is the molecular kinematic viscosity, y_{wall} is the normal distance from the wall. This expression is used to specify the value of ω directly for all values of $y^+ \leq 2.5$ provided there are 3-5 computational cells inside $y^+ = 2.5$, where y^+ is the dimensionless distance from the wall given by

$$y^+ = \frac{u_\tau y_{\text{wall}}}{\nu} \tag{2.42}$$

where u_τ is the friction velocity given by $\sqrt{\tau_w/\rho}$ and τ_w is the wall shear stress.

However, when dealing with coarser meshes there might not be a sufficient number of cells within the laminar sublayer. For such meshes, an automatic wall treatment method is used for near wall treatment of the k-ω turbulence model as described by Gao and Groth [56]. This model switches between the low-Reynolds-number formulation and the standard wall function depending on the mesh resolution. In the case of the wall function formulation, the expressions

$$k = \frac{u_\tau^2}{\sqrt{\beta_o^*}}, \qquad \omega = \frac{u_\tau}{\sqrt{\beta_o^*}\varkappa y_{\text{wall}}} \tag{2.43}$$

where $\varkappa = 0.41$ is the Kármán constant, are used to fully specify both k and ω for $y^+ \leq 30 - 250$. The automatic treatment switches between these two methods depending on mesh resolution using a blending function given by

$$k = \frac{u_\tau^2}{\beta_o^*}\frac{\min(y^+, 30)}{30}, \qquad \omega = \omega_o\sqrt{1 + \left(\frac{\omega_{wall}}{\omega_o}\right)^2} \tag{2.44}$$

where

$$\omega_o = \frac{6\nu}{\beta y^2}, \qquad \omega_{wall} = \frac{u_\tau}{\sqrt{\beta_o^*}\varkappa y_{\text{wall}}} \tag{2.45}$$

In the turbulent flow simulations discussed in Chapter 5, a relatively coarse mesh is used to start and automatic treatment is used only on the first cell off the wall. After obtaining an approximate solution on the coarse mesh and performing two or three levels

of refinement such that there are at least 2-3 cells within the laminar sublayer, the low-Reynolds-number formulation is used for the solution on the finest mesh.

The friction velocity, u_τ, and the dimensionless wall distance, y^+, are calculated simultaneously. The dimensionless velocity, u^+, is defined as

$$u^+ = \frac{\widetilde{u}}{u_\tau} \tag{2.46}$$

Next to the wall, where the flow is dominated by the effects of viscosity, the dimensionless velocity profile varies linearly with the dimensionless wall distance, such that

$$u^+ = y^+ \tag{2.47}$$

This layer is called the viscous sublayer. The next layer, called the log layer, is governed by the *law of the wall* which is given by

$$u^+ = \frac{1}{\varkappa} \ln y^+ + C \tag{2.48}$$

where $C \approx 0.5$ is an integration constant. The first guess of local value of y^+ is made using Equation (2.42) and Equation (2.46) and then Newton's method is used to iterate over Equation (2.48) to find the correct value of u_τ and y^+ for given values of ν and y_{wall}.

2.4 Chemical Kinetics

Modelling and evaluation of reaction rate source terms for accurately representing chemical kinetics is a major challenge in the simulation of combustion processes. Chemical reaction rates are highly non-linear functions of species concentrations and temperature, and severe problems are encountered in evaluating reaction rates for inclusion in species transport and energy balance equations. This section first introduces the Law of Mass Action, which is used for evaluating the reaction rate values based on species mass conservation. It is followed by the introduction of some simplified chemical-kinetic schemes for methane-air combustion and a discussion of the problems associated with the modelling of the effect of turbulence on chemical kinetics.

2.4.1 Law of Mass Action

The time rate of change of the species concentration, $\dot{\omega}_k$, can be calculated using a general form of the law of mass action [120]

$$\dot{\omega}_k = \frac{\mathcal{M}_k}{\rho} \sum_{r=1}^{Nr} (\nu''_{k,r} - \nu'_{k,r}) \left\{ \kappa_r^f \prod_{i=1}^{N} \left[\frac{\rho c_i}{\mathcal{M}_i} \right]^{\nu'_i} - \kappa_r^b \prod_{i=1}^{N} \left[\frac{\rho c_i}{\mathcal{M}_i} \right]^{\nu''_i} \right\}, \tag{2.49}$$

where $\mathcal{M}_k$ is the molecular mass of species k, $\nu'_{k,r}$ and $\nu''_{k,r}$ are the stoichiometric co-efficients for the reactants and for the products (related to species k in reaction r), respectively, κ_r^f and κ_r^b are forward and backward reaction rates, respectively, and Nr is the total number of reactions. The forward reaction rates, κ_r^f, for the Nr reactions are temperature dependent and are given for each reaction mechanism. The reverse reaction rates, κ_r^b, if not given, are defined in terms of the equilibrium constant, κ_r^{eq}, where

$$\frac{\kappa_r^f}{\kappa_r^b} = \kappa_r^{eq} \left(\frac{1}{RT} \right)^{\Sigma_s \nu_s} \tag{2.50}$$

and where

$$\kappa_r^{eq} = e^{-\frac{\Delta G_r^{P=1}}{RT}} \tag{2.51}$$

Here $\Delta G_r^{P=1}$ is the Gibbs free energy at atmospheric conditions for reaction r. The Gibbs free energy for each species is found from

$$G_k = h_k - T s_k \tag{2.52}$$

where the species enthalpy, h_k, and entropy, s_k, can be found using polytropic relations or using empirical data. In this instance, the empirical data compiled by Gordon and McBride [90, 91] are used again.

2.4.2 Methane-Air Combustion

While this thesis is concerned with treatments for detailed chemistry, it has been restricted to gaseous fuel combustion and, in particular, the combustion of methane and air. Both detailed and simple one-step mechanisms are considered herein for describing the latter and are discussed below.

2.4.2.1 GRI-Mech 3.0 Mechanism

The GRI-Mech 3.0 Mechanism [121] is arguably the most popular detailed-chemistry mechanism for the oxidation of methane today. It involves 53 species and 325 reaction

Rate	A	$Ea(\mathrm{J/(mol\ K)})$	a	b
k_o	1.3×10^8	2.0264×10^5	0.2	1.3

Table 2.1: Methane-air one-step chemical mechanism reaction rate coefficients.

steps. However, DNS of such a large system places heavy demands on computational resources. Alternative ways have been developed to incorporate the full effects of this chemical-kinetic scheme on reactive flows and are discussed in detail in Chapter 3.

2.4.2.2 One-Step Mechanism

Aside from the GRI-Mech 3.0 mechanism, for initial validation of the mathematical framework considered here, a simplified chemical mechanism for gaseous fuels has been used. The simplified mechanism was particularly useful for testing the proposed solution algorithm without adding complexities and computational overhead of more complex mechanisms.

For the gaseous methane-air combustion considered in the present work, the following reduced, one-step, five-species, chemical kinetic scheme of Westbrook and Dryer [122] is used for laminar flames

$$CH_4 + 2O_2 \rightarrow CO_2 + 2H_2O \tag{2.53}$$

The five species are methane (CH_4), oxygen (O_2), carbon dioxide (CO_2), water (H_2O), and nitrogen (N_2). Nitrogen is taken to be inert. This reaction mechanism uses Arrhenius like formulation for reaction rates. The one-step reaction only has a forward or overall reaction rate given by

$$k_o = A\ exp\left(\frac{Ea}{RT}\right)[CH_4]^a[O_2]^b \tag{2.54}$$

The coefficients for this reaction mechanism are given in Table 2.1.

2.4.3   Modelling Turbulence/Chemistry Interactions

The interaction between turbulence and chemical reactions is best characterized in terms of the turbulent Damköhler number, discussed earlier in Section 1.2. As the turbulent Damköhler number approaches infinity, the chemical time-scales become much smaller than the physical time-scales. In this case, equilibrium (fast) chemistry can be assumed. If the Damköhler number is close to zero, the chemical reactions occur more slowly compared to fluid transport phenomena, and then a frozen-chemistry fluid can be assumed.

The greatest interaction between turbulence and chemical reactions will occur when the Damköhler number is of the order of unity and in this case one must use finite-rate chemistry to model the chemical reactions.

As shown earlier in Equation (2.36), FANS-averaging of the species transport equation gives an unclosed term, $\bar{\dot{\omega}}_k$. The averaged reaction rate is not the same as the reaction rate evaluated in terms of the time-averaged quantities, i.e,

$$\bar{\dot{\omega}}_k \neq \dot{\omega}_k \left(\tilde{Y}_i, \tilde{T} \right) \tag{2.55}$$

Both turbulence and chemistry are highly non-linear in nature and are strongly coupled in reacting flows. The accurate prediction of mean reaction rates, $\bar{\dot{\omega}}_k$, which can be strongly influenced and enhanced by small-scale turbulent mixing, is a central challenge in modelling turbulent combustion processes. This makes it difficult to come up with a closure approximation for the time-averaged values of reaction rates, $\bar{\dot{\omega}}$.

A simple Taylor series expansion of the reaction rate term can be used to illustrate the problem clearly. For a simple irreversible reaction between fuel (F) and oxidizer (O) reacting to give a product (P)

$$\text{F} + s\text{O} \rightarrow (1+s)\text{P} \tag{2.56}$$

the fuel mass fraction reaction rate, $\dot{\omega}_\text{F}$, can be expressed from the Arrhenius law as [8]

$$\dot{\omega}_\text{F} = -A\rho^2 T^b Y_\text{F} Y_\text{O} \exp \left(-\frac{T_\text{A}}{T} \right) \tag{2.57}$$

where A is the pre-exponential constant, and T_A is the activation temperature. Using a Taylor series expansion, the mean reaction rate, $\bar{\dot{\omega}}_\text{F}$, can be expanded in the following form

$$\begin{aligned}
\bar{\dot{\omega}}_\text{F} = &-A\bar{\rho}^2 \widetilde{T}^b \widetilde{Y}_\text{F} \widetilde{Y}_\text{O} \exp \left(-\frac{T_\text{A}}{\widetilde{T}} \right) \\
&\times \left[1 + \frac{\widetilde{Y''_\text{F} Y''_\text{O}}}{\widetilde{Y}_\text{F} \widetilde{Y}_\text{O}} + C_1 \left(\frac{\widetilde{Y''_\text{F} T''}}{\widetilde{Y}_\text{F} \widetilde{T}} + \frac{\widetilde{Y''_\text{O} T''}}{\widetilde{Y}_\text{O} \widetilde{T}} \right) + C_2 \left(\frac{\widetilde{Y''_\text{F} T''}}{\widetilde{Y}_\text{F} \widetilde{Y}_\text{O}} + \frac{\widetilde{Y''_\text{O} T''}}{\widetilde{Y}_\text{O} \widetilde{T}} \right) + \dots \right]
\end{aligned} \tag{2.58}$$

where C_1 and C_2 are Taylor series coefficients. Modelling (specifying) the high-order correlations in Equation (2.58) is a huge challenge. Because of the highly non-linear nature of the unclosed averaged terms, large errors exist when only a few terms are retained. And also, it is strictly only valid for irreversible reactions and cannot be readily extended to realistic chemical schemes.

In order to calculate the mean reaction rate, a large number of alternative mean reaction rate formulations have been proposed [8, 10, 16, 123]. Bray [124] gives a good discussion of the various mean reaction rate models. The following section discusses one of the simplest models for handling turbulent-chemistry interactions in non-premixed flames, the eddy-dissipation model (EDM).

2.4.4 Eddy Dissipation Model

To avoid the complexities involved in modelling turbulence-chemistry interaction for complex chemical kinetic schemes, alternative ways of dealing with turbulent combustion have been developed. In this section the EDM, proposed by Magnussen and Hjertager [125] is discussed, which is based on the simple one step chemical reaction, given earlier in Equation (2.53). Note that these models tend to over-simply the chemical structure of the flames and are not capable of giving a detailed information about the structure and composition of turbulent flames. However, due to their simple formulation and low computational overhead involved, they are fairly popular in many of today's commercial CFD codes and form a good basis for cost comparisons with detailed-turbulence-chemistry interaction models to be discussed in the Chapter 3.

The EDM has been proposed for predicting the mean reaction rates for high Damköhler number flows in turbulent diffusion flames. The key idea is that chemistry does not play an explicit role while turbulent motions control the reaction rate. The mean reaction rate is thus mainly controlled by the characteristic turbulent time for turbulent mixing. The turbulent time-scale, $\mathcal{T}_{\mathrm{t}}$, is estimated from the dissipation rate per unit turbulent kinetic energy, ω, and is given by

$$\mathcal{T}_t \propto \frac{1}{\omega}$$

The EDM proposes that for a simple, single step and irreversible chemical reaction between a fuel and its oxidizer:

$$\mathrm{F} + s\mathrm{O} \rightarrow (1+s)\mathrm{P} \tag{2.59}$$
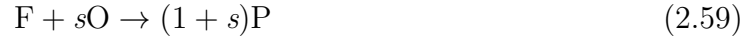
where s is the mass stoichiometric coefficient, the mean reaction rate of the fuel can be estimated as

$$\bar{\dot{\omega}}_{\mathrm{F}} = -\mathcal{C}_{\mathrm{EDM}} \ \frac{1}{\mathcal{T}_{\mathrm{t}}} \ \min\left(\widetilde{Y}_{\mathrm{F}}, \frac{\widetilde{Y}_{\mathrm{O}}}{s}, \beta\frac{\widetilde{Y}_{\mathrm{P}}}{(1+s)}\right), \tag{2.60}$$

where model constants, $\mathcal{C}_{\mathrm{EDM}}$ and β can be adjusted to incorporate various chemical features. In this work, the values of these constants used are $\mathcal{C}_{\mathrm{EDM}} = 4.0$ and $\beta = 0$.

Clearly, the reaction rate is limited by the deficient species and the turbulence mixing time. When $\beta \neq 0$, the products can also limit the rate since "this accounts for the burnt gases bringing the energy to burn the fresh reactants" [123]. Accordingly, $\bar{\omega}_O$ and $\bar{\omega}_P$ may be computed by

$$\bar{\omega}_O = s\,\dot{\omega}_F\,,$$

$$\bar{\omega}_P = -(1+s)\,\bar{\omega}_F\,.$$

In terms of mean mass fractions, the chemical reaction, Equation (2.59), may be written as

$$\nu_F'\,\widetilde{Y}_F + \nu_O'\,\widetilde{Y}_O \rightarrow \nu_P''\,\widetilde{Y}_P\,,$$
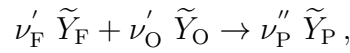
where ν_i' and ν_i'' are the stoichiometric coefficients of the reactants and products, respectively. The mass stoichiometric coefficient, s, can be related to the stoichiometric coefficients ν_i' by

$$s = \frac{\nu_O'\mathcal{M}_O}{\nu_F'\mathcal{M}_F}\,,$$

$$1 + s = \frac{\nu_P''\mathcal{M}_P}{\nu_F'\mathcal{M}_F}\,,$$

where $\mathcal{M}_F$, $\mathcal{M}_O$ and $\mathcal{M}_P$ are the molecular mass for fuel, oxidizer and product, respectively. In terms of molar stoichiometric coefficients, Equation (2.60) can be written as:

$$\bar{\omega}_F = -\mathcal{C}_{\mathrm{EDM}}\,\omega\,\nu_F'\mathcal{M}_F\ \min\left(\widetilde{Y}_F, \frac{\widetilde{Y}_O}{\nu_O'\mathcal{M}_O}, \beta\frac{\widetilde{Y}_P}{\nu_P''\mathcal{M}_P}\right)\,. \tag{2.61}$$

The EDM is manifestly easy to adopt for computational implementation because the reaction rate is calculated using mean values of mass fractions without additional transport equations. It is useful for the prediction of diffusion flames as well as for partially premixed flames. However, extensions of this model to full chemistry mechanisms is not straightforward [123]. Accounting for the effects of detailed chemistry on turbulent diffusion flames calls for alternative ways of looking at chemical kinetics, which are discussed more elaborately in the next chapter.

<div style="text-align: right;">*3*</div>

The Tabulated Chemistry Approach

3.1 Chapter Overview

In this chapter, three major challenges in numerical modelling of combustion processes will be addressed: accounting for the large number of intermediate species and reaction steps in combustion processes, modelling of the reaction rate source terms, and modelling the effect of turbulence on chemistry.

Most combustion processes involve thousands of intermediate species and reaction steps. An accurate representation of the flames will require tracking every species and reaction step involved in the combustion process, which is practically impossible. Detailed-chemistry mechanisms have been proposed for certain common fuels which predict the flame properties quite well by tracking a finite number of species [121, 126, 127]. However, the numerical modelling of these detailed-chemistry schemes are still prohibitively expensive for relevant industrial applications. For example, the detail mechanism proposed for oxidation of H_2 involves 8 species and 40 reaction steps [126]. The GRI-Mech 3.0 mechanism proposed for the oxidation of methane involves 53 species and 325 reaction steps [121] and even a rather simplified proposed mechanism for aviation jet fuels (n-decane combustion) due to Lindstedt and Maurice [128] involves 193 species and 1085 reaction steps. DNS of such large complex reaction mechanisms place heavy demands on computational resources and demands alternative ways of looking at this problem. Also, as already discussed in detail in Section 2.4.3, modelling the reaction rate terms in turbulent combusting flows is very challenging.

This chapter discusses in detail the PCM-FPI approach which has been developed for the handling detailed chemistry in a turbulent combusting flow. The next section reviews

the various other algorithms that exist presently for handling detailed-chemistry in turbulent combustion. It is followed by the introduction of an additional solution variable, called the mixture fraction, which is central to the understanding of diffusion flames. The following section introduces and gives a detailed discussion of the FPI tabulation approach, that has been implemented and developed in this thesis to handle detailed chemistry. It is followed by a discussion of the PCM approach, which is used to incorporate the influence of turbulent fluctuations on the chemical kinetics using numerical integration of the laminar solutions of FPI approach, and provide mean solutions for turbulent flames. The chapter concludes with a discussion about how to manage the table size and ways of coupling the PCM-FPI tables with the main flow solver.

3.2   Algorithms for Treating Detailed Chemical Kinetics

Although not fully inclusive, the computationally efficient techniques for the treatment of complex chemistry in combustion processes can be broadly categorized into two groups [129]: (i) chemical reduction techniques; and (ii) flamelet approaches. The *in Situ* Adaptive Tabulation (ISAT) approach proposed by Pope [130], based on the generation of look-up tables for chemical kinetics during direct simulations, falls somewhat outside this classification, but the classification is still useful nonetheless.

Chemical Reduction Techniques (CRT) are based on the observation that chemical processes are mainly determined by a small number of slow reactions. These methods assume that species involved in fast reaction processes are in a near quasi-equilibrium steady state. Computational savings are garnered by tracking only the finite-rate reactions and species involved in slow processes. CRT differ from each other mainly in how the fast and slow processes are determined and handled. The Systematic Reduction Method (SRM), as discussed in the review by Peters [131], invokes a steady-state assumption for species involved in fast chemical processes. This however involves a detailed study of all reaction steps and time scales, which can become quite involved for fuels with complex molecular structure [77]. The Computational Singular Perturbation (CSP) method proposed by Lam and Goussis [132] examines the Jacobian of the local chemical source terms with respect to the solution variables to identify slow processes. CSP is quite accurate; however, slow processes are calculated dynamically and the number of steady-state variables varies

continuously during the simulation, which can make the method computationally expensive. The Intrinsic Low Dimensional Manifold (ILDM) approach, proposed by Mass and Pope [7], is based on the analysis of the eigenstructure of the Jacobian of the local source terms to identify slow chemical processes. Based on this eigensystem analysis, a small subset of variables is identified which evolves slowly during combustion. These variables are then used to generate pre-computed look-up tables to be used during simulations for evaluating chemical kinetics. The ILDM method has been shown to fail in regions of flow where diffusion processes are as important as chemical processes and it generally does not yield good results in low temperature regions of flames as fast time scales have been neglected.

The Trajectory Generated Low Dimensional Manifold (TGLDM) is based on the same principles as the ILDM method, however, instead of the chemical reacting system, the TGLDM system computes a manifold using trajectories [133]. The trajectory is the path the system takes through composition space from the initial point to the chemical equilibrium composition. TGLDM methods have the advantage over ILDM methods that they guarantee convergence and that the reaction vector is always tangent to the trajectory. A disadvantage is that it is not yet clear how one can incorporate the effects of diffusion on the manifold with TGLDM methods, as has been done with ILDM methods [134].

Apart from the above methods, other approaches which can be categorized as CRTs are the Piecewise Reusable Implementation of Solution Mapping (PRISM) by Tonse et al. [135], Quasi-Steady-State-Assumption (QSSA) by Ren and Pope [136], Reaction-Diffusion-Manifold (REDIM) by Bykov and Maas [137], and the Invariant Constrained Equilibrium Edge Pre-Image Curve (ICE-PIC) by Ren and Pope [138]. The reader is referred to the original papers for a full discussion of these alternative techniques.

Flamelet approaches assume that the local chemical structure of a flame is independent of the physical complexity of the surrounding flow. Pre-generated solutions of chemical composition for simple flames are used to predict local chemical composition in more complex situations using solution mapping procedures and functions. Flamelet methods have become popular for the treatment of diffusion flames over the last 10-15 years. Several past attempts have been made to study the chemical properties of a diffusion flame as a function of one conserved scalar (Bilger [139], Libby and Williams [140]). In the Steady Laminar Flamelet Model (SLFM) of Peters [141], pre-computed detailed chemistry solutions of one-dimensional counter flow flames are used for the simulation of more general diffusion flames. For this, all flame properties at any point in the flow are

expressed in terms of mixture fraction and another scalar characterizing the dissipation of the mixture fraction [141]. Subsequent follow-on studies have considered the application of this formulation [142–144]. Smooke et al. [145] and Nishioka et al. [146] have compared multi-dimensional laminar diffusion flame simulation results to one-dimensional counter-flow flames and reported that there is good agreement between the structure of the two flames. Smooke et al. [145] observed that the flamelet model yields poor predictions for some species concentrations in fuel-rich regions. In a recent study of the flamelet model for laminar flames, Liu et al. [144] compared directly-calculated solutions with those of the flamelet approach for a co-flow diffusion flame and noted that numerical results depend quantitatively on the definition of dissipation rate and mixture fraction.

Flame-Prolongation of ILDM (FPI) and Flame-Generated Manifold (FGM) are two tabulated approaches developed independently by Gicquel et al. [147] and Oijen et al. [77], respectively. The two methods are conceptually similar and can be viewed as hybrids of the CRT and flamelet methods discussed above. They both use pre-tabulated solutions of flames that have simplified flow geometry, which are subsequently used for the simulation of more complex flames. A controlling parameter, called the progress of reaction variable is introduced to define the mapping between the tabulated solutions and local solutions within a combustion simulation. When detailed solutions of one-dimensional laminar premixed flames are used as the basis for the tabulation in the FPI approach, both FPI and FGM are essentially identical. The primary differences between the methods are then technical and relate simply to how the tabulated data is constructed and accessed. The FGM approach is based on tabulating data as a function of enthalpy and progress of reaction variable, while FPI stores data as a function of the mixture fraction and progress of reaction variable.

The FPI and FGM schemes are currently of great interest as they are potentially unifying approaches which can be applied to the full range of flames, i.e., premixed, partially-premixed, and non-premixed flames. For laminar premixed flames, Gicquel et al. [147] and Oijen et al. [77] indicated that their respective approaches are much faster than directly performing calculations with detailed chemistry. The FPI method was extended to diffusion flames by Vervisch et al. [74] and for non-adiabatic flames by Fiorina et al. [148]. Fiorina et al. [149] subsequently also assessed the performance of the FPI method for one-dimensional counter-flow flames. More recently, Galpin et al. [150] have examined different ways in which the FPI approach can be coupled to reactive flow solution methods.
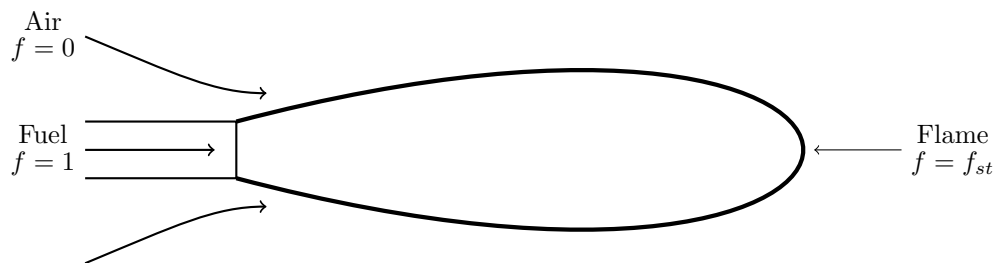
Figure 3.1: Schematic representation of the mixture fraction variable values in different parts of a diffusion flame.

An important concern is to incorporate the effects of unresolved turbulence on the reactive flow solutions. Bradley et al. [76, 151] have shown that probability density functions (PDF) can be used with known laminar flamelet solutions to account for turbulence, and this model has been used in conjunction with Reynolds-averaged Navier-Stokes (RANS) models. A number of studies have validated the use of PDFs for turbulent reacting flows [152–154]. More recently, Vervisch et al. [74], Domingo et al. [155, 156] and others have adopted a presumed PDF approach, leading to presumed conditional moment (PCM) modelling, in conjunction with the FPI approach for dealing with turbulent chemistry. In this approach, the presumed PDFs for some scalars are used to derive the mean reaction rates and species concentrations. The PCM approach was initially developed for dealing with turbulent premixed flames [149, 155, 157] and later extended for partially-premixed and diffusion flames [74, 158]. These methods have also been extended for performing with LES of turbulent flames [19, 79] and have been applied to different combustion regimes [80, 159].

The PCM-FPI scheme is considered in the present study to incorporate the effects of detailed chemistry on turbulent flames because of the recent and promising developments of this approach.

3.3 The Mixture Fraction Variable

A very useful quantity usually introduced for the description of non-premixed combustion is the mixture fraction, f. The mixture fraction gives an indication of the mixing level at any point in the flow and is defined as [15]

$$f = \frac{\text{mass of material having its origin in the fuel stream}}{\text{mass of mixture}} \tag{3.1}$$

The mixture fraction value varies from zero in the oxidizer feed to one in the fuel feed, as shown in the schematic diagram of Figure 3.1. For a non-reacting flow, if the system is homogeneous or if equal diffusivity of fuel, oxidizer, and the inert substances are assumed in an inhomogeneous system, the local value of any thermodynamic quantity, φ (temperature, mass fraction, etc.), can be expressed as a linear function of f using the relation

$$\varphi = \varphi_{\text{fuel stream contribution}} + \varphi_{\text{oxidizer stream contribution}} = \varphi_{F,0} f + \varphi_{O,0}(1 - f) \tag{3.2}$$

where $\varphi_{F,0}$ is the value of φ in the fuel stream and $\varphi_{O,0}$ represents the value of φ in the oxidizer stream (for example, $Y_{O_2,0} = 0.232$ in air). Hence, in a non-reacting flow, the value of any thermodynamic quantity at any point in the flow can be calculated by knowing the local value of mixture fraction and the states of the pure fuel and oxidizer feeds. For the reaction to occur, the fuel and the oxidizer must first mix with each other in a near stoichiometric ratio. The value of mixture fraction at the stoichiometric mixing point is referred to as f_{st} here and is illustrated in Figure 3.1.

The global reaction equation for complete combustion of a hydrocarbon fuel of general form $C_m H_n$ can be written as

$$\nu'_{\text{F}} C_m H_n + \nu'_{O_2} O_2 \rightarrow \nu''_{CO_2} CO_2 + \nu''_{H_2O} H_2O \tag{3.3}$$
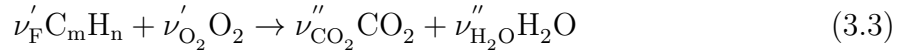
where ν'_{F} and $\nu'_{O_2} = (m + n/4)$ are the stoichiometric coefficients of fuel and oxygen, respectively. Using the above reaction, the change of mass fractions of the oxidizer and the fuel, dY_{O_2} and dY_{F} respectively, can be related to each other by

$$\frac{dY_{O_2}}{\nu'_{O_2} \mathcal{M}_{O_2}} = \frac{dY_{\text{F}}}{\nu'_{\text{F}} \mathcal{M}_F} \tag{3.4}$$

For a homogeneous system, this equation may be integrated to obtain

$$s Y_{\text{F}} - Y_{O_2} = s Y_{\text{F,u}} - Y_{O_2,u} \tag{3.5}$$

where $s = \nu'_{O_2} W_{O_2} / \nu'_{\text{F}} Y_{\text{F}}$ is the stoichiometric oxygen-to-fuel mass ratio and the subscript u denotes the initial conditions in the unburnt mixture. The mass fractions Y_{F} and Y_{O_2} correspond to any state of combustion between the unburnt and burnt state. Integrating the previous expression between the unburnt and any other state of combustion, the local mass fractions of fuel and oxidizer can be related to the mixture fraction as

$$f = \frac{s Y_F - Y_{O_2} + Y_{O_2,0}}{s Y_{F,0} + Y_{O_2,0}} \tag{3.6}$$

It is important to note that Equation (3.6) is valid only for relatively simple two-feed systems. If more than two-feeds enter into the combustion chamber, the concept of a single mixture fraction cannot be used. The flow analysis then requires introduction of multiple mixture fractions. The proposed numerical scheme considered herein is incapable of handling more than one mixture fraction value and further modifications would be required if such cases are to be considered in the future.

The PCM-FPI approach uses premixed flame solutions to represent the chemical kinetics of general diffusion flames. It is therefore important to relate the mixture fraction to another important chemical parameter, the equivalence ratio, ϕ, defined as

$$\phi = \frac{(\text{Air/Fuel})_{\text{stoic}}}{(\text{Air/Fuel})} = s\frac{Y_{\text{F}}}{Y_{\text{O}}} \tag{3.7}$$

The equivalence ratio is an important quantity as it gives a measure of the amount of fuel and oxidizer present in a given premixed fuel-oxidizer mixture. For a pure-mixing flow, the following relation can be derived between ϕ and f

$$\phi(f) = s\frac{Y_{\text{F}}}{Y_{\text{O}}} = s\frac{Y_{\text{F},0}f}{Y_{\text{O},0}(1-f)}, \tag{3.8}$$

$$f(\phi) = \frac{\phi}{\left(\phi + s\frac{Y_{\text{F},0}}{Y_{\text{O},0}}\right)} \tag{3.9}$$

In a diffusion flame, the equivalence ratio corresponds to the equivalence ratio obtained when premixing the same mass of fuel and oxidizer streams. It does not correspond to the global equivalence ratio for the burner.

The mixture fraction is also directly related to the chemical elements, as well as to the equivalence ratio. Using this general definition and summing the species transport equations together, one finds that all source terms associated with the chemical reactions cancel out each other (the total mass of the elements in a chemical reaction are conserved). The final mixture fraction transport equation is then of the form

$$\frac{\partial}{\partial t}(\rho f) + \frac{\partial}{\partial x_i}(\rho u_i f) = \frac{\partial}{\partial x_i}\left(\rho \mathcal{D}_f \frac{\partial f}{\partial x_i}\right) \tag{3.10}$$

where $\mathcal{D}_f$ is the molecular diffusivity term of the mixture fraction. The molecular diffusivity of the mixture fraction is discussed in details in Section 3.4 below.

Equation (3.10) is interesting as it shows that the mixture fraction is a conserved scalar (no chemical source terms are present), even in a reacting flow. This transport equation can be used to determine flame properties in complex diffusion flames by flamelet methods, as will be discussed in the next section.
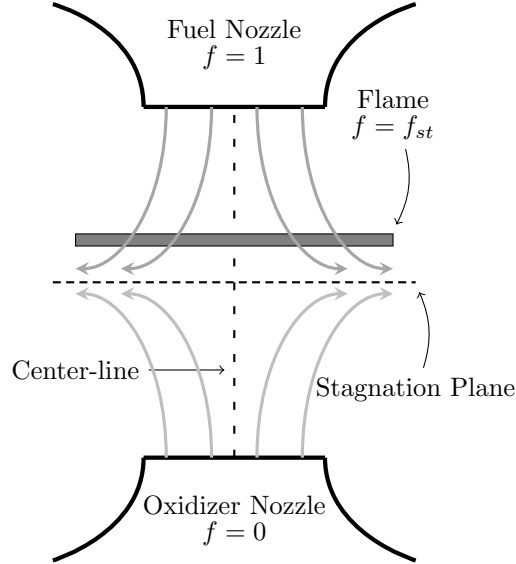
Figure 3.2: Schematic representation of a counter-flow flame. The solutions along the center-line are stored in a library and used during the simulations in the SLFM approach.

3.4   Steady Laminar Flamelet Model (SLFM)

Even though the SLFM is not the focus of the present study, it is a popular tabulated chemistry approach for the treatment of diffusion flames. The SLFM will therefore form a useful basis for comparing and evaluating the performance of the FPI approach, to be discussed in the sections to follow.

In the SLFM, all of the local thermochemical properties of a diffusion flame are expressed as a function of a single conserved scalar. This approach is based on the observation that the reaction zone in diffusion flames are limited to a thin region where reactants mix with each other in a stoichiometric ratio. Hence, the local instantaneous reaction zone structure is assumed to be the same as that of the structure along the axis of an axisymmetric quasi-steady laminar counter-flow flame as shown in Figure 3.2 [141].

Peters [141] has previously derived the flamelet equation of chemical species, k, having a mass fraction, Y_k, which for unity Lewis numbers can be written as

$$\rho \frac{\partial Y_k}{\partial t} = \rho \frac{\chi}{2} \frac{\partial^2 Y_k}{\partial f^2} + \dot{\omega}_k, \ \ (k = 1, \ldots, N) \tag{3.11}$$

where χ is the scalar dissipation rate defined as

$$\chi = 2\mathcal{D}_f \frac{\partial f}{\partial x_i} \frac{\partial f}{\partial x_i} \tag{3.12}$$

and where $\dot{\omega}_k$ is the mass reaction rate of species k produced by the chemical reactions, ρ is the mixture density, and χ is the scalar dissipation rate. Under the assumptions of unity Lewis number and further neglecting unsteady pressure changes and radiation heat transfer, it can be shown that the transport equation for the mixture fraction is equivalent to that for the mixture enthalpy (a conserved scalar, see Equation (3.10)) and the diffusion coefficient of the mixture fraction, $\mathcal{D}_f$, is equal to the thermal diffusivity of the mixture and given by

$$\mathcal{D}_f = \frac{\zeta}{\rho C_p} \tag{3.13}$$

where ζ is the mixture thermal conductivity [15].

The steady-state form of Equation (3.11) can be solved numerically using well developed methodologies and software. Here, Cantera [160], an open-source software package for chemically-reacting flows, is used to obtain steady-state solutions for counter-flow diffusion flames having different strain rates and hence different ranges of the scalar dissipation rates. Note that Cantera does not solve Equation (3.11) directly. Instead self-similar solutions are computed to the full low-Mach-number-limit Navier-Stokes equations for a reactive ideal gas mixture in an axisymmetric flow domain with an infinite radial extent (see Figure 3.2). The approach allows for arbitrary chemistry and arbitrary variation of the transport properties and is not limited to the assumption of unity Lewis number for species mass transport. Note however, the assumption of unity Lewis number is somewhat implicit in the derivation of the transport equation for the mixture fraction and the assumption that the diffusion coefficient for the mixture fraction is equal to the thermal diffusivity. For situations where this is not true, there is some inconsistency in the flamelet formulation as defined herein, although appropriate modifications are possible as outlined by Pitsch and Peters [161].

Solutions for a series of strain rates, ranging from smaller values (near equilibrium) to very larger values (approaching the quenching or extinction limit) are calculated using the Cantera software package. In the present work, the characteristic strain rate value for the counter-flow flame is defined as the velocity gradient at the stagnation point. While Equation (3.11) clearly indicates that the value of χ varies throughout the laminar flame solution, a single characteristic value of the scalar dissipation rate is chosen to represent the solution for each characteristic strain rate. Since most of the chemical activity occurs in the vicinity of the stoichiometric point of the flame, it is usually adequate to take the value of the scalar dissipation rate where mixture fraction is equal to the stoi-

chiometric value, χ_{st}, as the representative characteristic value [141, 144]. Some authors also use the value of χ at the maximum temperature as the characteristic rate [162]. For the methane-air flames being studied in this paper, these values are virtually identical and thus the stoichiometric dissipation rate, χ_{st}, is used here.

The counter-flow diffusion flame solutions are stored in a flamelet library such that any thermochemical quantity, φ, can be retrieved and expressed as $\varphi^{\mathrm{FL}} = \varphi(f, \chi_{st})$. For general combusting flows, the balance equation for the mixture fraction, Equation (3.10), is then solved instead of the full set of species continuity equations, and the local scalar dissipation rate, χ, is calculated at each point using Equation (3.12). Local values of f and χ are used to obtain the local chemical composition from the flamelet library using a bi-linear interpolation procedure.

The overall solution procedure for the SLFM approach for diffusion flames can be summarized as follows:

1. Obtain counter-flow numerical solutions using Cantera package for different strain rate values - from near equilibrium values of strain rate to the quenching limit strain rates.

2. For each solution, calculate the characteristic scalar dissipation rate value, χ_{st}, which represents that particular strain rate solution.

3. Store all solutions in a flamelet library such that any thermochemical quantity, φ, can be expressed uniquely as $\varphi = \varphi(f, \chi_{st})$.

4. Solve the transport equation for f, Equation (3.10), using a numerical scheme and calculate χ at each point using Equation (3.12) .

5. Use the local values of f and χ to get the local chemical composition from the flamelet library using bi-linear interpolation.

6. For values of χ greater than the quenching value of χ_{st}, use the pure-mixing solution as given by Equation (3.2).

Peters [141] mentions that NOx and soot particles are particularly sensitive to χ, but as the present work does not consider the formation of either of these pollutants, the variation in species concentration as a function of scalar dissipation rate should not be a significant factor. This observation is supported by the results of Figure 3.3, which
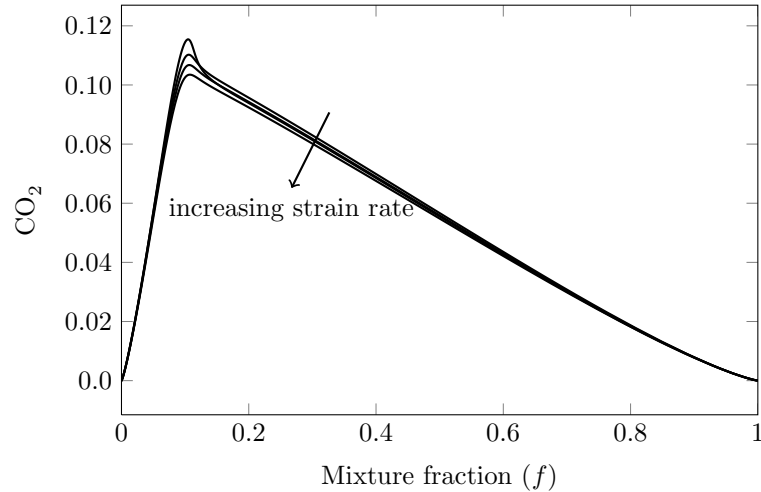
Figure 3.3: Variation of CO_2 concentration in the mixture fraction space for 30 different strain rate values for a methane-air flame. No significant variation is seen in the solution profile as a function of strain rate.

depicts the change in the distribution of the concentration of CO_2 for different values of the strain rate for methane-air laminar counter-flow flames. Similar behaviour is also observed for other thermochemical quantities. The effect of the number of tabulated strain rates is discussed further in Section 5.2.3.1.

For the methane-air flames of interest here, two different SLFM tabulation approaches are considered:

- **Approach 1, solve energy equation:** The species mass fractions from the Cantera solutions for one-dimensional counter-flow flames are stored in the flamelet library. During the simulation, the local values of f and χ are used to obtain mass fractions from the flamelet library. A consistent solution for the mixture temperature, T, is obtained by solving the full energy equation.

- **Approach 2, energy equation not solved:** The species mass fractions and temperature from the Cantera solutions for one-dimensional counter-flow flames are stored in the flamelet library. During the simulation, both mass fractions and temperature are read from the flamelet library as a function of local value of f and χ. The energy equation is not solved.

As the present study deals with largely adiabatic flames in which any heat losses due to radiation and soot formation are not considered, Approach 2 should be sufficient.
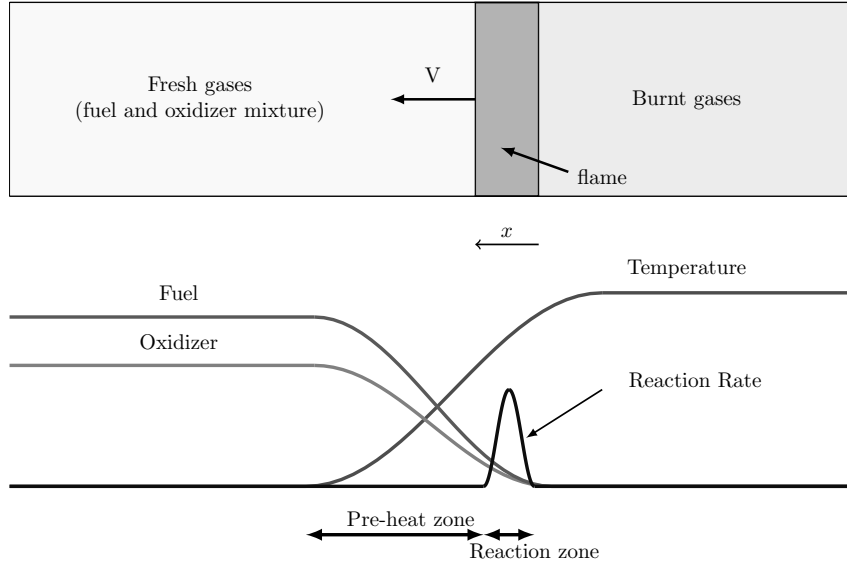
Figure 3.4: Schematic representation of a premixed flame with a flame speed of V. The bottom plot shows the profile of different quantities along the flame.

However, Approach 1 is a broader scheme as it can account for heat losses in a system as well. Approach 2 tends to be more popular in the research community, and so it will be insightful to compare their performances.

3.5   Flame Prolongation of ILDM (FPI)

3.5.1   Tabulation of Detailed Chemistry Solutions

Unlike the SLFM approach, which uses laminar counter-flow flame solutions for tabulation, the FPI method considered in this thesis is based on tabulating preliminary simulations of one-dimensional laminar premixed flame solutions at different equivalence ratios. Figure 3.4 shows the structure of a one-dimensional laminar premixed flame. In this case, all the flame properties, like the burnt gas composition, flame temperature, flame speed etc., are functions of the initial unburnt mixture being used, which is defined by the equivalence ratio of the mixture, ϕ, and the spatial coordinate, x, in the direction normal to the flame front. Hence, all flame properties can be uniquely expressed as

$$\varphi = \varphi(\phi, x) \tag{3.14}$$

In the FPI method, it is desirable to express all of the flame properties as a function of some local values of the premixed flamelet solutions. Equation (3.9) is used to replace the
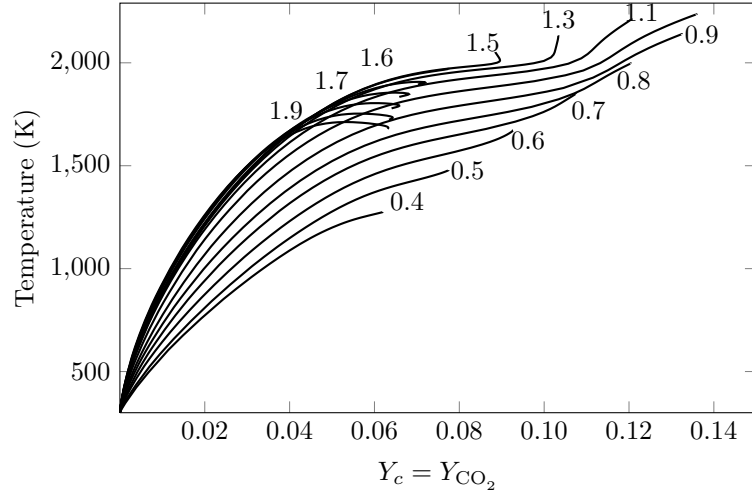
(a) Poor choice for Y_c
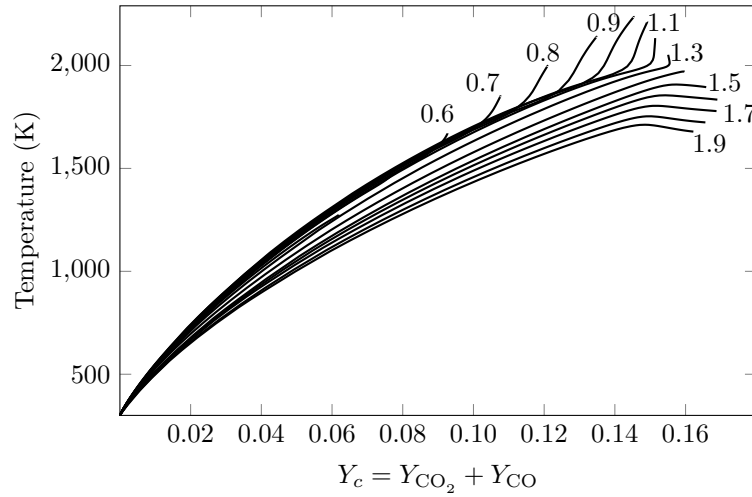
(b) Desirable choice for Y_c

Figure 3.5: Projection of adiabatic laminar premixed flames onto the (Y_c, T) space for different choices of Y_c for different equivalence ratios.

equivalence ratio term in Equation (3.14) by the mixture fraction variable. To eliminate the spatial coordinate in Equation (3.14), another solution variable, termed the progress of reaction variable, Y_c, is introduced. For simple hydrocarbons, Y_c can be defined as a linear combination of the species mass fractions, Y_i, as

$$Y_c(\phi, x) = \sum_{j=1}^{N} \alpha_j Y_j(\phi, x) \tag{3.15}$$

The progress of reaction variable is unique to every fuel-oxidizer composition and
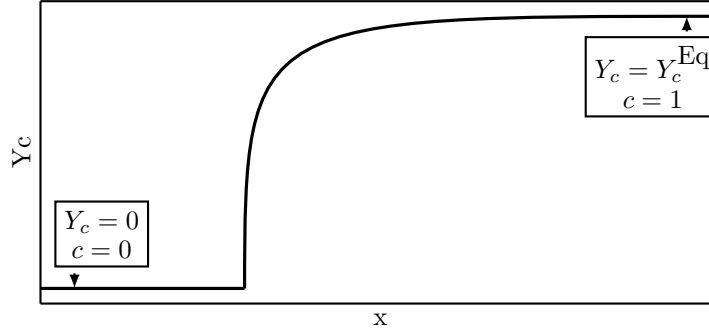
Figure 3.6: Schematic representation of the definition of equilibrium value of progress of reaction variable, Y_c^{Eq}, and progress variable, c, for a Cantera solution of a one-dimensional laminar premixed flame at a particular equivalence ratio.

should be chosen carefully such that there is a one-on-one correspondence between the spatial coordinate, x, and the progress of reaction variable, Y_c, for the entire range of equivalence ratios within the flammability envelope for premixed flames. Fiorina et al. [148] suggest that a linear combination of the mass fraction of CO_2 and CO is a good choice for the progress of reaction variable for methane-air combustion. The results of Figure 3.5 clearly demonstrates the validity of this choice. For the sake of argument, if Y_c is chosen to be the mass fraction of CO_2, Figure 3.5a shows that for rich equivalence ratios there is no longer a one-on-one correspondence between temperature and Y_c. But choosing Y_c as a linear combination of CO_2 and CO is an appropriate choice as there is a unique one-on-one correspondence between temperature and Y_c for all values of equivalence ratios.

Using an appropriate choice for Y_c, the final FPI tabulation is done as

$$\varphi^{\mathrm{FPI}} = \varphi(\phi, x) = \varphi(f(\phi), Y_c(x)) \tag{3.16}$$

It should be noted that even though, in theory, an appropriate choice of Y_c should give a monotonous solution, the numerical Cantera solutions do not always behave accordingly. Before tabulating, care should be taken make sure that the tabulated solution has a smooth monotonic profile.

For each equivalence ratio, the progress of reaction variable, Y_c, evolves from zero to its equilibrium value, $Y_c^{\mathrm{Eq}}(f(\phi))$. Vervisch et al. [74] propose the use of a normalized value of Y_c , called the progress variable, c, which is defined here as:

$$c = \frac{Y_c(f, x)}{Y_c^{\mathrm{Eq}}(f)} \tag{3.17}$$

Figure 3.6 schematically shows Y_c^{Eq} and c. The reasons for using c over Y_c will be discussed in more detail in Section 3.6.2. Hence, the final FPI tabulation is carried out as follows:

$$\varphi^{\mathrm{FPI}} = \varphi(f, c) \tag{3.18}$$

Both the number of grid points used in the one-dimensional domain and point distribution are different for the Cantera solutions for different equivalence ratios. In the present tabulation methodology, all Cantera solutions are interpolated to ensure that the same distribution in the c-space variable is used for all premixed flame solutions at each value of the mixture fraction in the final look up table.

The FPI approach uses the mixture fraction variable, f, and progress of reaction variable, Y_c, to obtain the chemical composition at any point in the flow from the look-up table. So apart from the regular mass, momentum, energy and species transport equations discussed in Section 2.3.2, two additional transport equations are solved - one each for the mixture fraction, f, and the progress of reaction variable, Y_c. The balance equation for f has already been given in Equation (3.10). The balance equation for Y_c is obtained using the linear combination of the transport equations of species used to define the progress of reaction, in Equation (3.15), and is of the form

$$\frac{\partial}{\partial t}\left(\rho Y_c\right) + \frac{\partial}{\partial x_i}\left(\rho u_i Y_c\right) = \frac{\partial}{\partial x_i}\left(\rho \mathcal{D}_{Y_c}\frac{\partial Y_c}{\partial x_i}\right) + \rho \dot{\omega}_{Y_c} \tag{3.19}$$

Two unknown terms appear in the last equation: $\mathcal{D}_{Y_c}$ and $\dot{\omega}_{Y_c}$. The reaction rate of the progress of reaction variable, $\dot{\omega}_{Y_c}$, is calculated using a linear combination of the reaction rates of the species used to define Y_c in Equation (3.15) and is given by

$$\dot{\omega}_{Y_c} = \sum_{j=1}^{N} \alpha_j \dot{\omega}_j \tag{3.20}$$

This quantity is also pre-computed and stored in the FPI table during table-generation and is read from the FPI table during the solution process, depending on the local values of f and Y_c. The molecular diffusivity of the progress of reaction variable, $\mathcal{D}_{Y_c}$, is defined as

$$\mathcal{D}_{Y_c} = \frac{\mu}{\rho \mathrm{Sc}_{Y_c}} \tag{3.21}$$

where Sc_{Y_c} is the progress of reaction Schmidt number. For the methane-air cases studied in the present work, Sc_{Y_c} is assumed to have a constant value of 1.0. However, when dealing with more diffusive fuel species like H_2, Sc_{Y_c} can become very important in

determining the distribution of the species. To deal with such fuel species, the present FPI table also has the scope to store one more variable, Sc_{Y_c}, which is calculated using the following expression

$$Sc_{Y_c} = \left(\sum_{j=1}^{N} \alpha_j \frac{\partial Y_j}{\partial x} \right) \left(\sum_{j=1}^{N} \alpha_j \frac{1}{Sc_j} \frac{\partial Y_j}{\partial x} \right)^{-1} \tag{3.22}$$

Nevertheless, as will be shown later in Section 5.2.3.2, a variable Schmidt number for progress of reaction does not affect the solution considerably for methane-air flames. Hence, a constant value of Sc_{Y_c} is used and Equation (3.22) has not been used in the present work.

It should be noted that diffusion flamelets could potentially be used to create the tabulated chemistry manifold as discussed by Delhaye et al. [129], but this has not been considered here. A focus of the present study is an evaluation of the FPI approach based on premixed laminar flamelets.

3.5.2   Extension to Non-Premixed Flames

Several methods have been suggested in literature for extending the FPI scheme to diffusion flames. Vervisch et al. [74] suggest constructing a mapping function from the FPI and a library of steady diffusion flamelets in order to get, from the FPI table, the species mass fractions representative of diffusion flame. This mapping function helps create a library of steady diffusion flamelets, as suggested by Peters [15]. The approach used in this thesis is based on the work by Fiorina et al. [158] who suggest using a linear extrapolation, between the last tabulated flame on the lean (or rich) side and the air (or fuel) stream, to complete the table outside of the premixed flame flammability limits.

Figure 3.7 illustrates the procedure used in the present work in order to obtain solutions outside the flammability limits for the FPI table generation. A linear interpolation is performed between the rich/lean flammability limit solution and the pure-mixing solution, i.e., $Y_c = 0$, given by Equation (3.2). As shown in Figure 3.7, to calculate the species mass fractions at a point P outside the premixed limits, a linear interpolation is performed between the points P_1 and P_2 such that the line P_1-P_2 is the shortest line between the lines $Y_c = 0$ and $f = f_{rich}$ passing through the point P, where f_{rich} and f_{lean} are the maximum and minimum mixture-fractions/equivalence-ratios, respectively, for which the laminar premixed flame solution exists. For pure methane, the lean equivalence ratio
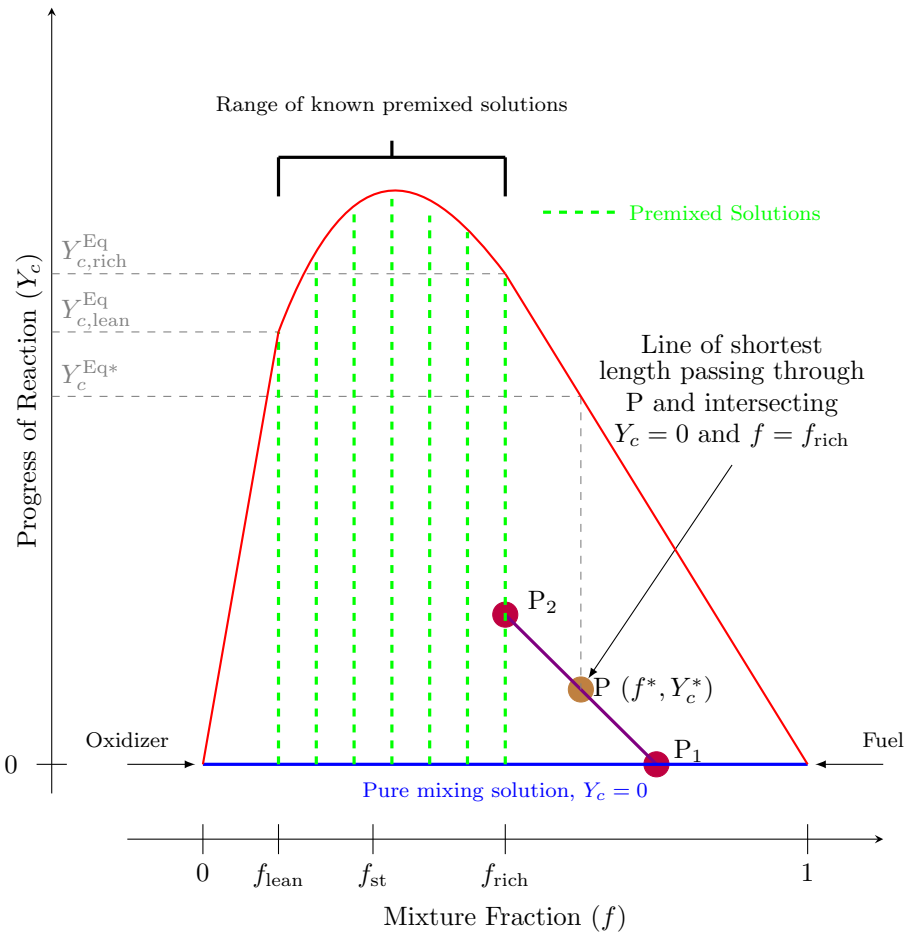
Figure 3.7: An schematic representation of the algorithm used for calculating the mass fractions outside the premixed limits in the FPI method for non-premixed flames. The reaction rates are simply set to zero outside the premixed limits.

is around 0.4 and rich equivalence ratio is around 2.0. The reaction rate of the progress of reaction variable, $\dot{\omega}_{Y_c}$, is set to zero outside the flammability limits of premixed flames.

The red line in Figure 3.7 corresponds to the values of Y_c^{Eq} for the different mixture fraction values. Outside the flammability limits, the Y_c^{Eq} line is extrapolated as a straight line from $(f_{\mathrm{rich}}, Y_{c,\mathrm{rich}}^{\mathrm{Eq}})$ to $(1,0)$ on the rich side and a straight line joining $(f_{\mathrm{lean}}, Y_{c,\mathrm{lean}}^{\mathrm{Eq}})$ to $(0,0)$ on the lean side. For a given value of mixture fraction, f, the value $Y_c^{\mathrm{Eq}*}$ is used to calculate the progress variable, c, depending on the local value of Y_c, to extract data from the FPI table.

Using the Cantera generated premixed solutions and the algorithm discussed above, FPI tables are generated which can be used directly in the prediction of laminar diffusion flames. The next section discusses how these laminar flame tables are further modified

so that the final tabulated data includes the effect of turbulence on chemical kinetics and can be used for fully turbulent diffusion flames.

3.6   Turbulence and FPI

The treatment of turbulence-chemistry interaction using the FPI approach is based on a stochastic approach where the reactive and diffusive properties of a flame are described using joint probability density functions (PDF) to model the effect of turbulence on the mean reacting flow-field. Therefore in order to predict non-equilibrium effects in turbulent diffusion flames, it is necessary to predict the joint distribution function of f and c. The next section discusses the PCM approach which addresses this problem. Pope [163] gives a more elaborate discussion on the properties and use of PDFs in turbulent flows.

3.6.1   Presumed Conditional Moment

The PDF, $P(G^*; x, t)$, for a random variable G, quantifies the probability of finding G within a range $[G^* - dG/2, G^* + dG/2]$ at a given location, x and time, t. This probability is equal to $P(G^*; x, t)dG$. Here G^* represents the sample space variable for G. The PDF satisfies several basic probability relations:

$$\int_G P(G^*; x, t)dG^* = 1 \tag{3.23}$$

$$\int_G G^* P(G^*; x, t)dG^* = \widetilde{G}(x, t) \tag{3.24}$$

$$\int_G (G^* - \widetilde{G})^2 P(G^*; x, t)dG^* = G_v(x, t) \tag{3.25}$$

Equation (3.24) and Equation (3.25) represent the mean and variance of the variable G, expressed as the first and second moments of the PDF, while Equation (3.23) reflects the fact that the probability of finding G over the full range of values is defined to be unity.

This procedure can be generalized to the case of multiple random variables. To calculate the mean of a variable, φ, which is dependent on (say) N independent variables, $w_1, \ldots, w_N$, such that $\varphi = \varphi(w_1, \ldots, w_N)$, a joint PDF $P(w_1^*, \cdots, w_N^*; x, t)$ is introduced. The mean value of φ is then estimated as

$$\widetilde{\varphi}(x, t) = \int_{w_1} \cdots \int_{w_N} \varphi(w_1^*, \cdots, w_N^*) P(w_1^*, \cdots, w_N^*; x, t)dw_1^* \cdots dw_N^* \tag{3.26}$$

As discussed earlier in Section 3.5.1, in the FPI approach, all thermochemical quantities, φ, are expressed as a function of two variables, the mixture fraction, f, and the progress variable, c, such that

$$\varphi^{\text{FPI}} = \varphi(f, c) \tag{3.27}$$

Hence, by simplifying Equation (3.26), the mean value of any FPI tabulated quantity can be expressed as

$$\widetilde{\varphi}(x, t) = \int_f \int_c \varphi^{\text{FPI}}(f^*, c^*) P(f^*, c^*) df^* dc^* \tag{3.28}$$

The joint PDF of f and c, given in Equation (3.28), can be decomposed using the conditional PDF for c for a given value of f^*, $P(c^*|f^*)$, using the relation

$$P(f^*, c^*) = P(c^*|f^*) P(f^*) \tag{3.29}$$

DNS results [74, 155, 164] and experimental results [165] have shown that it is appropriate to treat the mixture fraction and progress variable as statistically independent variables, i.e., $\widetilde{(c|f^*)} \approx \widetilde{c}$, provided an appropriate choice of progress variable is made. This hypothesis of statistical independence is not strictly exact, but has been found to be a reasonable approximation for appropriate choices of Y_c [155]. For example, in the experimental set-up studied by Barlow and Frank [165] for methane-air jet flames, it was observed that the conditional statistical behaviour of c constructed from the linear combination of CO and CO_2 weakly varies with mixture fraction. Hence, it can be assumed that

$$P(f^*, c^*) = P(f^*) P(c^*) \tag{3.30}$$

It is important to note that the hypothesis of statistical independence with f applies to c only, which is a normalized quantity, but not to the progress of reaction variable, Y_c, or any other quantity φ extracted from the table [155, 156]. Substituting Equation (3.29) in Equation (3.28) and using Equation (3.30), Equation (3.28) can be simplified to yield

$$\widetilde{\varphi}(x, t) = \widetilde{\varphi}^{\text{PCM}}(x, t) = \int_f \int_c \varphi^{\text{FPI}}(f^*, c^*) P(f^*) P(c^*) df^* dc^* \tag{3.31}$$

Equation (3.31) suggests that if the PDFs for both the mixture fraction and the progress variable are known, then the joint PDF approach can be used to calculate the mean of all FPI-tabulated quantities in a turbulent flow.

There are two common approaches to determine $P(f)$ and $P(c)$:

1. the PDF shape is presumed and characterized by a minimum number of parameters; and

2. a balance equation is solved directly for the PDF.

Since prediction methods for turbulent flows are generally based on monument's rather than on the PDF itself, the most convenient method to determining the PDF is to assume an n-parameter function and to relate the first n moments to these parameters. However, several researchers have used the direct approach of modelling and solving a transport equation for the PDF itself [59–61, 154, 166]. In the PDF transport equation, models of turbulent mixing and transport are required, but the effects of reaction appear in closed form, however complicated the reaction scheme. Solving PDF balance equations is a more sophisticated approach, but for the methane-air diffusion flames under consideration here, the presumed PDF approach has been used successfully in several previous studies, as discussed below, and is used in the present work.

As the mixture fraction, f, is bounded between 0 and 1, the choice of presumed PDFs is reduced to a small number of physically realistic functions. Richardson et al. [167] were the first to use a β-distribution as the choice of the PDF. Some other distributions like the sinusoidal PDF, "clipped Gauss" distribution and a triangular have also been investigated by other researchers [168–170]. A comparison between the different assumed PDFs was carried out by Jones [171] and Libby and Williams [172] who compare the calculated results with the experimental measurements of Kent and Bilger [173]. The results obtained show that the double delta function is unsatisfactory and both β and clipped Gaussian PDFs give very similar agreement with experimental data. In other more recent studies, beta-distributions have proven to be a very popular choice in PCM approaches [74, 164, 174, 175].

In the present study, the PDFs for both mixture fraction and progress reaction, $P(f)$ and $P(c)$, are assumed to be β-distributions, as this is the most widely used PDF and it has the distinct computational advantage that it can be fully described algebraically by just the first two moments. It does have the disadvantage that it cannot approximate bimodal PDFs which are frequently observed in intermittent free shear flows. A β-function has the form

$$P(Z^*) = \frac{(Z^*)^{(a-1)}(1 - Z^*)^{(b-1)}}{\int_0^1 (Z^+)^{(a-1)}(1 - Z^+)^{(b-1)} dZ^+} \tag{3.32}$$

The two parameters a and b defining the β-PDF the can be determined in terms of the

mean and variance as

$$a = \widetilde{Z}\left(\frac{\widetilde{Z}(1-\widetilde{Z})}{Z_v^2} - 1\right) \qquad b = a\left(\frac{1}{\widetilde{Z}} - 1\right) \tag{3.33}$$

The next section discusses how the PCM and the β-PDFs are used with the FPI approach.

3.6.2 Tabulation for PCM-FPI

Using Equation (3.17), the conditional mean of Y_c for a given value of f, f^*, $\widetilde{Y_c|f^*}$, maybe written as

$$\widetilde{Y_c|f^*} = \widetilde{c|f^*}Y_c^{\text{Eq}}(f^*) \tag{3.34}$$

Using the statistical independence argument, an approximation of the conditional mean can be expressed as

$$\widetilde{Y_c|f^*} \approx \widetilde{c}Y_c^{\text{Eq}}(f^*) \tag{3.35}$$

Integrating Equation (3.35) over the mixture fraction space with $P(f^*)$ leads to

$$\widetilde{Y}_c = \widetilde{c}\widetilde{Y_c^{\text{Eq}}} \tag{3.36}$$

where

$$\widetilde{Y_c^{\text{Eq}}} = \int_o^1 Y_c^{\text{Eq}}(f^*)P(f^*)df^* \tag{3.37}$$

As discussed earlier, the mixture fraction PDF, $P(f^*)$, is presumed from its first and second moments. This requires solving additional balance equations for the mean and the variance of mixture fraction, $\widetilde{f}$ and f_v, respectively. The balance equation for mixture fraction, Equation (3.10), can be used to derive the following equations [156, 175]

$$\frac{\partial}{\partial t}\left(\overline{\rho}\widetilde{f}\right) + \frac{\partial}{\partial x_i}\left(\overline{\rho}\widetilde{u}_i\widetilde{f}\right) = -\frac{\partial \tau_f}{\partial x_i} + \frac{\partial}{\partial x_i}\left(\overline{\rho}\mathcal{D}_f\frac{\partial \widetilde{f}}{\partial x_i}\right) \tag{3.38}$$

$$\frac{\partial}{\partial t}\left(\overline{\rho}f_v\right) + \frac{\partial}{\partial x_i}\left(\overline{\rho}\widetilde{u}_if_v\right) = \frac{\partial}{\partial x_i}\left(\overline{\rho}\mathcal{D}_f\frac{\partial f_v}{\partial x_i}\right) - \frac{\partial}{\partial x_i}\left(\tau_{f^2} - 2f\tau_f\right) + 2\overline{\rho}\mathcal{D}_f\frac{\partial f}{\partial x_i}\frac{\partial f}{\partial x_i}$$
$$-2\tau_f\frac{\partial f}{\partial x_i} - 2\overline{\rho}\chi_f \tag{3.39}$$

The unclosed turbulent fluxes, τ_f and $(\tau_{f^2} - 2f\tau_f)$, are modelled using a gradient transport hypothesis such that

$$\tau_f = -\mathcal{D}_t\frac{\partial \widetilde{f}}{\partial x_i} \tag{3.40}$$

$$(\tau_{f^2} - 2f\tau_f) = -\mathcal{D}_t\frac{\partial f_v}{\partial x_i}, \tag{3.41}$$

The unknown source term in Equation (3.39), the scalar dissipation rate of f, χ_f, is closed using a linear relaxation hypothesis given by

$$\chi_f = \mathcal{D}_t \frac{\partial \widetilde{f}}{\partial x_i} \frac{\partial \widetilde{f}}{\partial x_i} + C_f \omega f_v, \tag{3.42}$$

where C_f is the closure coefficient for f_v transport equation and is set to 1.0.

The definition of a mean flow quantity via Equation (3.31) also requires knowing the PDF of c, $P(c^*)$, which is also assumed to be a β-distribution. This requires knowledge of the values of both the mean and the variance of the progress variable, $\widetilde{c}$ and c_v, respectively. The value of $\widetilde{c}$ can be determined using Equation (3.36). Using the definition of variance, an expression for c_v can be derived as

$$c_v = \frac{Y_{cv}}{\widetilde{Y_c^{\mathrm{Eq}^2}}} + \widetilde{Y}_c^{\,2} \left(\frac{1}{\widetilde{Y_c^{\mathrm{Eq}^2}}} - \frac{1}{\widetilde{Y_c^{\mathrm{Eq}}}^2} \right) \tag{3.43}$$

where $\widetilde{Y_c^{\mathrm{Eq}^2}}$ is

$$\widetilde{Y_c^{\mathrm{Eq}^2}} = \int_o^1 Y_c^{\mathrm{Eq}^2}(f^*) P(f^*) df^* \tag{3.44}$$

It should be noted that Equation (3.44) and Equation (3.37) provide expressions for two different quantities, i.e.

$$\widetilde{Y_c^{\mathrm{Eq}^2}} \neq \widetilde{Y_c^{\mathrm{Eq}}}^2 \tag{3.45}$$

and both of these quantities are pre-computed independently and stored in the PCM-FPI table during the table generation process.

Calculating c and c_v requires prescription of the local values of $\widetilde{Y}_c$ and Y_{cv}. The transport equation for these two variables can be derived using Equation (3.19) as [156, 175]

$$\frac{\partial}{\partial t} \left(\overline{\rho} \widetilde{Y}_c \right) + \frac{\partial}{\partial x_i} \left(\overline{\rho} \widetilde{u}_i \widetilde{Y}_c \right) = -\frac{\partial}{\partial x_i} \left(\tau_{Y_c} \right) + \frac{\partial}{\partial x_i} \left(\overline{\rho} \mathcal{D}_{Y_c} \frac{\partial \widetilde{Y}_c}{\partial x_i} \right) + \overline{\rho} \widetilde{\dot{\omega}}_{Y_c} \tag{3.46}$$

$$\frac{\partial}{\partial t} \left(\overline{\rho} Y_{cv} \right) + \frac{\partial}{\partial x_i} \left(\overline{\rho} \widetilde{u}_i Y_{cv} \right) = \frac{\partial}{\partial x_i} \left(\overline{\rho} \mathcal{D}_{Y_c} \frac{\partial \widetilde{Y}_c}{\partial x_i} \right) - \frac{\partial}{\partial x_i} \left(\tau_{Y_c^2} - 2Y_c \tau_{Y_c} \right) + 2\overline{\rho} \mathcal{D}_{Y_c} \frac{\partial \widetilde{Y}_c}{\partial x_i} \frac{\partial \widetilde{Y}_c}{\partial x_i}$$

$$- 2\tau_{Y_c} \frac{\partial \widetilde{Y}_c}{\partial x_i} - 2\overline{\rho} \chi_{Y_c} + 2\overline{\rho} \left(\widetilde{Y_c \dot{\omega}_{Y_c}} - \widetilde{Y}_c \widetilde{\dot{\omega}}_{Y_c} \right) \tag{3.47}$$

Here again, the unclosed turbulent fluxes, τ_{Y_c} and $\left(\tau_{Y_c^2} - 2Y_c \tau_{Y_c} \right)$, are modelled using a

gradient transport hypothesis

$$\tau_{Y_c} = -\mathcal{D}_t \frac{\partial \widetilde{Y}_c}{\partial x_i} \tag{3.48}$$

$$\left(\tau_{Y_c^2} - 2Y_c\tau_{Y_c}\right) = -\mathcal{D}_t \frac{\partial Y_{cv}}{\partial x_i} \tag{3.49}$$

and the unclosed source term, the scalar dissipation rate of Y_c, χ_{Y_c}, is modeled as

$$\chi_{Y_c} = \mathcal{D}_t \frac{\partial \widetilde{Y}_c}{\partial x_i} \frac{\partial \widetilde{Y}_c}{\partial x_i} + C_{Y_c}\omega Y_{cv} \tag{3.50}$$

where C_{Y_c} is the closure coefficient for Y_{cv} transport equation set to 1.0.

The unknown reaction rate terms that appear in Equation (3.46) and Equation (3.47) are also extracted from the PCM-FPI table during the solution process. These values are pre-computed and stored in the table at the time of table-generation using the following expressions

$$\widetilde{\dot{\omega}}_{Y_c} = \int_o^1 \int_o^1 \dot{\omega}_{Y_c}^{\mathrm{FPI}} P(c^*)P(f^*)dc^*df^* \tag{3.51}$$

$$\widetilde{Y_c\dot{\omega}_{Y_c}} = \int_o^1 \int_o^1 c^* Y_c^{\mathrm{Eq}}(f^*)\dot{\omega}_{Y_c}^{\mathrm{FPI}} P(c^*)P(f^*)dc^*df^* \tag{3.52}$$

While the mean of both mixture fraction and progress variable are normalized quantities, the same cannot be said for their variances. For tabulation purposes, it is convenient if all the independent variables are normalized. To normalize the variances, a new term called the unmixedness or the segregation factor is introduced. In premixed flames, the maximum level of fluctuations of the progress variable is obtained when c is is fully segregated [124]. Under these circumstances, c_v takes its maximum value $c_v = \widetilde{c}/(1 - \widetilde{c})$. Using similar arguments for the mixture fraction, the variances of f and c are therefore normalized using the following expressions

$$S_f = \frac{f_v}{\widetilde{f}(1 - \widetilde{f})} \tag{3.53}$$

$$S_c = \frac{c_v}{\widetilde{c}(1 - \widetilde{c})} \tag{3.54}$$

where S_f and S_c are then the segregation factors of $\widetilde{f}$ and $\widetilde{c}$, respectively. This procedure appropriately normalizes the variances. The segregation factor tends to unity in the limit case of a flame behaving as a thin interface separating fresh and burnt gases. Then, the variance of each variable reaches its maximum value.

To summarize, in the final PCM-FPI table for the mean quantities of turbulent flames, every thermochemical quantity is stored as

$$\widetilde{\varphi} = \varphi^{\mathrm{PCM}}(\widetilde{f}, S_f, \widetilde{c}, S_c) \tag{3.55}$$

The final form of the additional transport equations solved for the PCM-FPI scalars are as follows

$$\frac{\partial}{\partial t}\left(\overline{\rho}\widetilde{f}\right) + \frac{\partial}{\partial x_i}\left(\overline{\rho}\widetilde{u}_i\widetilde{f}\right) = \frac{\partial}{\partial x_i}\left(\overline{\rho}\left(\mathcal{D}_f + \mathcal{D}_t\right)\frac{\partial \widetilde{f}}{\partial x_i}\right) \tag{3.56}$$

$$\frac{\partial}{\partial t}\left(\overline{\rho}f_v\right) + \frac{\partial}{\partial x_i}\left(\overline{\rho}\widetilde{u}_i f_v\right) = \frac{\partial}{\partial x_i}\left(\overline{\rho}\left(\mathcal{D}_f + \mathcal{D}_t\right)\frac{\partial f_v}{\partial x_i}\right) + 2\overline{\rho}\mathcal{D}_t\frac{\partial \widetilde{f}}{\partial x_i}\frac{\partial \widetilde{f}}{\partial x_i} - 2C_f\overline{\rho}\omega f_v \tag{3.57}$$

$$\frac{\partial}{\partial t}\left(\overline{\rho}\widetilde{Y}_c\right) + \frac{\partial}{\partial x_i}\left(\overline{\rho}\widetilde{u}_i\widetilde{Y}_c\right) = \frac{\partial}{\partial x_i}\left(\overline{\rho}\left(\mathcal{D}_{Y_c} + \mathcal{D}_t\right)\frac{\partial \widetilde{Y}_c}{\partial x_i}\right) + \overline{\rho}\widetilde{\dot{\omega}}_{Y_c} \tag{3.58}$$

$$\frac{\partial}{\partial t}\left(\overline{\rho}Y_{cv}\right) + \frac{\partial}{\partial x_i}\left(\overline{\rho}\widetilde{u}_i Y_{cv}\right) = \frac{\partial}{\partial x_i}\left(\overline{\rho}\left(\mathcal{D}_{Y_c} + \mathcal{D}_t\right)\frac{\partial \widetilde{Y}_c}{\partial x_i}\right) + 2\overline{\rho}\mathcal{D}_{Y_c}\frac{\partial \widetilde{Y}_c}{\partial x_i}\frac{\partial \widetilde{Y}_c}{\partial x_i}$$
$$- 2C_{Y_c}\overline{\rho}\omega Y_{cv} + 2\overline{\rho}\left(\widetilde{Y_c\dot{\omega}_{Y_c}} - \widetilde{Y}_c\widetilde{\dot{\omega}}_{Y_c}\right) \tag{3.59}$$

The PCM-FPI methodology discussed above outlines how the Cantera solutions for laminar premixed flames can be tabulated and integrated to create tables which contain averaged solutions. However tabulating the entire detailed-chemistry solution and performing numerical integration on the whole data set can get quite computationally expensive — especially when dealing with more complex fuels like aviation fuels. The next section discusses some ways to manage the PCM-FPI table size.

3.7   PCM-FPI Table Size

The FPI table size can be an important concern and can tax available computer memory when performing practical calculations, especially when dealing with non-premixed turbulent flames. Galpin [175] discuss techniques for reducing the number of species retained in the tabulated solutions without significantly affecting solution accuracy.

Following Galpin et al. [150], a careful study was performed to determine which species of the 53 species of the GRI-Mech 3.0 mechanism contribute the most to the total mass and energy of the flame. A subset of $M < N$ species was selected so that their combined contribution to the mass and energy budget dominate over the remaining $N - M$ species.
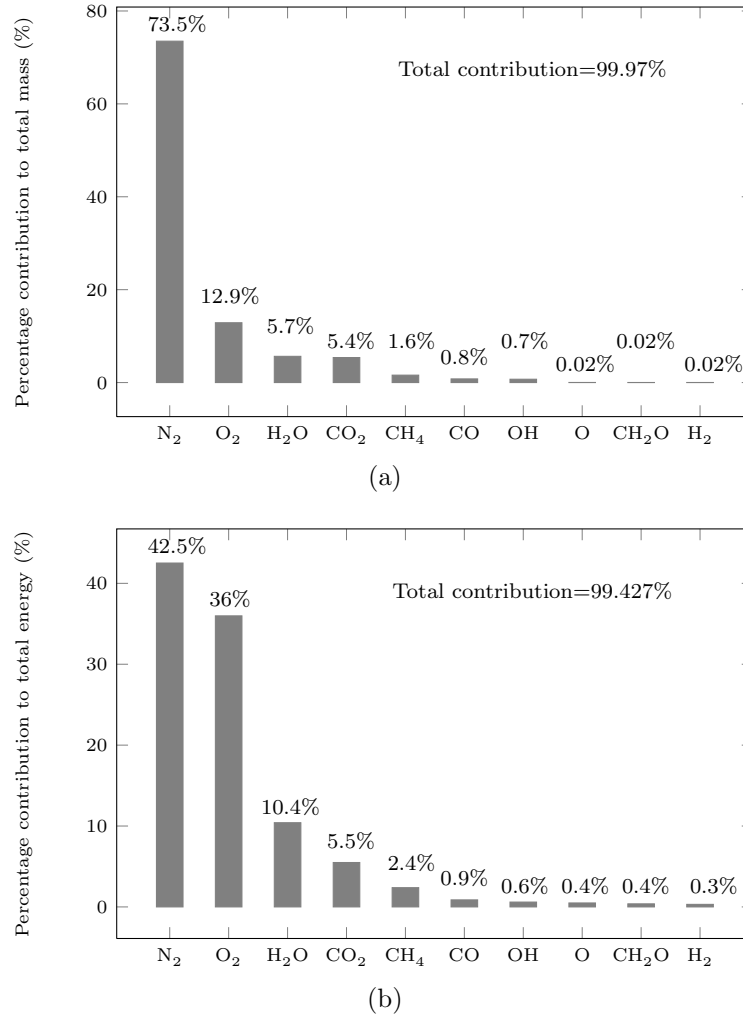
Figure 3.8: Percentage contribution of major species to the total mass and energy budget for equivalence ratio, $\phi = 0.75$.

A measure of the contribution of the species i to the total energy budget is given by $\mathcal{E}_i$, where

$$\mathcal{E}_i = \int_{-\infty}^{+\infty} h_i^f \dot{\omega}_i dx \tag{3.60}$$

and where h_i^f is the heat of formation of species i. The ratio

$$r_{e_i} = \frac{\mathcal{E}_i}{\sum_{j=1}^{N} \mathcal{E}_j} \tag{3.61}$$

informs on the relative contribution of species i to the total energy budget. Similarly, a measure of the contribution of species i to the total mass budget is given by $\mathcal{C}_i$, where

$$\mathcal{C}_i = \int_{-\infty}^{+\infty} Y_i dx \tag{3.62}$$

and the ratio

$$r_{m_i} = \frac{\mathcal{C}_i}{\sum_{j=1}^{N} \mathcal{C}_j} \tag{3.63}$$

informs on the relative contribution of species i to the total mass of the burning mixture. Figure 3.8 clearly shows that of the 53 GRI-Mech 3.0 mechanism species, only 7 species: CH_4, O_2, CO_2, CO, H_2O, H_2 and N_2, are needed to account for more than 99.5% of the total mass and energy of the mixture. Therefore, using the information for only these 7 species affords virtually a full description of the flame properties. However, in order to properly account for the elemental mass of the remaining species, additional species must also be tabulated. Careful studies have shown that H, OH and C_2H_2 are a good choice for these additional species in the case of methane-air flames [175]. Hence, the final look-up table in the current study stores data for a total of 10 species (7 major and 3 minor species for satisfying elemental mass balance).

Apart from the number of species stored, another important factor determining table size is the number of mixture fraction, progress reaction and segregation factor points stored (i.e., the dimensions for the independent variables in the table). By experience, more than 100 points are needed for the c-space variable for accurate integrations using the β-PDF and 120 mixture fraction points seems to give good results for methane-air flames. Of these 120 mixture fraction points, around half the points lie within the premixed flammability limits and half of them outside. Domingo et al. [156] and others [19] show that 20 points works for segregation factor of c for turbulent premixed flames and accordingly 20 points have been used for the segregation factor of f. To conclude, in the present study for methane-air reacting flows, the dimensions of the table used were ($121 \times 20 \times 121 \times 20$). The table was stored in a binary format and had a size of 537 MB. A study of the effect of FPI table-size on the results has also been carried out as part of this thesis and is summarized in Section 5.2.3.1.

3.8   Coupling Tabulated Data with Flow Solver

Three approaches are considered in this thesis for coupling the FPI tabulated data to the reactive flow solution algorithm used here. The three approaches are summarized as follows:

- **Approach 1 – Tabulated Mass Fractions**: The look-up table stores the mass fractions of the reduced set of species. The mass fractions of the major species are

Method	Tabulated	Species PDEs Solved	Methodology
(1)	$Y_i, \dot{\omega}_{Y_c}$	No	Get Y_i from table using $Y_i = Y_i(f, Y_c)$. Use Y_i directly in the solver.
(2)	$\dot{\omega}_i, \dot{\omega}_{Y_c}$	Yes	Get $\dot{\omega}_i$ from table using $\dot{\omega}_i = \dot{\omega}_i(f, Y_c)$. Use $\dot{\omega}_i$ in species PDEs for reaction rate source term.
(3)	$Y_i, \dot{\omega}_{Y_c}$	Yes	Get Y_i from table. Reconstruct $\dot{\omega}_i$ using $\dot{\omega}_i \approx \dot{\omega}_{Y_c} \frac{\partial Y_i}{\partial Y_c}$. Use these $\dot{\omega}$ values in species PDEs.

Table 3.1: Different ways of coupling the FPI look-up table to the flow solver. In all methods, $\dot{\omega}_{Y_c}$ for Y_c transport equation is obtained from the table.

used directly from the pre-computed solutions whereas the mass fractions of minor or additional species, such as C_2H_2 and H_2, are calculated by ensuring atomic mass conservation [150]. For example, when the detail chemistry solution of all 53 species is known, the conservation of atomic mass of carbon atoms provides the following expression for calculating $Y_{C_2H_2}$ in the reduced set of species:

$$Y_{C_2H_2} = \frac{\mathcal{M}_{C_2H_2}}{n_{C_{C_2H_2}}} \left(\sum_{j=1}^{N} Y_j \frac{n_{C_j} \mathcal{A}_C}{\mathcal{M}_j} - \sum_{\substack{j=1 \\ j \neq C_2H_2}}^{M} Y_j \frac{n_{C_j} \mathcal{A}_C}{\mathcal{M}_j} \right) \tag{3.64}$$

where $\mathcal{A}_k$ is the atomic weight of species k. Individual species transport equations are not solved. Instead, local values of f and Y_c are used to obtain the species concentrations from the table using bi-linear interpolation.

- **Approach 2 – Tabulated Reaction Rates**: The look-up table stores the reaction-rates of the reduced set of species. The reaction rates of the major species are used directly from the pre-computed solutions but the reaction rates of the additional minor species are evaluated by using atomic mass conservation [150]. For example, conservation of atomic mass of Carbon atoms gives the following expression for $\dot{\omega}_{C_2H_2}$:

$$\dot{\omega}_{C_2H_2} = -\frac{\mathcal{M}_{C_2H_2}}{n_{C_{C_2H_2}}} \sum_{\substack{j=1 \\ n_{C_j} \neq 0 \\ j \neq C_2H_2}}^{M} \frac{\dot{\omega}_j}{\mathcal{M}_j} \tag{3.65}$$

The transport equations for the mass fractions of each species in the reduced set, both major and minor species, are solved. The tabulated reaction rates stored as a function of local values of f and Y_c are used in evaluating the chemical source terms appearing in the species transport equations.

- **Approach 3 – Tabulated Mass Fractions & Estimated Reaction Rates**: Highly diffusive species can have large gradient values. Resolving these high values using tabulated species mass fraction needs highly refined tables. A bridge between the above two approaches is to use a mass fraction look-up table, like Approach 1, and reconstruct the species reaction rates using the mass fraction data. For this we need to link the species mass fraction and species reaction rates. A procedure for doing so is discussed below.

It is known that in the FPI scheme, $Y_i = Y_i(f, Y_c)$. To specify the evolution of Y_i in f-Y_c space, we start with the following known relations

$$\nabla Y_i = \frac{\partial Y_i}{\partial f}\nabla f + \frac{\partial Y_i}{\partial Y_c}\nabla Y_c \tag{3.66}$$

$$\nabla^2 Y_i = \frac{\partial^2 Y_i}{\partial f^2}|\nabla f|^2 + \frac{\partial Y_i}{\partial f}\nabla^2 f + \frac{\partial^2 Y_i}{\partial Y_c^2}|\nabla Y_c|^2 + \frac{\partial Y_i}{\partial Y_c}\nabla^2 Y_c + 2\frac{\partial^2 Y_i}{\partial f \partial Y_c}\nabla f \cdot \nabla Y_c \tag{3.67}$$

Introducing these equations in Equation (2.4) and combining them with Equation (3.10) and Equation (3.58), the following relation is obtained

$$\dot\omega_{Y_c}\frac{\partial Y_i}{\partial Y_c} = \rho\chi_f\frac{\partial^2 Y_i}{\partial f^2} + \rho\chi_{Y_c}\frac{\partial^2 Y_i}{\partial Y_c^2} + 2\rho\chi_{f,Y_c}\frac{\partial^2 Y_i}{\partial f \partial Y_c} + \dot\omega_i \tag{3.68}$$

where the scalar dissipation rates $\chi_f = \mathcal{D}|\nabla f|^2$, $\chi_{Y_c} = \mathcal{D}|\nabla Y_c|^2$ and the cross scalar dissipation rate, $\chi_{f,Y_c} = \mathcal{D}\nabla f \cdot \nabla Y_c$ have been introduced. The scalar dissipation rates are an indication of the physical time-scales. When the chemistry is much faster than transport in physical space, which is true for the infinitely fast chemistry assumption made here, all the $\chi/\dot\omega_{Y_c}$ ratios go to zero in Equation (3.68) and we have

$$\dot\omega_i = \dot\omega_{Y_c}\frac{\partial Y_i}{\partial Y_c} \tag{3.69}$$

Approach 3 therefore uses Equation (3.69) to reconstruct species reaction rates from tabulated mass fraction data. The species mass balance equations are then solved directly using this value of reaction rate. This approach avoids the need

Independent variables	Dependent variables
$\widetilde{f}$	$\widetilde{Y_c^{\text{Eq}}}(\widetilde{f})$ Equation (3.37)
$\widetilde{c}$	$\widetilde{Y_c^{\text{Eq}^2}}(\widetilde{f})$ Equation (3.44)
S_c	$\widetilde{\dot{\omega}}_{Y_c}(\widetilde{f}, S_f, \widetilde{c}, S_c)$ Equation (3.51)
S_f	$\widetilde{Y_c \dot{\omega}_{Y_c}}(\widetilde{f}, S_f, \widetilde{c}, S_c)$ Equation (3.52)
	$\widetilde{Y}_i(\widetilde{f}, S_f, \widetilde{c}, S_c)$ Equation (3.70)
	or $\widetilde{\dot{\omega}}_i(\widetilde{f}, S_f, \widetilde{c}, S_c)$ Equation (3.71)

Table 3.2: A summary of the data stored in the PCM-FPI look-up table.

for a large number of tabulated values, as in Approach 2, to account for the wide ranges in the magnitude of the reaction rates for the more diffusive species.

To summarize, Approach 1 and 3 store species mass fraction whereas Approach 2 stores the species reaction rate. Depending on the type of look-up table, i.e., whether the look-up table stores the reaction rates or the mass fractions, the mean value of each quantity is calculated using the following relations

$$\widetilde{Y}_i = \int_o^1 \int_o^1 Y_i^{\text{FPI}} P(c^*) P(f^*) dc^* df^* \tag{3.70}$$

$$\widetilde{\dot{\omega}}_i = \int_o^1 \int_o^1 \dot{\omega}_i^{\text{FPI}} P(c^*) P(f^*) dc^* df^* \tag{3.71}$$

The complete list of data stored in the look-up table have been summarized in Table 3.2.

In all of the above approaches, the conservation equations for mass, momentum, energy, are solved along with transport equations for the mixture fraction and progress of reaction variable. Table 3.1 summarizes these approaches. Note that for FPI tabulation, a formulation similar to the SLFM-Approach 2, in which the temperature is directly obtained from the tables and the energy equation is not solved, was not considered here.

3.9 Observations

In this thesis, the FPI, and for that matter, the SLFM tabulation methods are both coupled to a density-based solution algorithm of the compressible form of the Navier-Stokes equations for a reactive mixture. However, as all of the laminar flames considered
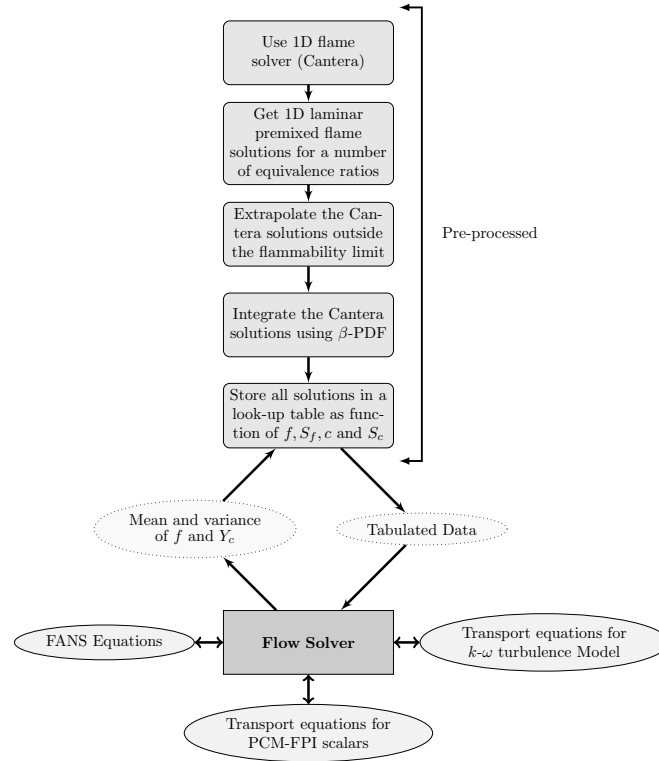
Figure 3.9: A flow chart showing the solution procedure for using the PCM-FPI methodology for turbulent diffusion flames.

in the present study are both steady and essentially isobaric, and radiation losses are not significant, the coupling of the tabulation methods with the solution algorithm is rather straightforward, as discussed in the previous sections of this chapter. The tabulations were performed for a single pressure (atmospheric pressure) and any small variations in pressure from the reference condition were ignored when using and accessing the tables. Nevertheless, for more general combustion processes involving non-adiabatic flames with acoustical phenomena and/or significant pressure variations, coupling of the tabulation methods to a compressible-flow solution method would be more involved and a multi-pressure tabulation procedure may be required. It should be stated however, issues of coupling of the FPI and SLFM methods to a solution algorithm for the governing flow equations are not the primary focus here. Galpin et al. [175] and the recent paper by Vicquelin et al. [81] discuss coupling of tabulated chemistry methods with various solution methods for the flow equations.

To conclude, the PCM-FPI methodology adopted herein is summarized in the flow chart of Figure 3.9.

4 Parallel Adaptive Mesh Refinement Finite-Volume Scheme

4.1 Chapter Overview

The governing Favre-averaged partial differential equations described in Section 2.3.2 and Section 3.6.2 fully describe the mean physical and chemical processes involved in a turbulent flame. In the present work, a parallel AMR finite-volume scheme is used to solve these partial differential equations. This chapter first gives a detailed discussion of the various components of the finite-volume formulation, i.e., the treatment of inviscid and viscous fluxes, the source terms, and the time marching scheme employed to integrate the coupled system of non-linear ordinary differential equation in time. This is followed by some additional discussion of the incorporation of finite-volume scheme within the proposed parallel-AMR framework. Please note that this chapter mostly focuses on the specific aspects of the finite-volume formulation and parallel-AMR scheme that have been used and developed as part of this thesis. For a more detailed discussion of the overall numerical solution scheme proposed here for solution of governing equations, please refer to the previous work by Sachdev et al. [40, 176] and Gao et al. [41, 57, 84, 85], which focused on the development of these aspects of the present numerical solution scheme.

4.2 Conservative Form of Equations

The final form of equations discussed in Section 2.3.2 and Section 3.6.2 can be re-expressed in conservation form using the matrix-vector notation in the following form:

$$\frac{\partial \mathbf{U}}{\partial t} + \vec{\nabla} \cdot \vec{\mathbf{F}} = \mathbf{S} \tag{4.1}$$

(a) Two-dimensional axisymmetric co-ordinate system (r, z, θ)

(b) Three-dimensional Cartesian coordinate system (x,y,z)
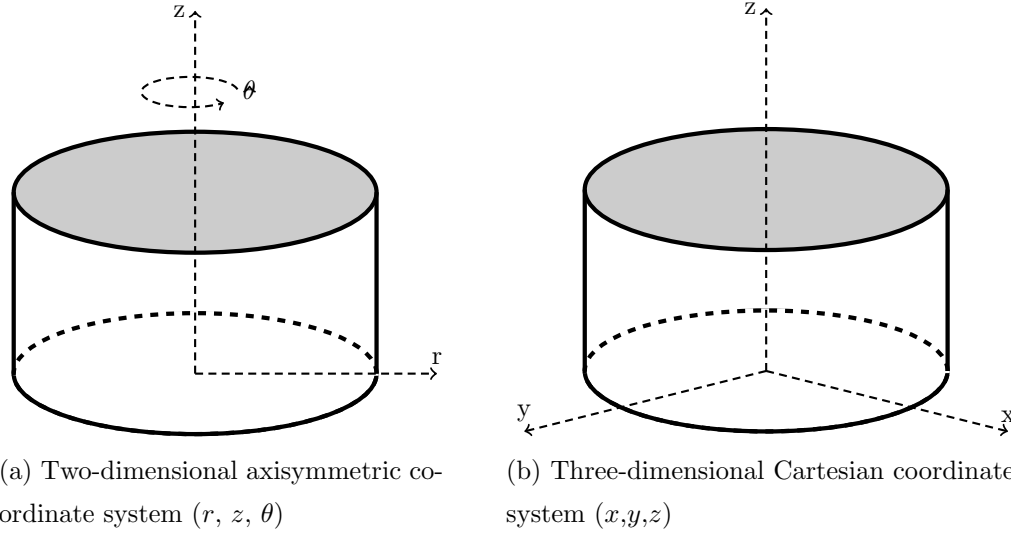
Figure 4.1: The two-dimensional and three-dimensional coordinate systems used in the present work. In an axisymmetric flow, there is no variation in the azimuthal (θ) direction. This symmetrical geometry can be exploited to reduce the complexity of the problem from three space dimensions to two.

where $\mathbf{U}$ is the vector of conserved variables, $\vec{\mathbf{F}}$ is the flux dyad, and $\mathbf{S}$ is the source term vector. The flux dyad, $\vec{\mathbf{F}}$, can be further decomposed into an inviscid and a viscous component and can be expressed as

$$\vec{\mathbf{F}} = \begin{cases} (\mathbf{F}_I - \mathbf{F}_V, \mathbf{G}_I - \mathbf{G}_V) & \text{for two-dimensional axisymmetric flow geometries}, \\ (\mathbf{F}_I - \mathbf{F}_V, \mathbf{G}_I - \mathbf{G}_V, \mathbf{H}_I - \mathbf{H}_V) & \text{for three-dimensional flow geometries}, \end{cases}$$

where $\mathbf{F}_I$ and $\mathbf{F}_V$ are the inviscid and viscous flux vectors in the radial direction for axisymmetric flows and in the x direction for three-dimensional flows, respectively, $\mathbf{G}_I$ and $\mathbf{G}_V$ are the inviscid and viscous flux vectors in the axial direction for the axisymmetric system and in the y direction for the three-dimensional case, respectively, and $\mathbf{H}_I$ and $\mathbf{H}_V$ are the inviscid and viscous flux vectors in the z direction for three-dimensional flows. The source term, $\mathbf{S}$, can be further decomposed as

$$\mathbf{S} = \begin{cases} -\frac{1}{r}(\mathbf{S}_{aI} - \mathbf{S}_{aV}) + \mathbf{S}_t + \mathbf{S}_p + \mathbf{S}_c & \text{for two-dimensional axisymmetric flow geometries}, \\ \mathbf{S}_t + \mathbf{S}_p + \mathbf{S}_c & \text{for three-dimensional flow geometries}. \end{cases}$$

where $\mathbf{S}_{aI}$ and $\mathbf{S}_{aV}$ are the source terms associated with the axisymmetric coordinate for inviscid and viscous fluxes, respectively, and $\mathbf{S}_t$, $\mathbf{S}_p$ and $\mathbf{S}_c$ are the source terms associated

with the turbulence modelling, transport equations for PCM-FPI scalars and finite-rate chemical kinetics respectively.

Using the preceding expressions, Equations (2.34)-(2.39) can be re-expressed for the two-dimensional axisymmetric flow geometries as

$$\frac{\partial \mathbf{U}}{\partial t} + \frac{\partial}{\partial r}(\mathbf{F}_\mathrm{I} - \mathbf{F}_\mathrm{V}) + \frac{\partial}{\partial z}(\mathbf{G}_\mathrm{I} - \mathbf{G}_\mathrm{V}) = -\frac{1}{r}(\mathbf{S}_\mathrm{aI} - \mathbf{S}_\mathrm{aV}) + \mathbf{S}_\mathrm{t} + \mathbf{S}_\mathrm{p} + \mathbf{S}_\mathrm{c} \qquad (4.2)$$

and the three-dimensional flow geometries as

$$\frac{\partial \mathbf{U}}{\partial t} + \frac{\partial}{\partial x}(\mathbf{F}_\mathrm{I} - \mathbf{F}_\mathrm{V}) + \frac{\partial}{\partial y}(\mathbf{G}_\mathrm{I} - \mathbf{G}_\mathrm{V}) + \frac{\partial}{\partial z}(\mathbf{H}_\mathrm{I} - \mathbf{H}_\mathrm{V}) = \mathbf{S}_\mathrm{t} + \mathbf{S}_\mathrm{p} + \mathbf{S}_\mathrm{c} \qquad (4.3)$$

where r and z denote the radial and the axial coordinates in the axisymmetric system and x, y, and z are the coordinates of the three-dimensional Cartesian frame, as shown in Figure 4.1.

The elements of the conserved solution vector, flux vectors, and source vectors are provided below for the three-dimensional coordinate system. Details of these terms for the two-dimensional axisymmetric coordinate system are not repeated here and are given in Section A.1 of Appendix A.

The vector of conserved solution variables, $\mathbf{U}$, is given by

$$\mathbf{U} = \left[\ \overline{\rho}, \ \overline{\rho}\widetilde{v}_x, \ \overline{\rho}\widetilde{v}_y, \ \overline{\rho}\widetilde{v}_z, \ \overline{\rho}\widetilde{e}, \ \overline{\rho}k, \ \overline{\rho}\omega, \ \overline{\rho}\widetilde{f}, \ \overline{\rho}f_v, \ \overline{\rho}\widetilde{Y}_c, \ \overline{\rho}Y_{cv}, \ \overline{\rho}\widetilde{Y}_1, \ \ldots, \overline{\rho}\widetilde{Y}_n \ \right]^\mathrm{T} \qquad (4.4)$$

The inviscid and viscous x-direction flux vectors, $\mathbf{F}_\mathrm{I}$ and $\mathbf{F}_\mathrm{V}$, are given by

$$\mathbf{F}_\mathrm{I} = \begin{bmatrix} \overline{\rho}\widetilde{v}_x \\ \overline{\rho}\widetilde{v}_x^2 + \overline{p} \\ \overline{\rho}\widetilde{v}_x\widetilde{v}_y \\ \overline{\rho}\widetilde{v}_x\widetilde{v}_z \\ (\overline{\rho}\widetilde{e} + \overline{p})\widetilde{v}_x \\ \overline{\rho}\widetilde{v}_x k \\ \overline{\rho}\widetilde{v}_x \omega \\ \overline{\rho}\widetilde{v}_x \widetilde{f} \\ \overline{\rho}\widetilde{v}_x f_v \\ \overline{\rho}\widetilde{v}_x \widetilde{Y}_c \\ \overline{\rho}\widetilde{v}_x Y_{cv} \\ \overline{\rho}\widetilde{v}_x \widetilde{Y}_1 \\ \vdots \\ \overline{\rho}\widetilde{v}_x \widetilde{Y}_n \end{bmatrix}, \qquad \mathbf{F}_\mathrm{V} = \begin{bmatrix} 0 \\ \overline{\tau}_{xx} + \lambda_{xx} \\ \overline{\tau}_{xy} + \lambda_{xy} \\ \overline{\tau}_{xz} + \lambda_{xz} \\ \mathcal{W} - q_x - q_{tx} + (\mu + \mu_t\sigma^*)\frac{\partial k}{\partial x} \\ (\mu + \mu_t\sigma^*)\frac{\partial k}{\partial x} \\ (\mu + \mu_t\sigma)\frac{\partial \omega}{\partial x} \\ \overline{\rho}(\mathcal{D}_f + \mathcal{D}_t)\frac{\partial \widetilde{f}}{\partial x} \\ \overline{\rho}(\mathcal{D}_f + \mathcal{D}_t)\frac{\partial f_v}{\partial x} \\ \overline{\rho}(\mathcal{D}_{Y_c} + \mathcal{D}_t)\frac{\partial \widetilde{Y}_c}{\partial x} \\ \overline{\rho}(\mathcal{D}_{Y_c} + \mathcal{D}_t)\frac{\partial Y_{cv}}{\partial x} \\ -\mathcal{J}_x^1 - \mathcal{J}_{tx}^1 \\ \vdots \\ -\mathcal{J}_x^n - \mathcal{J}_{tx}^n \end{bmatrix} \qquad (4.5)$$

where $\mathcal{W} = \widetilde{v}_x(\overline{\tau}_{xx} + \lambda_{xx}) + \widetilde{v}_y(\overline{\tau}_{xy} + \lambda_{xy}) + \widetilde{v}_z(\overline{\tau}_{xz} + \lambda_{xz})$. The y- and z-direction flux vectors $\mathbf{G}_I$, $\mathbf{G}_V$, $\mathbf{H}_I$, and $\mathbf{H}_V$ have similar forms and are given in Section A.2.

The source vectors, $\mathbf{S}_t$, $\mathbf{S}_c$, and $\mathbf{S}_p$ in Equation (4.3) contain terms related to the turbulence modelling, finite rate chemistry and terms related to the the transport equations for PCM-FPI scalars, respectively, and have the form

$$
\mathbf{S}_t = \begin{bmatrix} 0 \\ 0 \\ 0 \\ 0 \\ 0 \\ \mathcal{P} - \beta^*\overline{\rho}k\omega \\ \alpha\frac{\omega}{k}\mathcal{P} - \beta\overline{\rho}\omega^2 \\ 0 \\ 0 \\ 0 \\ 0 \\ 0 \\ \vdots \\ 0 \end{bmatrix}, \ \mathbf{S}_c = \begin{bmatrix} 0 \\ 0 \\ 0 \\ 0 \\ 0 \\ 0 \\ 0 \\ 0 \\ 0 \\ 0 \\ 0 \\ \overline{\rho}\overline{\dot{\omega}}_1 \\ \vdots \\ \overline{\rho}\overline{\dot{\omega}}_n \end{bmatrix}, \ \mathbf{S}_p = \begin{bmatrix} 0 \\ 0 \\ 0 \\ 0 \\ 0 \\ 0 \\ 0 \\ 2\overline{\rho}\mathcal{D}_t\frac{\partial\widetilde{f}}{\partial x_i}\frac{\partial\widetilde{f}}{\partial x_i} - 2C_f\overline{\rho}\omega f_v \\ \overline{\rho}\widetilde{\dot{\omega}}_{Y_c} \\ 2\overline{\rho}\mathcal{D}_t\frac{\partial\widetilde{Y_c}}{\partial x_i}\frac{\partial\widetilde{Y_c}}{\partial x_i} - 2C_{Y_c}\overline{\rho}\omega Y_{cv} + \\ 2\overline{\rho}\left(\widetilde{Y_c\dot{\omega}_{Y_c}} - \widetilde{Y}_c\widetilde{\dot{\omega}}_{Y_c}\right) \\ 0 \\ \vdots \\ 0 \end{bmatrix} \tag{4.6}
$$

where

$$
\mathcal{P} = \lambda_{xx}\frac{\partial\widetilde{v}_x}{\partial x} + \lambda_{xy}(\frac{\partial\widetilde{v}_x}{\partial y} + \frac{\partial\widetilde{v}_y}{\partial x}) + \lambda_{yy}\frac{\partial\widetilde{v}_y}{\partial y} + \lambda_{xz}(\frac{\partial\widetilde{v}_x}{\partial z} + \frac{\partial\widetilde{v}_z}{\partial x}) + \lambda_{yz}(\frac{\partial\widetilde{v}_y}{\partial z} + \frac{\partial\widetilde{v}_z}{\partial y}) + \lambda_{zz}\frac{\partial\widetilde{v}_z}{\partial z}
$$

4.3   Finite-Volume Methods

Finite-volume methods (FVM) are popular spatial discretization procedures. They have two primary advantages over other discretization methods:

1. FVM ensure that the discretization is conservative; and

2. FVM can be applied to irregular meshes without any coordinate transformation. As a result, they can be applied on unstructured meshes consisting of arbitrary polyhedra in three dimensions or arbitrary polygons in two dimensions.

FVM are applied to the integral form of the conservation equations. Applying the divergence theorem to the differential form of the system of governing equations, Equation (4.1), the following integral form can be obtained

$$\frac{\mathrm{d}}{\mathrm{d}t} \int_{V(t)} \mathbf{U} \mathrm{d}V + \oint_{\Omega(t)} \vec{n} \cdot \vec{\mathbf{F}} \, \mathrm{d}\Omega = \int_{V(t)} \mathbf{S} \mathrm{d}V \,, \tag{4.7}$$

where V is the control volume, Ω is the closed surface of the control volume, and $\vec{n}$ is the unit outward normal vector for the closed surface containing the volume V. The grids used in the present work are time independent and so the control volumes and surfaces are not a function of time. Hence, from hereon the terms $V(t)$ and $\Omega(t)$ in Equation (4.7) will simply be represented as V and Ω, respectively.

Lomax et al. [177] and Hirsch [178, 179] provide detailed discussions regarding conservation equations and their properties. In FVM, the integral form of the governing equations are enforced discretely in each of many small contiguous control volumes which cover the domain of interest. The conservation of any flow property, like mass, momentum and energy, within each finite control volume can be expressed as a balance between the net solution fluxes and sources tending to increase or decrease its value.

Some definitions are useful when solving Equation (4.7) via a finite-volume procedure. The average value of $\mathbf{U}$ and $\mathbf{S}$ inside each control volume of volume V are defined by integrations over the control volume as follows:

$$\overline{\mathbf{U}} \equiv \frac{1}{V} \int_{V} \mathbf{U} \mathrm{d}V \,, \tag{4.8}$$

$$\overline{\mathbf{S}} \equiv \frac{1}{V} \int_{V} \mathbf{S} \mathrm{d}V \,, \tag{4.9}$$

For a control volume that does not vary with time, substituting Equation (4.8)and (4.9) into Equation (4.7), Equation (4.7) can be expressed as

$$\frac{\mathrm{d}}{\mathrm{d}t} \overline{\mathbf{U}} + \frac{1}{V} \oint_{\Omega} \vec{n} \cdot \vec{\mathbf{F}} \, \mathrm{d}\Omega = \overline{\mathbf{S}} \,, \tag{4.10}$$

Now for three space dimensions, assuming that the control volume (i, j, k) is a polyhedron defined by N_f cell faces, as shown in Figure 4.2b, Equation (4.10) can be rewritten in semi-discrete form as a set of coupled ordinary differential equations as

$$\frac{\mathrm{d}}{\mathrm{d}t} \overline{\mathbf{U}}_{i,j,k} = -\frac{1}{V_{i,j,k}} \sum_{m=1}^{N_f} \vec{\mathbf{F}}_{i,j,k,m} \cdot \vec{n}_{i,j,k,m} \, \Delta A_{i,j,k,m} + \overline{\mathbf{S}}_{i,j,k} \tag{4.11}$$

(a) Two-dimensional quadrilateral cell   (b) Three-dimensional hexahedral cell
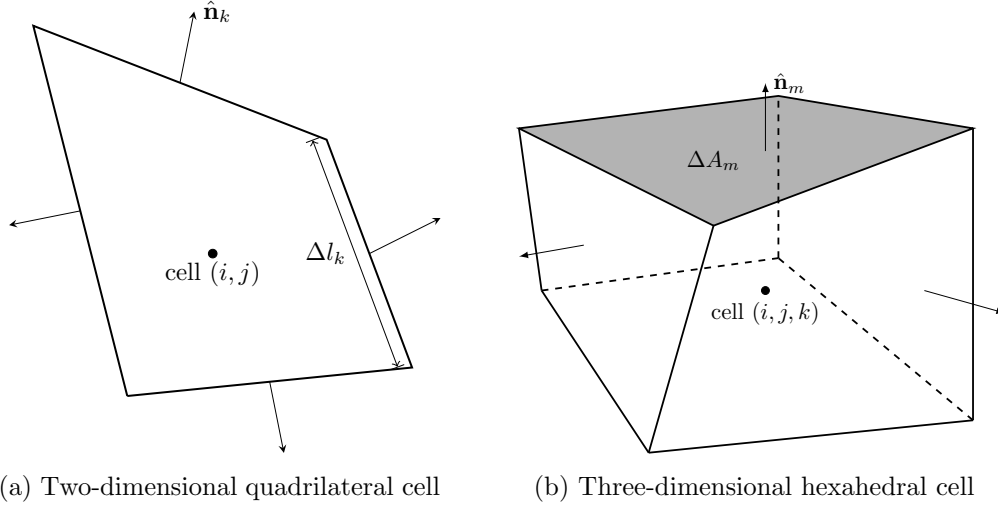
Figure 4.2: Unit Finite-Volume control volumes in two and three dimensions.

or

$$\frac{\mathrm{d}}{\mathrm{d}t}\overline{\mathbf{U}}_{i,j,k} = -\mathbf{R}_{i,j,k}(\overline{\mathbf{U}}),\tag{4.12}$$

where ΔA_m is unit surface area of the mth cell face, and $\mathbf{R}_{i,j,k}(\overline{\mathbf{U}})$ is the so-called residual operator for the control volume (i,j,k). A similar formulation can also be obtained for two-dimensional geometries and quadrilateral computational cells where Equation (4.11) simplifies to

$$\frac{\mathrm{d}}{\mathrm{d}t}\overline{\mathbf{U}}_{i,j} = -\frac{1}{A_{i,j}}\sum_{\mathrm{m}=1}^{N_{\mathrm{f}}}\vec{\mathbf{F}}_{i,j,k}\cdot\vec{n}_{i,j,k}\,\Delta l_{i,j,k} + \overline{\mathbf{S}}_{i,j}\tag{4.13}$$

and where $\Delta l_{i,j,k}$ is the length of the kth face of cell (i,j) and $\vec{n}_k$ is the normal to that face.

The overall solution procedure for solving Equation (4.7) within the proposed FVM can then be summarized in three basic steps:

1. **Reconstruction**: Given the value of $\overline{\mathbf{U}}$ for each control volume at the cell center, construct an approximation to $\mathbf{U}(\vec{x})$ at each point in each control volume. Use this approximation to find $\mathbf{U}$ at the control-volume boundary. The accuracy of the evaluation of cell-averaged solution and its derivatives for the cell-normal flux evaluation is dictated by the accuracy of this solution reconstruction procedure.

2. **Flux evaluation**: Evaluate $\mathbf{F}(\mathbf{U})$ at each cell boundary. Since there is a distinct approximation to $\mathbf{U}$ in each control volume, two distinct values of flux will generally be obtained at any point on the boundary between two control volumes. Apply
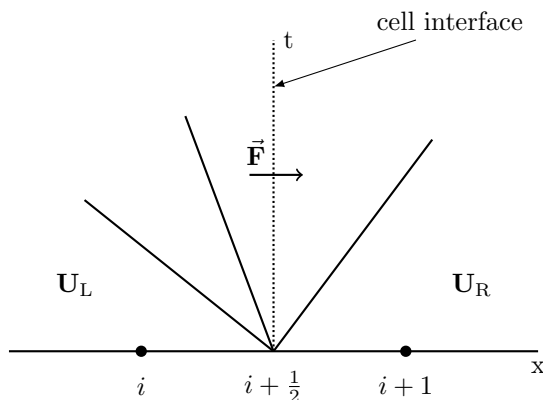
Figure 4.3: The Riemann Problem.

some strategy to resolve the discontinuity in the flux at the control-volume boundary to produce a single value of $\mathbf{F}(\mathbf{U})$ at any point on the boundary and integrate the flux to obtain net flux through the control-volume.

3. **Evolution**: Advance the solution in time to obtain new values of $\overline{\mathbf{U}}$ using an appropriate time marching scheme.

The solution fluxes, $\vec{\mathbf{F}}$, through the cell boundaries, given in Equation (4.11), can be generally categorized as either arising from wave propagation phenomena (hyperbolic fluxes) or from diffusion/viscous processes (elliptic fluxes). The evaluation of these numerical fluxes are described next. It should be noted that for notational simplicity, in the remainder of the thesis, the bar sign "$^-$" is dropped for cell-averaged solution and source vectors.

4.3.1   Inviscid (Hyperbolic) Flux Evaluation

The inviscid fluxes are evaluated on the cell boundaries using the approach used in Godunov-type upwind finite-volume methods [180]: by solving the locally one-dimensional Riemann problems. The Riemann problem, illustrated in Figure 4.3, is a special form of a one-dimensional initial value problem having discontinuous initial states (the situation on the interface between two control volumes) and is posed at the interface between adjacent cells. The solution of this problem provides a means for evaluating the numerical flux function at the cell boundaries. The inviscid flux, $\vec{\mathbf{F}}$, between cell (i, j, k) and cell $(i+1, j, k)$ is then given at the cell interface $(i + \frac{1}{2}, j, k)$ by

$$\vec{\mathbf{F}}_{i+\frac{1}{2},j,k} \cdot \vec{n} = \vec{\mathbf{F}}(\mathcal{R}P(\mathbf{U}_{\mathrm{L}}, \mathbf{U}_{\mathrm{R}})) = \vec{\mathbf{F}}(\mathcal{R}P(\overline{\mathbf{U}}_{i,j,k}, \overline{\mathbf{U}}_{i+1,j,k})), \qquad (4.14)$$

where $\mathbf{U}_\mathrm{L}$ and $\mathbf{U}_\mathrm{R}$ are left and right vectors, respectively, and $\mathcal{RP}$ represents the solution of the Riemann problem.

4.3.1.1   Approximate Riemann Solver: AUSM$^+$-up

Many algorithms have been proposed to solve the Riemann problem. The first method proposed by Godunov [181] preserves the solution monotonicity and is able to capture solution discontinuities, such as shocks, without introducing oscillations in the solutions. Exact Riemann solvers, such as the one proposed by Gottlieb and Groth [180], can be used for solving the Euler equations for an ideal polytropic gas. However, an approximate solution to this problem is often sufficient for use in a finite-volume scheme, since only an interface flux is needed, and the details of the sub-cell solution are averaged out after each time step. The approximate solvers can also be more readily extended for the treatment of more complex systems of partial differential equations, such as the additional transport equations being solved for dealing with turbulent combustion in the present research.

The most detailed upwind approximation scheme associated with the Riemann problem is found in the solvers of Roe [182], which is based on a local linearization of the flow equations, and Osher and Solomon [183], which replaces shock waves by inverted isotropic waves [184]. Since then, a family of more efficient and tractable approximate Riemann solvers have been developed such as the Roe [182], Harten-Lax-van-Leer-Einfeldt (HLLE) [185] and Advection Upstream Splitting Method (AUSM$^+$-up) [186] for dealing with more complicated systems such as those under consideration here. In the present work, the AUSM$^+$-up approximate Riemann solver proposed by Liou [186] was used. The AUSM$^+$-up scheme has been shown to be valid in low speed flows and robust for all Mach number regimes and hence this is a good choice for dealing with both low-Mach number and high-speed flows, encountered in the turbulent reactive flows of interest here. A detailed description of this approximate Riemann problem solver is given in Appendix B.

4.3.1.2   Piecewise Limited Linear Reconstruction

An important concern is the accuracy of the discretization methods. Simply using the left and the right cell-centre solutions to calculate the cell boundary fluxes gives a first-order accurate solution. For higher-order accuracy (i.e., second-order accuracy in smooth regions), a spatial reconstruction of the solution is required in each computational cell.
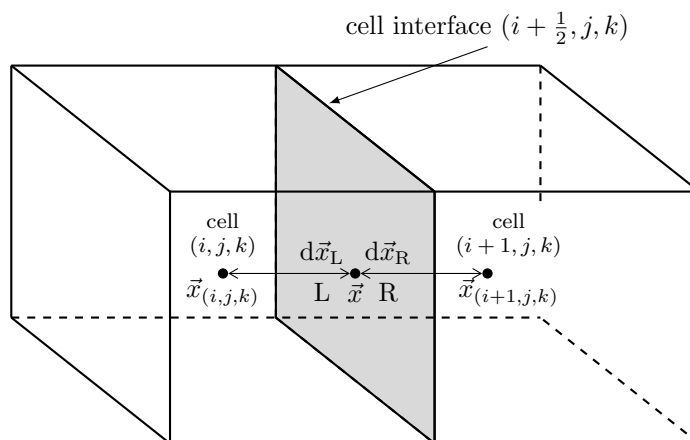
Figure 4.4: Illustrating different quantities used in Equation (4.15).

The emergence of high-resolution Godunov-type methods motivated the design of effective limiters for use in one-dimensional higher-order reconstructions [187]. Algorithms with high resolution in smooth regions and monotone resolution of discontinuities were devised based on the original concepts of nonlinear limiters introduced by Boris and Book [188] and van Leer [189]. These concepts which prevent the occurrence of numerical oscillations, were later generalized via the concept of total variation diminishing (TVD) by Harten [190]. The reader is referred to the paper by van Leer [187] for a systematic review and comparisons of various techniques related to this topic.

Even though the flows considered in this thesis do not have shocks, combusting flows contain regions of very sharp temperature and species gradients. These gradient values are specially large near high temperature regions of the flames. It is therefore desirable to have solution monotonicity in certain regions of the combusting flows and justifies the use of limiters for these cases.

In the present work, a higher-order Godunov-type finite-volume upwind formulation based on approximate Riemann solvers with a least-squares piece-wise limited linear solution reconstruction procedure is used to evaluate the components of the hyperbolic solution flux. Here, the values of the left and right solution states at a cell interface are determined by least-squares piece-wise limited linear solution reconstruction. For example, for cell (i, j, k), at the cell interface $(i + \frac{1}{2}, j, k)$, the flux has the form

$$\vec{\mathbf{F}}_{(i,j,k,m)} \cdot \vec{n}_{(i,j,k,m)} = \vec{\mathbf{F}}\Big(\mathcal{RP}\big(\mathbf{W}_{\mathrm{L}}, \mathbf{W}_{\mathrm{R}}, \vec{n}_{(i,j,k,m)}\big)\Big),$$

where $\vec{n}_{(i,j,k,m)}$ corresponds to the outward unit norm of the cell interface, $\mathcal{RP}$ represents the solution of the Riemann problem, and $\mathbf{W}_{\mathrm{L}}$ and $\mathbf{W}_{\mathrm{R}}$ are the left and right primitive

solution vectors from the piece-wise limited linear reconstruction procedure at the cell interface $(i + \frac{1}{2}, j, k)$, and are given by

$$\mathbf{W}_{\mathrm{L}} = \mathbf{W}_{i,j,k} + \Phi_{i,j,k} \vec{\nabla} \mathbf{W}_{i,j,k} \cdot \mathrm{d}\vec{x}_{\mathrm{L}} \,,$$

$$\mathbf{W}_{\mathrm{R}} = \mathbf{W}_{i+1,j,k} + \Phi_{i+1,j,k} \vec{\nabla} \mathbf{W}_{i+1,j,k} \cdot \mathrm{d}\vec{x}_{\mathrm{R}} \tag{4.15}$$

using the slope limiter, Φ. The quantities $\mathrm{d}\vec{x}_{\mathrm{L}} = \vec{x} - \vec{x}_{i,j,k}$, $\mathrm{d}\vec{x}_{\mathrm{R}} = \vec{x} - \vec{x}_{i+1,j,k}$ and $\vec{x}$ are shown in Figure 4.4. $\mathbf{W}_{i,j,k}$ and $\mathbf{W}_{i+1,j,k}$ are cell-averaged primitive solution vectors in the neighbouring cells.

The slope limiter, Φ, is introduced to limit the solution gradient in order to ensure solution monotonicity. In the present work, the limiter proposed by Venkatakrishnan [191] has been used and it is given by

$$\Phi_{i,j,k} = \begin{cases} \phi\left(\dfrac{\mathbf{W}_{\mathrm{max}} - \mathbf{W}_{i,j,k}}{\mathbf{W}_k - \mathbf{W}_{i,j,k}}\right) & \text{for} & \mathbf{W}_k - \mathbf{W}_{i,j,k} > 0 \\[2ex] \phi\left(\dfrac{\mathbf{W}_{\mathrm{min}} - \mathbf{W}_{i,j,k}}{\mathbf{W}_k - \mathbf{W}_{i,j,k}}\right) & \text{for} & \mathbf{W}_k - \mathbf{W}_{i,j,k} < 0 \\[2ex] 1 & \text{otherwise} \end{cases} \,, \tag{4.16}$$

where $\phi(y)$ is a smooth function given by

$$\phi(y) = \frac{y^2 + 2y}{y^2 + y + 2} \,. \tag{4.17}$$

and $\mathbf{W}_{\mathrm{max}} = \max(\mathbf{W}_{i,j,k}, \mathbf{W}_{\mathrm{neighbours}})$, $\mathbf{W}_{\mathrm{min}} = \min(\mathbf{W}_{i,j,k}, \mathbf{W}_{\mathrm{neighbours}})$, and $\mathbf{W}_k$ is the unlimited reconstructed solution value at the kth flux quadrature point.

4.3.1.3   Gradient Evaluation - Least-Squares Approach

The gradients of the primitive variables, $\vec{\nabla} \mathbf{W}$, are determined by applying a least-squares approach [192], a technique which is suitable for both structured and unstructured mesh and relies on a stencil formed by the nearest and possibly next to nearest neighbouring cells. For the boundary stencil, a layer of ghost cells containing boundary condition information are used to generalize the procedure without reducing the reconstruction stencil. For a cell-centered discretization in three dimensions, the stencil is formed by joining the nearest twenty-six neighbouring cell centroids. The approximate gradients using the least-squares gradient construction procedure are obtained by minimizing the error defined by

$$\sum_{k=1}^{k=N} \epsilon_{ik}^2 = \sum_{k=1}^{k=N} (\Delta \mathbf{W}_{ik} - \vec{\nabla} \mathbf{W}_i \cdot \mathrm{d}\vec{x}_{ik})^2 \,, \tag{4.18}$$

where $\Delta \mathbf{W}_{ik} = \mathbf{W}_i - \mathbf{W}_k$, $\mathrm{d}\vec{x}_{ik} = \vec{x}_i - \vec{x}_k$, and $N = 8$ for two dimensions, or $N = 26$ for three dimensions. The $3{\times}3$ system of linear algebraic equations resulting from the minimization problem can be expressed as

$$
\begin{bmatrix} \overline{(\Delta x)^2} & \overline{\Delta x \Delta y} & \overline{\Delta x \Delta z} \\ \overline{\Delta x \Delta y} & \overline{(\Delta y)^2} & \overline{\Delta y \Delta z} \\ \overline{\Delta x \Delta z} & \overline{\Delta y \Delta z} & \overline{(\Delta z)^2} \end{bmatrix} \begin{bmatrix} \frac{\partial \mathbf{W}}{\partial x} \\ \frac{\partial \mathbf{W}}{\partial y} \\ \frac{\partial \mathbf{W}}{\partial z} \end{bmatrix} = \begin{bmatrix} \overline{\mathbf{W}\Delta x} \\ \overline{\mathbf{W}\Delta y} \\ \overline{\mathbf{W}\Delta z} \end{bmatrix} ,
\tag{4.19}
$$

where

$$
\overline{\Delta x^2} = \frac{1}{N} \sum_{k=1}^{N} \Delta x_{ki}^2,
\tag{4.20}
$$

$$
\overline{\Delta x \Delta y} = \frac{1}{N} \sum_{k=1}^{N} \Delta x_{ki} \Delta y_{ki},
\tag{4.21}
$$

and

$$
\overline{\Delta \mathbf{W} \Delta x} = \frac{1}{N} \sum_{k=1}^{N} \Delta \mathbf{W}_{ki} \Delta x_{ki} .
\tag{4.22}
$$

The other terms have a similar form. The above terms only depend on grid geometry and so can be precomputed and stored. Solutions of the $3{\times}3$ linear system represented by Equation (4.19) can be readily obtained using Cramer's rule.

4.3.2 Viscous Flux Calculation

The evaluation of viscous component of the numerical flux depends on both the solution state and its gradients at the cell interfaces, i.e

$$
\mathbf{F}_\mathrm{V} = \mathbf{F}_\mathrm{V}(\mathbf{W}_{i+\frac{1}{2},j,k}, \vec{\nabla}\mathbf{W}_{i+\frac{1}{2},j,k})
\tag{4.23}
$$

where $\mathbf{W}_{i+\frac{1}{2},j,k}$ is the primitive solution vector at the cell interface which is evaluated by averaging the left and the right reconstructed solution states,

$$
\mathbf{W}_{i+\frac{1}{2},j,k} = \frac{(\mathbf{W}_\mathrm{L} + \mathbf{W}_\mathrm{R})}{2} .
\tag{4.24}
$$

To evaluate the gradients for the primitive variables at the cell interfaces, $\vec{\nabla}\mathbf{W}_{(i+\frac{1}{2},j,k)}$, divergence theorem is applied to a polygon, formed by joining the centroids of cells, vertices of cells, or both, in a path surrounding the face. The present work adopts

(a) Face gradient reconstruction in two-dimensions

(b) Face gradient reconstruction in three-dimensions
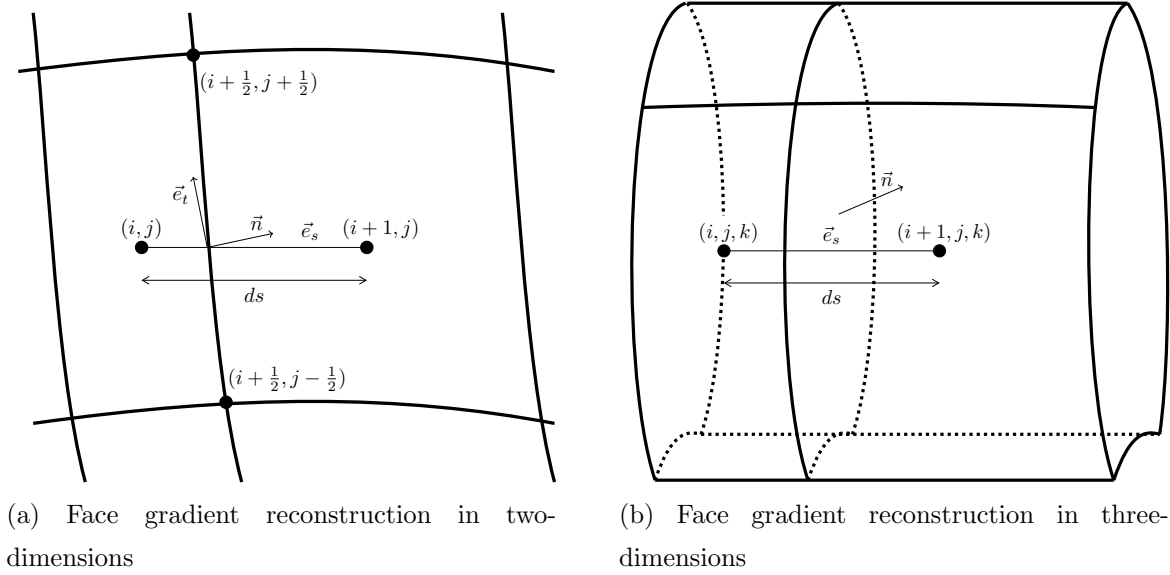
Figure 4.5: Face gradient reconstruction for viscous flux evaluation.

the procedure of Green-Gauss integration over the diamond path using the linearity-preserving weighting function derived by Holmes and Connell to evaluate the gradients on each cell interface in two space dimensions as

$$\vec{\nabla}\mathbf{W}_{i+\frac{1}{2},j} = \frac{\vec{n}}{\vec{n}\cdot\vec{e_s}}\left(\frac{\mathbf{W}_{i+1,j}-\mathbf{W}_{i,j}}{ds} + \frac{\mathbf{W}_{i+\frac{1}{2},j+\frac{1}{2}}-\mathbf{W}_{i+\frac{1}{2},j-\frac{1}{2}}}{dl}\vec{e_t}\cdot\vec{e_s}\right) \tag{4.25}$$

In Equation (4.25), ds is the distance between two centroids, dl is the face length, and unit vectors, $\vec{e_t}$, $\vec{n}$, and $\vec{e_s}$ are the tangential vector, face norm, and the distance vector from the cell centroid to its neighbour's as shown in Figure 4.5a.

For three space dimensions, as shown in Figure 4.5b, the edges of the diamond path are replaced by surfaces. In this thesis, the cell-face gradients are evaluated using the formula proposed by Mathur and Murthy [193]

$$\vec{\nabla}\mathbf{W}\bigg|_{i+\frac{1}{2},j,k} = \frac{\mathbf{W}_{i+1,j,k}-\mathbf{W}_{i,j,k}}{ds}\frac{\vec{n}}{\vec{n}\cdot\vec{e_s}} + \left(\overline{\vec{\nabla}\mathbf{W}} - \overline{\vec{\nabla}\mathbf{W}}\cdot\vec{e_s}\frac{\vec{n}}{\vec{n}\cdot\vec{e_s}}\right), \tag{4.26}$$

where $\overline{\vec{\nabla}\mathbf{W}}$ is the weighted average of the cell centred gradient at the cell interface given by

$$\overline{\vec{\nabla}\mathbf{W}}\bigg|_{i+\frac{1}{2},j,k} = \alpha\vec{\nabla}\mathbf{W}_{i,j,k} + (1-\alpha)\vec{\nabla}\mathbf{W}_{i+1,j,k}. \tag{4.27}$$

The weighting factor, α, is based on cell volume ratios and is given by

$$\alpha = \frac{V_{i,j,k}}{(V_{i,j,k}+V_{i+1,j,k})} \tag{4.28}$$

M	First Order					Second Order				
	2	3	4	5	6	2	3	4	5	6
α_1	0.3333	0.1481	0.0833	0.0533	0.0370	0.4242	0.1918	0.1084	0.0685	0.0482
α_2	1	0.4000	0.2609	0.1263	0.0851	1	0.4929	0.2602	0.1602	0.1085
α_3		1	0.4265	0.2375	0.1521		1	0.5052	0.2898	0.1885
α_4		1	1	0.4414	0.2562			1	0.5060	0.3050
α_5				1	0.4512				1	0.5063
α_6					1					1

Table 4.1: Multi-stage coefficients for optimal first and second order schemes.

4.4 Explicit Temporal Discretization Scheme

The semi-discrete form of the governing equations is given in a compact form by Equation (4.12) above. For steady-state time-invariant reactive flows of interest here, the time coordinate represents the solution evolution coordinate. Here, the system of equations is marched until the transient part of the solution is removed, such that

$$\mathbf{R}(\mathbf{U}) = 0 \tag{4.29}$$

Lomax et al. [177] contains elaborate discussions and analysis of different time-marching schemes. For the present steady-state calculations, the explicit optimally-smoothing multi-stage scheme developed by van Leer et al. [194] has been adopted. This scheme was designed to provide optimal damping of the high frequency content of the solution when using an upwind scheme for the one-dimensional linear convection equation. The M stage time-marching scheme is given by

$$\mathbf{U}_0 = \mathbf{U}_n \tag{4.30}$$

$$\mathbf{U}_k = \mathbf{U}_0 + \alpha_m \Delta t \mathbf{R}(U_{k-1}), \text{for k} = 1,\dots,\text{M} \tag{4.31}$$

$$\mathbf{U}_{n+1} = \mathbf{U}_M, \tag{4.32}$$

where $\mathbf{U}_n$ and $\mathbf{U}_{n+1}$ are the solution state vectors at time step n and $n+1$ respectively. The coefficients for schemes with 2-6 stages are given in Table 4.1. Multi-dimensional optimally-smoothing schemes for Euler and Navier-Stokes equations have been investigated by van Leer and his co-workers [195, 196], but these time-marching schemes have not been implemented in the present work.

4.5   Block-Based Adaptive Mesh Refinement (AMR)

Following the approach developed by Groth et al. [39, 197], a flexible block-based hier-archical data structure is used in conjunction with the finite-volume scheme described in previous sections to felicitate automatic solution-directed mesh adaptation on multi-block hexahedral/quadrilateral mesh according to physics-based refinement criteria. The AMR schemes are very effective in treating problems with disparate length scales. They permit local mesh refinement and thereby minimize the number of computational cells required for a particular calculation. The AMR formulation used in the present work, borrows from previous work by Berger and co-workers [21, 22, 28, 32, 198, 199] , Quirk [24], Quirk and Hanebutte [27], and De Zeeuw and Powell [26], De Zeeuw [200] for Carte-sian mesh and has similarities with the block-based approaches described by Quirk and Hanebutte [27] and Berger and Saltzman [28]. Some other researchers have considered the extension of Cartesian mesh adaptation procedures to more arbitrary quadrilateral and hexagonal mesh [201, 202].

The block-based AMR algorithm and parallel implementation being used in the present work has been described in detail in a recent works by Sachdev et al. [40, 176] and Gao et al. [41, 57, 84, 85]. However, for the sake of completeness, the main aspects of the block-based AMR algorithm are outlined in the remainder of this chapter.

4.5.1   Refinement and Coarsening of Solution Blocks

The finite-volume scheme described before in Section 4.3 is applied to multi-block body-fitted mesh where the grid is composed of a number of structured blocks. Each of these blocks consists of $N_i \times N_j$ quadrilateral cells in two-dimensional grids or $N_i \times N_j \times N_k$ hexahedral cells in three-dimensional grids, where N_i, N_j and N_k are even integers greater than or equal to four. Mesh adaptation is accomplished by refining or coarsening of particular grid blocks. Regions where more resolution is required, a "parent" block is refined by dividing it into four or eight "children" blocks, depending on the grid-dimensionality. Each of the children block are self-similar to the parent blocks, i.e., they have the same number of cells as the parent and thereby double the resolution in the region of interest. Figure 4.6 illustrates AMR refinement in two and three dimensions. Figure 4.6b shows two neighbouring $8 \times 8 \times 8$ hexahedral blocks of a three-dimensional mesh, one of which has undergone one level of refinement and other

(a)   Two-dimensional
grid

(b) Three-dimensional grid
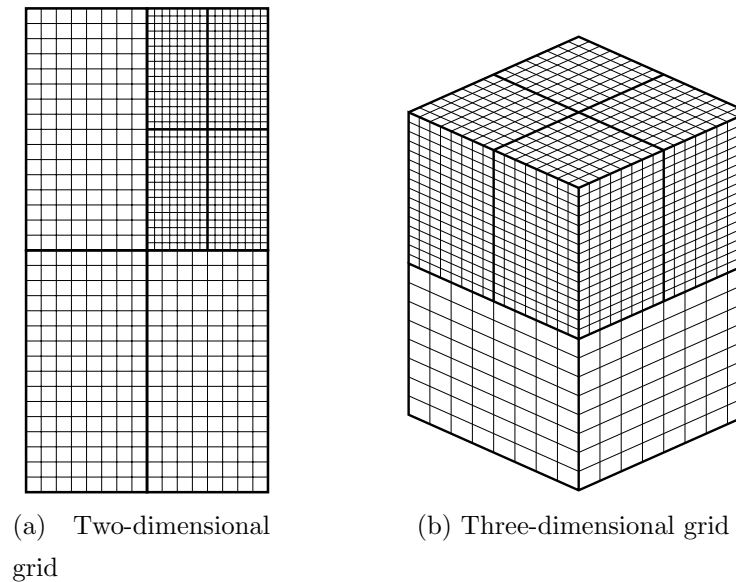
Figure 4.6: One level of Mesh Refinement in two and three dimensional grid.

has not. The grid adaptation is constrained such that the grid resolution does not change by more than a factor of two between two adjacent blocks and the minimum resolution is not less than that of the initial mesh.

For grid refinement, a second-order averaging procedure combines the Taylor series expansion of the grid metrics at each node of a given coarse face to approximate locations of new nodes on the fine mesh. The second-order method helps not only to preserve the original stretching of the coarse grid, but also maintains the smoothness of the initial grid. Provided that the boundary can be represented by a continuous surface, this approach helps to avoid the need for projecting the locations of the refined-mesh boundary nodes exactly onto the physical geometry. However, for the simple flow geometries considered herein, algebraic relations are used to ensure that the boundary nodes conform to the physical boundaries.

Coarsening of the computational mesh is accomplished simply by reversing the refinement procedure. This is done by the eliminating the mesh points, and thereby reverting the fine mesh to its original unrefined structure. The coarsened mesh retains only every second node of the fine mesh. Accordingly, four solution blocks are merged into one solution block in two-dimensional grids and eight solution blocks into one for three-dimensional grids.

A measure of the efficiency of the block-based AMR scheme can be obtained by

defining the refinement efficiency, η, as

$$\eta = 1 - \frac{N_{\text{cells}}}{N_{\text{uniform}}} \tag{4.33}$$

where N_{cells} is the total number of cells in the present grid and N_{uniform} is the total number of cells that would have been used on a uniform mesh composed of cells of the finest size on the current mesh. The efficiency of the AMR scheme improves as the number of refinement levels increase.

4.5.2 Refinement Criteria

In the present AMR framework, a heuristic set of refinement criteria based on the physical understanding of the flow properties of interest is used (so called physics-based refinement criteria). For the turbulent reacting flows considered here, the following measures are used:

$$\epsilon_1 \propto \left| \vec{\nabla} \overline{\rho} \right| \qquad \epsilon_2 \propto \left| \vec{\nabla} \cdot \vec{u} \right| \qquad \epsilon_3 \propto \left| \vec{\nabla} \otimes \vec{u} \right| , \tag{4.34}$$

$$\epsilon_4 \propto \left| \vec{\nabla} k \right| \qquad \epsilon_5 \propto \left| \vec{\nabla} \omega \right| \qquad \epsilon_6 \propto \left| \vec{\nabla} T \right| \qquad \epsilon_7 \propto \left| \vec{\nabla} Y_{\text{k}} \right| . \tag{4.35}$$

in the decision to refine or coarsen a solution block. The first three quantities, i.e., the local measures of density gradient, compressibility and the vorticity of the mean flow field enable the detection of contact surfaces, shocks and shear layers and are particularly useful for non-reacting flows. The next two quantities, the gradients of the turbulent kinetic energy and the gradient of the specific dissipation rate of turbulent kinetic energy, respectively, relate to the structure of the turbulent field. The last two quantities measure the gradients of mean temperature and mean concentration for species k, respectively, and provide reliable detection of flame fronts and combustion zones for reactive flows. In addition, for RANS models, the quantity y^+, the dimensionless wall distance from the wall surface, can also be used as a measure to direct the refinement. A smaller y^+ indicates that the location is closer to the wall surface.

Using these measures, the decision for refinement/coarsening of a given solution block is determined according to the following procedure:

1. calculate the refinement measures for each cell and assign the maximum value for all cells as the refinement measure for the solution block;

2. determine the global minimal and maximal values of the refinement criteria of all solution blocks; and
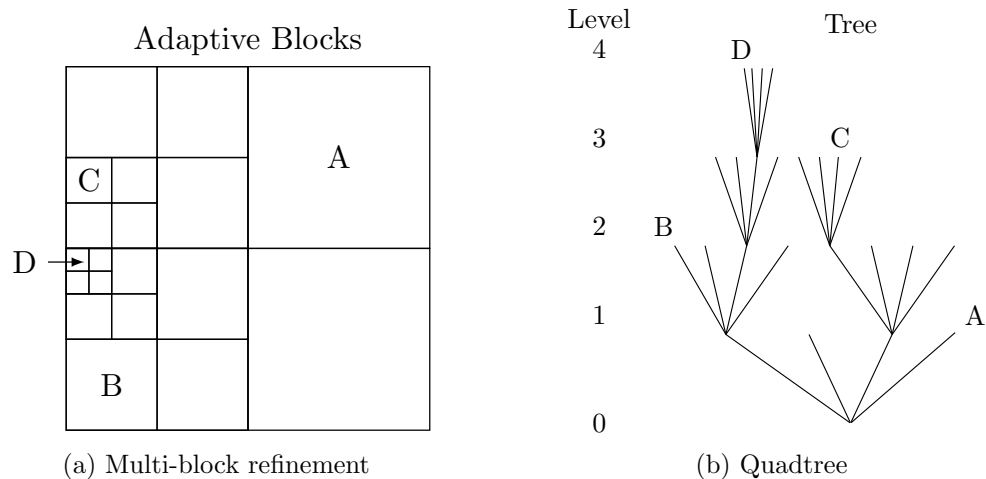
Figure 4.7: Multi-block quadrilateral AMR mesh showing solution blocks at various levels of refinement and the corresponding quadtree data structure.

3. mark solution blocks to be refined/coarsened by comparing the refinement measures to the refinement/coarsening thresholds scaled by the global extrema; i.e., blocks with refinement measures below some specified minimum measure are coarsened and blocks with measures above some upper bound are refined.

4.5.3 Solution Block Connectivity

A flexible block-based hierarchical tree-like data structure is used to maintain the connectivity of the solution blocks in the multi-block mesh. In particular, quadtree and octree data structures are used for tracking the connectivity of blocks in the two- and the three-dimensional grids, respectively. For the two-dimensional grid, Figure 4.7a shows multi-block quadrilateral AMR mesh solution blocks at various levels of refinement. Figure 4.7b illustrates the corresponding quadtree data structure used to keep track of mesh refinement and the connectivity between solution blocks. Figure 4.8 depicts a three-dimensional multi-block hexahedral AMR mesh consisting of solution blocks at various levels of refinement and the corresponding octree data structure.

Each block requires information of its neighbours in order to exchange solution and/or geometry information during the solution procedure. The blocks are matched to one another using block faces defined from coordinate information at the corners of the quadrilateral/hexahedral blocks. Neighbour information across each boundary element of a block is then stored, including the neighbour index, matching faces and orientation.
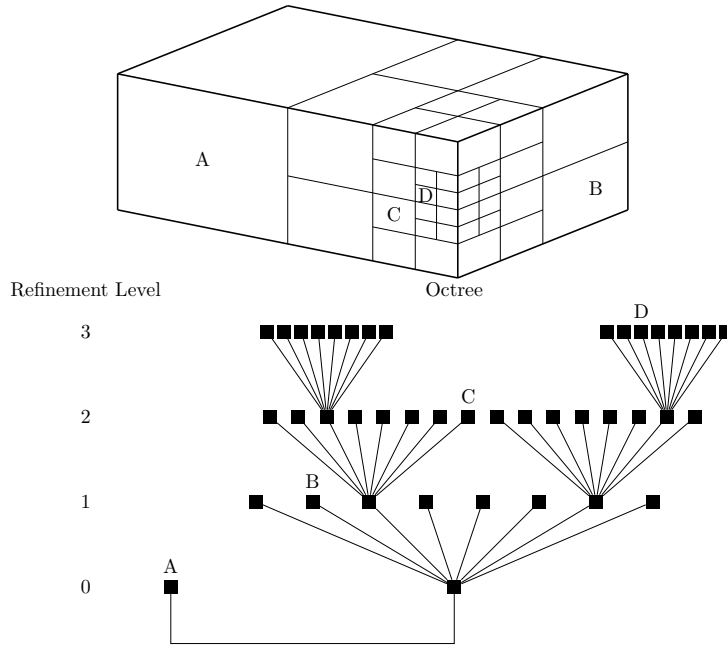
Figure 4.8: Multi-block hexahedral AMR mesh showing solution blocks at various levels of refinement and the corresponding octree data structure [203].

(a) Two space dimensions   (b) Three space dimensions
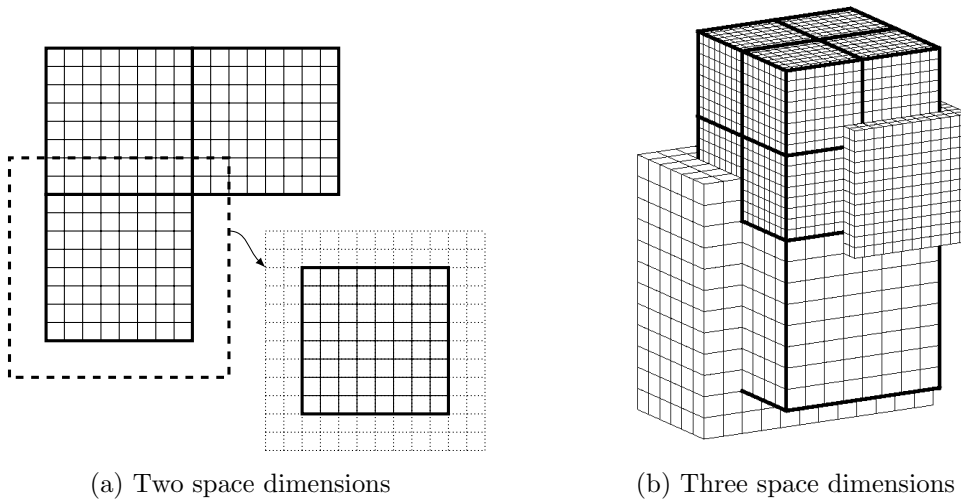
Figure 4.9: The overlapping "ghost" cells contain solution information from neighbouring blocks [203].

There are some particular exceptions to this method when dealing with corners of unstructured root-blocks. Their special treatments is discussed in the thesis by Gao [41].

Knowing their neighbours helps each block to share solution information between adjacent blocks having common interfaces by employing additional layers of overlapping

ghost cells. Figures 4.9a and 4.9b show the ghost cells used for two- and three-dimensional solution blocks, respectively. When the ghost cells are updated, buffers are used to facilitate the exchange of messages between blocks. A one-dimensional buffer with the sending block's information is loaded, but with that information re-ordered according to the neighbouring block's orientation. The unloading of the buffer is therefore straightforward. Also, the interface fluxes computed on more refined blocks are used to correct the interface fluxes computed on coarser neighbouring blocks to ensure that the solution fluxes are conserved across block interfaces.

4.6 Parallel Implementation via Domain Decomposition

Domain decomposition is a technique for solving PDEs by decomposing an original domain into a set of smaller sub-domains [204]. In parallel computing for computational fluid dynamics, domain decomposition involves decomposing a computational mesh and distributing the sub-meshes among the processors in a multi-processor architecture. In this thesis, the multi-block quadrilateral/hexahedral mesh and tree data structure lends itself naturally to domain decomposition and enables efficient and scalable implementations of the solution algorithm for the reactive gaseous mixture conservation equations on distributed-memory multi-processor architectures [40]. The solution blocks can be easily distributed to the processors, with more than one block permitted on each processor as shown in Figure 4.10.

For homogeneous architectures (identical processors), as used herein for all parallel computations, an effective load balancing is achieved by exploiting the self-similar nature of the solution blocks and simply distributing the blocks equally among the processors. Message passing of the ghost-cell values and flux corrections is performed in an asynchronous fashion with gathered wait states and message consolidation [94]. Placing nearest-neighbour blocks on the same processor can also help to reduce the overall communication costs. This is usually realized by utilizing space-filling curves which can provide rather high quality partitions at very low computational costs [205–207] due to their "proximity preserving" mappings of a multi-dimensional space to one-dimensional space. In this work, a Morton ordering space-filling curve is adopted to provide nearest-neighbour ordering of the solution blocks in the multi-block quadrilateral and hexa-
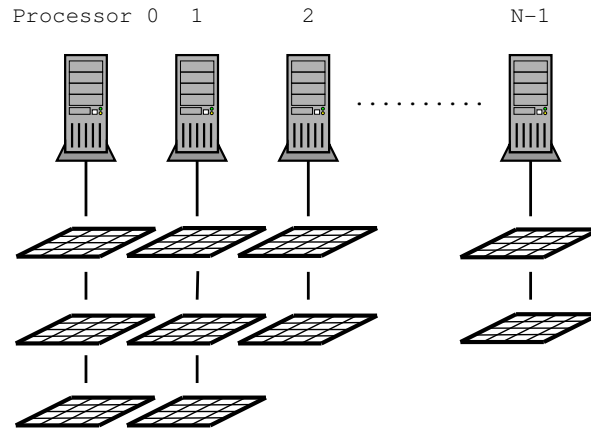
Figure 4.10: Domain decomposition is carried out by farming the solution blocks out to the separate processors, with more than one block permitted on each processor.

hedral AMR meshes, and improve the parallel performance of the proposed solution method [207].

A parallel implementation of the block-based AMR scheme has been developed using the C++ programming language and the message passing interface (MPI) library [203, 208, 209]. Domain decomposition is carried out by farming the solution blocks out to the separate processors, with more than one block permitted on each processor. The domain decomposition procedure used here is an efficient and highly scalable parallel algorithm that has been applied to the prediction of laminar combusting flows [55], turbulent combusting flows [57, 84], turbulent multi-phase rocket motor core flows [210], micro-scale flows [211], and compressible flows with a high-order scheme [212], in two space dimensions and the predictions for turbulent combusting flows in three space dimensions [203].

Validation Results for the Proposed Numerical Scheme

5.1 Chapter Overview

This chapter presents numerical results obtained for different reactive and non-reactive flow configurations using the proposed numerical scheme for modelling turbulent diffusion flames, both for two and three dimensional flow geometries. All of the flow-geometries studied in this thesis are relatively simple. However, each case was chosen to study and validate the performance of a certain aspect of the proposed combustion model and numerical solution scheme. Numerical results for three different laminar flame configurations are considered first. An examination of the performance of the proposed solution method for laminar flames was important in order to establish that the proposed FPI formulation and its extension to the diffusion flame regimes were performing as expected. The numerical results obtained using the proposed FPI scheme for laminar diffusion flames are compared to the numerical predictions of the SLFM approach and available experimental data. The discussion of the laminar flame results is followed by the study of two non-reacting turbulent flow configurations to verify the successful implementation of the k-ω turbulence model, both in two and three dimensional flow geometries. The chapter concludes with the study of a turbulent methane-air diffusion flame, which brings together all key aspects of the proposed numerical scheme - turbulence modelling, the FPI approach for diffusion flames, the PCM-FPI approach for modelling turbulence-chemistry interaction, the AMR scheme and the parallel implementation. The numerical results for the turbulent flame are compared to the available experimental results. The detailed-chemistry PCM-FPI numerical results are also compared to the one-step reduced mechanism, discussed earlier in Section 2.4.2.2. It should be noted that the results for

Figure 5.1: Grid and boundary conditions used for one-dimensional methane-air premixed flame simulations.

the one-step mechanisms are considered herein merely as a baseline for comparison of computational costs and not for any assessment of the accuracy of the tabulated chemistry approaches. Clearly, a simplified one-step approach will not be as accurate as the methods based on tabulation of detailed chemistry.

The parallel implementation of the proposed parallel AMR scheme was carried out on two parallel clusters: the General Purpose Cluster (GPC) of the SciNet Consortium and the High Performance Aerospace Computational Facility (HPACF). The GPC is an IBM iDataPlex cluster based on Intel's Nehalem architecture. It consists of 3780 nodes with a total of 30,240 2.5GHz cores, with 16GB RAM per node (2GB per core). Approximately one quarter of the cluster are interconnected with non-blocking 4x-DDR InfiniBand, which have been used for most of the simulations of three-dimensional flow geometries, while the rest of the nodes are connected with gigabit ethernet. The HPACF is a parallel cluster of 4-way Hewlett-Packard ES40, ES45, and Integrity rx4640 servers with a total of 244 Alpha and Itanium 2 processors. It uses a low-latency Myrinet network and switch are used to interconnect the servers in the cluster. HPACF was mostly used for smaller problems like the two-dimensional laminar flames.

5.2 Laminar Flames

5.2.1 One-Dimensional Laminar Premixed Flame

The performance and predictive capabilities of the FPI approaches were first investigated for stationary one-dimensional laminar premixed methane-air flames with equivalence ratios ranging from ϕ=0.4 to ϕ=2.0. Since the FPI-tabulated-chemistry approach is based on the tabulation of one-dimensional laminar premixed flame solutions, it is of interest to see how well the FPI approach can reproduce the detailed-chemistry Cantera solutions of one-dimensional laminar premixed flames. Similar analysis has also been done in previous works by Domingo et al. [156] and Galpin et al. [150].

A two-dimensional rectangular grid with dimensions $50\,\text{mm}$ by $0.65\,\text{mm}$ was used for the numerical simulation of this flame. A highly stretched mesh with 160 cells in the direction normal to the flame front and 2 cells in the direction normal to the flame velocity was used. The finest cell size near the flame front was of the order of $0.01\,\text{mm}$ and the coarse cell size near the boundary was of the order of $1.2\,\text{mm}$. The grid used for this flame has been shown in Figure 5.1. Neumann-type boundary conditions were used for all quantities on the north and south face of the grid. The boundary condition on the west end is a inflow condition i.e, the pressure and density are held constant, and the inlet velocity is calculated based on balancing mass flux, i.e.

$$v_{in} = \frac{\rho_{out} v_{out}}{\rho_{in}} \tag{5.1}$$

where v_{in} and ρ_{in} are the velocity and density values at the inlet and v_{out} and ρ_{out} are the velocity and density values at the outlet. The east boundary it is set to an outflow boundary condition i.e., Neumann-type boundary condition for all quantities but pressure, which is fixed.

When not using the FPI approach, the solution domain was initialized by setting the composition of the left half to an unburnt mixture based on the equivalence ratio and the right half was set to a burnt equilibrium composition for the same mixture. When initializing for FPI, the progress variable, c, is calculated along the domain using an error function

$$c = \frac{1}{2}\left(1 + \text{erf}\left(\frac{\sqrt{\pi}x}{\delta}\right)\right) \tag{5.2}$$

where δ is the unstrained laminar flame thickness, $0.446 \times 10^{-3}\,\text{m}$. The corresponding values for $f(\phi)$ and c are read from the look-up table to initialize the domain.

The Cantera package was used to obtain solutions for one-dimensional laminar premixed flames needed for generating the FPI look-up table. Sixty-four solutions corresponding to different equivalence ratios in the flammability limit ranging from $\phi{=}0.4$ to $\phi{=}2.0$ were used. For each value of ϕ, the premixed flame solution contained 155 points in c-space. These points were non-uniformly distributed such that there were more points in regions of high gradients. No PDF integration was performed for this flame because the only possible value for both S_c and S_f is zero for a laminar flame. The final dimensions of the look-up table were $(64{\times}1{\times}155{\times}1)$.

Figures 5.2a and 5.2b compare the results obtained using the three FPI approaches to directly-calculated results obtained using both the one-step mechanism and the full

(a) Predicted flame-speed versus equivalence ratio.

(b) Predicted burnt gas temperature versus equivalence ratio.
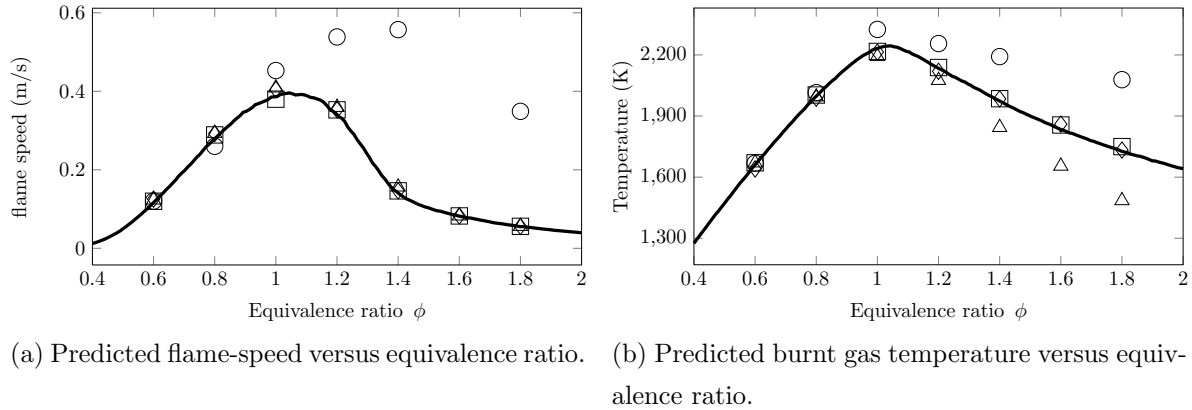
Figure 5.2: Predicted solutions of one-dimensional laminar methane-air premixed flames. Line: Detailed Chemistry, square: FPI-Approach 1, triangle: FPI-Approach 2, diamond: FPI-Approach 3, circle: one-step mechanism.

GRI-Mech 3.0 mechanism without any tabulation. Both the predicted flame speed and burnt-gas or flame temperature are shown. Figure 5.2a shows extremely good agreement between the laminar flame speeds predicted by all three FPI approaches and the detailed chemistry solution using Cantera over the entire flammability range. Not surprisingly, there is also a significant improvement over the results obtained from the simplified one-step mechanism, which without modification cannot accurately predict the flame speed for the entire flammability range. It should be noted, that all the FPI predictions were made using the reduced set of ten species, as discussed earlier in Section 3.5. These results show that the reduction procedure is a valid simplification for controlling the size of the look-up table, as was shown previously by other authors [156, 175]. However, the comparisons of flame temperature in Figure 5.2b clearly show the differences between the reaction rate tabulation method and mass fraction tabulation methods. The FPI-Approach 2 under-predicts the burnt gas temperature for rich flame conditions.

Figure 5.3 takes a closer look at the species mass fractions predicted by each FPI-Approach. The results of the figure show that the mass fractions of some minor species, like OH and CO, are poorly predicted by FPI-Approach 2. This occurs because the magnitude of the reaction rate gradients for these species are very large near the flame front and the discretization of c-space using 155 points is not sufficient to accurately capture the solution of minor species. A significantly higher number of tabulated points in c-space would be required to remedy this situation. It is for this reason that only FPI-Approaches 1 and 3 have been used in the remainder of the flame validation cases

(a) CO_2 predictions

(b) H_2O predictions

(c) CO predictions
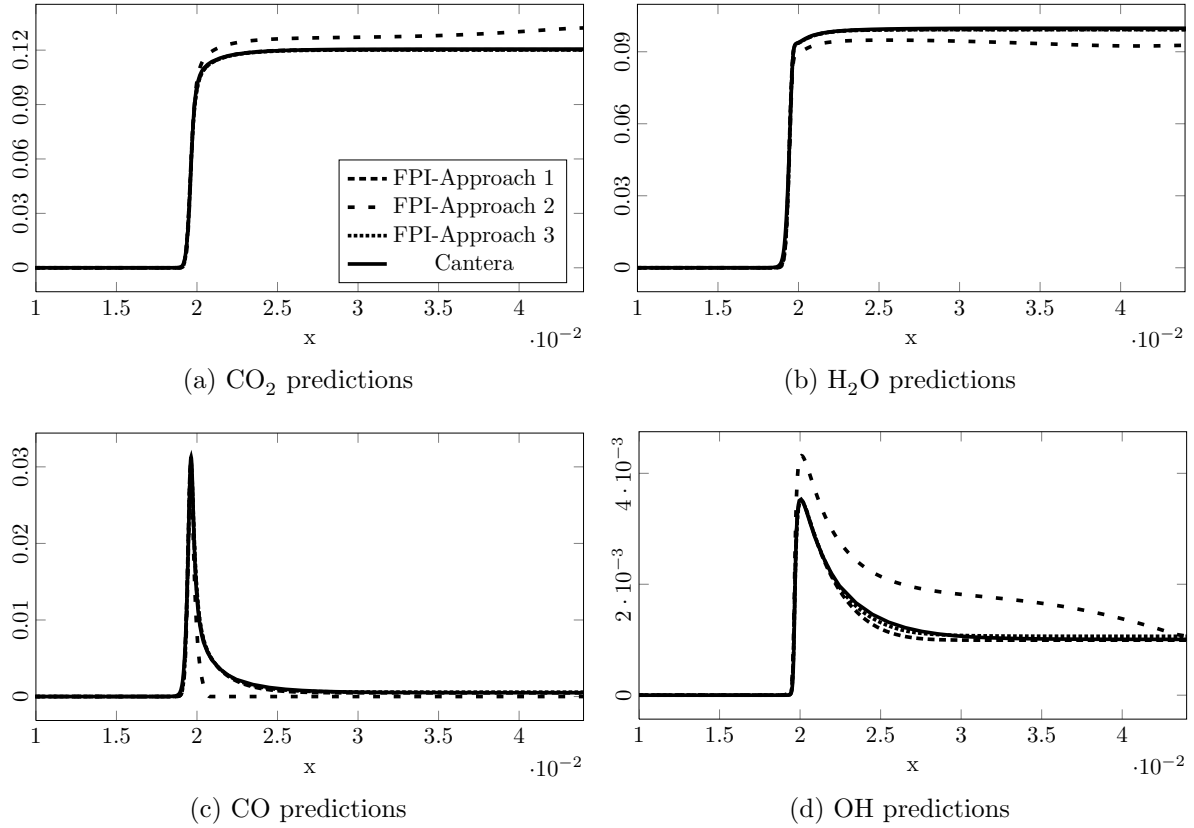
(d) OH predictions

Figure 5.3: Predicted variation of species concentrations through one-dimensional laminar methane-air premixed flame obtained using the three different FPI coupling schemes for $\phi = 0.8$.

(a) Detail chemistry predictions.

(b) FPI-Approach 3 predictions.
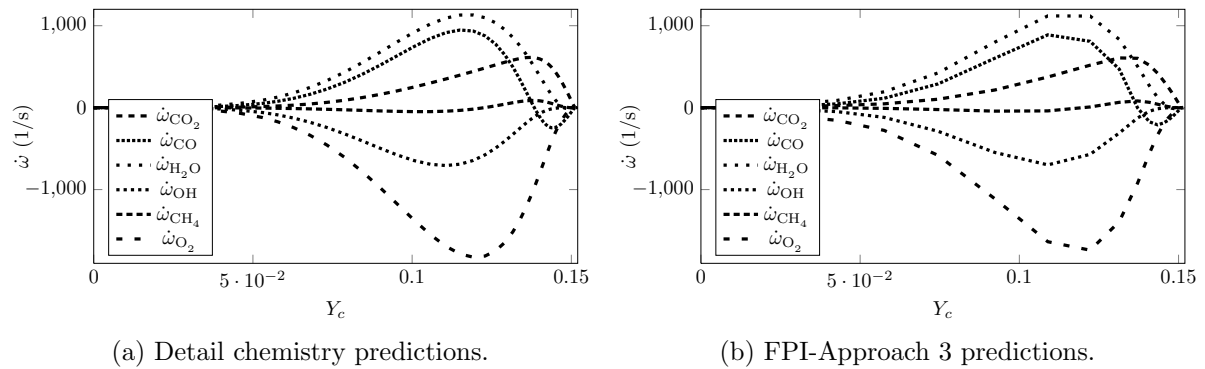
Figure 5.4: Predicted variations of the reaction rates for different species within a one-dimensional laminar methane-air premixed flame for $\phi = 1.2$.
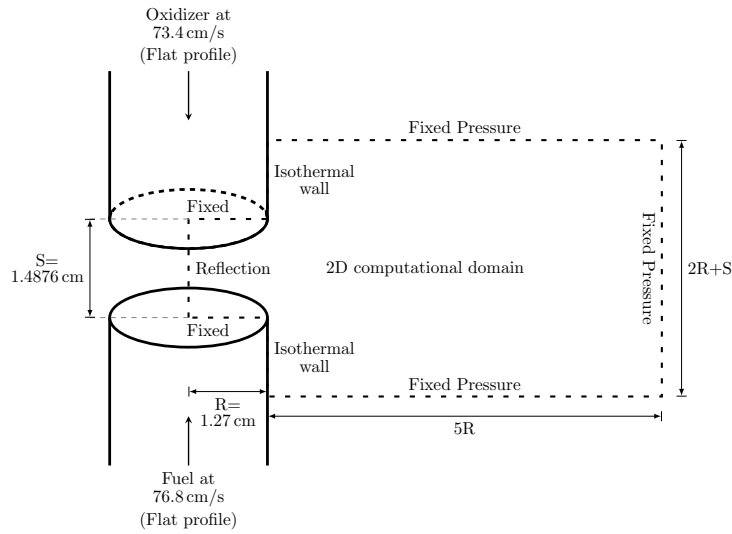
Figure 5.5: A schematic diagram showing the dimensions of the counter-flow flame burner studied here [213]. The dashed line shows the computational domain used to simulate the experimental setup and the boundary conditions used.

to follow.

As FPI-Approach 3 is based on the reconstruction of reaction rates, it is also of interest to show how well the method predicts the reaction rate values for different species for the laminar premixed case. Figure 5.4 compares the reaction rate predicted by Cantera and the reconstructed reaction rate predicted by FPI-Approach 3. The tabulated predictions are almost exact, both in their shape and magnitude.

5.2.2   Laminar Counter-flow Methane-air Flame

As discussed in detail earlier in Section 3.4, the SLFM approach is based on the assumption that for the same value of a conserved scalar at any point in the flow, the local structure of a general laminar diffusion flame is the same as that of any simplified laminar diffusion flame. Most commonly, the detailed chemistry solutions of simplified laminar one-dimensional counter-flow diffusion flames are used to generate flamelet libraries which can be used for more complex flow geometries, as proposed by Peters [141]. It is therefore important to compare the performance of the FPI approach with the SLFM approach for predicting the counter-flow diffusion flames, as the FPI uses premixed flamelet solutions for predicting diffusion flames.

The experimental setup by Puri, Seshadri, Smooke, and Keyes [213] for an opposed-

(a) Initial Coarse Grid - 30 blocks.   (b) Grid after 1 level of refinement - 63 blocks.

(c) Grid after 2 levels of refinement - 120 blocks.   (d) Grid after 3 levels of refinement - 191 blocks.
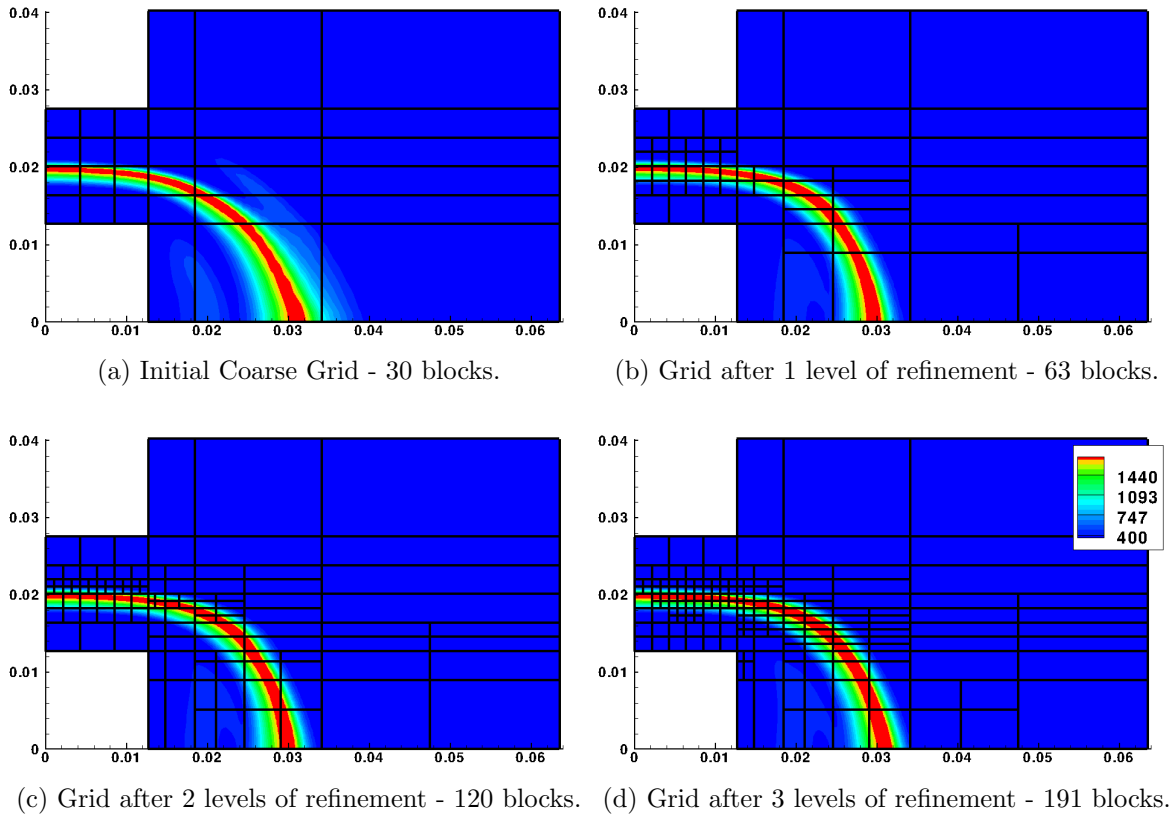
Figure 5.6: Temperature contours, obtained using the FPI-Approach 3, shown for laminar methane-air counter-flow grid for three levels of AMR refinement. The grid refines along the high temperature region.

jet flame was used as the validation case as it provides a good set of experimental data to which results can be compared. Figure 5.5 shows the dimensions of the experimental setup. A methane-air counter-flow flame was setup using two ducts, each with an inner diameter of 2.54 cm and with a separation distance of 1.4876 cm. The axial velocities of methane and air were 76.8 cm/s and 73.4 cm/s, respectively. A number of fine wire screens were placed in the duct to reduce turbulence ensuring a flat laminar velocity profile at the exit of the duct.

The computational domain and boundary conditions used for the numerical simulation of this experiment are also shown in Figure 5.5. Using the axisymmetric geometry of this flow configuration, a two-dimensional computational domain was used to predict the flame structure. A reflection boundary condition is used on the left boundary representing the symmetry plane. The inflow boundary conditions for both the ducts are

Experimental	Cantera	One-Step	FPI Approach 1	FPI Approach 3	SLFM Approach 1	SLFM Approach 2
1950 K	1980 K	2169 K	1897 K	1912 K	2031 K	1985 K

Table 5.1: Maximum temperature predicted by different numerical methods for counter-flow methane-air flame.

kept fixed. All of the far-field boundaries are set to constant atmospheric pressure and zero gradient for all other physical properties. The solution domain was initialized with a uniform solution state corresponding to quiescent air at 298 K, except for a thin region in between the fuel and oxidizer inlets, which is initialized with an equilibrium burnt gas composition of the fuel and oxidizer.

The laminar counter-flow solutions were obtained using six different chemical-kinetic approaches. The Cantera package was used to obtain the detailed-chemistry counter-flow solution using the GRI-Mech 3.0 mechanism. Solutions were obtained for four tabulated chemistry approaches: FPI-Approach 1, FPI-Approach 3, SLFM-Approach 1, and SLFM-Approach 2. All tabulated schemes were based on the GRI-Mech 3.0 mechanism. The FPI look-up table used for this problem, for both FPI-Approach 1 and FPI-Approach 3, were of the dimension $(121 \times 1 \times 121 \times 1)$, with 60 mixture fraction points inside the flammability limits and the rest outside. The data in the SLFM look-up table is tabulated as a function of 167 mixture fraction values distributed non-uniformly between 0 and 1, and 5 scalar dissipation rate values. Solutions were also obtained using the one-step mechanism.

The grid used for the counter-flow case is show in Figure 5.6. The temperature contours shown in this figure were obtained using the FPI-Approach 3. The initial grid consists of 30 blocks, each block with 16 by 16 grid points (7680 cells). More blocks are located in between the two reactant inlets, where most of the physical activity is taking place. After obtaining an initial approximate solution on the coarse grid, the flow-field calculations were carried out on three adaptively refined grids, each consisting of a number of 16×16 cell blocks: 63 blocks (16 128 cells), 120 blocks (30 720 cells), 191 blocks (48 896 cells). The refinement efficiency of the AMR scheme after three levels of refinement was 0.75. The refinement criteria was chosen to be the density gradient in order to track the region of maximum chemical activity. The new grid blocks are mostly concentrated halfway between the ducts along the flame. This example for the refined grid shows the potential of the AMR method, in terms of being able to refine areas of
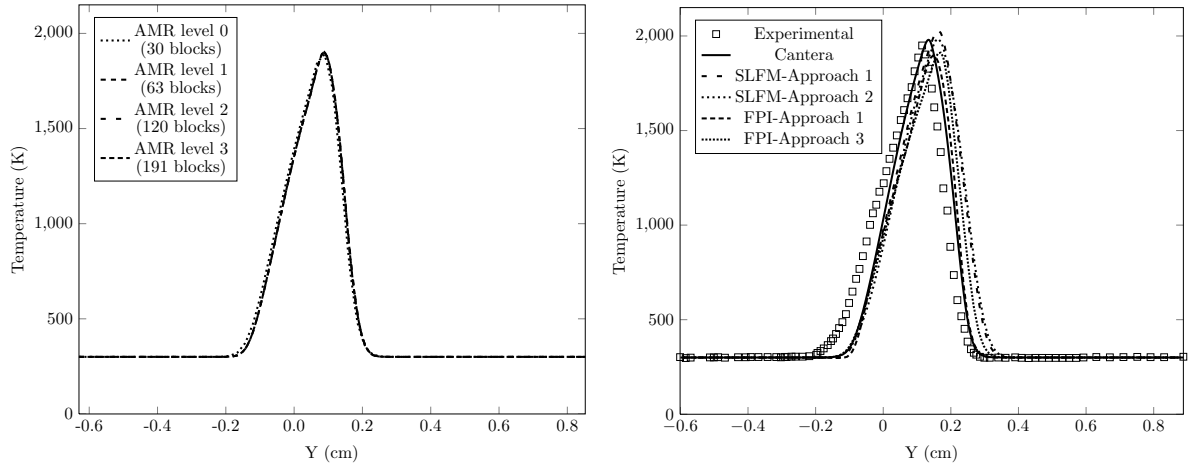
(a) Predicted centre-line temperature profiles, using FPI-Approach 3, for different AMR levels.

(b) Predicted centre-line temperature profiles predicted by different tabulation schemes.

Figure 5.7: Predicted centre-line temperature profiles for the laminar counter-flow flame.

maximum activity. The centre-line temperature profile predicted at different levels of AMR refinement have been compared in Figure 5.7a. It is seen that these temperature profiles agree with each other extremely well, showing that a grid converged solution was obtained.

The predicted high temperature region in Figures 5.6 extend a long way outside the duct. This can be attributed to the fact that, in the experimental setup, an inert curtain of N_2 was used. This curtain acts as a coolant and inhibits the high temperature region to spread further. As discussed before in Section 3.3, the present numerical implementation was setup to handle only one fuel and one oxidizer stream, i.e., deal with a single mixture fraction variable. To account for another stream of flow, modifications to the present implementation would be needed to account for multiple mixture fractions.

The maximum temperature predicted by each numerical approach is summarized in Table 5.1. The flamelet approaches tend to over-predict the temperature, while the FPI approaches under-predict the temperature by almost the same magnitude. The SLFM-Approach 2 has the best agreement with experiment, which is expected as it directly uses the temperature predicted by Cantera for the opposed jet diffusion flame. However, the agreement between tabulated chemistry results and experiment are much better than the one-step mechanism, which over-predicts the temperature by more than 200 K. The centre-line profiles of temperature and major species predicted by both the SLFM and FPI approaches are compared to the experimental data provided by Puri et
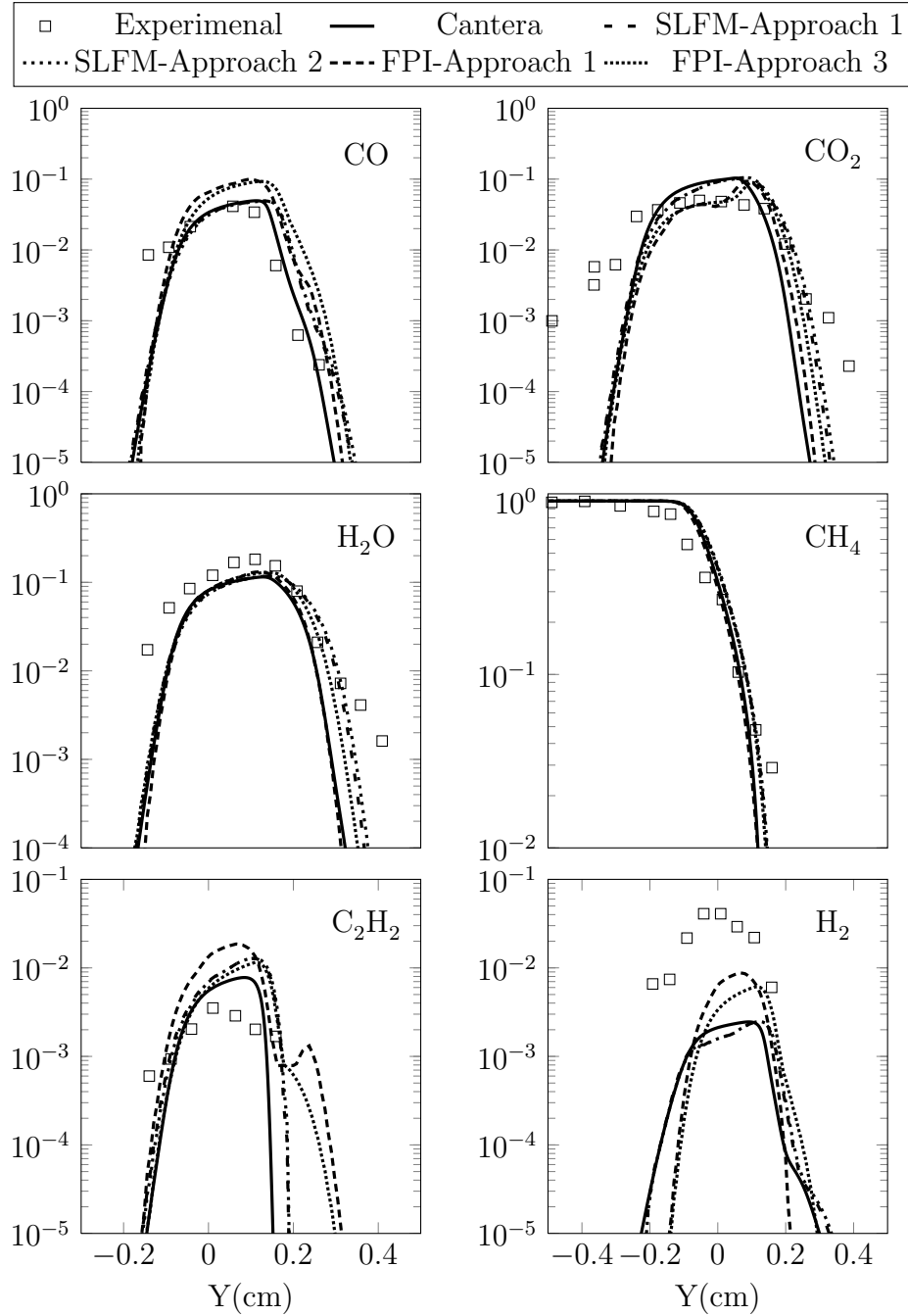
Figure 5.8: Centre-line species mole fraction concentrations predicted by different tabulation schemes for the methane-air counter-flow flame.

al. [213] in Figure 5.7b. It can be seen that all the tabulation methods reproduce the species and temperature profiles reasonably well. The temperature profiles predicted by the tabulation methods however are shifted to the right by around 6 mm as compared to the experimental results. Both the FPI schemes actually are in better agreement with
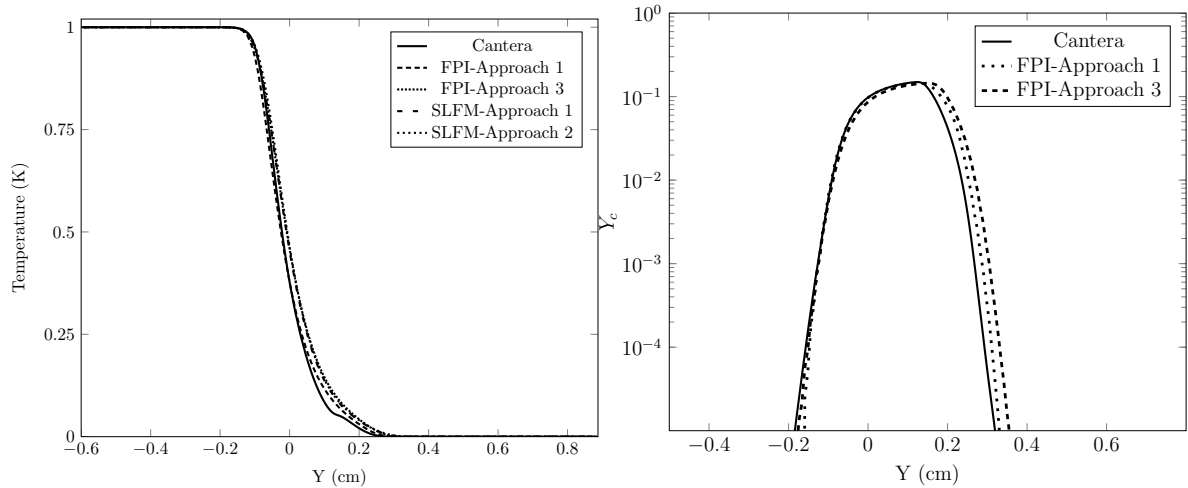
(a) Predicted centre-line mixture fraction profiles. (b) Predicted centre-line progress of reaction variable profiles.

Figure 5.9: Comparison of predicted mixture fraction and progress of reaction profiles for different for the laminar methane-air counter-flow flame.

experimental results on the right side of the temperature curve, where the temperature is falling and returning to the atmospheric temperature. The major and minor species predicted by FPI and SLFM approaches are shown in Figure 5.8. Good agreement is seen between the experimental results and the results predicted by the tabulation methods. Both the FPI and SLFM schemes predict the major species profiles with similar accuracy and look in good agreement with the experimental data. Figure 5.8 show that the tabulation schemes predict the profiles of minor species, like C_2H_2 and H_2, as well, but the predicted magnitudes are not in as good agreement as the major species. If one considers the prediction of carbon monoxide, the discrepancy in the maximum CO concentration relative to the experimental value is approximately a factor of two and are similar for both the FPI and SLFM approaches. This level of accuracy is similar to that obtained in the earlier numerical simulations of this counter-flow flame [213].

It should be noted that an accurate prediction of temperature is required for NO_x prediction and inaccuracies in the temperature of 50 K are somewhat significant. Nevertheless, the progress of reaction variable would need to be re-defined for FPI in order to predict NO formation [71, 214, 215].

Figures 5.9 depicts predicted centre-line profiles of the mixture fraction, f, and the progress of reaction variable, Y_c, for the directly calculated computation obtained using
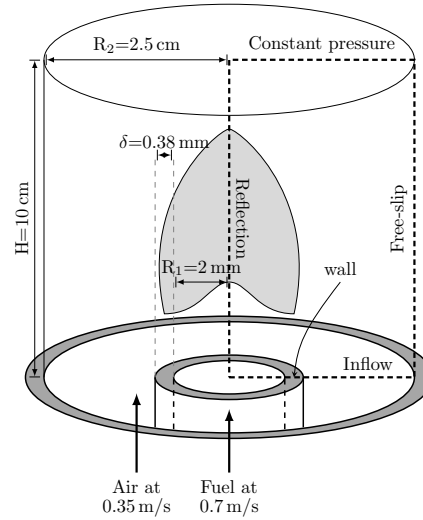
Figure 5.10: Schematic diagram of the laminar co-flow diffusion flame. The computational domain and boundary conditions used are also shown.

Cantera and the various FPI and SLFM tabulated chemistry methods. The FPI and SLFM approaches appear to be able to reproduce quite accurately the profiles for the mixture fraction for this counter flow case, whereas slightly larger errors are observable in the FPI methods predictions of the progress variable. The differences in the predicted values of Y_c would seem to be the cause of the observed errors in the predicted temperature profiles.

The preceding results quite clearly demonstrate that the FPI approach can successfully predict a counter-flow flame profile with virtually the same accuracy as the SLFM approach, a method based entirely on tabulated counter-flow solutions. The results therefore also provide strong justification for the use of the FPI methods based on premixed flamelets in the numerical simulation of more general diffusion flames.

5.2.3   Laminar Co-flow Diffusion Flame

The FPI and SLFM approaches were also compared and assessed when applied to the solution of the steady laminar co-flow diffusion flame studied previously by Mohammed et al. [216], Day and Bell [49] and Northrup and Groth et al. [55]. Numerical predictions of this axisymmetric flame and burner were obtained on a computational domain that was rectangular in shape with dimensions 10 cm by 2.5 cm, as shown in Figure 5.10. The axis of symmetry was aligned with the left boundary and the right far-field boundary was taken to be a free-slip boundary. The top or outlet of the flow domain was open to
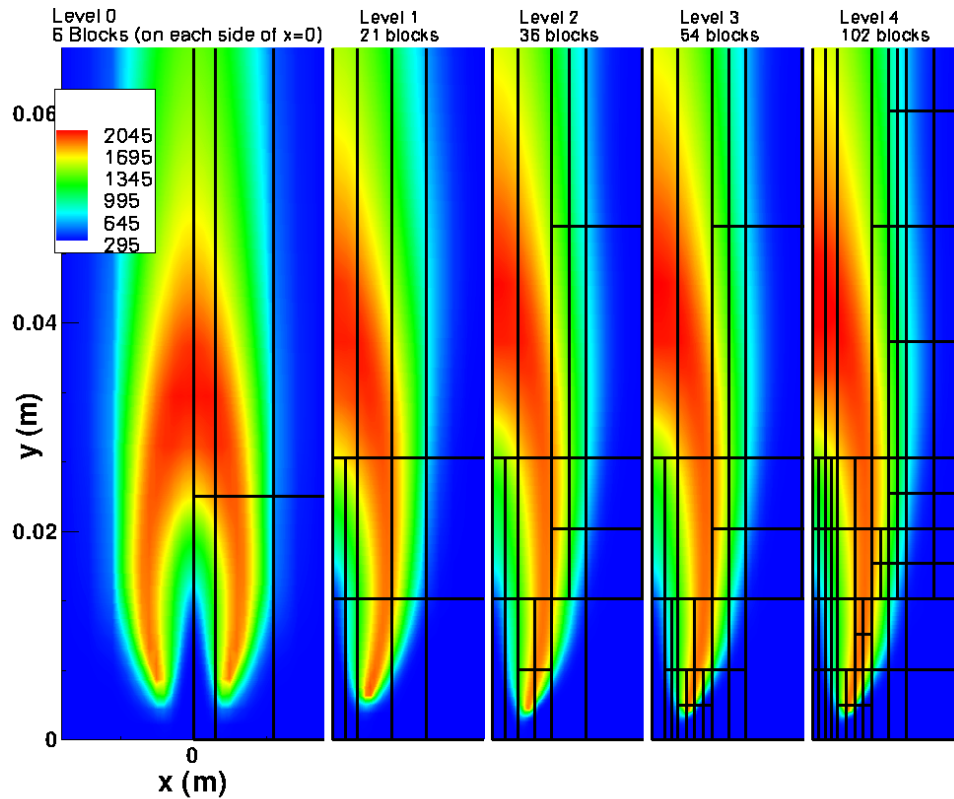
(a) Grids for four levels of AMR.
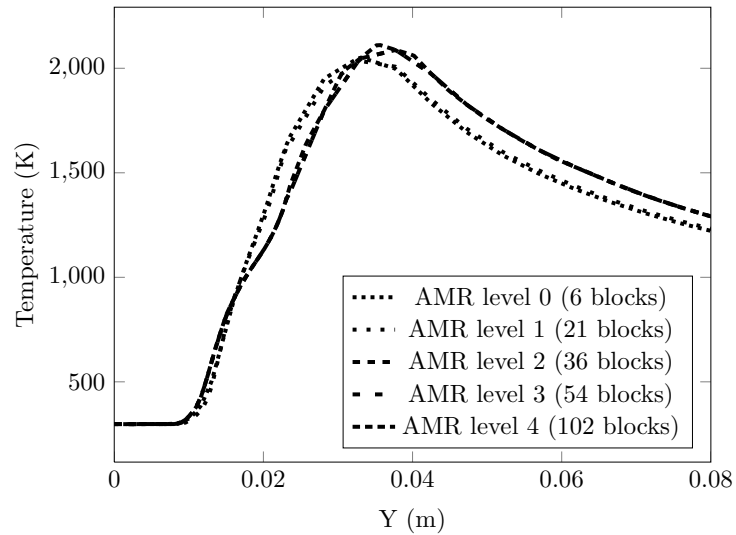
(b) Predicted axial temperature profiles

Figure 5.11: Predicted temperature distribution and profiles for the laminar co-flow diffusion flame for four levels of AMR. The results shown here are FPI-Approach 1.
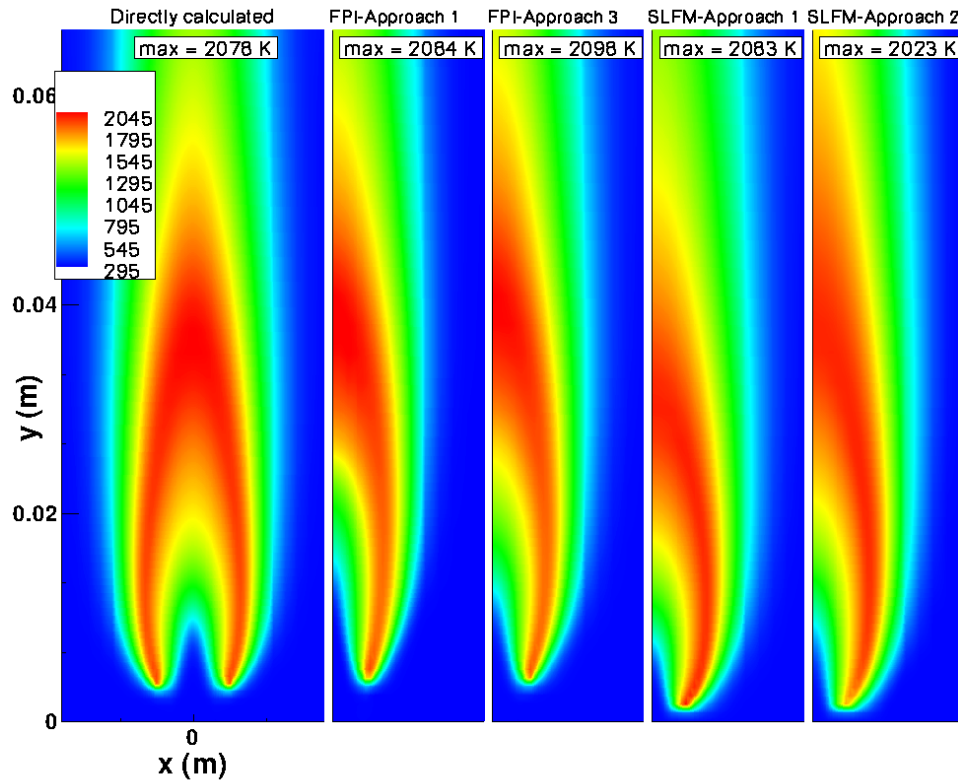
(a) Predicted temperature contours
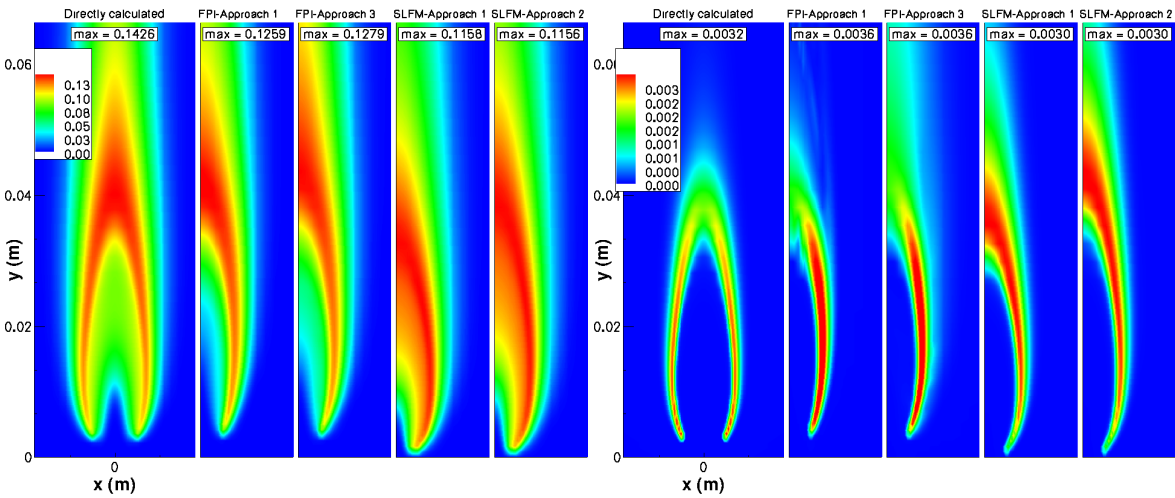
(b) Predicted CO_2 mass fraction contours   (c) Predicted OH mass fraction contours

Figure 5.12: Predicted temperature and species distributions for the methane-air laminar co-flow diffusion flame obtained using direct-calculation and different tabulated chemistry approaches.

a stagnant reservoir. The bottom or inlet was divided into three distinct regions. The innermost region ($r = 0$ to $R_1 = 2\,\text{mm}$) was the fuel inlet which injects a nitrogen diluted methane fuel mixture ($Y_{CH_4} = 0.5149$, $Y_{N_2} = 0.4851$) at $298\,\text{K}$ with a parabolic velocity profile having a maximum velocity of $0.7\,\text{m/s}$. The Mach number and Reynolds number based on the fixed diluted methane flow in the fuel inlet were $M = 0.0016$ and $Re = 169$. The next region ($\delta = 0.38\,\text{mm}$) was a small gap associated with annular wall separating the fuel and the oxidizer. The third region ($r = 2.38\,\text{mm}$ to $R_2 = 2.5\,\text{cm}$) contains the co-flowing oxidizer, air ($Y_{O_2} = 0.232$, $Y_{N_2} = 0.768$) at $298\,\text{K}$, with a uniform velocity of $0.35\,\text{m/s}$. Free-slip boundary conditions was applied to the outer boundary in this region.

The solution domain was initialized with a uniform solution state corresponding to quiescent air at $298\,\text{K}$, except for a thin region across the fuel and oxidizer inlets, which was initialized with an equilibrium burnt gas composition of the fuel and oxidizer. Additional details concerning the setup for this diffusion flame can be found in the papers by Mohammed et al. [216] and Bell et al. [49].

Figure 5.11a shows the application of the AMR scheme for the co-flow diffusion flame. The solutions shown are for the FPI-Approach 1. The initial computational mesh consisted of 6 blocks, each of 8 by 16 cells, in x and y directions respectively. The smallest cell size was of the dimension $0.25\,\text{mm}$ by $1.4\,\text{mm}$. After getting the first approximate solution, AMR is performed on the solution 4 times with temperature gradient as the refinement criterion. The threshold for refinement is set to 0.5 and the threshold for coarsening is set to 0.3. The solution blocks adapt themselves along the regions of maximum temperature gradient. After each refinement, the number of blocks increase from 6 (768 cells) to 21(2688 cells), 36(4608 cells), 54(6912 cells) to 102(13 056 cells). Figure 5.11b compares the axial temperature profiles predicted at different AMR levels using the FPI-Approach 1. It was found that after two levels of AMR, there was no change in the predicted profile, which shows that a grid converged solution was obtained.

The following cases were run for the laminar co-flow flame: (1) direct calculation using the GRI-Mech 3.0 mechanism; (2) FPI-Approach 1 based on GRI-Mech 3.0 mechanism; (3) FPI-Approach 3 based on GRI-Mech 3.0 mechanism; (4) SLFM-Approach 1 based on GRI-Mech 3.0 mechanism; ; (5) SLFM-Approach 2 based on GRI-Mech 3.0 mechanism; (6) direct calculation using the one-step mechanism; (7) FPI-Approach 1 based on one-step mechanism; and (8) FPI-Approach 3 based on one-step mechanism. Note that the cases with the one-step mechanism were run for comparisons of computational costs, as shown later in Table 5.4, and not for assesing the accuracy of the FPI schemes.

The dimension of the FPI tables was ($100 \times 1 \times 155 \times 1$) and that of the SLFM table was (155×18).

	Directly calculated	FPI Approach 1	FPI Approach 3	SLFM Approach 1	SLFM Approach 2
Size of table	N/A	1.9 MB	1.9 MB	0.069 MB	0.0635 MB
CPU time/iteration	0.0770 (10.84)	0.007 12 (1.03)	0.007 53(1.09)	0.006 93(1.0)	0.006 97 (1.001)
% time spent in reading tables	N/A	0.3	0.4	1.0	0.6
% time spent in calculating $\dot{\omega}_i$	43.04	N/A	0.4	N/A	N/A
Predicted flame height	3.56 cm	3.33 cm	3.52 cm	2.61 cm	3.26 cm
Predicted lift-off height	1.15 cm	1.25 cm	1.45 cm	0.08 cm	0.10 cm
Predicted max. temperature	2078 K	2084 K	2098 K	2083 K	2023 K

Table 5.2: Summary of comparisons of tabulated chemistry methods for diffusion flame with GRI-Mech 3.0 chemical mechanism.

	Directly calculated	FPI Approach 1	FPI Approach 3	SLFM Approach 1	SLFM Approach 2
One-step	2181 K	2173 K	2169 K	N/A	N/A
GRI-Mech 3.0	2078 K	2084 K	2098 K	2083 K	2023 K

Table 5.3: Maximum temperature calculated for the laminar co-flow diffusion flame using different chemical kinetic schemes. The maximum centre-line temperature reported by Mohammed et al. [216] is between 2025 K and 2029 K.

	Directly calculated	FPI-Approach 1	FPI-Approach 3
One-step	0.003 96(1)	0.004 33(1.09)	0.004 36(1.1)
GRI-Mech 3.0	0.0770 (19.44)	0.007 12 (1.8)	0.007 53(1.9)

Table 5.4: CPU time required per iteration for different chemical kinetic schemes for the laminar co-flow diffusion flame.

(a) Axial temperature profile

(b) Axial temperature profile

(c) Radial temperature profile at $y = 2.5\,\mathrm{cm}$

(d) Radial temperature profile at $y = 7\,\mathrm{cm}$
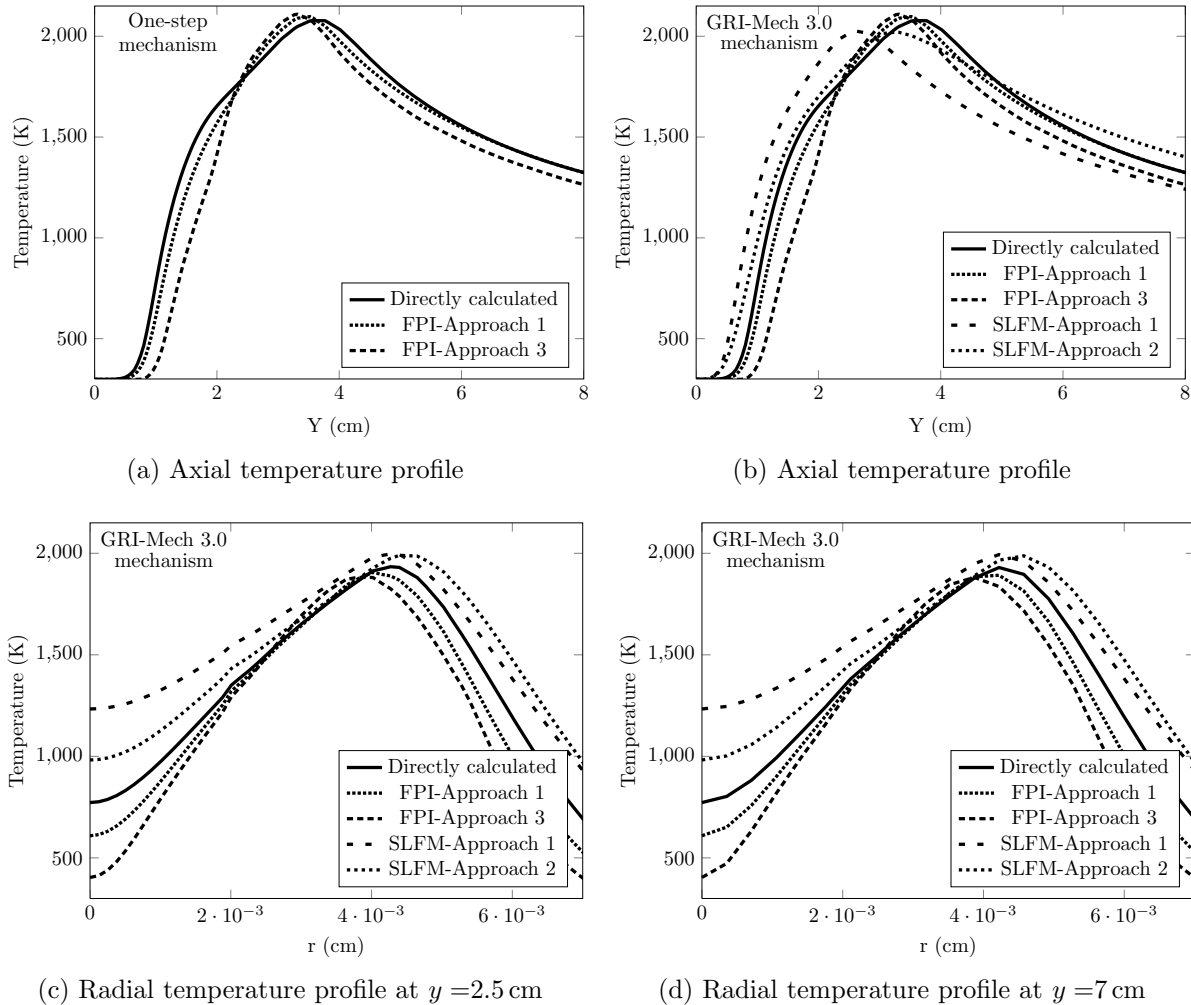
Figure 5.13: Predicted temperature profiles by the tabulated-chemistry approaches at different locations in the computational domain for the laminar co-flow diffusion flame.

Predicted distributions of the temperature, carbon dioxide and hydroxyl radical obtained using direct calculation and tabulated chemistry for the FPI Approaches 1 and 3 and the SLFM Approaches 1 and 2 with the GRI-Mech 3.0 mechanism are compared in Figure 5.12. Furthermore, predicted temperature profiles obtained using both the one-step and detailed chemical mechanisms are shown in Figure 5.13. Figure 5.13a and Figure 5.13b show that the FPI approaches recover the temperature predictions obtained using direct calculation for both the one-step mechanism and the GRI-Mech 3.0 mechanism extremely well. Figure 5.12a and Figure 5.13b indicate that the FPI schemes predict the high-temperature regions of the flame much better than does the SLFM approach, for which this region is more spread out when the GRI-Mech 3.0 mechanism is

used. Figure 5.13c and Figure 5.13d also show that the predicted centre-line and radial
temperature profiles of the directly-calculated solutions are quite accurately recovered by
FPI approaches for detailed mechanisms. Figure 5.13b shows that the SLFM-Approach 1
predicts the highest temperature much earlier than all other methods and the high tem-
perature region in the SLFM-Approach 2 extends further downstream higher up in the
flame than for the other approaches. Again not surprisingly the maximum temperature
predicted by the detailed-chemistry schemes are much closer to the experimental results
reported by Mohammed et al. [216] than the results predicted by the simple one-step
mechanism, indicating the importance of finite-rate chemistry for diffusion flames of this
type. An accurate balance between transport and chemical reaction rates is needed to
predict accurately the flame temperature and this cannot be provided by simple one-step
mechanisms for the diffusion flame.

Predictions of the mass fraction of some major and minor species are shown in Fig-
ure 5.14. The FPI approaches reproduce the magnitude and profiles predicted by the
detailed-chemistry very well. However, note that in Figure 5.14d the OH radical ex-
hibits higher diffusion in the FPI-Approach 3 results. This can be probably attributed
to the use of species transport equations only on the reduced set of tabulated species.
However, the agreement between the maximum concentration of OH predicted by the
FPI method and direct calculation is much better in comparison to that achieved by the
SLFM approach.

Figures 5.15 and 5.16 depict predicted two-dimensional distributions and centre-line
profiles of the mixture fraction, f, and the progress of reaction variable, Y_c, for the co-
flow flame obtained using the directly calculated computation and the various FPI and
SLFM tabulated chemistry methods. Again, the mixture fraction seems reasonably well
predicted by all models, which is quite positive, but slightly larger errors are noticeable in
the progress variable used in the FPI method. These errors in the progress variable would
seem to correlate reasonably well with the observed errors in the predicted temperature
field shown in Figure 5.12a above.

Table 5.2 provides a detailed summary of the comparisons between the tabulation
methods and computational costs involved for the diffusion flame with the detailed GRI-
Mech 3.0 mechanism. The advantages of the FPI over the flamelet approaches is again
evident when considering some of the global properties of the flame predicted by each
scheme. The FPI results are in much better agreement with directly-calculated results
for overall flame height and lift-off height. Table 5.2 also shows that the CPU time per

(a) Predicted CO_2 mass fraction

(b) Predicted CO mass fraction

(c) Predicted H_2O mass fraction

(d) Predicted OH mass fraction
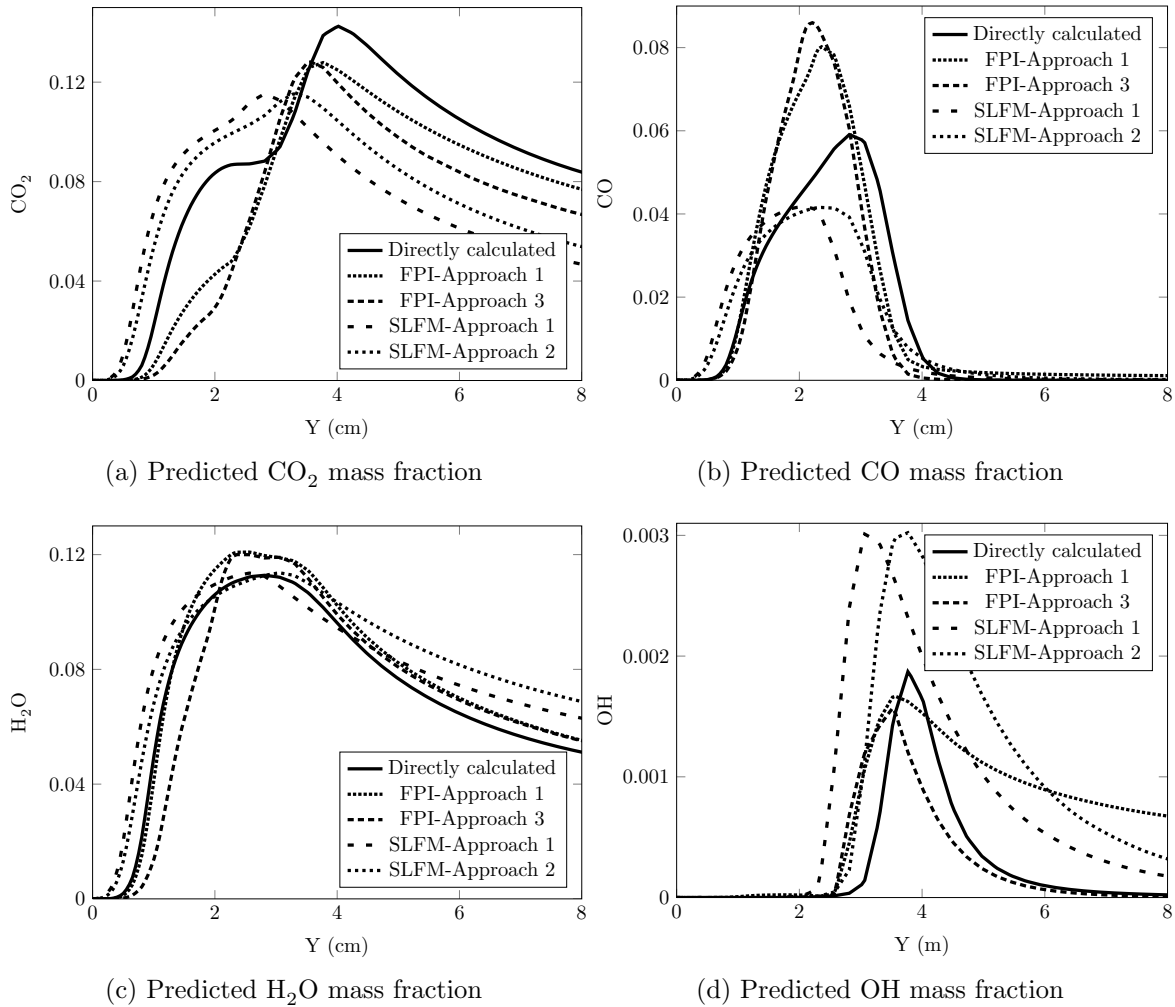
Figure 5.14: Predicted centre-line species profiles by the tabulated-chemistry approaches for methane-air laminar co-flow diffusion flame.

iteration is almost the same for the FPI and flamelet approaches. Moreover, all of these tabulation schemes are almost 11 times faster than directly solving the full set of species balance equations. This is because direct calculation of the reaction rates for the detailed methane-air chemical kinetic mechanism requires almost 43% of the computational time while evaluation and retrieval of tabulated data in the flamelet approaches requires less than 0.4% of the processor time.

In contrast to the results for the detailed mechanism, it is interesting that, for the one-step mechanism, use of the FPI tabulated approaches results in a slightly higher computational cost compared with the cost of the directly-calculated simulation. This is due to the additional overhead associated with interpolating tabulated values that is not

(a) Predicted mixture fraction contours. (b) Predicted centre-line progress of reaction variable contours.
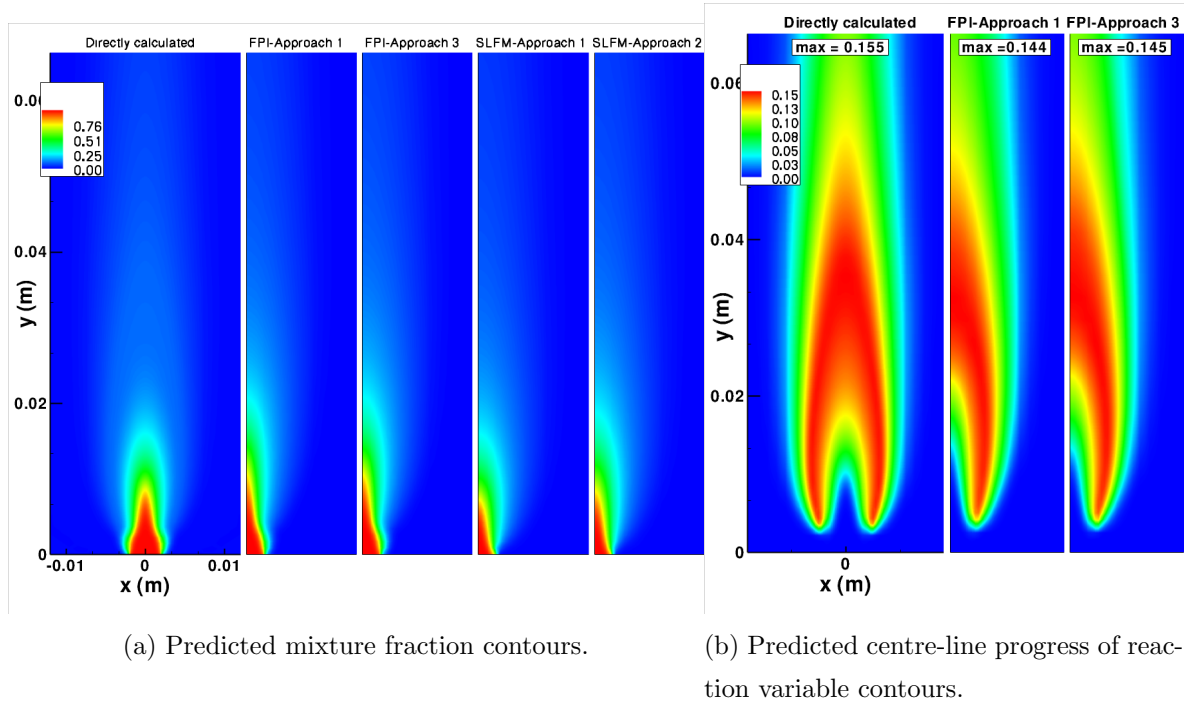
Figure 5.15: Comparison of predicted mixture fraction and progress of reaction contours for the laminar methane-air co-flow flame.

(a) Predicted centre-line mixture fraction profiles. (b) Predicted centre-line progress of reaction variable profiles.
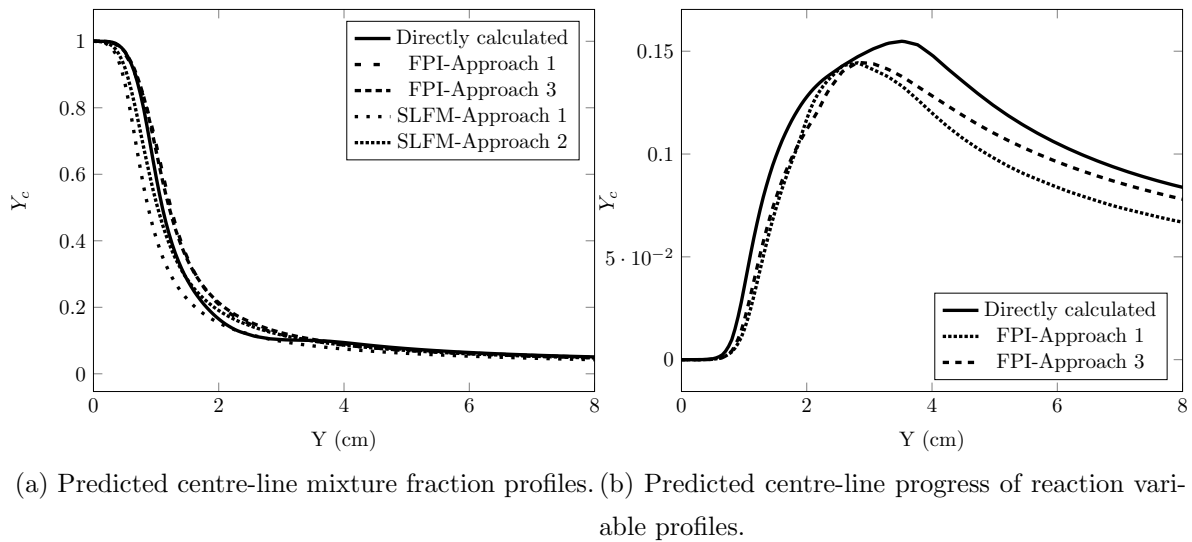
Figure 5.16: Comparison of predicted mixture fraction and progress of reaction profiles for the laminar methane-air co-flow flame.

offset by a significant reduction in the number of partial differential equations that must be solved. Obviously, the computationally payoffs of tabulation methods can really only

(a) Predicted CO_2 mass fraction

(b) Predicted OH mass fraction
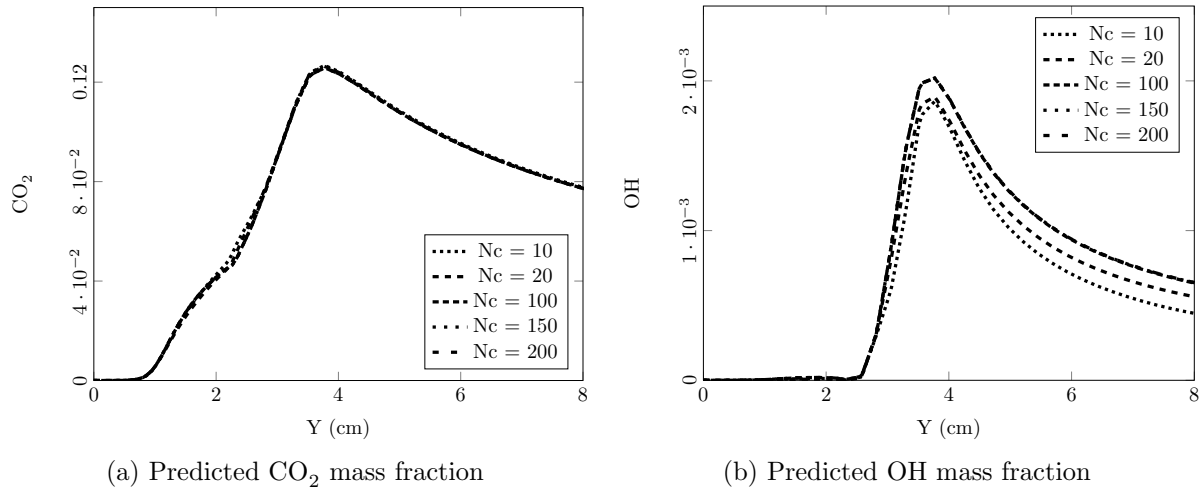
Figure 5.17: Predicted centre-line species profiles for different number of progress variable values, Nc, in the FPI table obtained using the FPI-Approach 3 for laminar co-flow diffusion flame.

(a) Predicted CO_2 mass fraction

(b) Predicted OH mass fraction
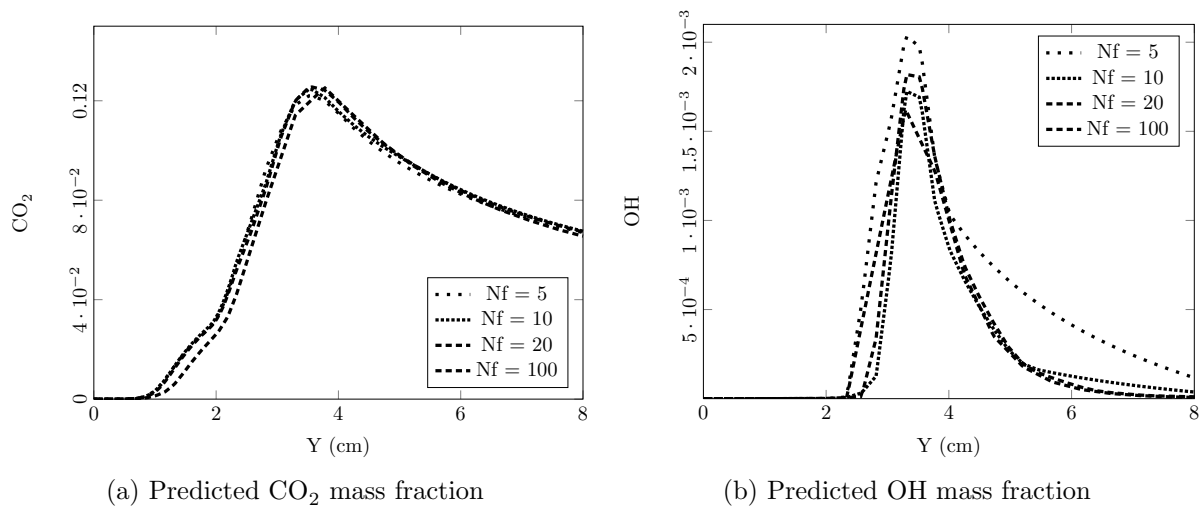
Figure 5.18: Predicted centre-line species profiles for different number of mixture fraction values, Nf, in the FPI table obtained using the FPI-Approach 1 for laminar co-flow diffusion flame.

be fully realized for larger reaction mechanisms.

5.2.3.1   Effect of Look-up Table Size on Results

Figure 5.17 and Figure 5.18 provides an indication of how predicted species mass fractions

are affected by the size of the FPI tables. The predicted centre-line profiles of the mass fractions of both major and minor species are depicted for different numbers of f and c points in the FPI tables. It is evident that major species, such as CO_2, are fairly independent of table size. However, for minor species, such as OH, the FPI predictions are more strongly dependent on the size of the table. For table sizes greater than 50, the results appear to be essentially independent of the tabulation procedure.
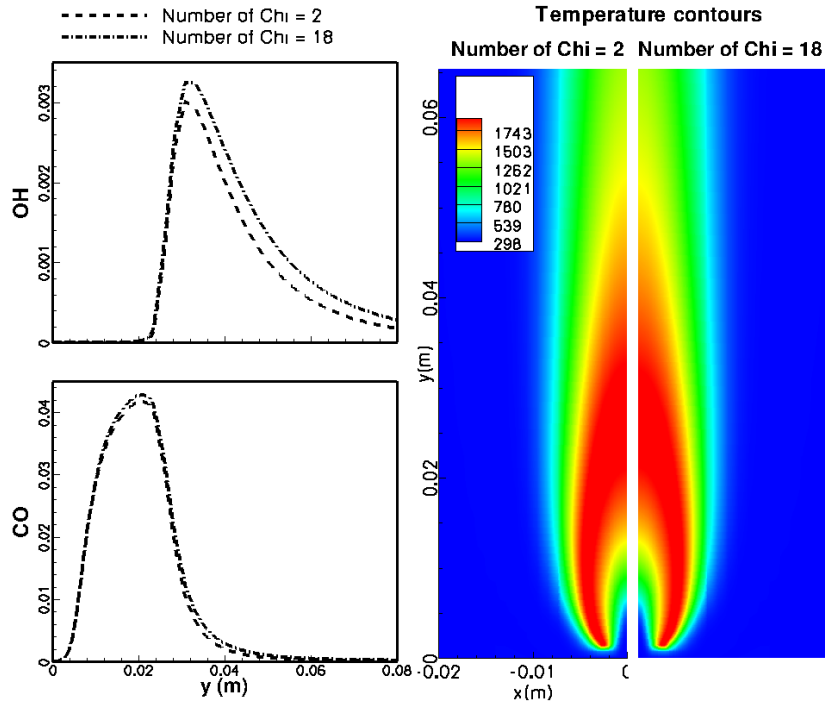
Figure 5.19: The SLFM approach predictions of species mass fraction profiles along the center line and the temperature distribution for laminar co-flow diffusion flame obtained using two different flamelet libraries with GRI-Mech 3.0 chemical mechanism.

Figure 5.19 compares the results for two SLFM table sizes: one table built using only two values for the scalar dissipation rate, χ, and the other using 18 different values. Although major species are also not greatly affected by the size of the flamelet library, minor species exhibit slight variations from the directly-calculated results. It would seem for these near equilibrium flames, the SLFM approach results are not very sensitive to the number of tabulated scalar dissipation rates. As reported by Peters [141], for equilibrium flows, the scalar dissipation rate, χ, only becomes significant when trying to capture accurately NOx or soot formation, which is not of interest here.
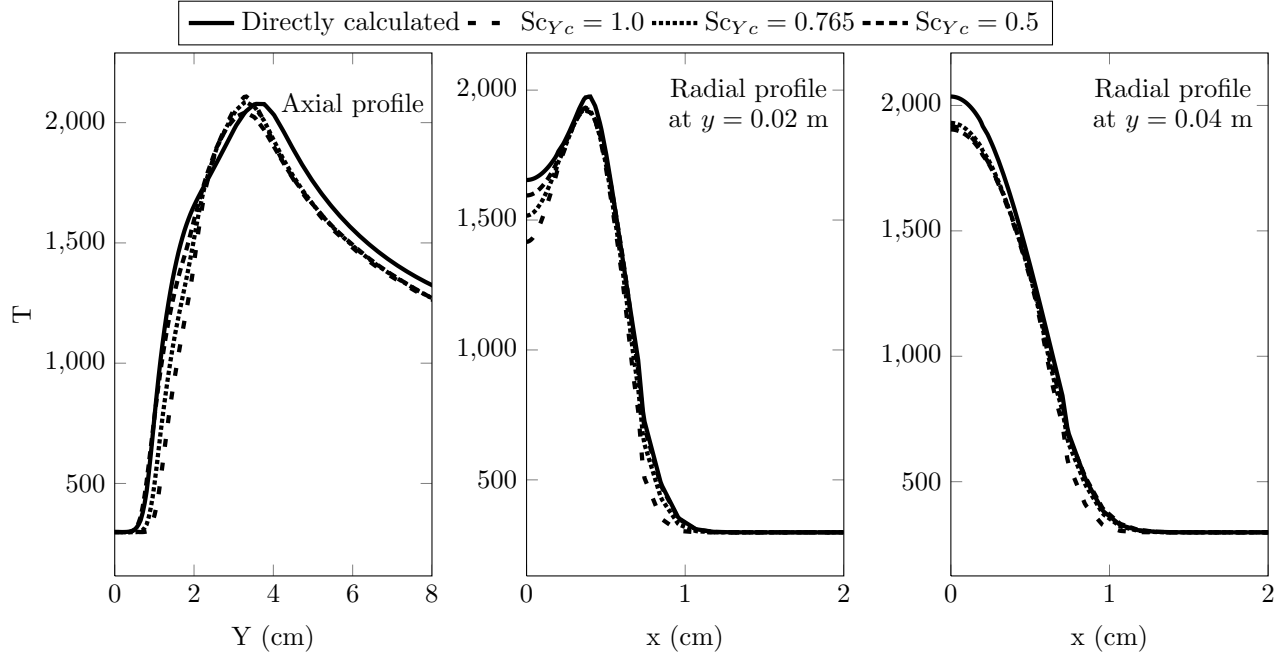
Figure 5.20: Comparison of predicted temperature profiles for laminar co-flow methane-air flame with different constant values of the progress of reaction variable Schmidt number, Sc_{Y_c}.

5.2.3.2   Effect of Progress Variable Schmidt Number

As discussed earler in Section 3.5.1, for the methane-air cases studied in the present work, Sc_{Y_c} is set to a constant value of 1.0. However, Sc_{Y_c} can also be calculated using the following expression, which is dependent on the local values of the Schmidt number of the species used to define the progress of reaction variable.

$$\text{Sc}_{Y_c} = \left(\sum_{j=1}^{N} \alpha_j \frac{\partial Y_j}{\partial x} \right) \left(\sum_{j=1}^{N} \alpha_j \frac{1}{\text{Sc}_j} \frac{\partial Y_j}{\partial x} \right)^{-1} \tag{5.3}$$

Figure 5.20 shows the effect of Sc_{Y_c} on the predicted temperature profiles for laminar co-flow methane-air flame. The value of Sc_{Y_c} calculated using Equation (3.22) varies in the range of 0.7 to 0.8. However, as seen in the temperature profiles in Figure 5.20, changing the value of Sc_{Y_c} from 0.5 to 1.0 changes the predicted temperature only by around 2 %. This shows that the value for Sc_{Y_c} does not greatly affect the methane-air flames. In fact, these results would strongly suggest that the errors in the predictions for the progress variable compared to directly calculated results is most strongly affected by the treatment for the reaction rates (based on premixed laminar flamelets) in the

(a) Velocity profile   (b) Turbulent kinetic energy profile
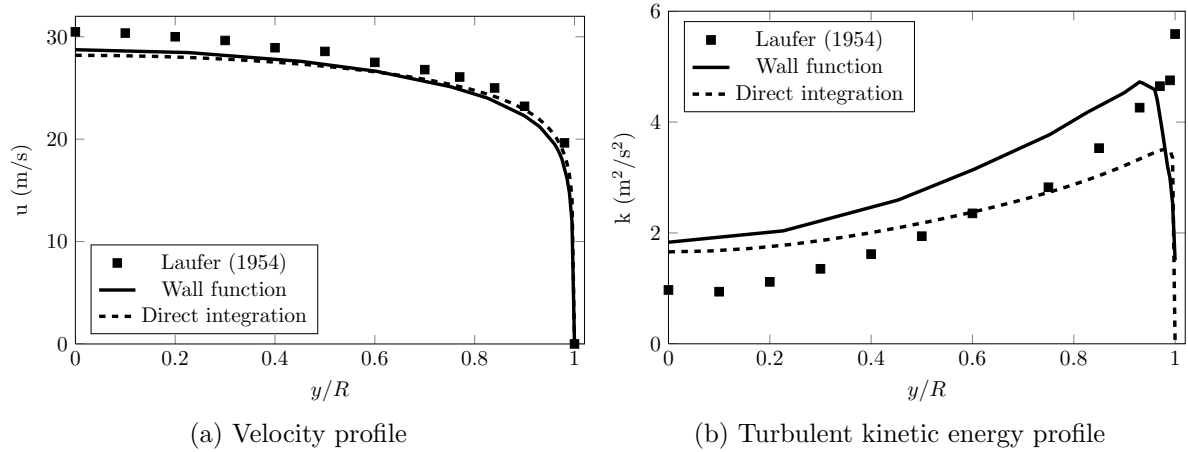
Figure 5.21: Comparison of predicted solutions using the proposed numerical scheme for two-dimensional axisymmetric flows with experimental data for fully developed turbulent pipe flow, Re=50 000.

tabulated approach, and not by modelling of diffusion process. Hence, in the present work a constant value of Sc_{Y_c} has been used in all other computations.

5.3   Non-Reactive Turbulent Flows

5.3.1   Fully-Developed Turbulent Pipe Flow

As partial validation of the proposed numerical scheme and turbulence modelling a non-reacting, fully-developed turbulent pipe flow case was first considered. Numerical predictions were compared to the experimental data provided by Laufer [217] for a turbulent pipe flow with Reynolds number of 50 000. The numerical results were obtained using two numerical schemes: one for two-dimensional flow geometries and the other for three-dimensional flow-geometries. In both cases, the flow was initialized using an analytical turbulent pipe flow solution. Dirichlet boundary condition was used at the inlet for all quantities and Neumann-type boundary condition was applied at the outlet for all quantities except pressure which was fixed.

5.3.1.1   Two-Dimensional Axisymmetric Results

The pipe flow was first computed using the numerical scheme for two-dimensional axisymmetric flow geometries. Solutions for the k-ω turbulence model with both direct

(a) Velocity profile

(b) Turbulent kinetic energy profile
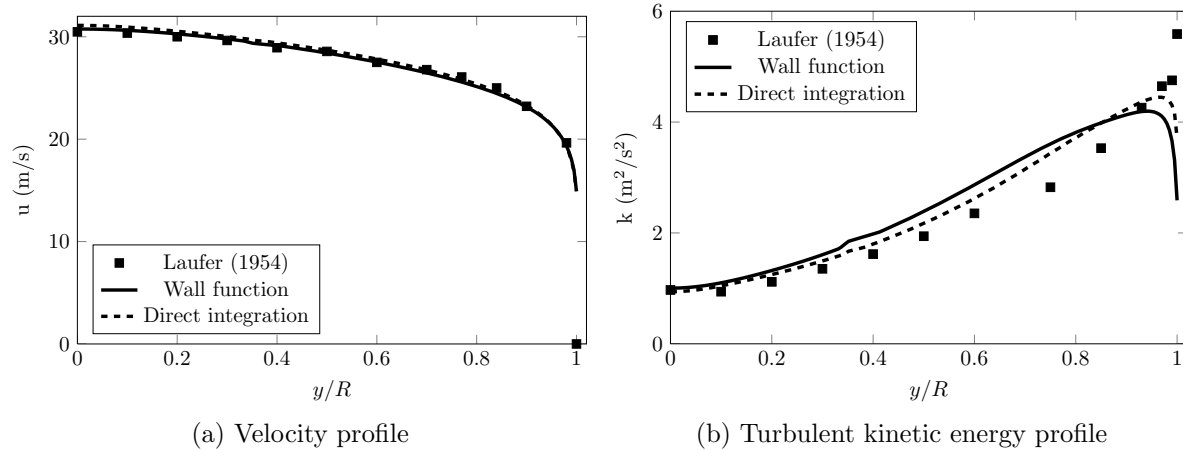
Figure 5.22: Comparison of predicted solutions using the proposed numerical scheme for three-dimensional flows with experimental data for fully developed turbulent pipe flow, Re=50 000.

integration to the wall and standard wall functions are compared to measured mean axial velocity and turbulent kinetic energy in Figure 5.21. The computations with direct integration are performed using 128 cells in the radial direction with around 13 cells within the laminar sublayer. The first cell of the wall was located at $y^+ \approx 0.04$. The calculations with the wall function formulation was performed using just 32 cells in the radial direction with the first cell at $y^+ \approx 2.54$ and around 6 cells within $y^+ = 250$. Both the schemes predict the velocity profile very well, and expected trends are observed for turbulent kinetic energy. As expected, the present implementation of the k-ω model with direct integration and wall functions are both capable of accurately reproducing the characteristic features of fully-developed turbulent pipe flow.

5.3.1.2   Fully Three-Dimensional Results

The pipe flow was simulated using the proposed numerical scheme for three-dimensional flow geometries. Solutions for the k-ω turbulence model with both direct integration to the wall and standard wall functions are compared to measured mean axial velocity and turbulent kinetic energy in Figure 5.22. Calculations for the wall function formulation were performed using 16 cells in the radial direction with the first cell located at $y^+ \approx$ 43. The grid for the direct integration formulation was obtained by performing one uniform AMR on the coarse grid used for standard wall function. This meant that

(a) Schematic diagram of the Sydney bluff-body burner.

(b) The three-dimensional grid used for the numerical simulation of the bluff-body burner flows
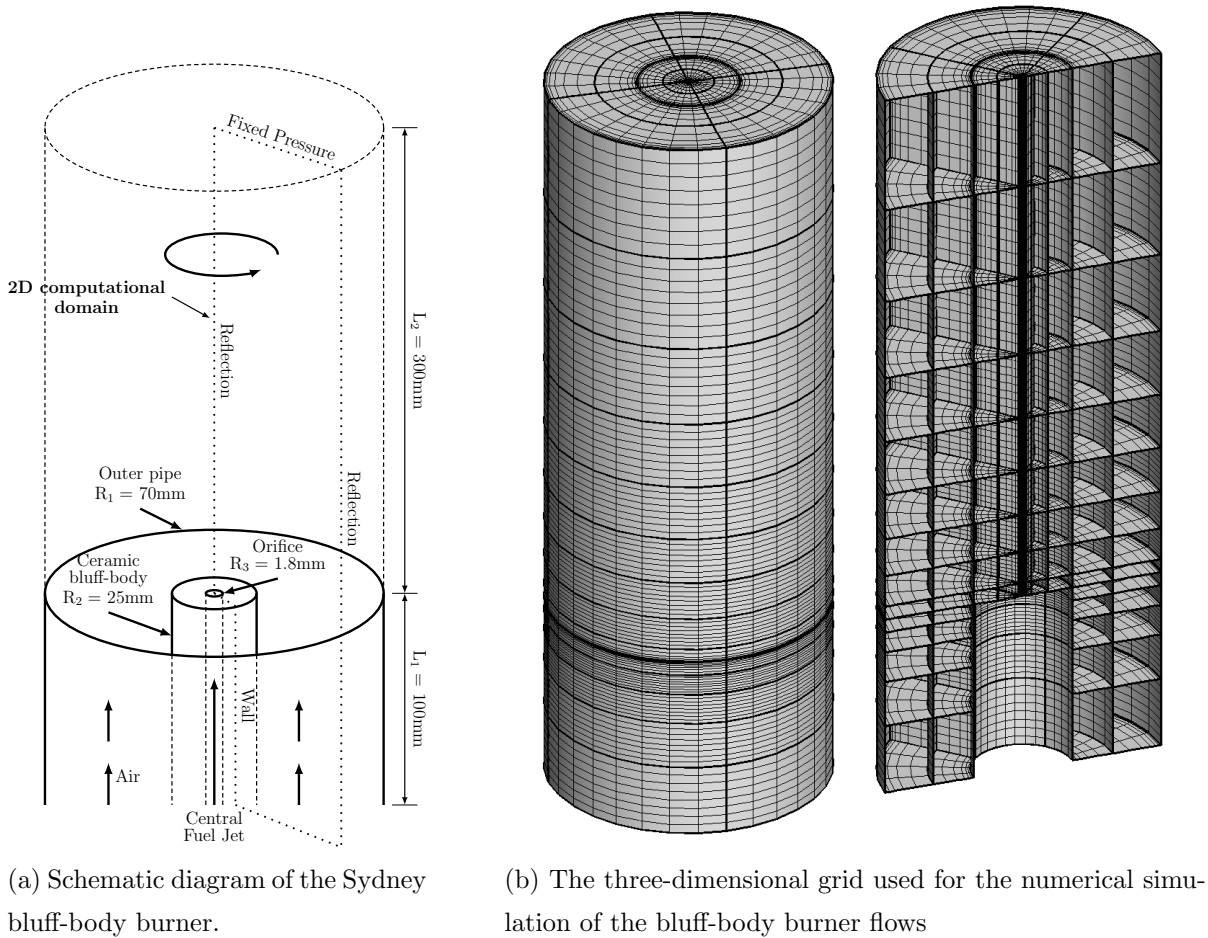
Figure 5.23: The experimental setup of the bluff-body burner and the grids used for its numerical simulation.

calculations with the direct integration formulation were performed using 64 cells in the radial direction with 3 to 4 of those cells lying within the laminar sublayer. The first cell off the wall was located at $y^+ \approx 0.6$. As with the two-dimensional axisymmetric results, good agreement can be seen between the experimental data and the numerically predicted results shown in Figure 5.22 .

5.3.2 Bluff-Body Burner

The Sydney bluff-body configuration, which forms part of the experimental database of the International Workshop on Measurement and Computation of Turbulent Non-premixed Flames (TNF) [218], has also been considered in the present work. This burner has been investigated and used for verification and validation purposes in several recent

studies by Masri et al. [219, 220, 221, 222], Fallot et al. [223], Dally et al. [224, 225], Turpin and Troyes [226] and Gao and Groth [57, 85, 203]. Two flows in the bluff-body burner configuration have been considered in the present study: a non-reacting flow to further validate the k-ω turbulence model and a reacting flow with pure methane as the fuel. The results for the non-reacting case are considered first below and results for the reactive cases will be discussed in Section 5.4.1 to follow.

A schematic diagram of the Sydney bluff-body burner configuration is shown in Figure 5.23a. The figure also shows the two-dimensional computational domain used for the numerical simulation of this burner, using the fact that it is an axisymmetric configuration. The bluff-body has a radius $R_2 = 25$ mm and length $L_1 = 100$ mm and is located co-axially with the air flow inlet. The orifice at the centre of the bluff-body has a radius $R_3 = 1.8$ mm. The outer cylinder for air inflow has a radius of $R_1 = 70$ mm. Adiabatic wall boundary conditions are used for the boundaries representing the bluff body. Dirichlet boundary conditions are used for the air inlet and the orifice. The axis of symmetry of the two-dimensional computational domain is aligned with the centre-line of the bluff-body. A reflection boundary condition is used at the outer boundary. The outlet of the flow domain, at a distance $L_2 = 300$ mm from the bluff body, has Neumann-type boundary conditions for all properties except pressure which is held constant.

5.3.3   Non-Reacting Bluff-Body Burner Flow Conditions

The non-reacting flow field for the bluff-body burner was first studied to further validate the turbulence model implementation and the proposed numerical scheme. Air was injected from both the fuel and the air inlet. Air was injected at the base of the bluff-body at 300 K with a parabolic profile having a mean velocity of 61 m/s. The mean velocity and temperature of the co-flow air were 20 m/s and 300 K respectively. The solution domain, everywhere except the fuel inlet, was initialized with a uniform solution state corresponding to quiescent air at 300 K. The Reynolds number and the Mach number of the high-speed jet were Re=193 000 and Ma=0.18.

5.3.3.1   Two-Dimensional Axisymmetric Results

The non-reacting bluff-body burner flow was first simulated using the proposed numerical scheme for two-dimensional axisymmetric flows. The flow-field calculations were carried out on four adaptively refined grids, each consisting of a number of 8×8 cell blocks: 20
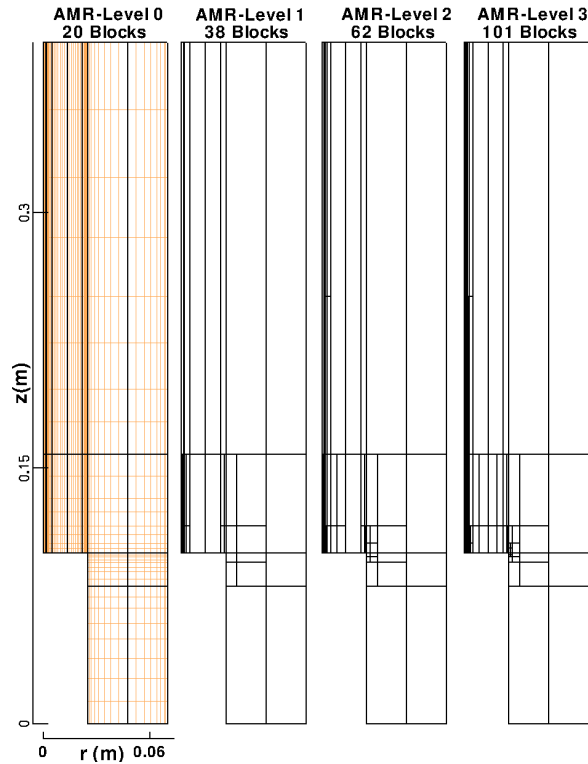
Figure 5.24: The two-dimensional grid used for non-reacting bluff-body burner flow at different levels of AMR. Velocity gradient was chosen as the refinement criterion.

blocks (1280 cells); 38 blocks (3584 cells); 62 blocks (3968 cells); and 101 blocks (6464 cells). The final mesh resolution was such that there were 3 to 4 cells within the laminar sublayer region close to the wall. These grids at different AMR levels for the non-reacting flow are shown in Figure 5.24.

Figure 5.25a shows the predicted mean axial velocity contours and streamlines and reveals the formation of a double vortex structure in the recirculation zone. The two vortices are important in controlling fuel/oxidizer mixing. The calculations indicate that the recirculation zone extends to $x/D_b \approx 0.8$. This is slightly less than the experimentally observed value of $x/D_b = 1.0$. The agreement between the predictions and experiment is further confirmed by a comparison of the predicted axial (centre-line) profile of the mean axial velocity component to the experimental results as depicted in Figure 5.25b. Also, the comparisons of the predicted radial profiles of the mean axial velocity to the measured data at two locations are shown in Figures 5.25c and 5.25d. The results in all these figures clearly indicate that there is reasonably good agreement between the numerical predictions and experimental data. It should also be noted that the predicted results

(a) Velocity contour

(b) Velocity profile along the axis

(c) Radial velocity profile at $x/D_b = 0.6$

(d) Radial velocity profile at $x/D_b = 1.0$

Figure 5.25: Comparison of predicted and measured velocity profiles of mean axial velocity at various locations downstream from the base of the bluff-body burner for non-reacting flow with air jet.

shown here for the non-reacting bluff-body burner configuration are in good agreement with previous numerical predictions of Gao et al. [84] (not shown).

5.3.3.2   Fully Three-Dimensional Results

The non-reacting bluff-body burner flow was also simulated using the proposed numerical scheme for three-dimensional flow geometries. The flow-field calculations were carried out on four adaptively refined grids, each consisting of a number of 8×8×8 cell blocks: 108 blocks (55 296 cells); 165 blocks (84 480 cells); 219 blocks (112 128 cells); and 388 blocks (198 656 cells). These grids at different AMR levels for the non-reacting flow are shown in Figure 5.26. The velocity gradient was chosen as the refinement criterion. The threshold for refinement was chosen to be 0.5 and the threshold for coarsening was 0.1. The AMR meshes shown in the figure indicate that there is a significant increase in block density around the fuel inlet region with every level of AMR refinement as it is the region with highest velocity gradient. The refinement efficiency of the AMR scheme after three levels of refinement was 0.968.

      The agreement between the predictions and experiment is confirmed by a comparison

AMR-Level 0
108 Blocks

AMR-Level 1
165 Blocks

AMR-Level 2
219 Blocks

AMR-Level 3
388 Blocks
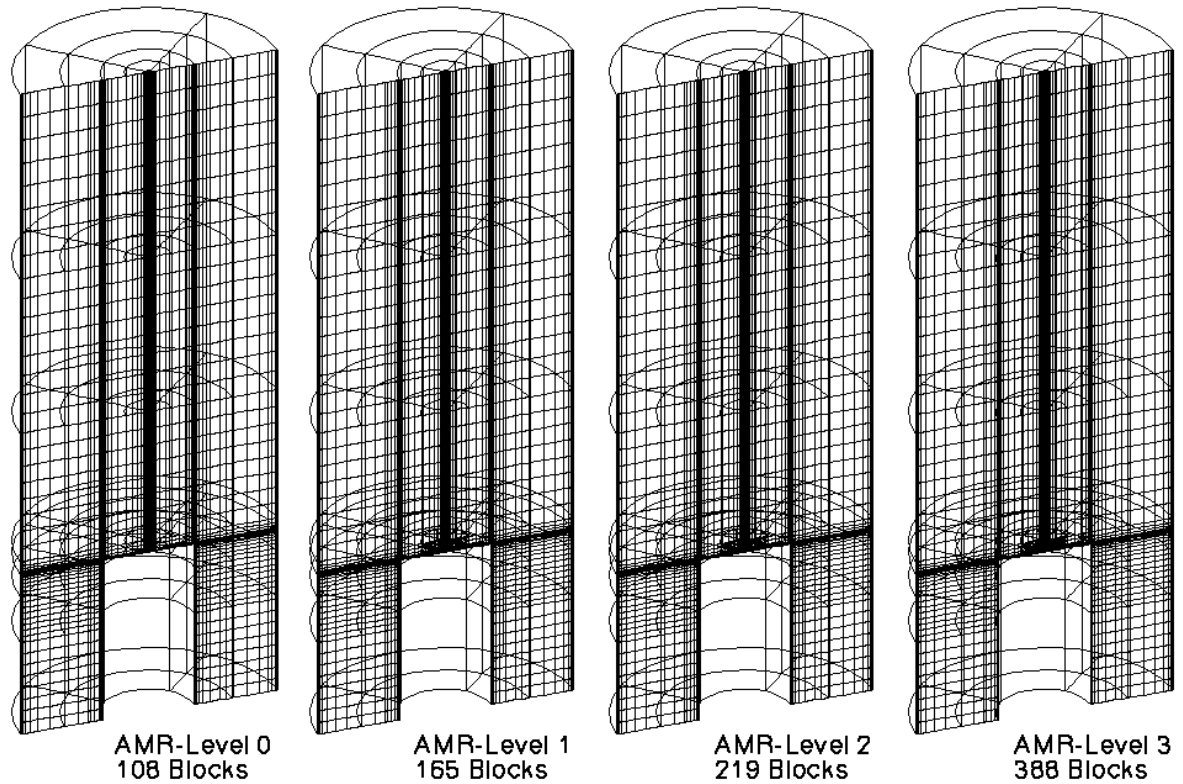
Figure 5.26: The sliced cross-sections of the three-dimensional grid used for bluff-body non-reacting flow at different levels of AMR refinement. Velocity gradient was chosen as the refinement criterion.

of the predicted axial (centre-line) profile of the mean axial velocity component to the experimental results as depicted in Figure 5.27b. Also, the comparisons of the predicted radial profiles of the mean axial velocity to the measured data at two locations are shown in Figure 5.27c and Figure 5.27d. As in the axisymmetric case, all of these figures again show reasonably good agreement between the numerical results and experimental data.

5.4 Turbulent Diffusion Flames

5.4.1 Bluff-Body Burner

A reacting flow for the same bluff-body burner configuration, discussed earlier in Section 5.3.2, was also studied. In this case a methane gaseous fuel jet was injected at the base of the bluff-body with bulk velocity of $104\,\mathrm{m/s}$ at $300\,\mathrm{K}$. The bulk velocity of co-flow air was $30\,\mathrm{m/s}$. The Reynolds and Mach number of the methane jet are $\mathrm{Re} = 315\,000$

(a) Velocity contour

(b) Velocity profile along the axis

(c) Radial velocity profile at $x/D_b = 0.6$

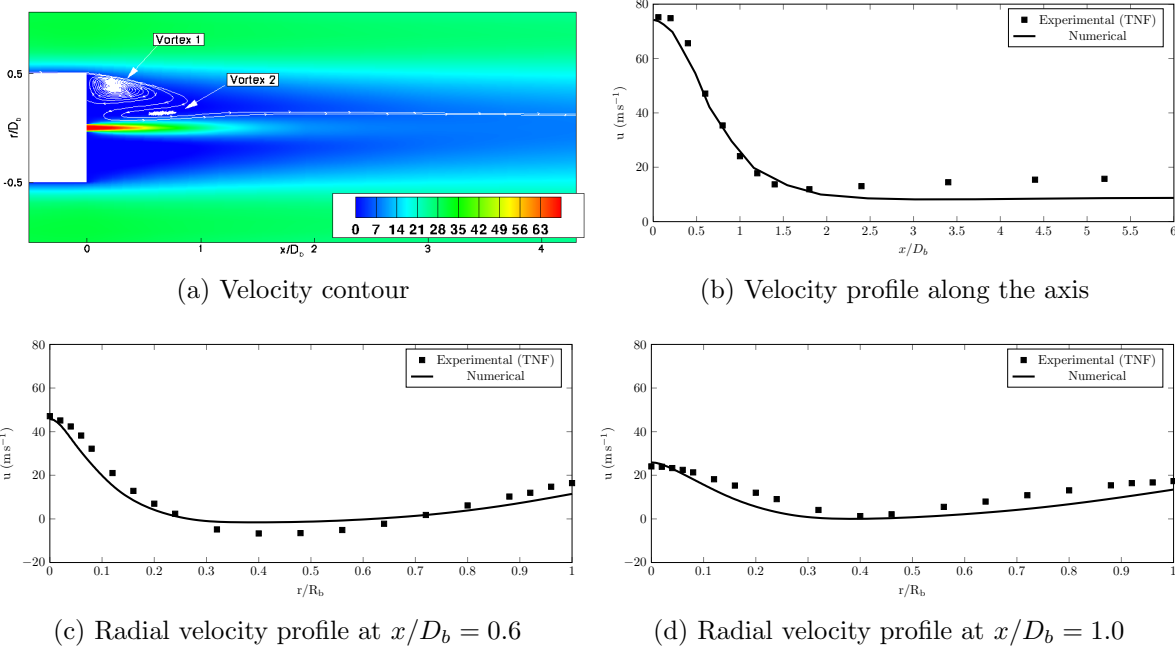(d) Radial velocity profile at $x/D_b = 1.0$
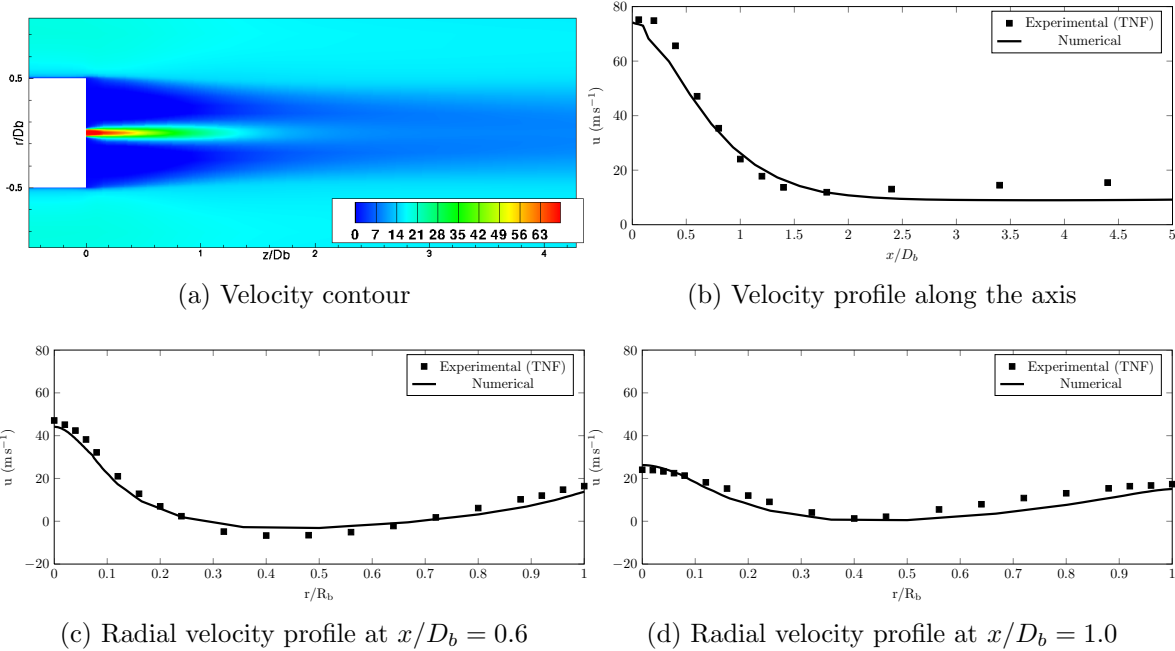
Figure 5.27: Comparison of predicted and measured velocity profiles of mean axial velocity at various locations downstream from the base of the bluff-body burner for non-reacting flow with air jet using the proposed numerical scheme for three-dimensional flow geometries.

and Ma = 0.24.

5.4.1.1   Two-Dimensional Axisymmetric Results

The grid used for simulating the reacting flow using the numerical scheme for two-dimensional axisymmetric flows is shown in Figure 5.28a. An initial coarse grid consisted of 28 blocks, each with 16×16 cells, for a total of 7168 cells. After obtaining an approximate solution on this initial mesh, the grid was refined twice using the AMR scheme to arrive at two successively refined grids having the following resolutions: 46 blocks (11 776 cells) and 59 blocks (15 104 cells) respectively. The sequence of these adaptively refined mesh is shown in Figure 5.28a. Inspection of the numerical solutions on these three grids, as show in Figure 5.28b, revealed that a grid converged solution was obtained on the finest mesh after two levels of AMR and this mesh was used when making comparisons of the predicted results for this flame.

The PCM-FPI table used for these results has a dimension of $(121 \times 25 \times 121 \times 25)$. Vervisch et al. [74] mention that at least 100 points are necessary of both f and c to
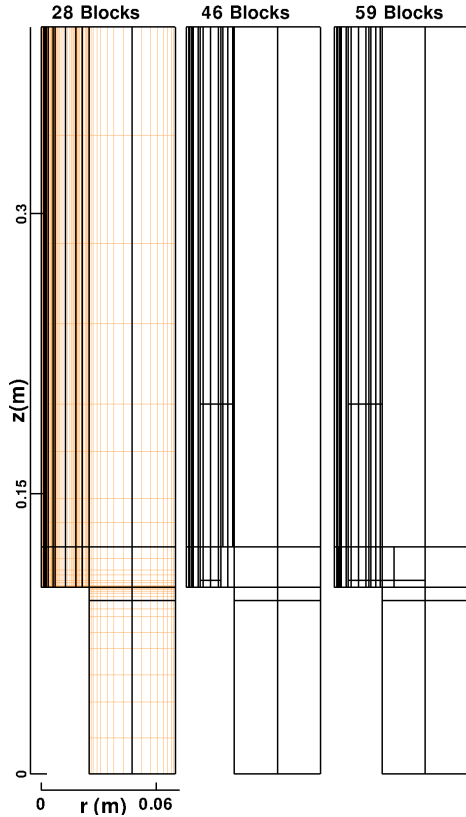
(a) The two-dimensional grids used for bluff-body reacting flow at different levels of AMR refinement. Temperature gradient was chosen as the refinement criterion.
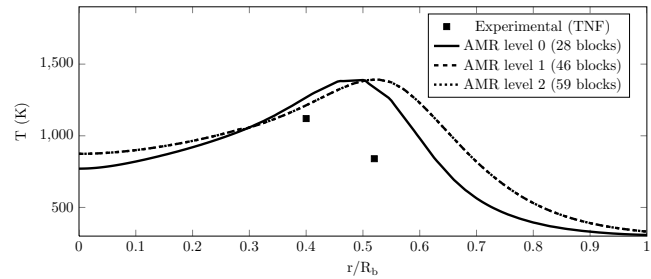
(b) Radial profile of temperature at $x/D_b = 1.92$ downstream from the base of the bluff-burner burner after different levels of AMR refinement

Figure 5.28: AMR grid refinement results for two-dimensional grid for the reacting flow. Grid converged solution was obtained after two levels of AMR.

	Experimental	EDM	PCM-FPI Approach 1	PCM-FPI Approach 3
Maximum predicted temperature	1200 K	1659 K	1357 K	1359 K
CPU time/iteration (normalized)	N/A	0.002 55 (1)	0.006 12 (2.4)	0.006 37 (2.5)

Table 5.5: Performance comparison of different numerical methods, using the proposed numerical scheme for two-dimensional axisymmetric flow geometries, for bluff-body burner methane-air turbulent reacting flow.

integrate it with the β-PDF. A lesser number of points was found to lead to inaccurate integrations. The number of segregation points were chosen based on the the previous studies by Hernàndez-Pérez et al. [19] and Domingo et al. [156].

(a) Predicted temperature contour

(b) Predicted CO_2 contour

(c) Predicted H_2 contour

(d) Predicted OH contour
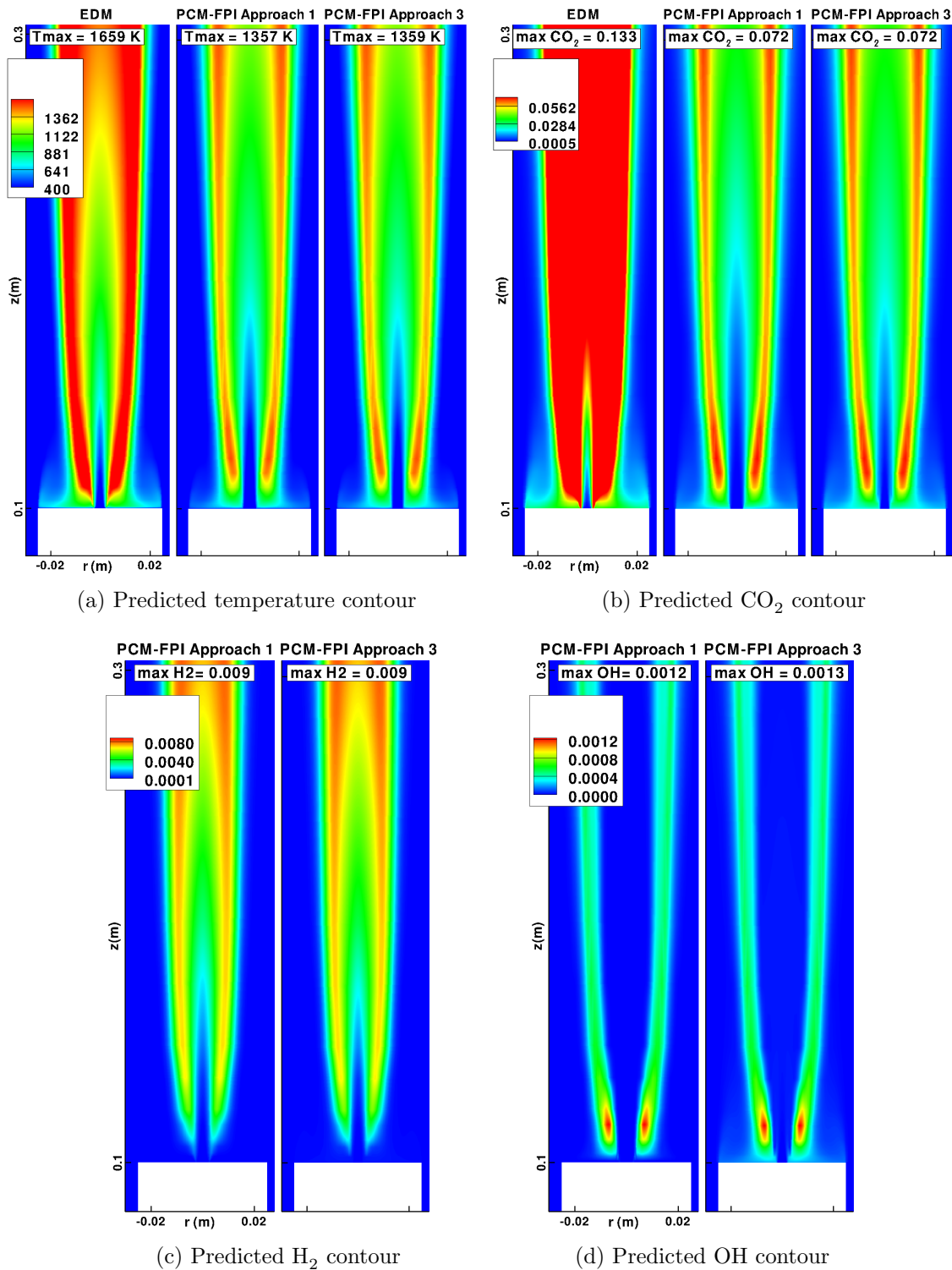
Figure 5.29: The solution contours predicted by different numerical schemes for the Sydney bluff-body burner for a reacting flow with methane jet using the proposed numerical scheme for two-dimensional axisymmetric flow geometries.
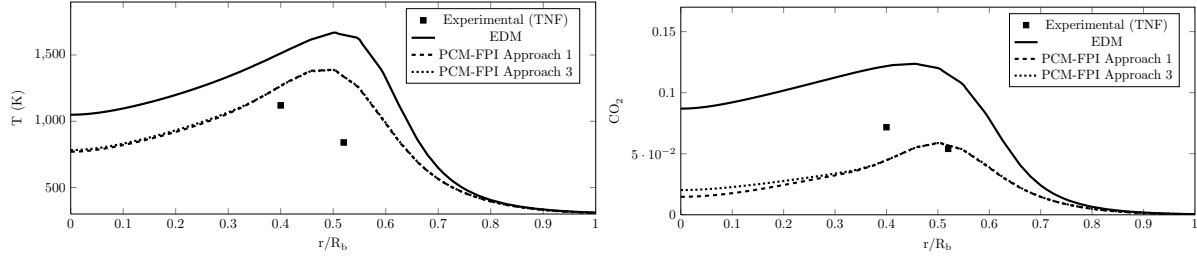
(a) Predicted radial profile of mean temperature (b) Predicted radial profile of mass fraction of CO_2

Figure 5.30: Comparison of predicted profiles and measured data at $x/D_b = 1.92$ downstream from the base of the bluff-burner burner using the proposed numerical scheme for two-dimensional axisymmetric flow geometries for reacting flow with methane jet.

The temperature contours predicted by the proposed solution algorithm with the EDM one-step mechanism are compared with the solutions obtained using both the PCM-FPI approaches in Figure 5.29a for the methane-air bluff-body burner. All three of the schemes predict similar temperature distributions, however the maximum temperature predicted by PCM-FPI schemes are around 300 K less than the value provided by EDM. This is expected as the EDM essentially assumes that any fuel and air that mixes is burnt and does not account for any endothermic reactions, while the PCM-FPI scheme does not assume that the combustion is complete and accounts for endothermic reactions via the tabulated chemistry. Moreover, significant differences can be seen in the distribution of major species contours predicted by both the approaches. The maximum mass fraction of CO_2 predicted by the EDM is almost twice than that predicted by the PCM-FPI. This can be attributed to the fact that the EDM reaction mechanism does not involve any pathways or reactions for CO_2 consumption. Also, in the EDM scheme, much higher concentrations of CO_2 can be found in the central part of the flame compared to the PCM-FPI results, for which the highest concentrations of carbon dioxide lie only along the outer surface of the diffusion flame.

The predicted mean temperature and CO_2 mass fraction radial profiles at $x/D_b = 1.92$ downstream from the base of the burner are compared the to the available experimental data in Figure 5.30. Both figures show that the PCM-FPI results are in much better agreement with the experimental data in comparison to the EDM results. The maximum temperatures predicted by each scheme are shown in Table 5.5. These maximum temperatures predicted by the PCM-FPI approaches are also in better agreement with the experimental results than those of the EDM.

Mesh level	0	1	2	3	4
N_{blocks}	229	565	1265	1965	3589
N_{cells}	117 248	289 280	647 680	1 006 080	1 837 568
η	0.000	0.692	0.914	0.983	0.996

Table 5.6: Mesh-refinement statistics for the multi-block hexahedral mesh for the bluff-body burner turbulent diffusion flame.

The relative cost of each scheme has also been compared in Table 5.5. As expected, the PCM-FPI schemes are computationally more expensive than the EDM scheme, but the difference is only by a factor of about 2.5. This result is quite significant for it shows that predictions for minor species like H_2, OH, C_2H_2 etc., as shown in Figure 5.29, can be readily obtained using the tabulation method for less than three times the cost of the EDM. Such accurate predictions are obviously not possible with a simple EDM approach.

5.4.1.2 Fully Three-Dimensional Results

The Sydney bluff-body burner was also simulated using the proposed numerical scheme for three-dimensional flow geometries. The flow-field calculations were carried out on four adaptively refined grids, each consisting of a number of $8 \times 8 \times 8$ cell blocks: 229 blocks (117 248 cells); 565 blocks (289 280 cells); 1265 blocks (647 680 cells); 1965 blocks (1 006 080 cells); and 3589 blocks (1 837 568 cells). These grids at different AMR levels for the reacting flow are shown in Figure 5.31a. Density gradient was chosen as the refinement criterion, with a threshold for refinement as 0.5 and the threshold for coarsening as 1.0. Block refinement can be seen along the flame front where the maximum density gradient exists. Figure 5.31 strongly demonstrates the capability of the AMR algorithm to refine the grid in regions of maximum physical activity. Figure 5.31b shows the radial profile of temperature at $x/D_b = 1.92$ downstream from the base of the burner for different levels of AMR. It can be seen that after two levels of AMR, a grid converged solution was obtained. An AMR refinement efficiency of 0.996 was obtained after four levels of refinement.

Figure 5.32 compares the predicted distribution of temperature and some species in the solution domain. The maximum temperature predicted by the PCM-FPI approach is almost 500 K lower than the temperature predicted by the EDM scheme. It is also closer to the recorded maximum experimental data of 1200 K. Figure 5.33 shows the solution
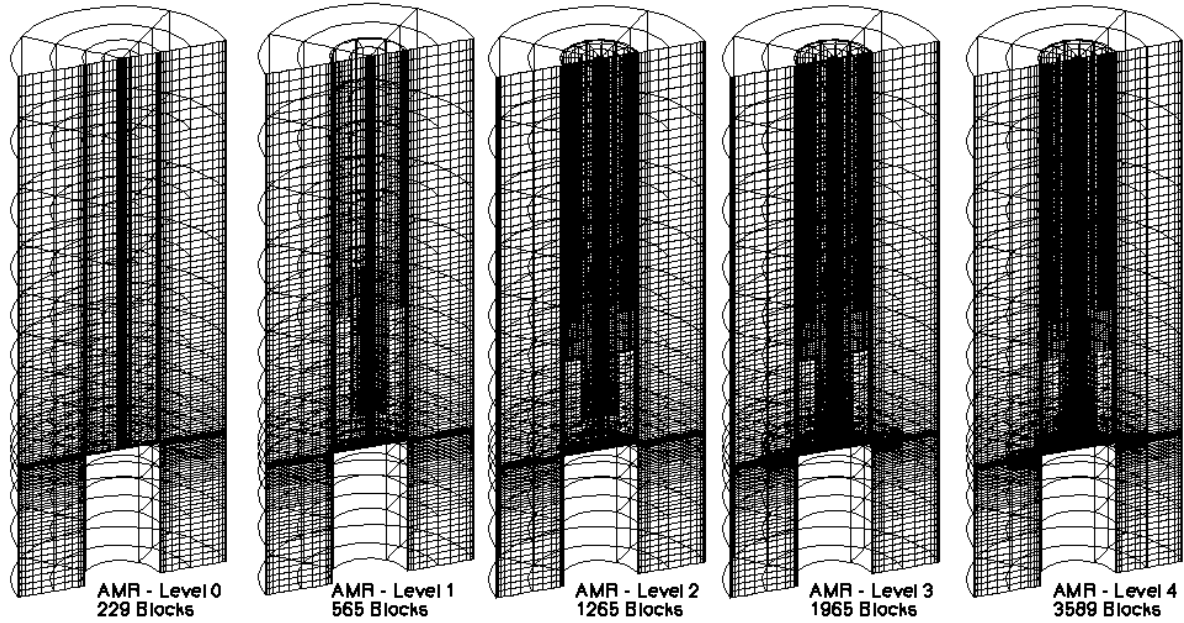
(a) The sliced three-dimensional grid after different levels of AMR refinement. Density gradient was chosen as the refinement criterion. Refinement can be seen at along the flame front where the maximum gradient exits. The grid shown is for the PCM-FPI Approach 1.
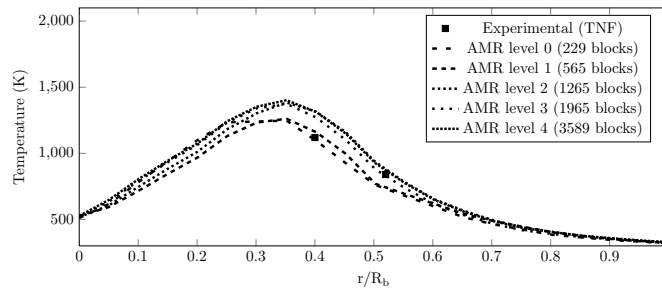
(b) Predicted temperature profiles at $x/D_b = 1.92$ downstream from the base of the bluff-burner burner after different levels of AMR refinement

Figure 5.31: AMR results using the proposed numerical scheme for fully three-dimensional flow geometries for bluff-body burner methane-air reacting flow.

profiles obtained using the different numerical approaches to treat chemistry. Figure 5.33a shows that the temperature profiles are in far better agreement with the experimental data, in comparison to the EDM result. In Figure 5.33b the EDM passes through the experimental points considerably closely than the PCM-FPI lines do. However, the variation between the maximum CO_2 predicted by EDM and that of the experimental data is much higher in comparison to the PCM-FPI results. Apart from this, the PCM-

(a) Temperature contour

(b) CO_2 contour

(c) H_2 contour
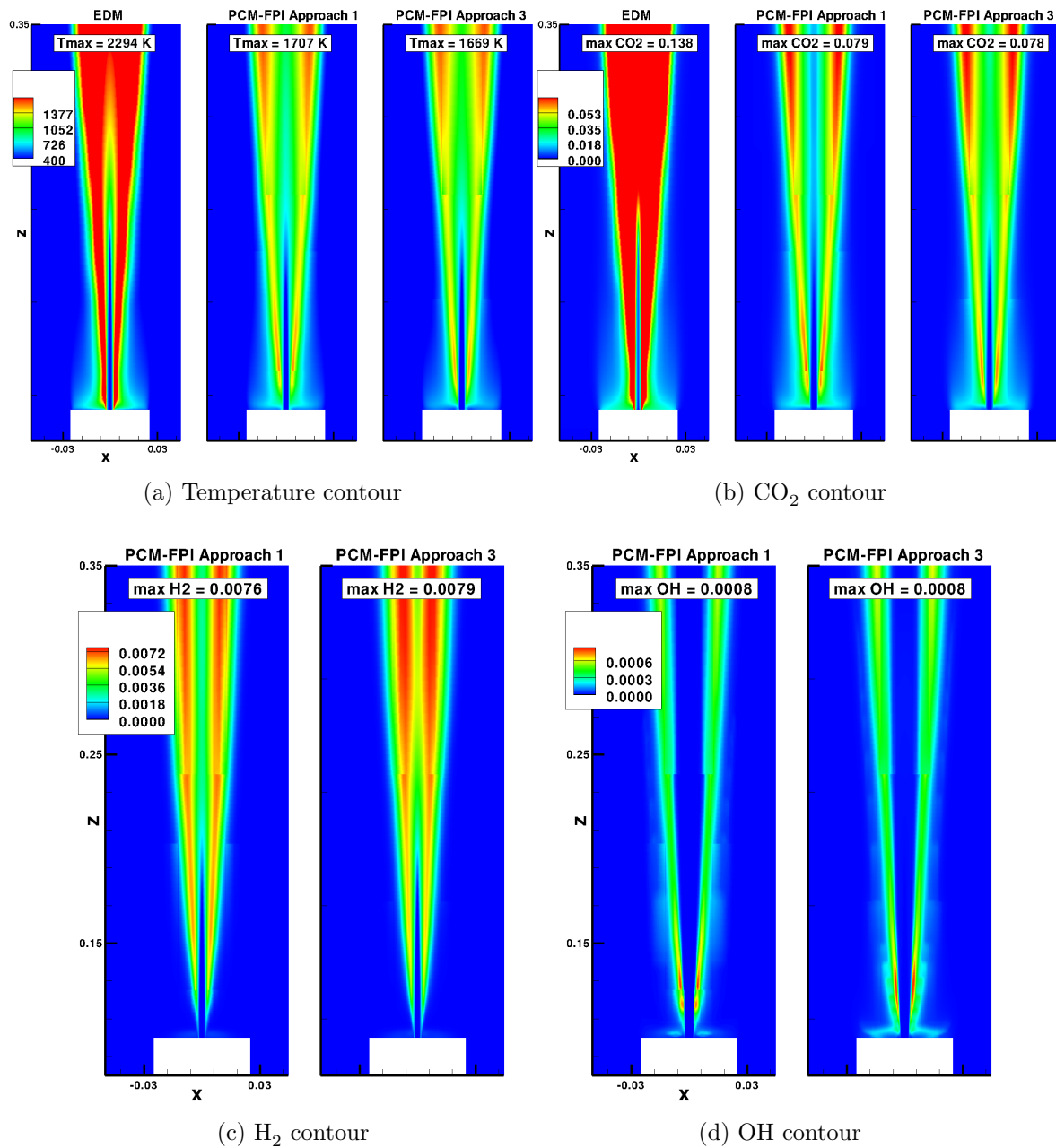
(d) OH contour

Figure 5.32: The solution contours predicted for different chemical kinetic mechanisms, using the present numerical scheme, for methane-air diffusion flame.

FPI approach also gives predictions for the minor species like OH, CO, and, C_2H_2, as shown in Figure 5.32c and Figure 5.32d, which is not possible to obtain using the EDM approach.

Table 5.7 compares the computational cost of each chemical-kinetic scheme. The cost of the PCM-FPI scheme is only marginally higher than the EDM methods. This

(a) Radial profile of temperature

(b) Radial profile of CO_2 mass fraction
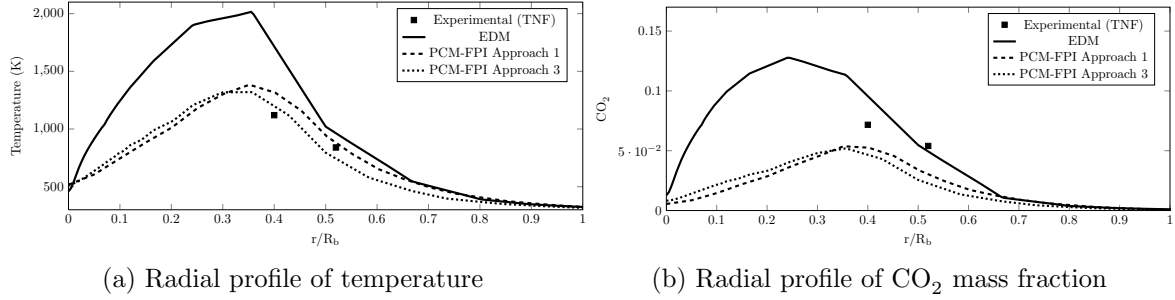
Figure 5.33: Comparison of predicted profiles and measured data at $x/D_b = 1.92$ downstream from the base of the bluff-burner burner using the numerical scheme for three-dimensional flow geometries for reacting flow with methane jet.

EDM	PCM-FPI Approach 1	PCM-FPI Approach 3
4.4858 (1)	4.593 (1.024)	4.666 (1.04)

Table 5.7: The CPU time per iteration for different chemical kinetic mechanisms, using the numerical scheme for three-dimensional flow geometries, for bluff-body burner methane-air reacting flow - the figures in bracket show the normalized value.

result is very encouraging as it shows that by using the PCM-FPI approach detail-chemistry results can be obtained without much computational overhead in comparison to the EDM scheme. It is also significantly different in comparison to the numerical scheme for two-dimensional flow geometries, where the PCM-FPI approach was around 2.5 times more expensive. This can be attributed to the fact that the computational cost involved in reconstruction for the three-dimensional geometry is lot more than the two-dimensional geometry. The additional computational cost associated with the PCM-FPI Approaches is comparable to the computational cost involved for two-dimensional FVM, but is insignificant compared to the three-dimensional FVM. Hence, when used with the numerical scheme for two-dimensional geometry, it affects the cost significantly, while when used with the numerical scheme for three-dimensional geometry, the computational cost remains practically unaffected.

It is noted that the temperature is somewhat over-predicted by the proposed parallel AMR numerical scheme for the reacting bluff-body burner flow in comparison to the reported experimental data. This may be because the effects of radiation and soot formation are not included in the calculations. However, Merci et al. [227, 228] argue that, since the bluff-body flame is unconfined and very little soot is formed, radiation

effects should be relatively small. Some other reasons for the differences may be related to the time averaging of the solution and/or the use of β-distribution for averaging the tabulated quantities. It could be of interest to investigate the dependence of the temperature predictions on the presumed PDF by using other averaging procedures in conjunction with the tabulated chemistry.

5.5   Parallel performance

The parallel performance of the proposed algorithm was assessed for strong scaling as part of this research. Strong scaling is a measure of the ability to demonstrate a proportionate increase in parallel speedup with more processors. For a strong scaling test, the problem size is generally held fixed while the number of processors used to perform the computation is varied. Scaling is measured by the parallel speedup, S_p, and efficiency, η_p, which are then defined as

$$S_p = \frac{t_1}{t_p} \tag{5.4}$$

$$\eta_p = \frac{S_p}{p} \tag{5.5}$$

where t_p is the total wall times required to solve the problem with p processors.

Strong scaling of both PCM-FPI tabulated approaches were examined. For both approaches, the strong scaling test was carried out using a grid which consisted of 1832 grid blocks. These grids were obtained after one level of uniform AMR refinement on the initial grid of 229 blocks. The work load per processor was varied without affecting the partitioning of the mesh by changing the number of blocks assigned to each processor. As a result, only the effect of inter-processor communication on parallel efficiency was taken into account.

The resulting relationship between parallel speedup, efficiency, and number of processors is shown in Figure 5.34 for the methane-air turbulent diffusion flame Sydney bluff-body configuration. Excellent parallel performance is achieved with an efficiency of 80 % and 87 % for PCM-FPI Approach 1 and PCM-FPI Approach 3, respectively, for up to 1832 processors. These results clearly show that the proposed PCM-FPI algorithm scales extremely well within the parallel AMR solution scheme.
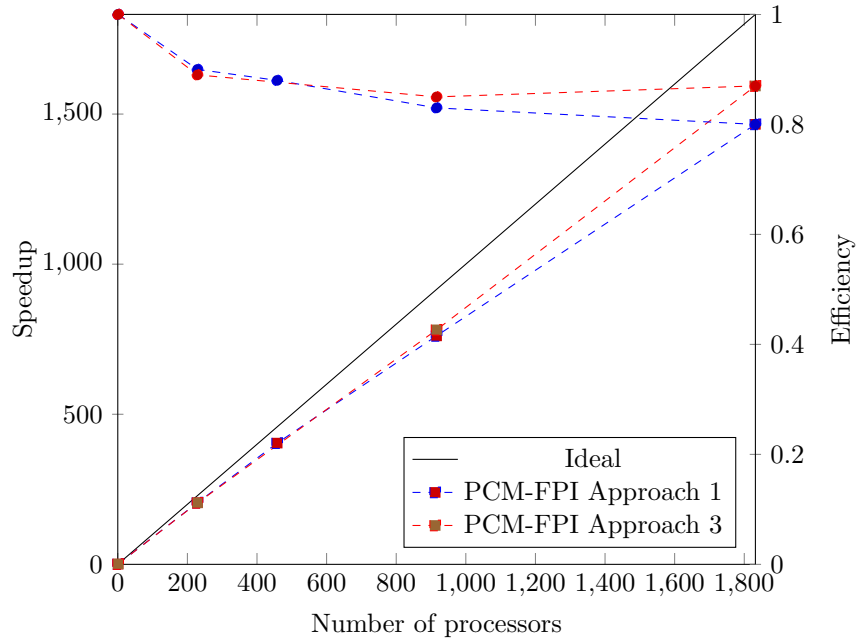
Figure 5.34: Parallel performance of the proposed solution algorithm showing the strong scaling for the PCM-FPI Approach 1 and the PCM-FPI Approach 3 for the methane-air turbulent diffusion flame simulations. Sqaure dots represent the parallel speedup and the blue dots represent the parallel efficiency.

5.6   Observations

This chapter has examined the application of the proposed PCM-FPI FANS-based parallel AMR numerical approach for simulation of turbulent diffusion flames, as discussed in the previous four chapters. The FPI scheme was first used to reproduce the detailed-chemistry results for one-dimensional laminar premixed flames. It was shown that the FPI-Approach 1 and FPI-Approach 3 are better in terms of reproducing Cantera results as compared to the FPI-Approach 2. This was attributed to the fact that discretizing the c-space in 155 points was not sufficient to capture the huge variation in reaction-rate magnitudes.

The laminar counter-flow flame was simulated using both the FPI approach and the SLFM approach and the results were compared to detailed-chemistry Cantera results and experimental data. It was found that the FPI schemes performed as well as the SLFM approach in predicting the species and temperature profiles associated with laminar diffusion flames.

A laminar co-flow diffusion flame was studied and the results of FPI approach were

compared to the results obtained using direct simulation of the GRI-Mech 3.0 detailed-chemistry mechanism. Excellent agreement was seen between directly-calculated results and the PCM-FPI results. It was also found that for this flame the agreement between directly calculated results and FPI scheme was better in comparison to the SLFM approach. At the same time, it was found that the tabulated approaches were almost 11 times faster than the detailed-chemistry approach, which showed that FPI is capable of reproducing detailed-chemistry results at a significantly lower computational cost. The laminar co-flow diffusion flame and the counter-flow flame results provided a strong justification for the use of the FPI methods, based on premixed flamelets, in the numerical simulation of more general diffusion flames. Also, for each of these flames, the detailed-chemistry tabulated-approach results were in far better agreement with experimental and direct calculation results as compared to simplified one-step chemical-kinetic mechanism results.

As a final validation study, a methane-air turbulent diffusion flame using the Sydney bluff-body burner experimental setup was simulated using the proposed PCM-FPI algorithm. The results were compared to the simplified Eddy Dissipation Model (EDM). Much better agreement was obtained between PCM-FPI and experimental results in comparison to EDM. This trend was observed for the numerical schemes developed for both two-dimensional and three-dimensional flow geometries.

The AMR capability of refining the grid along the area of maximum physical activity was also shown for every flame successfully. For three-dimensional flow-geometries, high refinement efficiency, of the order of 0.99, was obtained. A strong-scaling test was done on the PCM-FPI approaches to test the parallel performance of the present numerical scheme. Excellent parallel performance was achieved with an efficiency of over 80% for 1832 processors for both the PCM-FPI Approach 1 and 3.

Apart from the above mentioned cases, results were also shown for several non-reacting turbulent flows, and good agreement was seen between experimentally measured data and the predicted profiles obtained using the proposed numerical scheme.

6

Conclusions, Contributions and Recommendations

This chapter provides a summary of the results presented in Chapter 2 through Chapter 5 and reviews the major contributions of this thesis. These summaries can be found in the following section. In addition, a list of recommendations is provided for future work in Section 6.2 and some concluding remarks in Section 6.3.

6.1 Conclusions and Contributions

6.1.1 Table generation/coupling algorithm for PCM-FPI

In this thesis, a table-generation algorithm for PCM-FPI tables was developed and implemented within a density-based compressibility solver, that can be used to sort through available detailed-chemistry solutions and arrange them in easily accessible format to the flow-solver and at the same time be extremely flexible in terms of size, structure, and fuel-oxidizer compositions it can handle. It should be noted that although density-based compressible flow solver, the full effects of compressibility and pressure variations have not been studied as part of this thesis. This has been reserved for future follow-on research.

The FPI table-generation algorithm uses a β-PDF to integrate laminar flamelet results to obtain mean reactive flow solutions which can be used for turbulent flames and thereby account for the effects of strong turbulence-chemistry interactions. Even though only β-PDFs has been considered here, the present implementation allows for other PDFs to be considered without much additional effort in the table-generation process. The accuracy and the size of the tables are of immense importance when dealing with turbulent non-premixed flames. Various coupling methods, as discussed before in Chapter 3, have

been used and examined in an attempt to minimize the table size. The mass fraction tabulation approach, referred to as FPI-Approach 1 and FPI-Approach 3 in this text, gave the best results for the methane-air flames considered here.

Even though not directly related to the thesis objective, a table-generation and coupling algorithm was also developed for the SLFM approach. The SLFM approach is a very popular tabulated-chemistry approach for diffusion flames and provided a good basis for comparing and evaluating the performance of the PCM-FPI methodology as described previously.

The effect of table size on the accuracy of predicted results has been examined. For FPI approaches, surprisingly coarse tables can be used successfully reproduce the species concentrations of major species; however, more refined tables are needed to predict the minor species accurately. For the SLFM approach, it was found that for methane-air flames considered herein, the results are not greatly affected by the number of tabulated values used for the scalar dissipation rate.

The effect of progress variable Schmidt number, Sc_{Y_c}, on the solution was also studied. It was found that the value for Sc_{Y_c} does not greatly affect the methane-air flames considered herein. The results strongly suggest that the errors in the predictions for the progress variable compared to directly calculated results is mostly affected by the treatment for the reaction rates (based on premixed laminar flamelets) in the tabulated approach, and not by modelling of the diffusion process. Hence, in the present work a constant value of Sc_{Y_c} was used.

6.1.2   Extension of PCM-FPI to Non-Premixed Flames

The primary focus of this research work has been the evaluation of the extension of the FPI algorithm for diffusion flames. In the present work, a new approximation procedure has been developed for dealing with flow-conditions outside the flammability limits of premixed flames. This new algorithm is partially based on the previous works but is still novel in comparison to other existing methods. The proposed approach has been discussed in detail in Section 3.5.2.

The validity of PCM-FPI method is well established by the different diffusion-flames that have been studied in this thesis. The proposed algorithm is almost 11 times as fast as solving the same problem using full detailed-chemistry without tabulation for laminar flames in two-dimensions. Good agreement was demonstrated, both qualitatively and

quantitatively, when comparing the directly-calculated results and FPI-based solutions.

An original contribution of this thesis included the head-to-head comparisons made between the SLFM approach and the FPI approach. Both the tabulated-chemistry schemes were implemented in the same flow-solver, which allowed all of the solution parameters to remain exactly the same except for the treatment of the chemical kinetics which was varied. It was found that both the FPI and the SLFM approaches can be successfully applied to the laminar diffusion flames and reproduce the effects of detail chemistry and predict major and minor species concentrations at a much lower computational cost.

The opposed-jet flame study results strongly demonstrate that FPI approaches, based on tabulated solutions of premixed flamelets, are capable of predicting diffusion flame structure as well, if not better, than flamelet approaches, which are based on tabulated solutions of steady diffusion flames. It was also found that SLFM approaches over-predict the concentrations of minor species in most regions of the co-flow flame. Similar findings have been reported in earlier studies of the SLFM approach. Also, the predicted flame height and lift-off-height of the FPI approaches are much closer to the directly-calculated chemistry results than those of the SLFM. The FPI approaches were found to be able to deal more readily with regions of high scalar dissipation rate for the mixture fraction.

These findings coupled with the ability of FPI approaches to handle both premixed and non-premixed flames, make the FPI tabulated approaches very appealing compared to SLFM approaches. While the concept of FPI tabulation is essentially an *ansatz* (i.e., an educated guess that is later verified by its results), the findings of the present study would certainly lend strong support for its use in the numerical prediction of combustion processes.

6.1.3 Modelling the Effects of Turbulence on Detailed Chemistry

A PCM-FPI tabulation approach for detailed-chemistry has been implemented for turbulent diffusion flames using a FANS-based turbulence model. The two-equation k-ω turbulence model has been used with an automatic-wall-treatment formulation for near-wall-treatment of turbulence quantities. Numerical predictions for fully-developed turbulent pipe flow and non-reacting bluff-body co-flow case were considered. The predicted results for both the non-reacting cases show good agreement with the measured experi-

mental data and provide partial verification of the proposed fully-coupled finite-volume scheme.

Predicted results for a methane-air flame in a bluff-body burner using the PCM-FPI have also been compared to results obtained with a simplified one-step mechanism/EDM approach. As anticipated, significant improvements are observed in the predictions of flame properties using the PCM-FPI approach. The predicted temperature and species profiles using the PCM-FPI approach are in much better agreement with experimental results in comparison to the EDM predictions. Both PCM-FPI approaches yield almost identical results for temperature and major species mass fractions. The relative computational costs involved with each numerical schemes is also compared. Even though PCM-FPI schemes tend to be more expensive than the simplified EDM approach for two-dimensional geometries as would be expected, surprisingly, the extra cost is not significantly higher (only slightly more than a factor of two). For three-dimensional geometries the cost involved in PCM-FPI is almost the same as for the simplified EDM. Comparing the improvement in results for the added computational costs involved, the PCM-FPI approach definitely appears to be a promising method for dealing with a range of turbulent reactive flows. The proposed finite-volume scheme has also been shown to be very effective in providing accurate and robust solutions for the reactive flow case.

6.1.4   Parallel AMR Implementation

A major original contribution of this thesis is the implementation of the FANS-based PCM-FPI solution methodology for turbulent diffusion flames in a parallel AMR solution framework. The parallel performance of the PCM-FPI scheme was investigated on a large parallel distributed-memory multi-processor cluster. It was found that the algorithm scales extremely well with an efficiency of over 80% for up to 1850 processors.

The AMR capability of the algorithm was also examined for the three-dimensional grid used for the Sydney bluff-body burner. Maximum grid refinement was seen in regions with highest value of temperature gradient, which demonstrated the solution-adaptivity of the AMR scheme. A refinement efficiency of 0.996 was achieved after four levels of refinement. This implies that just by using 0.4 % of the number of grid points, as would be needed otherwise if a uniform grid was used, a grid converged solution was obtained.

6.1.5 Summary of Contributions

To summarize, using the proposed solution methodology, the computational time savings have been achieved in three major ways:

1. Using the PCM-FPI methodology, detailed-chemistry effects were modelled on turbulent diffusion flames on fully three-dimensional grids at practically the same cost as the simplified EDM one-step chemistry.

2. The AMR capability of the proposed numerical scheme enables us to get grid converged solution by only using 0.4% of the number of grid points, if instead an uniform grid was used.

3. The parallel scheme helps to distribute the work over a number of processors. In the present numerical scheme, an increase in computational speed by a factor of around 1600 times was obtained by using 1832 processors. Even though the parallel speed-up does not increase ideally with the increase in number of processors, this increase in speed is significant, and shows that computation speed can be increased further by increasing the number of processors.

6.2 Recommendations for Future Research

The following is a list of recommendations for future research.

Implicit Time-Marching Schemes: The proposed solution method considered in this thesis uses an explicit time-marching scheme which will obviously be impractical for more complex three-dimensional geometries. It is recommended that implicit Newton-Krylov-Schwarz time marching methods be investigated for PCM-FPI methods, as they can help getting converged solution much faster and at the same time they are well-suited to be implemented with the block-based AMR scheme [229–231].

PCM-FPI Specializations: Recently, a number of works have reported the extension of PCM-FPI to more specialized flame configurations, such as auto-ignition, partially-premixed flames [159, 232], lifted-flames [80] etc. For dealing with more practical combustion flow-configurations, these modifications should be considered and implemented.

FANS to LES: The present numerical scheme adopts a FANS-based equations for modelling turbulence. The next obvious step will be to consider the extension to LES for turbulence modelling of diffusion flames. By their very nature, LES simulations give more detailed description of the eddy-structure of the turbulent flames, as shown in the recent thesis research for premixed flames by Perez [233], and have the potential to provide more accurate results for practical combusting flow geometries.

Higher Order Reconstruction: Further improvements to the the current solution framework is possible through the use of high-order finite-volume schemes, which has been proposed and evaluated recently by Ivan and Groth [212, 234–236].

6.3 Epilogue

The future for energy demands most probably lies in renewable and nuclear sources of energy, but by the time it happens, it is important to conserve the existing resources and preserve the environment to the greatest extent possible. With increasing pressure on the available natural resources and fuels, the demand for more efficient and environmentally friendly burners is constantly on a rise. Using computational methods for designing engines for transportation systems and power generation can be really useful, as it provides information which is not possible by any other means of investigation.

The present work addresses one of the most important topics in present-day combustion research - modelling detailed-chemistry effects in turbulent combustion. Even though the present results are very fundamental, they look promising and obviously need further extension to be applied in more practical real-life burners. However, the present approach does shows significant reductions in terms of computational cost and provides a tool for studying and understanding certain aspects of turbulent diffusion flames, which were computationally too demanding before. Hopefully, with the addition of more sophisticated turbulence models and other improvements suggested in the previous section, this numerical tool will be able to capture combustion processes effectively in practical devices.

APPENDICES

$\mathcal{A}$
Governing Equation Systems

A.1 Two-Dimensional Axisymmetric Formulation

The divergence form of Equation (4.7) is obtained by applying Gauss's theorem to the flux integral, leading to

$$\frac{\partial \mathbf{U}}{\partial t} + \nabla \cdot \vec{\mathbf{F}} = \mathbf{S} \tag{A.1}$$

where $\mathbf{U}$ the cell-averaged solution vector, $\mathbf{F}$ is the flux dyad and $\mathbf{S}$ is the source term vector. The complete set of equations is reformulated in conservation form for two dimensional axisymmetric coordinate frames as

$$\frac{\partial \mathbf{U}}{\partial t} + \frac{\partial}{\partial r}(\mathbf{F}_\mathrm{I} - \mathbf{F}_\mathrm{V}) + \frac{\partial}{\partial z}(\mathbf{G}_\mathrm{I} - \mathbf{G}_\mathrm{V}) = -\frac{1}{r}(\mathbf{S}_\mathrm{aI} - \mathbf{S}_\mathrm{aV}) + \mathbf{S}_\mathrm{t} + \mathbf{S}_\mathrm{p} + \mathbf{S}_\mathrm{c} \tag{A.2}$$

where r and z denote the radial and axial coordinates, $\mathbf{F}_\mathrm{I}$ and $\mathbf{F}_\mathrm{V}$ the inviscid and viscous flux vectors in radial direction, $\mathbf{G}_\mathrm{I}$ and $\mathbf{G}_\mathrm{V}$ the inviscid and viscous flux vectors in axial direction, $\mathbf{S}_\mathrm{aI}$, $\mathbf{S}_\mathrm{aV}$ are the inviscid and viscous source terms due to the axisymmetric co-ordinates, and $\mathbf{S}_\mathrm{t}$, $\mathbf{S}_\mathrm{p}$ and $\mathbf{S}_\mathrm{c}$ are the source terms due to turbulence, transport equations for PCM-FPI scalars and chemical reactions, respectively. Each of these terms are given below.

$$\mathbf{U} = \left[\; \overline{\rho},\; \overline{\rho}\widetilde{v}_r,\; \overline{\rho}\widetilde{v}_z,\; \overline{\rho}\widetilde{e},\; \overline{\rho}k,\; \overline{\rho}\omega,\; \overline{\rho}\widetilde{f},\; \overline{\rho}f_v,\; \overline{\rho}\widetilde{Y}_c,\; \overline{\rho}Y_{cv},\; \overline{\rho}\widetilde{Y}_1,\; \ldots, \overline{\rho}\widetilde{Y}_n \;\right]^\mathrm{T} \tag{A.3}$$

$$
\mathbf{F}_{\mathrm{I}} =
\begin{bmatrix}
\overline{\rho}\widetilde{v}_r \\
\overline{\rho}\widetilde{v}_r^2 + \bar{p} \\
\overline{\rho}\widetilde{v}_r\widetilde{v}_z \\
(\overline{\rho}\widetilde{e} + \bar{p})\widetilde{v}_r \\
\overline{\rho}\widetilde{v}_r k \\
\overline{\rho}\widetilde{v}_r \omega \\
\overline{\rho}\widetilde{v}_r \widetilde{f} \\
\overline{\rho}\widetilde{v}_r f_v \\
\overline{\rho}\widetilde{v}_r \widetilde{Y}_c \\
\overline{\rho}\widetilde{v}_r Y_{cv} \\
\overline{\rho}\widetilde{v}_r \widetilde{Y}_1 \\
\vdots \\
\overline{\rho}\widetilde{v}_r \widetilde{Y}_n
\end{bmatrix},
\qquad
\mathbf{F}_{\mathrm{V}} =
\begin{bmatrix}
0 \\
\overline{\tau}_{rr} + \lambda_{rr} \\
\overline{\tau}_{rz} + \lambda_{rz} \\
-q_r - q_{tr} + (\mu + \mu_t\sigma^*)\frac{\partial k}{\partial x} + v_r(\overline{\tau}_{rr} + \lambda_{rr}) + v_z(\overline{\tau}_{rz} + \lambda_{rz}) \\
(\mu + \mu_t\sigma^*)\frac{\partial k}{\partial r} \\
(\mu + \mu_t\sigma)\frac{\partial \omega}{\partial r} \\
\overline{\rho}(\mathcal{D}_f + \mathcal{D}_t)\frac{\partial \widetilde{f}}{\partial r} \\
\overline{\rho}(\mathcal{D}_f + \mathcal{D}_t)\frac{\partial f_v}{\partial r} \\
\overline{\rho}(\mathcal{D}_{Y_c} + \mathcal{D}_t)\frac{\partial \widetilde{Y}_c}{\partial r} \\
\overline{\rho}(\mathcal{D}_{Y_c} + \mathcal{D}_t)\frac{\partial Y_{cv}}{\partial r} \\
-\mathcal{J}_r^1 - \mathcal{J}_{tr}^1 \\
\vdots \\
-\mathcal{J}_r^n - \mathcal{J}_{tr}^n
\end{bmatrix}
\tag{A.4}
$$

$$
\mathbf{G}_{\mathrm{I}} =
\begin{bmatrix}
\overline{\rho}\widetilde{v}_z \\
\overline{\rho}\widetilde{v}_z\widetilde{v}_z \\
\overline{\rho}\widetilde{v}_z^2 + \bar{p} \\
(\overline{\rho}\widetilde{e} + \bar{p})\widetilde{v}_z \\
\overline{\rho}\widetilde{v}_z k \\
\overline{\rho}\widetilde{v}_z \omega \\
\overline{\rho}\widetilde{v}_z \widetilde{f} \\
\overline{\rho}\widetilde{v}_z f_v \\
\overline{\rho}\widetilde{v}_z \widetilde{Y}_c \\
\overline{\rho}\widetilde{v}_z Y_{cv} \\
\overline{\rho}\widetilde{v}_z \widetilde{Y}_1 \\
\vdots \\
\overline{\rho}\widetilde{v}_z \widetilde{Y}_n
\end{bmatrix},
\qquad
\mathbf{G}_{\mathrm{V}} =
\begin{bmatrix}
0 \\
\overline{\tau}_{zr} + \lambda_{zr} \\
\overline{\tau}_{zz} + \lambda_{zz} \\
-q_z - q_{tz} + (\mu + \mu_t\sigma^*)\frac{\partial k}{\partial z} + v_r(\overline{\tau}_{zr} + \lambda_{zr}) + v_z(\overline{\tau}_{zz} + \lambda_{zz}) \\
(\mu + \mu_t\sigma^*)\frac{\partial k}{\partial z} \\
(\mu + \mu_t\sigma)\frac{\partial \omega}{\partial z} \\
\overline{\rho}(\mathcal{D}_f + \mathcal{D}_t)\frac{\partial \widetilde{f}}{\partial z} \\
\overline{\rho}(\mathcal{D}_f + \mathcal{D}_t)\frac{\partial f_v}{\partial z} \\
\overline{\rho}(\mathcal{D}_{Y_c} + \mathcal{D}_t)\frac{\partial \widetilde{Y}_c}{\partial z} \\
\overline{\rho}(\mathcal{D}_{Y_c} + \mathcal{D}_t)\frac{\partial Y_{cv}}{\partial z} \\
-\mathcal{J}_z^1 - \mathcal{J}_{tz}^1 \\
\vdots \\
-\mathcal{J}_z^n - \mathcal{J}_{tz}^n
\end{bmatrix}
\tag{A.5}
$$

$$
\mathbf{S}_{\mathrm{a}} =
\begin{bmatrix}
\overline{\rho}\widetilde{v}_r \\
\overline{\rho}\widetilde{v}_r^2 \\
\overline{\rho}\widetilde{v}_r\widetilde{v}_z \\
(\overline{\rho}\widetilde{e} + \overline{p})\widetilde{v}_r \\
\overline{\rho}\widetilde{v}_r k \\
\overline{\rho}\widetilde{v}_r \omega \\
\overline{\rho}\widetilde{v}_r \widetilde{f} \\
\overline{\rho}\widetilde{v}_r f_v \\
\overline{\rho}\widetilde{v}_r \widetilde{Y}_c \\
\overline{\rho}\widetilde{v}_r Y_{cv} \\
\overline{\rho}\widetilde{v}_r \widetilde{Y}_1 \\
\vdots \\
\overline{\rho}\widetilde{v}_r \widetilde{Y}_n
\end{bmatrix}
, \qquad
\mathbf{S}_{\mathrm{aV}} =
\begin{bmatrix}
0 \\
(\overline{\tau}_{rr} + \lambda_{rr}) - (\overline{\tau}_{\theta\theta} + \lambda_{\theta\theta}) \\
(\overline{\tau}_{rz} + \lambda_{rz}) \\
-q_r - q_{tr} + (\mu + \mu_t\sigma^*)\frac{\partial k}{\partial r} + \mathcal{W} \\
(\mu + \mu_t\sigma^*)\frac{\partial k}{\partial r} \\
(\mu + \mu_t\sigma)\frac{\partial \omega}{\partial r} \\
\overline{\rho}(\mathcal{D}_f + \mathcal{D}_t)\frac{\partial \widetilde{f}}{\partial r} \\
\overline{\rho}(\mathcal{D}_f + \mathcal{D}_t)\frac{\partial f_v}{\partial r} \\
\overline{\rho}(\mathcal{D}_{Y_c} + \mathcal{D}_t)\frac{\partial \widetilde{Y}_c}{\partial r} \\
\overline{\rho}(\mathcal{D}_{Y_c} + \mathcal{D}_t)\frac{\partial Y_{cv}}{\partial r} \\
-\mathcal{J}_r^1 - \mathcal{J}_{tr}^1 \\
\vdots \\
-\mathcal{J}_r^n - \mathcal{J}_{tr}^n
\end{bmatrix}
\tag{A.6}
$$

where $\mathcal{W} = v_r(\overline{\tau}_{rr} + \lambda_{rr}) + v_z(\overline{\tau}_{rz} + \lambda_{rz})$.

$$
\mathbf{S}_{\mathrm{t}} =
\begin{bmatrix}
0 \\
0 \\
0 \\
0 \\
\mathcal{P} - \beta^*\overline{\rho}k\omega \\
\alpha\frac{\omega}{k}\mathcal{P} - \beta\overline{\rho}\omega^2 \\
0 \\
0 \\
0 \\
0 \\
0 \\
\dots \\
0
\end{bmatrix}
, \quad
\mathbf{S}_{\mathrm{c}} =
\begin{bmatrix}
0 \\
0 \\
0 \\
0 \\
0 \\
0 \\
0 \\
0 \\
0 \\
0 \\
\overline{\rho}\dot{\overline{\omega}}_1 \\
\dots \\
\overline{\rho}\dot{\overline{\omega}}_N
\end{bmatrix}
, \quad
\mathbf{S}_{\mathrm{p}} =
\begin{bmatrix}
0 \\
0 \\
0 \\
0 \\
0 \\
0 \\
2\overline{\rho}\mathcal{D}_t\frac{\partial \widetilde{f}}{\partial x_i}\frac{\partial \widetilde{f}}{\partial x_i} - 2C_f\overline{\rho}\omega f_v \\
\overline{\rho}\dot{\widetilde{\omega}}_{Y_c} \\
2\overline{\rho}\mathcal{D}_t\frac{\partial \widetilde{Y}_c}{\partial x_i}\frac{\partial \widetilde{Y}_c}{\partial x_i} - 2C_{Y_c}\overline{\rho}\omega Y_{cv} + \\
2\overline{\rho}\left(\widetilde{Y_c\dot\omega_{Y_c}} - \widetilde{Y}_c\widetilde{\dot\omega}_{Y_c}\right) \\
0 \\
\vdots \\
0
\end{bmatrix}
\tag{A.7}
$$

with

$$
\mathcal{P} = \lambda_{rr}\frac{\partial \widetilde{v}_r}{\partial r} + \lambda_{rz}\left(\frac{\partial \widetilde{v}_r}{\partial z} + \frac{\partial \widetilde{v}_z}{\partial r}\right) + \lambda_{zz}\frac{\partial \widetilde{v}_z}{\partial z} + \lambda_{\theta\theta}\frac{\widetilde{v}_r}{r}
\tag{A.8}
$$

A.2   Three-Dimensional Formulation

For three-dimensional flows, the flux and source terms can be expanded to have the following form

$$\frac{\partial \mathbf{U}}{\partial t} + \frac{\partial}{\partial x}(\mathbf{F}_\mathrm{I} - \mathbf{F}_\mathrm{V}) + \frac{\partial}{\partial y}(\mathbf{G}_\mathrm{I} - \mathbf{G}_\mathrm{V}) + \frac{\partial}{\partial z}(\mathbf{H}_\mathrm{I} - \mathbf{H}_\mathrm{V}) = \mathbf{S}_\mathrm{t} + \mathbf{S}_\mathrm{p} + \mathbf{S}_\mathrm{c} \qquad (A.9)$$

where x, y, and z are the coordinates of the three-dimensional Cartesian frame, $\mathbf{F}_\mathrm{I}$ and $\mathbf{F}_\mathrm{V}$ are the inviscid and viscous flux vectors in the radial direction for axisymmetric flows and in the x direction for three-dimensional flows, respectively, $\mathbf{G}_\mathrm{I}$ and $\mathbf{G}_\mathrm{V}$ are the inviscid and viscous flux vectors in the axial direction for the axisymmetric system and in the y direction for the three-dimensional case, respectively, and $\mathbf{H}_\mathrm{I}$ and $\mathbf{H}_\mathrm{V}$ are the inviscid and viscous flux vectors in the z direction for three-dimensional flows, $\mathbf{S}_\mathrm{a}$ and $\mathbf{S}_\mathrm{aV}$ are the source terms associated with the axisymmetric coordinate for inviscid and viscous fluxes, respectively, and $\mathbf{S}_\mathrm{t}$, $\mathbf{S}_\mathrm{p}$ and $\mathbf{S}_\mathrm{c}$ are the source terms associated with the turbulence modelling, transport equations for PCM-FPI scalars and finite-rate chemical kinetics respectively. Each of these terms are given below

$$\mathbf{U} = \left[\ \bar{\rho},\ \bar{\rho}\widetilde{v}_x,\ \bar{\rho}\widetilde{v}_y,\ \bar{\rho}\widetilde{v}_z,\ \bar{\rho}\widetilde{e},\ \bar{\rho}k,\ \bar{\rho}\omega,\ \bar{\rho}\widetilde{f},\ \bar{\rho}f_v,\ \bar{\rho}\widetilde{Y}_c,\ \bar{\rho}Y_{cv},\ \bar{\rho}\widetilde{Y}_1,\ \ldots,\bar{\rho}\widetilde{Y}_n\ \right]^\mathrm{T} \qquad (A.10)$$

$$\mathbf{F}_\mathrm{I} = \begin{bmatrix} \overline{\rho}\widetilde{v}_x \\ \overline{\rho}\widetilde{v}_x^2 + \bar{p} \\ \overline{\rho}\widetilde{v}_x\widetilde{v}_y \\ \overline{\rho}\widetilde{v}_x\widetilde{v}_z \\ (\overline{\rho}\widetilde{e} + \bar{p})\widetilde{v}_x \\ \overline{\rho}\widetilde{v}_x k \\ \overline{\rho}\widetilde{v}_x \omega \\ \overline{\rho}\widetilde{v}_x \widetilde{f} \\ \overline{\rho}\widetilde{v}_x f_v \\ \overline{\rho}\widetilde{v}_x \widetilde{Y}_c \\ \overline{\rho}\widetilde{v}_x Y_{cv} \\ \overline{\rho}\widetilde{v}_x \widetilde{Y}_1 \\ \vdots \\ \overline{\rho}\widetilde{v}_x \widetilde{Y}_n \end{bmatrix}, \quad \mathbf{F}_\mathrm{V} = \begin{bmatrix} 0 \\ \overline{\tau}_{xx} + \lambda_{xx} \\ \overline{\tau}_{xy} + \lambda_{xy} \\ \overline{\tau}_{xz} + \lambda_{xz} \\ \mathcal{W}_x - q_x - q_{tx} + (\mu + \mu_t\sigma^*)\frac{\partial k}{\partial x} \\ (\mu + \mu_t\sigma^*)\frac{\partial k}{\partial x} \\ (\mu + \mu_t\sigma)\frac{\partial \omega}{\partial x} \\ \overline{\rho}(\mathcal{D}_f + \mathcal{D}_t)\frac{\partial \widetilde{f}}{\partial x} \\ \overline{\rho}(\mathcal{D}_f + \mathcal{D}_t)\frac{\partial f_v}{\partial x} \\ \overline{\rho}(\mathcal{D}_{Y_c} + \mathcal{D}_t)\frac{\partial \widetilde{Y}_c}{\partial x} \\ \overline{\rho}(\mathcal{D}_{Y_c} + \mathcal{D}_t)\frac{\partial Y_{cv}}{\partial x} \\ -\mathcal{J}_x^1 - \mathcal{J}_{tx}^1 \\ \vdots \\ -\mathcal{J}_x^n - \mathcal{J}_{tx}^n \end{bmatrix} \qquad (A.11)$$

$$\mathbf{G}_{\mathrm{I}} = \begin{bmatrix} \overline{\rho}\widetilde{v}_y \\ \overline{\rho}\widetilde{v}_x\widetilde{v}_y \\ \overline{\rho}\widetilde{v}_y^2 + \overline{p} \\ \overline{\rho}\widetilde{v}_y\widetilde{v}_z \\ (\overline{\rho}\widetilde{e} + \overline{p})\widetilde{v}_y \\ \overline{\rho}\widetilde{v}_y k \\ \overline{\rho}\widetilde{v}_y \omega \\ \overline{\rho}\widetilde{v}_y \widetilde{f} \\ \overline{\rho}\widetilde{v}_y f_v \\ \overline{\rho}\widetilde{v}_y \widetilde{Y}_c \\ \overline{\rho}\widetilde{v}_y Y_{cv} \\ \overline{\rho}\widetilde{v}_y \widetilde{Y}_1 \\ \vdots \\ \overline{\rho}\widetilde{v}_y \widetilde{Y}_n \end{bmatrix}, \quad \mathbf{G}_{\mathrm{V}} = \begin{bmatrix} 0 \\ \overline{\tau}_{yx} + \lambda_{yx} \\ \overline{\tau}_{yy} + \lambda_{yy} \\ \overline{\tau}_{yz} + \lambda_{yz} \\ \mathcal{W}_y - q_y - q_{ty} + (\mu + \mu_t\sigma^*)\frac{\partial k}{\partial y} \\ (\mu + \mu_t\sigma^*)\frac{\partial k}{\partial y} \\ (\mu + \mu_t\sigma)\frac{\partial \omega}{\partial y} \\ \overline{\rho}(\mathcal{D}_f + \mathcal{D}_t)\frac{\partial \widetilde{f}}{\partial y} \\ \overline{\rho}(\mathcal{D}_f + \mathcal{D}_t)\frac{\partial f_v}{\partial y} \\ \overline{\rho}(\mathcal{D}_{Y_c} + \mathcal{D}_t)\frac{\partial \widetilde{Y}_c}{\partial y} \\ \overline{\rho}(\mathcal{D}_{Y_c} + \mathcal{D}_t)\frac{\partial Y_{cv}}{\partial y} \\ -\mathcal{J}_y^1 - \mathcal{J}_{ty}^1 \\ \vdots \\ -\mathcal{J}_y^n - \mathcal{J}_{ty}^n \end{bmatrix} \quad (\mathrm{A.12})$$

$$\mathbf{H}_{\mathrm{I}} = \begin{bmatrix} \overline{\rho}\widetilde{v}_z \\ \overline{\rho}\widetilde{v}_z \\ \overline{\rho}\widetilde{v}_z\widetilde{v}_y \\ \overline{\rho}\widetilde{v}_z^2 + \overline{p} \\ (\overline{\rho}\widetilde{e} + \overline{p})\widetilde{v}_z \\ \overline{\rho}\widetilde{v}_z k \\ \overline{\rho}\widetilde{v}_z \omega \\ \overline{\rho}\widetilde{v}_z \widetilde{f} \\ \overline{\rho}\widetilde{v}_z f_v \\ \overline{\rho}\widetilde{v}_z \widetilde{Y}_c \\ \overline{\rho}\widetilde{v}_z Y_{cv} \\ \overline{\rho}\widetilde{v}_z \widetilde{Y}_1 \\ \vdots \\ \overline{\rho}\widetilde{v}_z \widetilde{Y}_n \end{bmatrix}, \quad \mathbf{H}_{\mathrm{V}} = \begin{bmatrix} 0 \\ \overline{\tau}_{zx} + \lambda_{zx} \\ \overline{\tau}_{zy} + \lambda_{zy} \\ \overline{\tau}_{zz} + \lambda_{zz} \\ \mathcal{W}_z - q_z - q_{tz} + (\mu + \mu_t\sigma^*)\frac{\partial k}{\partial z} \\ (\mu + \mu_t\sigma^*)\frac{\partial k}{\partial z} \\ (\mu + \mu_t\sigma)\frac{\partial \omega}{\partial z} \\ \overline{\rho}(\mathcal{D}_f + \mathcal{D}_t)\frac{\partial \widetilde{f}}{\partial z} \\ \overline{\rho}(\mathcal{D}_f + \mathcal{D}_t)\frac{\partial f_v}{\partial z} \\ \overline{\rho}(\mathcal{D}_{Y_c} + \mathcal{D}_t)\frac{\partial \widetilde{Y}_c}{\partial z} \\ \overline{\rho}(\mathcal{D}_{Y_c} + \mathcal{D}_t)\frac{\partial Y_{cv}}{\partial z} \\ -\mathcal{J}_x^1 - \mathcal{J}_{tz}^1 \\ \vdots \\ -\mathcal{J}_x^n - \mathcal{J}_{tz}^n \end{bmatrix} \quad (\mathrm{A.13})$$

where $\mathcal{W}_x = \widetilde{v}_x(\overline{\tau}_{xx} + \lambda_{xx}) + \widetilde{v}_y(\overline{\tau}_{xy} + \lambda_{xy}) + \widetilde{v}_z(\overline{\tau}_{xz} + \lambda_{xz})$, $\mathcal{W}_y = \widetilde{v}_x(\overline{\tau}_{yx} + \lambda_{yx}) + \widetilde{v}_y(\overline{\tau}_{yy} + \lambda_{yy}) + \widetilde{v}_z(\overline{\tau}_{yz} + \lambda_{yz})$ and $\mathcal{W}_z = \widetilde{v}_x(\overline{\tau}_{zx} + \lambda_{zx}) + \widetilde{v}_y(\overline{\tau}_{zy} + \lambda_{zy}) + \widetilde{v}_z(\overline{\tau}_{zz} + \lambda_{zz})$.

$$
\mathbf{S}_{\mathrm{t}} = \begin{bmatrix} 0 \\ 0 \\ 0 \\ 0 \\ 0 \\ \mathcal{P} - \beta^* \overline{\rho} k \omega \\ \alpha \frac{\omega}{k} \mathcal{P} - \beta \overline{\rho} \omega^2 \\ 0 \\ 0 \\ 0 \\ 0 \\ 0 \\ \ldots \\ 0 \end{bmatrix} , \quad
\mathbf{S}_{\mathrm{c}} = \begin{bmatrix} 0 \\ 0 \\ 0 \\ 0 \\ 0 \\ 0 \\ 0 \\ 0 \\ 0 \\ 0 \\ 0 \\ \overline{\rho} \dot{\overline{\omega}}_1 \\ \ldots \\ \overline{\rho} \dot{\overline{\omega}}_N \end{bmatrix} , \quad
\mathbf{S}_{\mathrm{p}} = \begin{bmatrix} 0 \\ 0 \\ 0 \\ 0 \\ 0 \\ 0 \\ 0 \\ 2\overline{\rho} \mathcal{D}_t \frac{\partial \widetilde{f}}{\partial x_i} \frac{\partial \widetilde{f}}{\partial x_i} - 2C_f \overline{\rho} \omega f_v \\ \overline{\rho} \dot{\widetilde{\omega}}_{Y_c} \\ 2\overline{\rho} \mathcal{D}_t \frac{\partial \widetilde{Y}_c}{\partial x_i} \frac{\partial \widetilde{Y}_c}{\partial x_i} - 2C_{Y_c} \overline{\rho} \omega Y_{cv} + \\ 2\overline{\rho} \left(\widetilde{Y_c \dot{\omega}_{Y_c}} - \widetilde{Y}_c \dot{\widetilde{\omega}}_{Y_c} \right) \\ 0 \\ \vdots \\ 0 \end{bmatrix}
\quad \text{(A.14)}
$$

with

$$
\mathcal{P} = \lambda_{xx} \frac{\partial \widetilde{v}_x}{\partial x} + \lambda_{xy}\left(\frac{\partial \widetilde{v}_x}{\partial y} + \frac{\partial \widetilde{v}_y}{\partial x}\right) + \lambda_{yy} \frac{\partial \widetilde{v}_y}{\partial y} + \lambda_{xz}\left(\frac{\partial \widetilde{v}_x}{\partial z} + \frac{\partial \widetilde{v}_z}{\partial x}\right) + \lambda_{yz}\left(\frac{\partial \widetilde{v}_y}{\partial z} + \frac{\partial \widetilde{v}_z}{\partial y}\right) + \lambda_{zz} \frac{\partial \widetilde{v}_z}{\partial z}
$$

AUSM$^+$-up Approximate Riemann Solver

The AUSM$^+$-up scheme is the latest version in the AUSM-family [186, 237, 238] which is valid at all speed regimes and in a Mach-number-independent fashion. The difference between AUSM-family of schemes and other schemes is that the inviscid flux is split into two parts: (i) the convective part of the fluxes, $\mathbf{F}_c$; and (ii) pressure contributions to the fluxes, $\mathbf{P}$. The inviscid fluxes, $\mathbf{F}_I$, of the governing equations can then be written as:

$$\mathbf{F}_I = \mathbf{F}_c + \mathbf{P} = \dot{m}\mathbf{\Phi} + \mathbf{P} \tag{B.1}$$

where $\dot{m} = \overline{\rho}\widetilde{u}_x$ is the mass flux and vector $\mathbf{\Phi}$ is the vector of primitive variables such that

$$\dot{m}\mathbf{\Phi} = \overline{\rho}\widetilde{v}_x \left[\ 1 \, , \widetilde{v}_x \, , \widetilde{v}_y \, , \widetilde{v}_z \, , \widetilde{H} \, , k \, , \omega \, , f \, , f_v \, , Y_c \, , Y_{cv} \, , Y_1 \, , \ldots \, , Y_n \ \right]^{\mathrm{T}} \tag{B.2}$$

and

$$\mathbf{P} = \left[\ 0 \, , \bar{p} \, , 0 \, , 0 \, , 0 \, , 0 \, , 0 \, , 0 \, , 0 \, , 0 \, , 0 \, , 0 \, , \ldots \, , 0 \, , \ \right]^{\mathrm{T}} \tag{B.3}$$

In what follows, the cell interface labeled by subscript "1/2" straddles two neighboring cells labeled by subscripts "L" and "R", respectively, lying to the left and right of the interface.

The numerical flux, $\mathbf{F}_{1/2}$, at cell interface can be expressed in terms of mass flux $\dot{m}$ and vector $\mathbf{\Phi}$ as

$$\mathbf{F}_{1/2} = \dot{m}_{1/2}\mathbf{\Phi}_{\mathrm{L/R}} + \mathbf{P}_{1/2}, \tag{B.4}$$

where, $\mathbf{\Phi}_{\mathrm{L/R}}$ is the left and right vectors and will be determined in a simple upwind scheme,

$$\mathbf{\Phi} = \begin{cases} \mathbf{\Phi}_{\mathrm{L}}, & \text{if } \dot{m}_{1/2} > 0, \\ \mathbf{\Phi}_{\mathrm{R}}, & \text{otherwise.} \end{cases} \tag{B.5}$$

The mass flux, $\dot{m}$, is defined as

$$\dot{m}_{1/2} = u_{1/2}\bar{\rho}_{\text{L/R}} = a_{1/2}M_{1/2} \begin{cases} \bar{\rho}_{\text{L}}, & \text{if } u_{1/2} > 0, \\ \bar{\rho}_{\text{R}}, & \text{otherwise,} \end{cases} \tag{B.6}$$

where $u_{1/2}$ is the interface convective velocity, $a_{1/2}$ is the interface speed of the sound, $M_{1/2}$ is the interface Mach number, and $\bar{\rho}_{\text{L/R}}$ is the left and right density convected by $u_{1/2}$.

The interface Mach number, $M_{1/2}$, is determined in terms of the flow Mach number in the left neighbour and right neighbour cells, M_{L} and M_{R}, respectively, and evaluated using

$$M_{1/2} = \mathcal{M}^+_{(m)}(M_{\text{L}}) + \mathcal{M}^-_{(m)}(M_{\text{R}}) + M_p. \tag{B.7}$$

The split Mach numbers $\mathcal{M}^\pm_{(m)}$ are polynomial functions of degree $m = 1, 2, 4$, as given in [237] and have the form:

$$\mathcal{M}^\pm_{(4)}(M) = \begin{cases} \mathcal{M}^\pm_{(1)}, & \text{if } |M| \geq 1, \\ \mathcal{M}^\pm_{(2)}(1 \mp 16\beta\mathcal{M}^\mp_{(2)}), & \text{otherwise,} \end{cases} \tag{B.8}$$

where

$$\mathcal{M}^\pm_{(1)}(M) = \frac{1}{2}(M \pm |M|), \tag{B.9}$$

$$\mathcal{M}^\pm_{(2)}(M) = \pm\frac{1}{4}(M \pm 1)^2. \tag{B.10}$$

The left and right Mach numbers, $M_{\text{L/R}}$, can be defined by convective velocity, $u_{1/2}$, and the speed of sound, $a_{1/2}$, as follows:

$$M_{\text{L/R}} = \frac{u_{\text{L/R}}}{a_{\text{L/R}}}. \tag{B.11}$$

The pressure diffusion term, M_p, introduced to enhance calculations for low flow speeds or multi-phase flow, is defined to be

$$M_p = -\frac{K_p}{f_a}\max(1 - \sigma_p\bar{M}^2, 0)\frac{p_{\text{R}} - p_{\text{L}}}{\bar{\rho}_{1/2}a_{1/2}^2}, \tag{B.12}$$

where

$$\bar{\rho}_{1/2} = \frac{\bar{\rho}_{\text{L}} + \bar{\rho}_{\text{R}}}{2}, \tag{B.13}$$

$$a_{1/2} = \frac{a_{\text{L}} + a_{\text{R}}}{2}, \tag{B.14}$$

and

$$\bar{M}^2 = \frac{u_{\text{L}}^2 + u_{\text{R}}^2}{2a_{1/2}} \tag{B.15}$$

with $0 \leq K_p \leq 1$ and $\sigma_p \leq 1$. The scaling factor is defined by the reference Mach number M_0 as follows:

$$f_a(M_0) = M_0(2 - M_0) \in [0, 1], \tag{B.16}$$

where the reference Mach number is given by

$$M_0^2 = \min(1, \max(\bar{M}^2, M_\infty^2)) \in [0, 1]. \tag{B.17}$$

The formula for evaluating the pressure flux is similar to that for the mass flux and takes the form

$$p_{1/2} = \mathcal{P}_{(n)}^+(M_\mathrm{L})p_\mathrm{L} + \mathcal{P}_{(n)}^-(M_\mathrm{R})p_\mathrm{R} + p_u, \tag{B.18}$$

where $n = 1, 3, 5$ correspond to the degree of the polynomials $\mathcal{P}^\pm$, as in $\mathcal{M}^\pm$. In general, the fifth-degree polynomials proposed by Liou [237] are preferred because they are found to yield more accurate solutions. They are also expressed in terms of the split Mach number and can be written as

$$\mathcal{P}_{(5)}^\pm(M) = \begin{cases} \frac{1}{M}\mathcal{M}_{(1)}^\pm, & \text{if } |M| \geq 1, \\ \mathcal{M}_{(2)}^\pm[(\pm 2 - M) \mp 16\alpha M \mathcal{M}_{(2)}^\mp], & \text{otherwise,} \end{cases} \tag{B.19}$$

and the velocity difference (diffusion) term p_u is evaluated by

$$p_u = -K_u \mathcal{P}_{(5)}^+(M_\mathrm{L})\mathcal{P}_{(5)}^-(M_\mathrm{R})(\bar{\rho}_\mathrm{L} + \bar{\rho}_\mathrm{R})(f_a a_{1/2})(u_\mathrm{L} + u_\mathrm{R}), \tag{B.20}$$

using the parameters

$$\alpha = \frac{3}{16}(-4 + 5f_a^2) \in \left[-\frac{3}{4}, \frac{3}{16}\right], \tag{B.21}$$

$$\beta = \frac{1}{8} \tag{B.22}$$

with $0 \leq K_u \leq 1$. In this thesis work, $K_p = 0.25$, $K_u = 0.75$, and $\sigma_p = 1.0$ are used [186].

A more complete and detailed discussion is given in the recent paper by Liou [186].

References

[1] Department of Energy. Annual energy review, 2008. http://www.eia.doe.gov/aer, 2009.

[2] Chung K. Law. *Combustion Physics*. Cambridge University Press, 2006.

[3] Department of Energy. Annual energy review, 2006. http://www.eia.doe.gov/aer, 2007.

[4] International Energy Agency. CO_2 emissions from fuel combustion. http://www.iea.org/, 2009.

[5] United Nations. Kyoto protocol to the united nations framework convention on climate change. http://unfccc.int/resource/docs/convkp/kpeng.html, 1998.

[6] United Nations Framework Convention on Climate Change. Copenhagen accord. http://unfccc.int/resource/docs/2009/cop15/eng/l07.pdf, 2009.

[7] U. Maas and S. B. Pope. Simplifying chemical kinetics: Intrinsic low-dimensional manifolds in composition space. *Combustion and Flame*, pages 239–264, 1992.

[8] D. Veynante and Luc Vervisch. Turbulent combustion modeling. *Progress in Energy and Combustion Science*, 28:193–266, 2002.

[9] R. W. Bilger, S. B. Pope, K. N. C. Bray, and J. F. Driscoll. Paradigms in turbulent combustion research. *Proceedings of the Combustion Institute*, 30:21–42, 2005.

[10] A. M. Eaton, L. D. Smoot, S. C. Hill, and C. N. Eatough. Components, formulations, solutions, evaluation, and application of comprehensive combustion models. *Progress in Energy and Combustion Science*, 25:387–436, 1999.

[11] U. Piomelli. Large-eddy simulation: Achievements and challenges. *Prog. Aerospace Sci.*, 35:335–362, 1999.

[12] D. Veynante and T. Poinsot. Large eddy simulation of combustion instabilities in turbulent premixed burners. Annual Research Briefs 253–274, Center for Turbulence Research, NASA Ames/Stanford Univ., 2000.

[13] L. Selle, G. Lartigue, T. Poinsot, P. Kaufmann W. Krebs, and D. Veynante. Large-eddy simulation of turbulent combustion for gas turbines with reduced chemistry. In *Proceedings of the Summer Program*, pages 333 – 344, 2002.

[14] H. Pitsch. Large-eddy simulation of turbulent combustion. *Annual Review of Fluid Mechanics*, 38:453–482, 2006.

[15] Norbert Peters. *Turbulent Combustion*. Cambridge University Press, Cambridge, 1st edition, 2000.

[16] T. Poinsot and D. Veynante. *Theoretical and Numerical Combustion*. R.T. Edwards Inc., 2001.

[17] L. Vervisch. DNS and LES of turbulent combustion. Computational Fluid Dynamics in Chemical Reaction Engineering IV, June 19-24, 2005, Barga, Italy, 2005.

[18] D. Veynante and T. Poinsot. *New Tools in Turbulence Modeling, Les Houches School*, chapter Reynolds averaged and Large Eddy Simulation modeling for turbulent combustion, pages 105–135. Springer, 1997. URL http://www.cerfacs.fr/~cfdbib/repository/houches97.pdf.

[19] F. E. Hernàndez-Pérez, F.T.C. Yuen, C.P.T. Groth, and Ö.L.Gulder. LES of a laboratory-scale turbulent premixed bunsen flame using FSD, PCM-FPI and thickened flame models. accepted in the Proceedings of the Combustion Institute, doi:10.1016/j.proci.2010.06.010., 2010.

[20] R. O. Fox, editor. *Computational Models for Turbulent Reacting Flows*. Cambridge University Press, Cambridge, 2003.

[21] M. J. Berger. Adaptive mesh refinement for hyperbolic partial differential equations. *Journal of Computational Physics*, 53:484–512, 1984.

[22] M. J. Berger and P. Colella. Local adaptive mesh refinement for shock hydrodynamics. *Journal of Computational Physics*, 82:67–84, 1989.

[23] M.C. Thompson and J.H. Ferziger. An adaptive multigrid technique for the incompressible navier-stokes equations. *Journal of Computational Physics*, 82(1):94–121, 1989.

[24] J. J. Quirk. *An Adaptive Grid Algorithm for Computational Shock Hydrodynamics*. PhD thesis, Cranfield Institute of Technology, January 1991.

[25] K. G. Powell, P. L. Roe, and J. Quirk. Adaptive-mesh algorithms for computational fluid dynamics. In M. Y. Hussaini, A. Kumar, and M. D. Salas, editors, *Algorithmic Trends in Computational Fluid Dynmaics*, pages 303–337. Springer-Verlag, New York, 1993.

[26] D. De Zeeuw and K. G. Powell. An adaptively refined Cartesian mesh solver for the Euler equations. *Journal of Computational Physics*, 104:56–68, 1993.

[27] J. J. Quirk and U. R. Hanebutte. A parallel adaptive mesh refinement algorithm. Report 93-63, ICASE, August 1993.

[28] M. J. Berger and J. S. Saltzman. AMR on the CM-2. *Applied Numerical Mathematics*, 14:239–253, 1994.

[29] A. S. Almgren, T. Buttke, and P. Colella. A fast adaptive vortex method in three dimensions. *Journal of Computational Physics*, 113:177–200, 1994.

[30] J.B. Bell, M.J. Berger, J.S. Saltzman, and M. Welcome. A three-dimensional adaptive mesh refinement for hyperbolic conservation laws. *SIAM Journal on Scientific Computing*, 15:127–138, 1994.

[31] R. B. Pember, J. B. Bell, P. Colella, W. Y. Crutchfield, and M. L. Welcome. An adaptive cartesian grid method for unsteady compressible flow in irregular regions. *Journal of Computational Physics*, 120:278–304, 1995.

[32] M. J. Aftosmis, M. J. Berger, and J. E. Melton. Robust and efficient Cartesian mesh generation for component-base geometry. *AIAA Journal*, 36(6):952–960, 1998.

[33] A. S. Almgren, J. B. Bell, P. Colella, L. H. Howell, and M. J. Welcome. A conservative adaptive projection method for the variable density incompressible navier-stokes equations. *Journal of Computational Physics*, 142:1–46, 1998.

[34] R. B. Pember, L.H. Howell, J.B. Bell, P. Colella, W. Y. Crutchfield, M. A. Fiveland, and J.P. Jessee. An adaptive projection method for unsteady, low mach number combustion. *Combustion Science and Technology*, 140:123–168, 1998.

[35] J.P. Jessee, W.A. Fiveland, L.H. Howell, P. Colella, and R.B. Pember. An adaptive mesh refinement algorithm for the radiative transport equation. *Journal of Computational Physics*, 139(2):380–398, 1998.

[36] P. Colella, M. Dorr, and D. Wake. Numerical solution of plasma-fluid equations using locally refined grids. *Journal of Computational Physics*, 152:550–583, 1999.

[37] L.H. Howell, R.B. Pember, P. Colella, J.P. Jessee, and W. A. Fiveland. A conservative adaptive-mesh algorithm for unsteady, combined-mode heat transfer using the discrete ordinates method. *Numerical Heat Transfer*, 35:407–430, 1999.

[38] C. P. T. Groth, D. L. De Zeeuw, K. G. Powell, T. I. Gombosi, and Q. F. Stout. A parallel solution-adaptive scheme for ideal magnetohydrodynamics. Paper 99-3273, AIAA, June 1999.

[39] C. P. T. Groth, D. L. De Zeeuw, T. I. Gombosi, and K. G. Powell. Global three-dimensional MHD simulation of a space weather event: CME formation, interplanetary propagation, and and interaction with the magnetosphere. *Journal of Geophysical Research*, 105(A11):25,053–25,078, 2000.

[40] J. S. Sachdev, C. P. T. Groth, and J. J. Gottlieb. A parallel solution-adaptive scheme for predicting multi-phase core flows in solid propellant rocket motors. *International Journal of Computational Fluid Dynamics*, 19(2):157–175, 2005.

[41] X. Gao. *A Parallel Solution-Adaptive Method for Turbulent Non-Premixed Combusting Flows.* PhD thesis, University of Toronto, August 2008.

[42] W.C. Reynolds and M. Fatica. Stanford center for integrated turbulence simulations. Technical Paper 54–63, Stanford University, Marh/April 2000.

[43] G. Medic, G. Kalitzin, D. You, M. Herrmann, F. Ham, E. van der Weide, H. Pitsch, and J. Alonso. Integrated rans/les computations of turbulent flow through a turbofan jet engine. Annual Research Briefs 275–285, Stanford University, 2006.

[44] C. C. Douglas, A. Ern, and M. D. Smooke. Numerical simulation of flames using multigrid methods. In J. Wang, M. B. Allen, B. M. Chen, and T. Mathew, editors, *Iterative Methods in Scientific Computation*, volume 4 of *IMACS Series in Computational and Applied Mathematics*, pages 149–154. New Brunswick, 1998.

[45] A. Ern. *Vorticity-Velocity Modeling of Chemically Reacting Flows*. PhD thesis, Yale University, 1994.

[46] A. Ern, C.C. Douglas, and M.D. Smooke. Detailed chemistry modeling of laminar diffusion flames on parallel computers. *International Journal of Supercomputer Applications and High Performance Computing*, 10:225–236, 1995.

[47] F. Desprez. Practical aspects and experiences numerical simulation of a combustion problem on a paragon machine. *Parallel Computing*, 21:495–508, 1995.

[48] B. Nkonga and P. Charrier. Generalized parcel method for dispersed spray and message passing strategy on unstructured meshes. *Parallel Computing*, 28:369–398, 2002.

[49] J.B. Bell, M.S. Day, A.S. Almgren, M. J. Lijewski, and C. A. Rendleman. Adaptive numerical simulation of turbulent premixed combustion. In *Proceedings of the First MIT Conference on Computational Fluid and Solid Mechanics*, page 1, June 2001.

[50] J.B. Bell, M.S. Day, A.S. Almgren, M. J. Lijewski, and C. A. Rendleman. A parallel adaptive projection method for low Mach number flows. *International Journal for Numerical Methods in Fluids*, 40:209–216, 2002.

[51] J. Bell. AMR for low mach number reacting flow. http://repositories.cdlib.org/lbnl/ LBNL-54351, 2004.

[52] J. B. Bell, M.S. Day, C.A. Rendleman, S.E. Woosley, and M.A.Zingale. Adaptive low mach number simulations of nuclear flame microphysics. *Journal of Computational Physics*, 195:677–694, 2004.

[53] M. S. Day and J. B. Bell. Simulation of premixed turbulent flames. *Journal of Physics*, 46:43–47, 2006.

[54] John B. Bell, Marcus S. Day, Joseph F. Grcar, Michael J. Lijewski, James F. Driscoll, and Sergei A. Filatyev. Numerical simulation of a laboratory-scale turbulent slot flame. *Proceedings of the Combustion Institute*, 31:1299–1307, 2007.

[55] S. A. Northrup and C. P. T. Groth. Solution of laminar diffusion flames using a parallel adaptive mesh refinement algorithm. Paper 2005–0547, AIAA, January 2005.

[56] X. Gao and C. P. T. Groth. Parallel adaptive mesh refinement scheme for turbulent non-premixed combusting flow prediction. Paper 2006-1448, AIAA, January 2006.

[57] X. Gao and C. P. T. Groth. A parallel adaptive mesh refinement algorithm for predicting turbulent non-premixed combusting flows. *International Journal of Computational Fluid Dynamics*, 20(5):349–357, 2006.

[58] M. R. J. Charest, C. P. T. Groth, and Ö. L. Gülder. A computational framework for solving laminar reacting flows with soot formation. *Combustion Theory and Modelling*, 14(6):793–825, 2010.

[59] S. B. Pope. Transport equation for the joint probability density function of velocity and scalars in turbulent flow. *Physics of Fluids*, 24:588–596, 1981.

[60] S. B. Pope and Y. L. Chen. The velocity-dissipation probability density function model for turbulent flows. *Physics of Fluids*, pages 1437–1449, 1990.

[61] S. B. Pope and Emily S. C. Ching. Stationary probability density functions: An exact result. *Physics of Fluids*, pages 1529–1531, 1993.

[62] W. Kendal Bushe and Helfried Steiner. Conditional moment closure for large eddy simulation of nonpremixed turbulent reacting flows. *Physics of Fluids*, 11(7):1896–1906, 1999.

[63] R. W. Bilger. Conditional moment methods for turbulent reacting flows. *Physics of Fluids*, 5:436–444, 1993.

[64] A. Yu. Klimenko. Multicomponent diffusion of various admixtures in turbulent flow. *Fluid Dynamics (USSR)*, 25:327–334, 1990.

[65] M. R. Roomina and R. W. Bilger. Conditional moment closure (CMC) predictions of a turbulent methane-air jet flame. *Combustion and Flame*, 125(3):1176–1195, 2001.

[66] Y. M. Wright, G. De Paola, K. Boulouchos, and E. Mastorakos. Simulations of spray autoignition and flame establishment with two-dimensional CMC. *Combustion and Flame*, 143(4):402–419, 2005.

[67] Seung Hyun Kim, Chan Ho Choi, and Kang Y. Huh. Second-order conditional moment closure modeling of turbulent $CH_4/H_2/N_2$ jet diffusion flame. *Proceedings of the Combustion Institute*, 30:735–742, 2005.

[68] Paiboon Sripakagorn, Satoshi Mitarai, George Kosály, and Heinz Pitsch. Extinction and reignition in a diffusion flame: a direct numerical study. *Journal of Fluid Mechanics*, 518:231–2259, 2004.

[69] N. Swaminathan and R. W. Bilger. Analyses of conditional moment closure for turbulent premixed flames. *Combustion Theory and Modelling*, 5:241–260, 2001.

[70] H. Steiner and W. K. Bushe. Large eddy simulation of a turbulent reacting jet with conditional source-term estimation. *Physics of Fluids*, 13:754–769, 2001.

[71] M. Wang, J. Huang, and W. K. Bushe. Simulation of a turbulent non-premixed flame using conditional source-term estimation with trajectory generated low-dimensional manifold. *Proceedings of the Combustion Institute*, 31:1701–1709, 2007.

[72] B. Jin, R. Grout, and W. K. Bushe. Conditional source-term estimation as a method for chemical closure in premixed turbulent reacting flow. *Flow Turbulence and Combustion*, 81:563–582, 2008.

[73] M. M. Salehi, W. K. Bushe, and K. J. Daun. Application of conditional source-term estimation model for turbulence-chemistry interactions in a premixed flame. accepted in Combustion Theory and Modelling, doi: 10.1080/1364783, 2010.

[74] Luc Vervisch, Raphaël Hauguel, Pascale Domingo, and Matthieu Rullaud. Three facets of turbulent combustion modelling: DNS of premixed V-flame, LES of lifted nonpremixed flame and RANS of jet-flame. *Journal of Turbulence*, 4:1–36, 2004.

[75] Derek Bradley, L. K. Kwa, A. K. C. Lau, M. Missaghi, and S. B. Chin. Laminar flamelet modeling of recirculating premixed methane and propane-air combustion. *Combustion and Flame*, 71:109–122, 1988.

[76] D. Bradley, P. H. Gaskell, and X. J. Gu. The mathematical modeling of liftoff and blowoff of turbulent non-premixed methane jet flames at high strain rates. In *Twenty Seventh Symposium (International) on Combustion*, volume 27, pages 1199–1206, 1998.

[77] J. A. van Oijen and L. P. H. de Goey. Modeling of premixed laminar flames using flamelet-generated manifolds. *Combustion Science and Technology*, 161:113–137, 2000.

[78] J. A. van Oijen, F. A. Lammers, and L. P. H. de Goey. Modeling of complex premixed burner systems by using flame-generated manifold. *The Combustion Institute*, 127:2124–2134, 2001.

[79] V. Subramanian, P. Domingo, and L. Vervisch. Large eddy simulation of forced ignition of an annular bluff-body burner. *Combustion and Flame*, 157:579–601, 2010.

[80] Jean-Baptiste Michel, Olivier Colin, Christian Angelberger, and Denis Veynante. Using the tabulated diffusion flamelet model ADF-PCM to simulate a lifted methane-air jet flame. *Combustion and Flame*, 156:1318–1331, 2009.

[81] R. Vicquelin, B. Fiorina, S. Payet, N. Darabiha, and O. Gicquel. Coupling tabulated chemistry with compressible CFD solvers. Accepted in the Proceedings of the Combustion Institute, 2011.

[82] Joost A. M. de Swart, Rob J. M. Bastiaans, Jeroen A. van Oijen, L. Philip H. de Goey, and R. Stewart Cant. Inclusion of preferential diffusion in simulations of premixed combustion of hydrogen/methane mixtures with flamelet generated manifolds. *Flow Turbulence Combustion*, 85:473–511, 2010.

[83] Xi Jiang, K. H. Luo, , L. P. H. de Goey, R. J. M. Bastiaans, and J. A. van Oijen. Swirling and impinging effects in an annular nonpremixed jet flame. *Flow Turbulence Combustion*, 86:63–88, 2011.

[84] X. Gao, S. A. Northrup, and C. P. T. Groth. Parallel solution-adaptive method for two-dimensional non-premixed combusting flows. *Progress in Computational Fluid Dynamics*, 11(2):76–95, 2010.

[85] X. Gao and C. P. T. Groth. A parallel solution-adaptive method for three-dimensional turbulent non-premixed combusting flows. *Journal of Computational Physics*, 229(5):3250–3275, 2010.

[86] D.C. Wilcox. *Turbulence Modeling for CFD*. DCW Industries, 2002.

[87] K.K. Kuo. *Principles of Combustion*. John Wiley & Sons, 1986.

[88] Rutherford Aris. *Vectors, Tensors and the Basic Equations of Fluid Mechanics*. Dover Publications, New Jersey, 1989.

[89] J. D. Anderson. *Modern Compressible Flow with Historical Perspective*. McGraw-Hill, New York, 1990.

[90] S. Gordon and B. J. McBride. Computer program for calculation of complex chemical equilibrium compositions and applications I. analysis. Reference Publication 1311, NASA, 1994.

[91] B. J. McBride and S. Gordon. Computer program for calculation of complex chemical equilibrium compositions and applications ii. users manual and program description. Reference Publication 1311, NASA, 1996.

[92] C. R. Wilke. A viscosity equation for gas mixtures. *Journal of Chemical Physics*, 18:517–519, 1950.

[93] W. C. Gardiner. *Combustion Chemistry*. Springer-Verlag New York Inc., Boca Raton, 1984.

[94] S. A. Northrup. A parallel adaptive-mesh refinement scheme for predicting laminar diffusion flames. Master's thesis, University of Toronto, 2004.

[95] H. Tennekes and J. L. Lumley. *A First Course in Turbulence*. The MIT Press, Cambridge, Massachussets, 1983.

[96] A. N. Kolmogorov. Local structure of turbulence in an incompressible fluid for very large reynodls number. *Comptes rendus (Doklady) de l'Academie des Scinces de l'U.S.S.R*, 31:301–305, 1941.

[97] A. N. Kolmogorov. On degeneration of isotropic turbulence in an incompressible viscous liquid. *Comptes rendus (Doklady) de l'Academie des Scinces de l'U.S.S.R*, 31:538–540, 1941.

[98] D.C. Wilcox. *Turbulence Modeling for CFD*. DCW Industries, 2006.

[99] A. Favre. Statisical equations in turbulent gases. *SIAM*, pages 231–266, 1969.

[100] T. Cebeci and A. M. O. Smith. *Analysis of Turbulent Boundary Layers*. Academic Press, Toronto, 1974.

[101] B. Baldwin and H. Lomax. Thin-layer appromixation and algebraic model for separated turbulent flows. 16th AIAA Science Meeting, Huntsville, Ala., January 1978.

[102] L. Prandtl. Über ein neues formelsystem für die ausgebildete turbulenz. Nacr. Akad. Wiss. Göttingen, Math-Phys, 1945.

[103] P. Bradshaw, D. H. Ferris, and N. P. Atwell. Calculation of boundary layer development using the turbulent kinetic energy equation. *Journal of Fluid Mechanics*, 28:593–616, 1967.

[104] B. S. Baldwin and T. J. Barth. A one-equation turbulence transport model for high reynolds number wall-bounded flows, 1990. NASA Technical Memorandum 102847.

[105] P. R. Spalart and S. R. Allmaras. A one-equation turbulence model for aerodynamic flows. Paper 92-0439, AIAA, January 1992.

[106] T. J. Coakley. Turbulence modeling methods for the compressible navier-stokes equations. 16th AIAA Fluid and Plasma Dynamics Conference, Danvers, MA, July 1983.

[107] C. G. Speziale, R. Abid, and E. C. Anderson. A critical evaluation of two-equation models for near wall turbulence. Technical report, ICASE, June 1990.

[108] Shia-Hui Peng, Lars Davidson, and Sture Holmberg. A modified low-reynolds-number k-ω model for recirculating flows. *Journal of Fluids Engineering*, 119(4): 867–875, 1997.

[109] B. R. Smith. The k-kl turbulence and wall layer model for compressible flows. Paper 90-1483, AIAA, 1990.

[110] S. Zeierman and M. Wolfshtein. Turbulent time scale for turbulent flow calculations. *AIAA Journal*, 24(10):1606–1610, 1986.

[111] B. E. Launder and I. B. Sharma. Application of the energy-dissipation model of turbulence to the calculation of flow near a spinning disc. *Letters in Heat and Mass Transfer*, 1:131–137, 1974.

[112] D. C. Wilcox. Reassessment of the scale determining equation for advanced turbulence models. *AIAA Journal*, 26(11):1299–1310, October 1988.

[113] F. R. Menter. Two-equation eddy-viscosity turbulence models for engineering applications. *AIAA Journal*, 32(8):1598–1605, August 1994.

[114] R. M. C. So T. T. Sommer and Y. G. Lai. A near wall two-equation model for turbulent heat fluxes. Technical report, International Journal of Heat and Mass Transfer, 1992.

[115] B. Parent and J. P. Sislian. Validation of wilcox k-ω model for flows characteristic to hypersonic airbreathing propulsion. Technical Report 2, AIAA, 2004.

[116] D. Alexander. *Explicit Characteristic-Based High-Resolution Algorithms for Hyperbolic Conservation Laws with Stiff Source Terms*. PhD thesis, University of Toronto, 2006.

[117] W. Rodi. Experience with two-layer models combining the k-e model with a one-equation model near the wall. Technical report, AIAA, 1991.

[118] H. C. Chen and V. C. Patel. Near-wall turbulence models for complex flows including separation. *AIAA Journal*, 26(4):641–648, 1984.

[119] C. C. Chieng and B. E. Launder. On the calculation of turbulent heat transport downstream from an abrupt pipe expansion. *Numerical Heat Transfer*, 3:189–207, 1981.

[120] J. D. Anderson. *Hypersonic and High Temperature Gas Dynamics.* McGraw-Hill, New York, 1989.

[121] G. P. Smith, D. M. Golden, M. Frenklach, N. W. Moriarty, B. Eiteneer, M. Goldenberg, C. T. Bowman, R. K. Hanson, S. Song, W. C. Gardiner, V. V. Lissianski, and Z. Qin. GRI-Mech 3.0. http://www.me.berkeley.edu/gri_mech/.

[122] C. K. Westbrook and F. L. Dryer. Simplified reaction mechanisms for the oxidation of hydrocarbon fuels in flames. *Combustion Science and Technology*, 27:31–43, 1981.

[123] D.Veynante L. Vervisch. Turbulent combustion modeling. In *Introduction to turbulent combustion Lecture Series 1999-04*. von Karman Institute for Fluid Dynamics, Rhode Saint Genese, Belgium, 1999.

[124] K. N. C. Bray. The challenge of turbulent combustion. Paper, Twenty-Sixth Symposium (International) on Combustion/The Combustion Institute, 1996.

[125] B.F. Magnussen and B.H. Hjertager. On mathematical modeling of turbulent combustion with special emphasis on soot formation and combustion. In *Sixteenth Symposium (International) on Combustion*, pages 719–729. The Combustion Institute, 1976.

[126] Stephen R. Turns, editor. *An Introduction to Combustion.* McGraw-Hill, New York, 2000.

[127] H. J. Curran, P. Gaffuri, W. J. Pitz, and C. K. Westbrook. A comprehensive modeling study of iso-octane oxidation. *Combustion and Flame*, 129(3):253–280, 2002.

[128] R. P. Lindstedt and L. Q. Maurice. Detailed chemical-kinetic model for aviation fuels. *Journal of Plasma Physics*, 16:187–195, 2000.

[129] S. Delhaye, L. M. T. Somers, J. A. van Oijen, and L. P. H. de Goey. Incorporating unsteady flow-effects in flamelet-generated manifolds. *Combustion and Flame*, 155: 133–144, 2008.

[130] S. B. Pope. Computationally efficient implementation of combustion chemistry using *in situ* adaptive tabulation. *Combustion Theory and Modelling*, 1:41–63, 1997.

[131] N. Peters. Reducing mechanisms, 1991.

[132] S. H. Lam and D. A. Goussis. Conventional asymptotics and computational singular perturbation for simplified kinetics modeling, 1991.

[133] S. B. Pope and U. Maas. Simplifying chemical kinetics: Trajectory generated low-dimensional manifolds. *Mechanical and Aerospace Engineering Report:FDA 93-11*, 1993.

[134] M. Wang, J. Huang, A. Frisque, and W. K. Bushe. Generating trajectories for low-dimensional manifolds using the stochastic particle model. *Combustion Theory and Modelling*, 12(2):249–267, 2008.

[135] Shaheen R. Tonse, Nigel W. Moriarty, Michael Frenklach, and Nancy J. Brown. Computational economy improvements in prism. *International Journal of Chemical Kinetics*, 35(9):237–253, 2003.

[136] Zhuyin Ren and Stephen B. Pope. Entropy production and element conservation in the quasi-steady-state approximation. *Combustion and Flame*, 137:251–254, 2004.

[137] V. Bykov and U. Maas. The extension of ILDM concept to reaction-diffusion manifolds. *AIAA Journal*, 11(6):839–862, 2007.

[138] Zhuyin Ren and Stephen B. Pope. Reduced description of complex dynamics in reactive systems. *Journal of Physical Chemistry*, 111:8464–8474, 2007.

[139] R. W. Bilger. Turbulent flows with nonpremixed reactants. *Turbulent reacting flows*, pages 65–113, 1980.

[140] Paul A. Libby and F. A. Williams. Turbulent flows involving chemical reactions. *Annual Rev. of Fluid Mechanics*, 8:351–376, 1976.

[141] N. Peters. Laminar diffusion flamelet models in non-premixed turbulent combustion. *Prog. Energy Combustion Sci.*, 10:319–339, 1984.

[142] M. Chen, M. Herrmann, and N. Peters. Flamelet modeling of lifted turbulent methane/air and propane/air jet diffusion flames. *Proceedings of the Combustion Institute*, 28:167–174, 2000.

[143] Z. Wen, S. Yun, M. J. Thomson, and M. F. Lightstone. Modeling soot formation in turbulent kerosene/air jet diffusion flames. *Combustion and Flame*, 135:323–340, 2003.

[144] Fengshan Liu, Hongsheng Guo, and Gregory J. Smallwood. Evaluation of the laminar diffusion flamelet model in the calculation of an axisymmetric coflow laminar ethylene-air diffusion flame. *Combustion and Flame*, 144:605–618, 2006.

[145] M. D. Smooke, Y. Xu, R. M. Zurn, P. Lin, J. H. Frank, and M. B. Long. Computational and experimental study of OH and CH radicals in axisymmetric laminar diffusion flames. *The Combustion Institute*, 24:813–821, 1992.

[146] M. Nishioka, Y. Takemoto, H. Yamashita, and T. Takeno. Effects of multidimensionality on a diffusion flame. *The Combustion Institute*, 26:1071–1077, 1996.

[147] Olivier Gicquel, Nasser Darabiha, and Dominique Thévenin. Laminar premixed hyrogen/air counterflow flame simulations using flame prolongation of ILDM with differential diffusion. In *Proceedings of the Combustion Institute*, volume 28, pages 1901–1908, 2000.

[148] B. Fiorina, R. Baron, O. Gicquel, L. Vervisch, S. Carpentier, and N. Darabiha. Modelling non-adiabatic partially premixed flames using flame-prolongation of ILDM. *Combustion Theory and Modelling*, 7:449–470, 2003.

[149] B. Fiorina, O. Gicquel, L. Vervisch, S. Carpentier, and N. Darabiha. Premixed turbulent combustion modeling using tabulated detailed chemistry and PDF. *Proceedings of the Combustion Institute*, 30:867–874, 2005.

[150] Jéremy Galpin, Alexandre Naudin, Luc Vervich, Christian Angelberger, Olivier Colin, and Pascale Domingo. Large-eddy simulation of a fuel-lean premixed turbulent swirl-burner. *Combustion and Flame*, 155:247–266, 2008.

[151] Derek Bradley and A. K. C. Lau. The mathematical modelling of premixed turbulent combustion. *Pure and Applied Chemistry*, 62:803–814, 1990.

[152] J.-Y. Chen and W. Kollmann R. W. Dibble. Pdf modeling of turbulent nonpremixed methane jet flames. *Combustion Science and Technology*, 64(4):315–346, 1989.

[153] A. T. Norris and S. B. Pope. Modeling of extinction in turbulent diffusion flames by the velocity-dissipation-composition pdf method. *Combustion and Flame*, 100: 211–220, 1995.

[154] Vivek Saxena and Stephen B. Pope. Pdf simulations of turbulent combustion incorporating detailed chemistry. *Combustion and Flame*, 117:340–350, 1999.

[155] Pascale Domingo, Luc Vervisch, and Raphaël Hauguel Sandra Payet. DNS of a premixed turbulent V flame and LES of a ducted flame using a FSD-PDF subgrid scale closure with FPI-tabulated chemistry. *Combustion and Flame*, pages 566–586, 2005.

[156] P. Domingo, L. Vervisch, and D. Veynante. Large-eddy simulation of a lifted methane jet flame in a vitiated coflow. *Combustion and Flame*, 152:415–432, 2008.

[157] G. Ribert, M. Champion, O. Gicquel, N. Darabiha, and D. Veynante. Modeling nonadiabatic turbulent premixed reactive flows including tabulated chemistry. *Combustion and Flame*, 141:271–280, May 2005.

[158] B. Fiorina, O. Gicquel, L. Vervisch, S. Carpentier, and N. Darabiha. Approximating the chemical structure of partially premixed and diffusion counterflow flames using FPI flamelet tabulation. *Combustion and Flame*, 140:147–160, 2005.

[159] Jean-Baptiste Michel, Olivier Colin, and Denis Veynante. Comparison of differing formulations of the PCM model by their application to the simulation of an auto-igniting H_2/air jet. *Flow Turbulence Combustion*, pages 33–60, 2009.

[160] D. Goodwin and H. K. Moffat. Cantera. http://code.google.com/p/cantera/.

[161] H. Pitsch and N. Peters. A consistent flamelet formulation for non-premixed combustion considering differential diffusion effects. *Combustion and Flame*, 114:26–40, 1998.

[162] S. K. Liew, K. N. C. Bray, and J. B. Moss. A stretched laminar flamelet model of turbulent nonpremixed combustion. *Combustion and Flame*, 56:199, 1984.

[163] Stephen B. Pope. *Turbulent Flows*. Cambridge University Press, Cambridge, 2000.

[164] Rullaud Matthieu. *Modélisation de la combustion turbulente via une méthode de tabulation de la cinétique chimique détaillée couplée à des fonctions densités de probabilité Application aux foyers aéronautiques*. PhD thesis, L'INSA De ROUEN, June 2004.

[165] R. S. Barlow and J. H. Frank. Effects of turbulence on species mass fractions in methane/air jet flames. In *Twenty-Seventh Symposium (International) on Combustion*, pages 1087–1095, Pittsburgh, 1998. The Combustion Institute.

[166] Thomas D. Dreeben and Stephen B. Pope. Probability density function and reynolds-stress modeling of near-wall turbulent flows. *Physics of Fluids*, 9:154–163, 1997.

[167] J. M. Richardson, H. C. Howard, and R. W. Smith. page 814, 1953.

[168] D. B. Spalding. Concerning fluctuations in a round turbulent free jet. *Chemical Engineering Science*, 26:95–107, January 1971.

[169] F. C. Lockwood and A. S. Naguib. The prediction of fluctuations in the properties of free, round-jet, turbulent, diffusion flames. *Combustion and Flame*, 24:109–124, 1975.

[170] R. P. Rhodes and A. P. T. Harsha. On putting the 'turbulence' in turbulent reacting flows. Paper 72-68, AIAA, 1972.

[171] W. P. Jones. Models for turbulent flows with variable density and combustion. In W. Kollmann, editor, *von Karman Institute for Fluid Dynamics Lecture Series 1979-2, Prediction Methods for Turblent Flows*. Hemisphere Publication Corp., Washington, 1980.

[172] P. A. Libby and F. A. Williams. *Turbulent flows with nonpremixed reactants*. Springer-Verlag, Berlin, 1980.

[173] H. J. Kent and R. W. Bilger. Turbulent diffusion flames. In *Fourteenth International Symposium on Combustion*, page 615, 1973.

[174] P.A. Libby and F. A. Williams, editors. *Turbulent reacting flows*, chapter 4. Academic Press Inc., 1994.

[175] Jérémy Galpin. *Modélisation LES de la combustion avec une prise en compte des effets de cinétique détaillée et en perspective d'application moteur*. PhD thesis, IFP, Division Techniques d'Applications Énergétiques, September 2007.

[176] J. S. Sachdev. *Parallel Solution-Adaptive Method for Predicting Solid Propellant Rocket Motor Core Flows*. PhD thesis, University of Toronto, April 2007.

[177] Harvard Lomax, Thomas H. Pullian, and David W. Zingg. *Fundamentals of Computational Fluid Dynamics*. Springer-Verlag, New York, 2001.

[178] C. Hirsch. *Numerical Computation of Internal and External Flows, Volume 1, Fundamentals of Numerical Discretization*. John Wiley & Sons, Toronto, 1989.

[179] C. Hirsch. *Numerical Computation of Internal and External Flows, Volume 2, Computational Methods for Inviscid and Viscous Flows*. John Wiley & Sons, Toronto, 1990.

[180] J. J. Gottlieb and C. P. T. Groth. Assessment of Riemann solvers for unsteady one-dimensional inviscid flows of perfect gases. *Journal of Computational Physics*, 78:437–458, 1988.

[181] S. K. Godunov. Finite-difference method for numerical computations of discontinuous solutions of the equations of fluid dynamics. *Matematicheskii Sbornik*, 47: 271–306, 1959.

[182] P. L. Roe. Approximate Riemann solvers, parameter vectors, and difference schemes. *Journal of Computational Physics*, 43:357–372, 1981.

[183] S. Osher and F. Solomon. Upwind difference schemes for hyperbolic systems of conservation laws. *Mathematics of Computation*, 38(158):339–374, 1982.

[184] B. van Leer. On the relation between the upwind-difference schemes of Godunov's engquist osher and roe. *SIAM Journal for Scientific and Statistical Computing*, 5: 1–20, 1984.

[185] B. Einfeldt. On Godunov-type methods for gas dynamics. *SIAM Journal on Numerical Analysis*, 25:294–318, 1988.

[186] Meng-Sing Liou. A sequel to AUSM, part II: AUSM$^+$-up for all speeds. *Journal of Computational Physics*, 214:137–170, 2006.

[187] B. van Leer. Upwind and high-resolution methods for compressible flow: From donor cell to residual distribution schemes. *Communications in Computational Physics*, 1(2):192–206, 2006.

[188] J. P. Boris and D. L. Book. Flux-corrected transport. i. shasta, a fluid transport algorithm that works. *Journal of Computational Physics*, 11:38–69, 1973.

[189] B. van Leer. Towards the ultimate conservative difference scheme. II. Monotonicity and conservation combined in a second order scheme. *Journal of Computational Physics*, 14:361–370, 1974.

[190] A. Harten. High resolution schemes for hyperbolic conservation laws. *Journal of Computational Physics*, 49:357–393, 1983.

[191] V. Venkatakrishnan. On the accuracy of limiters and convergence to steady state solutions. Paper 93-0880, AIAA, January 1993.

[192] T. J. Barth. Recent developments in high order k-exact reconstruction on unstructured meshes. Paper 93-0668, AIAA, January 1993.

[193] S. R. Mathur and J. Y. Murthy. A pressure-based method for unstructured meshes. *Numerical Heat Transfer*, 31:191–215, 1997.

[194] B. van Leer, C. H. Tai, and K. G. Powell. Design of optimally-smoothing multi-stage schemes for euler equations. Paper 89-1933-CP, AIAA, June 1989.

[195] J. F. Lynn and B. van Leer. Multi-stage schemes for the Euler and Navier-Stokes equations with optimal smoothing. Paper 93-3355-CP, AIAA, July 1993.

[196] B. Kleb, B. van Leer, and B. Wood. Matching multi-stage schemes to viscous flow. Paper 2005-4708, AIAA, June 2005.

[197] C. P. T. Groth, D. L. De Zeeuw, T. I. Gombosi, and K. G. Powell. Three-dimensional MHD simulation of coronal mass ejections. *Advances in Space Research*, 26(5):793–800, 2000.

[198] M. J. Berger. *Adaptive Mesh Refinement for Hyperbolic Partial Differential Equations*. PhD thesis, Stanford University, January 1982.

[199] M. J. Berger and R. J. LeVeque. An adaptive Cartesian mesh algorithm for the Euler equations in arbitrary geometries. Paper 89-1930, AIAA, June 1989.

[200] D. L. De Zeeuw. *A Quadtree-Based Adaptively-Refined Cartesian-Grid Algorithm for Solution of the Euler Equations.* PhD thesis, University of Michigan, September 1993.

[201] R. L. Davis and J. F. Dannenhoffer. Decomposition and parallelization strategies for adaptive grid-embedding techniques. *International Journal of Computational Fluid Dynamics*, 1:79–93, 1993.

[202] M. Sun and K. Takayama. Conservative smoothing on an adaptive quadrilateral grid. *Journal of Computational Physics*, 150:143–180, 1999.

[203] X. Gao and C. P. T. Groth. Parallel adaptive mesh refinement scheme for three-dimensional turbulent non-premixed combustion. Paper 2008-1017, AIAA, January 2008.

[204] B. Smith, P. Bjorstad, and W. Gropp. *Domain Decomposition: Parallel Multilevel Methods for Elliptic Partial Differential Equations.* Cambridge University Press, 1996.

[205] C.-W. Ou and S. Ranka. Thoughts on the chimera method of simulation of three-dimensional viscous flow. In *Proceedings of the 5th Symposium on the Frontiers of Massively Parallel Computation*, pages 367–374, McLean, VA, February 1995, 1995. IEEE Computer Society Press.

[206] J.R. Pilkington and S. B. Baden. Dynamic partitioning of non-uniform structured workloads with space-filling curves. Paper 3, IEEE Transaction on Parallel and Distributed Systems, 1996.

[207] M. J. Aftosmis, M. J. Berger, and S. M. Murman. Applications of space-filling curves to cartesian methods for cfd. Paper 2004-1232, AIAA, January 2004.

[208] W. Gropp, E. Lusk, and A. Skjellum. *Using MPI.* MIT Press, Cambridge, Massachussets, 1999.

[209] W. Gropp, E. Lusk, and R. Thakur. *Using MPI-2.* MIT Press, Cambridge, Massachussets, 1999.

[210] J. S. Sachdev and C. P. T. Groth. A mesh adjustment scheme for embedded boundaries. *Communications in Computational Physics*, 2(6):1095–1124, 2007.

[211] J. G. McDonald and C. P. T. Groth. Numerical modeling of micron-scale flows using the gaussian moment closure. Paper 2005-5035, AIAA, June 2005.

[212] L. Ivan and C. P. T. Groth. High-order central eno finite-volume scheme with adaptive mesh refinement. Paper 2007-4323, AIAA, June 2007.

[213] I. K. Puri, K. Seshadri, M. D. Smooke, and D. E. Keyes. A comparison between numerical calculations and experimental measurements of the structure of a counterflow methane-air diffusion flame. *Combustion Science and Technology*, 56:1–22, 1987.

[214] Fernando Biagioli and Felix Güthe. Effect of pressure and fuel-air unmixedness on NO_x emissions from industrial gas turbine burners. *Combustion and Flame*, 151: 274–288, 2007.

[215] Guillaume Godel, Pascale Domingo, and Luc Vervisch. Tabulation of NOx chemistry in large-eddy simulation of non-premixed turbulent flames. *Proceedings of the Combustion Institute*, 32:1555–1561, 2009.

[216] R. K. Mohammed, M. A. Tanoff, M. D. Smooke, A. M. Schaffer, and M. B. Long. Computational and experimental study of a forced, time-varying, axisymmetric, laminar diffusion flame. In *Twenty-Seventh Symposium (International) on Combustion*, pages 693–702, Pittsburgh, 1998. The Combustion Institute.

[217] J.Laufer. The structure of turbulence in fully developed pipe flow. Report 1174, NACA, 1954.

[218] International workshop on measurement and computation of turbulent non-premixed flames. http://www.ca.sandia.gov/TNF/.

[219] A. R. Masri, R. W. Dibble, and R. S. Barlow. The structure of turbulent non-premixed flames of methanol over a range of mixing rates. *Combustion and Flame*, 89:167–185, 1992.

[220] A. R. Masri, R. W. Dibble, and R. S. Barlow. Raman-rayleigh measurements in bluff body stabilised flames of hydrocarbon fuels. In *Twenty-fourth Symposium (International) on Combustion*, pages 317–324. The Combustion Institute, 1992.

[221] A. R. Masri, B. B. Dally, and R. S. Barlow. The structure of the recirculation zone of a bluff-body combustor. In *Twenty-fifth Symposium (International) on Combustion*, pages 1301–1308. The Combustion Institute, 1994.

[222] A. R. Masri, J. B. Kelman, and B. B. Dally. The instantaneous spatial structure of the recirculation zone in bluff-body stabilised flames. In *Proceedings of the Combustion Institute*, pages 1031–1038. The Combustion Institute, 1998.

[223] L. Fallot, M. Gonzalez, R. Elamraoui, and M. Obounou. Modelling finite-rate chemistry effects in nonpremixed turbulent combustion: Test on the bluff-body stabilized flame. *Combustion and Flame*, 110:298–318, 1997.

[224] B. B. Dally, D. F. Fletcher, and A. R. Masri. Modelling of turbulent flames stabilised on a bluff-body. *Combustion Theory and Modelling*, 2:193–219, 1998.

[225] B. B. Dally, A. R. Masri, R. S. Barlow, and G. J. Fiechtner. Instantaneous and mean compositional structure of bluff-body stabilised nonpremixed flames. *Combustion Theory and Modelling*, 114:119–148, 1998.

[226] G. Turpin and J. Troyes. Validation of a two-equation turbulence model for axisymmetric reacting and non-reacting flows. Paper 2000–3463, AIAA, July 2000.

[227] B. Merci. *An Unstructured Parallel Algorithm for Large Eddy and Conjugate Heat Transfer Simulations*. PhD thesis, Ghent University, 2000.

[228] B. Merci, E. Dick, J. Vierendeels, D. Roekaerts, and T. W. J. Peeters. Application of a new cubic turbulence model to piloted and bluff-body diffusion flames. *Combustion and Flame*, 126(1-2):1533–1556, 2001.

[229] S. A. Northrup and C. P. T. Groth. Solution of laminar combusting flows using a parallel implicit adaptive mesh refinement algorithm. Fourth International Conference on Computational Fluid Dynamics, Ghent, Belgium, July 10–14, 2006, July 2006.

[230] S. A. Northrup and C. P. T. Groth. Prediction of unsteady laminar flames using a parallel implicit adaptive mesh refinement algorithm. In *Proceedings of the U. S. National Combustion Meeting, Ann Arbor, Michigan, U.S.A., May 17–20, 2009*, page paper 23H3, 2009.

[231] C. P. T. Groth and S. A. Northrup. Parallel implicit adaptive mesh refinement scheme for body-fitted multi-block mesh. Paper 2005-5333, AIAA, June 2005.

[232] Jean-Baptiste Michel, Olivier Colin, and Denis Veynante. Modeling ignition and chemical structure of partially premixed turbulent flames using tabulated chemistry. *Combustion and Flame*, 152:80–99, 2008.

[233] Francisco Emanuel Hernàndez Pérez. *Subfilter Scale Modelling For Large Eddy Simulation Of Lean Hydrogen-Enriched Turbulent Premixed Combustion*. PhD thesis, University of Toronto, 2011.

[234] L. Ivan and C. P. T. Groth. High-order Central ENO finite-volume scheme with adaptive mesh refinement for the advection-diffusion equation. In *Proceedings of the 5th International Conference on Computational Fluid Dynamics, Seoul, Korea, July 7–11*, 2008.

[235] L. Ivan and C. P. T. Groth. High-order solution-adaptive central essentially non-oscillatory (ceno) method for viscous flows. Paper 2011–367, AIAA, January 2011.

[236] Lucian Ivan. *Development of High-Order CENO Finite-Volume Schemes with Block-Based Adaptive Mesh Renfinement*. PhD thesis, University of Toronto, June 2011.

[237] M.-S. Liou and C. J. Steffen. A new flux splitting scheme. *Journal of Computational Physics*, 107:23–39, 1993.

[238] M.-S. Liou. A sequel to AUSM: AUSM$^+$. *Journal of Computational Physics*, 129: 364–382, 1996.